



Virginia Commonwealth University  
**VCU Scholars Compass**

---

Theses and Dissertations

Graduate School

---

2016

## Electrochemical Studies of Cerium and Uranium in LiCl-KCl Eutectic for Fundamentals of Pyroprocessing Technology

Dalsung Yoon

Follow this and additional works at: <https://scholarscompass.vcu.edu/etd>

 Part of the [Nuclear Engineering Commons](#)

© The Author

---

Downloaded from

<https://scholarscompass.vcu.edu/etd/4602>

This Dissertation is brought to you for free and open access by the Graduate School at VCU Scholars Compass. It has been accepted for inclusion in Theses and Dissertations by an authorized administrator of VCU Scholars Compass. For more information, please contact [libcompass@vcu.edu](mailto:libcompass@vcu.edu).

# Electrochemical Studies of Cerium and Uranium in LiCl-KCl Eutectic for Fundamentals of Pyroprocessing Technology

A dissertation submitted in partial fulfillment of the requirements for the degree of Doctor of Philosophy

by  
Dalsung Yoon

Mechanical and Nuclear Engineering, Virginia Commonwealth University

Richmond, Virginia

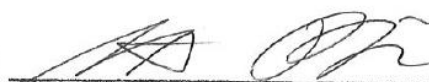
December 2016

Major Professor: Supathorn Phongikaroon, Ph.D

Mechanical and Nuclear Engineering  
Virginia Commonwealth University

This is to certify that the dissertation prepared by Dalsung Yoon entitled “Electrochemical Studies of Cerium and Uranium in LiCl-KCl Eutectic for Fundamentals of Pyroprocessing Technology” has been approved by his committee as satisfactory completion of the dissertation requirement for the degree of Doctor of Philosophy.

Major Professor:



Date: 12-8-2016

**Supathorn Phongikaroon, Ph.D.**

Committee  
Members:



Date: 12/13/2016

**Sama Bilbao y Leon, Ph.D.**



Date: 12-13-2016

**Jessika V. Rojas, Ph.D.**



Date: 12-5-2016

**Julio C. Alvarez, Ph.D.**



Date: December 2,  
2016

**Vivek Utgikar, Ph.D**

## ACKNOWLEDGMENTS

First of all, I would like to thank my advisor, Supathon (Supy) Phongikaroon. Without his guidance, patience, and understanding, I would not make it this far, especially with my publications and dissertation. Not only that, I would not forget about him considering me in his family circle when I look back at my PhD life in some day. Also, I want to thank my committee members, Drs. Sama, Rojas, Alvarez, Utgikar for taking time to improve the quality of my research and dissertation. Also, I want to express the gratefulness to Department of Mechanical and Nuclear Engineering at VCU for these opportunities and supports.

I would like to recall all people in Idaho Falls. I started my Ph. D program in University of Idaho (UI) with Dr. Supy. Thank you for the warm hospitality when I and my family first came to the United States. Specially, I was lucky to meet Alice and mom Debbie at UI. Also, I would like to thank Robert, Josh, Mike, and Michael for all discussions and helps allowing me to adapt to these new circumstances. Mike and Michael had been good teachers for me to learn some slangs but unfortunately they are far from me now. Mom and dad (Dabbie and Rick), I love you the most and thank you for taking us into your family. My family had a hard time to forget about the activities in Idaho, especially going out camping with you guys. Also, I want to thank Korean families, Drs. Choi, Yoo, Yoon, Ahn, Cho, Kim, and Park for taking care of me and my family. I miss all of these people and wonderful memories in Idaho Falls.

As coming back to Richmond area, I would like to thank all fellow students. Thanks Ammon for doing a carpool to work and brain storming throughout our Ph.D. program. Thanks Michael and Hunter for discussions on electrochemical topics and talks in the lab. Also, I want to thank Samaneh, Taha, and Riyadh. In addition, I am truly grateful to Noah's family for helping and hanging out with my family.

Finally, I am indebted to my family, specially my wife, Jihyun, for full support and taking care of our children (Dongwook, Dayoung, and Jara). Although I spent so much time in the lab for my research, I would like to say that I love all of you. Lastly, I would like to send my gratefulness and love to my dad, mom, grandmother, brother, and my parents-in-law living in Korea.

## TABLE OF CONTENTS

<b>ACKNOWLEDGMENTS .....</b>	<b>iii</b>
<b>LIST OF TABLES .....</b>	<b>viii</b>
<b>LIST OF FIGURES .....</b>	<b>x</b>
<b>LIST OF ABBREVIATIONS AND SYMBOLS .....</b>	<b>xvi</b>
<b>ABSTRACT .....</b>	<b>xix</b>
<b>Chapter 1 Introduction.....</b>	<b>1</b>
1.1 Pyroprocessing.....	3
1.2 Electrorefiner (ER).....	4
1.3 Motivation.....	8
1.4 Goal/Outcome .....	9
1.5 Approach.....	10
1.6 Organization of the Dissertation .....	11
<b>Chapter 2 Literature Survey.....</b>	<b>13</b>
2.1 Molten salt in electrorefining and general electrochemistry.....	13
2.2 Uranium Studies.....	14
2.2.1 Redox process and Apparent Standard Potential ( $E^{0*}$ ) .....	15
2.2.2 Diffusion coefficient .....	18
2.2.3 Exchange current density .....	20
2.3 Review of the electrochemical techniques.....	22
2.3.1 Cyclic voltammetry (CV) .....	22
2.3.2 Open circuit potential (OCP) .....	26
2.3.3 Electrochemical impedance spectroscopy (EIS).....	27
2.3.4 Tafel and linear polarization (LP) methods .....	32

2.4 Summary .....	34
<b>Chapter 3 Experimental setup and procedures .....</b>	<b>35</b>
3.1 Equipment .....	35
3.2 Experimental preparation.....	41
3.2.1 Reagents and crucibles.....	41
3.2.2 Electrodes: Working, Counter, and Reference Electrode .....	43
3.2.3 Electrode assembly .....	47
3.2.4 Sample preparations for ICP-MS Analysis.....	49
3.3 Summary .....	50
<b>Chapter 4 Experimental Development with Ce as a Surrogate Material for U (Preliminary studies) .....</b>	<b>52</b>
4.1 Electrochemical properties and analyses of $\text{CeCl}_3$ in LiCl-KCl eutectic salt.....	52
4.1.1 Introduction.....	52
4.1.2 Particular experimental setup and routine.....	53
4.1.3 Results and Discussion .....	55
4.1.3.1 Cyclic voltammetry (CV) of the LiCl-KCl- $\text{CeCl}_3$ system.....	55
4.1.3.2 Electrochemical impedance spectroscopy (EIS).....	64
4.1.3.3 Analysis on practical application .....	74
4.1.4 Conclusions.....	77
4.2 Electrochemical and Thermodynamic Properties of $\text{CeCl}_3$ on Liquid Cadmium Cathode (LCC) in LiCl-KCl Eutectic Salt .....	78
4.2.1 Introduction.....	78
4.2.2 Detailed Experimental Setup and Preparation .....	80
4.2.3 Results and Discussion .....	84
4.2.3.1 Cyclic voltammetry (CV) of the LiCl-KCl- $\text{CeCl}_3$ on the LCC .....	84
4.2.3.2 Open circuit chronopotentiometry in LiCl-KCl- $\text{CeCl}_3$ - $\text{CdCl}_2$ .....	89

4.2.3.3 Linear polarization (LP) and Tafel methods on LCC in LiCl-KCl-CeCl <sub>3</sub> .....	97
4.2.4 Conclusions.....	102
4.3 Summary .....	103
<b>Chapter 5 Uranium Electrochemical Studies in Molten LiCl-KCl Eutectic .....</b>	<b>105</b>
5.1 Introduction.....	105
5.2 Detailed Experimental Setup and Program.....	106
5.3 Results and discussion .....	108
5.3.1 Diffusion coefficient of UCl <sub>3</sub> in LiCl-KCl .....	108
5.3.2 Apparent standard potentials of U <sup>3+</sup> /U via CV and OCP .....	113
5.3.3 Activity coefficient of UCl <sub>3</sub> .....	119
5.3.4 Exchange current density of U <sup>3+</sup> /U.....	122
5.3.4.1 EIS.....	122
5.3.4.2 LP and Tafel methods .....	128
5.3.4.3 Cyclic voltammetry (CV) .....	133
5.3.4.4 Data comparison and practical analysis .....	135
5.3.5 Effects of GdCl <sub>3</sub> on U properties .....	141
5.4 Summary .....	145
<b>Chapter 6 Summary and Future Work .....</b>	<b>148</b>
6.1 Background.....	148
6.2 Literature Data for U and Electrochemical Techniques .....	148
6.3 Experimental setup and procedure.....	150
6.4 Preliminary studies with Ce surrogate .....	151
6.4.1 Measurement of Ce properties by using a solid cathode in LiCl-KCl.....	151
6.4.2 Measurement of Ce properties on liquid cadmium cathode .....	154
6.5 Measurements of uranium properties.....	156

6.6 Future Works .....	161
<b>Reference</b> .....	162
Appendix A. Data from Literatures .....	172
Appendix B. Data from U-Gd mixtures.....	175
Appendix C. Exchange Current Density of $\text{Sm}^{3+}/\text{Sm}^{2+}$ Reaction in LiCl-KCl Molten Salt .....	180



## LIST OF TABLES

<b>Table 1.1</b> Reprehensive used driver fuel composition and equilibrium potential of the elements	7
<b>Table 1.2</b> The fission product dissolution (wt%) from used EBR-II driver fuel into LiCl-KCl salt [19].....	8
<b>Table 1.3</b> Estimated schedule and timeframe for the present project .....	11
<b>Table 2.1</b> Physical properties of the salt mixtures [34-36] .....	14
<b>Table 2.2</b> Summary of electrochemical techniques used in each chapter and measured properties .....	34
<b>Table 3.1</b> Material summaries for reagents and crucibles used in the present study .....	43
<b>Table 3.2</b> Potential differences between Ag/AgCl reference electrodes and Cl <sub>2</sub> /Cl reference at different temperatures [60] .....	47
<b>Table 4.1</b> Detailed experimental program for electrochemical measurements of CeCl <sub>3</sub> .....	55
<b>Table 4.2</b> Steps of CV measurements and data acquisition .....	58
<b>Table 4.3</b> Diffusion coefficients (D) measured from CV experiments and activation energy (E <sub>a</sub> ) at different concentrations and temperatures .....	61
<b>Table 4.4</b> Thermodynamic information from the literature [53]and calculated values .....	64
<b>Table 4.5</b> Steps for the measurements of EIS spectra and curve fitting.....	70
<b>Table 4.6</b> The applied overpotential ( $\eta$ ) and measured charge transfers (R <sub>ct</sub> ) times electrode surface area (S) values at different concentrations and temperatures .....	71
<b>Table 4.7</b> Calculated exchange current density (i <sub>0</sub> ) and rate constant (k <sup>0</sup> ) for the charge transfer at different concentrations and temperatures .....	72
<b>Table 4.8</b> Steps for the measurements of CV data using LCC.....	87
<b>Table 4.9</b> Summary of the measurement step for OCC method .....	93
<b>Table 4.10</b> The partial molar Gibbs free energies and activities of Ce in two-phase coexisting state at various temperatures .....	93
<b>Table 4.11</b> The enthalpies and entropies of Ce-Cd intermetallic compound formations.....	97
<b>Table 4.12</b> Description for data acquisition from LP and Tafel methods .....	98
<b>Table 4.13</b> The values of i <sub>0</sub> of Ce on Cd measured by both Tafel and LP methods .....	101
<b>Table 5.1</b> Electrolyte concentration and the working electrode surface area for each experimental run .....	108

<b>Table 5.2</b> Thermodynamic information from the literature [53] and calculated values .....	121
<b>Table 5.3</b> Thermodynamic data evaluated by OCP and CV methods.....	121
<b>Table 5.4</b> Summary of $i_0$ and $k^0$ for $U/U^{3+}$ reaction measured by the EIS method.....	128
<b>Table 5.5</b> Linear models for concentration (mole fraction) and temperature (K) dependence..	138
<b>Table 5.6</b> The pre-exponential factors and activation energies for $U/U^{3+}$ based on the data from EIS measurements.....	141
<b>Table 5.7</b> Thermodynamic properties of $UCl_3$ in $LiCl-KCl-UCl_3-GdCl_3$ mixture salts .....	146
<b>Table 6.1</b> Diffusion coefficients and activity coefficients of $UCl_3$ in $LiCl-KCl$ salt.....	153
<b>Table 6.2</b> Linear relationships of the exchange current densities against the inverse temperature based on the experimental data .....	153
<b>Table 6.3</b> Summary of apparent standard, Gibb free energy, and activity coefficient of $UCl_3$ .	158
<b>Table 6.4</b> Summary of the uranium properties with $GdCl_3$ additions.....	160
<b>Table A.1</b> Summary of literatures performed to understand U properties in application of pyroprocessing technology .....	172
<b>Table A.2</b> Summary of diffusion coefficients for $U^{3+}$ in $LiCl-KCl$ from literatures .....	173
<b>Table A.3</b> Summary of apparent standard potentials of $U/U^{3+}$ from literatures .....	173
<b>Table A.4</b> Thermodynamic properties of $UCl_3$ in $LiCl-KCl$ reported by literature.....	174
<b>Table A.5</b> Exchange current density of $U/U^{3+}$ in $LiCl-KCl$ from literature studies .....	174
<b>Table C.1</b> Impedance parameters measured from the curve fitting analysis .....	184
<b>Table C.2</b> The calculated $i_0$ and $k^0$ at different concentrations and temperatures .....	184

## LIST OF FIGURES

<b>Figure 1.1</b> Schematic flowsheet of pyroprocessing based on spent fuel treatment. ....	4
<b>Figure 1.2</b> Engineering scale electrorefiner at INL Fuel Conditioning Facility, Mark IV (left) and Mark V (right) [19]. ....	6
<b>Figure 2.1</b> Comparison of the apparent standard potential in LiCl-KCl salt reported by various researchers (Note: CV = cyclic voltammetry, CP = chronopotentiometry, and OCP = open circuit potential). ....	17
<b>Figure 2.2</b> Activity coefficients of $\text{UCl}_3$ in LiCl-KCl reported by previous literatures.....	18
<b>Figure 2.3</b> Plot of the diffusion coefficients of $\text{UCl}_3$ in LiCl-KCl salt reported by various researchers.....	19
<b>Figure 2.4</b> Plot of $i_0$ from literatures. The values were measured with a tungsten electrode.....	21
<b>Figure 2.5</b> (a) Illustrations of (a) a typical potential waveform in CV, and (b) a typical reversible CV response with reduction and oxidation reactions. ....	23
<b>Figure 2.6</b> An example of OCP measurement in 0.5 wt % $\text{UCl}_3$ -LiCl-KCl eutectic salt at 773 K. ....	27
<b>Figure 2.7</b> Sinusoidal potential input and sinusoidal current response in typical EIS measurements [58]. ....	30
<b>Figure 2.8</b> An equivalent circuit for Voigt model which is composed with resistance and capacitance. ....	31
<b>Figure 2.9</b> An ideal Nyquist curve for the Voigt model. $R_s$ is bulk solution resistance and $R_{ct}$ is the charge transfer resistance on electrode surface. ....	31
<b>Figure 2.10</b> An example of Tafel plot for anodic and cathodic branches [55]. ....	33
<b>Figure 2.11</b> An example of current-potential curve at small overpotential region. ....	33
<b>Figure 3.1</b> Glovebox systems (RAMI (top) and RAMII (bottom)) for electrochemical experiments. ....	37
<b>Figure 3.2</b> (a) Digital control panel on the glovebox systems reading oxygen and water levels and (b) a portable oxygen analyzer from Advanced Instruments Inc. ....	38
<b>Figure 3.3</b> Pancake detector frisking meter (left) and hand survey meter (right) from Atlantic Nuclear Corporation.....	38
<b>Figure 3.4</b> (a) Kerrlab melting furnace, and (b) Muffle furnace from Thermo Scientific. ....	39

<b>Figure 3.5</b> Mettler Toledo balance placed in the glovebox systems. ....	39
<b>Figure 3.6</b> VSP-300 potentiostat/galvanostat, Biologic Science Instrument. ....	40
<b>Figure 3.7</b> Agilent 7900 ICP-MS instrument installed in the Radiochemistry laboratory. ....	40
<b>Figure 3.8</b> Depleted uranium samples: (a) LiCl-KCl - 73 wt% $\text{UCl}_3$ eutectic, and (b) uranium plates provided by INL. ....	42
<b>Figure 3.9</b> Alumina crucible (left) and Inconel crucible (right) placed in safety crucible for preliminary and uranium studies, respectively. ....	42
<b>Figure 3.10</b> (a) Tungsten rod sheathed with alumina tube, (b) measurement of submerged electrode area in the salt by using digital caliper. ....	45
<b>Figure 3.11</b> Prepared AgCl salt rods. ....	46
<b>Figure 3.12</b> (a) Pyrex tube with thin end for ionic conductivity, (b) Ag/AgCl reference built in Pyrex tube. ....	46
<b>Figure 3.13</b> Electrode assembly for electrochemical applications. ....	48
<b>Figure 3.14</b> Electrode assembly parts and its diagram. ....	49
<b>Figure 4.1</b> Schematic sketch of the experimental setup of all electrochemical experiments. ....	54
<b>Figure 4.2</b> Cyclic-voltammogram of pure LiCl-KCl eutectic salt at 773 K at the scan rate of 0.1 $\text{V s}^{-1}$ . Tungsten rod (2 mm in diameter) was used as cathode electrode, and the surface area was 0.471 $\text{cm}^2$ . ....	56
<b>Figure 4.3</b> Cyclic-voltammogram of $\text{CeCl}_3$ in LiCl-KCl at 773 K at scan rates of 0.05, 0.1, 0.15, and 0.2 $\text{V s}^{-1}$ : (a) 0.5 wt % $\text{CeCl}_3$ , (b) 2 wt % $\text{CeCl}_3$ (c) 4 wt % $\text{CeCl}_3$ . ....	57
<b>Figure 4.4</b> Plots of the peak currents versus the square roots of the scan rates at (a) 0.5 wt%, (b) 2 wt%, (c) 4 wt% $\text{CeCl}_3$ . ....	59
<b>Figure 4.5</b> Plots of diffusion coefficient of $\text{Ce}^{3+}$ versus inverse temperature at different $\text{CeCl}_3$ concentrations (0.5, 2, and 4 wt %). ....	60
<b>Figure 4.6</b> Plot of apparent standard potentials versus temperature. ....	63
<b>Figure 4.7</b> Activity coefficients of $\text{CeCl}_3$ in LiCl-KCl, compared with literature values. ....	63
<b>Figure 4.8</b> Equivalent circuit for the electrochemical cell showing bulk solution resistance, charge transfer resistance, CPEs and Warburg impedance. ....	66
<b>Figure 4.9</b> Nyquist plot for 0.5 wt % of $\text{CeCl}_3$ in LiCl-KCl at 723 K on a tungsten electrode. The frequency was from 50 kHz to 50 mHz, and the amplitude of applied sinus potential was 10 mV. ....	

Applied potentials were ranging from -2.169 to -2.174 V with an equilibrium potential of -2.169 V.....	66
<b>Figure 4.10</b> Measured and fitted Nyquist plots at temperatures of 698, 723, 748, 773, and 798 K: (a) 0.5 wt % $\text{CeCl}_3$ ; (b) 2 wt % $\text{CeCl}_3$ ; and (c) 4 wt % $\text{CeCl}_3$ . ....	69
<b>Figure 4.11</b> Plots of exchange current densities versus inverse temperature from various experiment sets at $\text{CeCl}_3$ concentrations of 0.5 wt%, 2wt%, and 4 wt%, compared with values measured by Marsden and Pesic [61]. ....	70
<b>Figure 4.12</b> Plot of $\ln(i_0)$ versus inverse temperature showing Arrhenius dependency.....	73
<b>Figure 4.13</b> Plot of $i_0/I_0$ versus $\exp(-E_a/RT)$ . ....	74
<b>Figure 4.14</b> Plot of diffusion coefficients for $\text{UCl}_3$ from other studies, comparing with the diffusion coefficients of $\text{CeCl}_3$ in this study. ....	75
<b>Figure 4.15</b> Plot of the exchange current densities for $\text{U}^{3+}/\text{U}$ reaction from other research studies comparing with those of $\text{Ce}^{3+}/\text{Ce}$ measured in this study. ....	76
<b>Figure 4.16</b> A schematic design of the experimental setup for electrochemical experiments. ....	82
<b>Figure 4.17</b> Purified Cd rods under argon environment. ....	83
<b>Figure 4.18</b> Solid cadmium cooled fast to room temperature in a Pyrex crucible and (b) a sketch showing measured dimensions of half elliptical dome. ....	83
<b>Figure 4.19</b> Cyclic voltammograms of a $\text{LiCl-KCl-1 wt\% CeCl}_3$ solution on the LCC at 748 K with the surface area of $0.729 \text{ cm}^2$ .....	85
<b>Figure 4.20</b> (a) The cyclic voltammogram of a $\text{LiCl-KCl-1 wt\% CeCl}_3$ after subtraction of background current of $\text{LiCl-KCl}$ , and (b) peak cathodic currents as a function of the square root of the scan rate. The surface area was $0.729 \text{ cm}^2$ . ....	86
<b>Figure 4.21</b> Plot of the diffusion coefficients of $\text{Ce}^{3+}$ on the LCC versus inverse temperature, comparing with values on the tungsten cathode measured in Section 4.1.....	89
<b>Figure 4.22</b> A cyclic voltammogram of $\text{LiCl-KCl-CeCl}_3\text{-CdCl}_2$ with the scan rate of $50 \text{ mV s}^{-1}$ . Concentrations of $\text{CeCl}_3$ and $\text{CdCl}_2$ were $6.86 \times 10^{-5} \text{ mol cm}^{-3}$ and $7.81 \times 10^{-6} \text{ mol cm}^{-3}$ , respectively. ....	90
<b>Figure 4.23</b> An example of the open circuit chronopotentiogram of Ce at Cd-coated tungsten electrode at 773 K. The applied current was $1 \mu\text{A}$ . ....	92
<b>Figure 4.24</b> Variation of the Gibbs free energies of Ce-Cd intermetallic compound formations as a function of temperature. ....	96

<b>Figure 4.25</b> Tafel plots for $\text{Ce}^{3+}/\text{Ce}$ on the LCC with respect to incremental change of Ce mole fraction in Cd. The scan rate was $0.5 \text{ mV s}^{-1}$ , and the surface area was $0.731 \text{ cm}^2$ .....	100
<b>Figure 4.26</b> Plots of current versus potential in the region of small overpotential for $\text{Ce}^{3+}/\text{Ce}$ redox in the LiCl-KCl at 773 K at different mole fractions of Ce in Cd. The scan rate of $0.5 \text{ mV s}^{-1}$ and the surface area of $0.731 \text{ cm}^2$ were used for all measurements.....	100
<b>Figure 4.27</b> Plots of $i_0$ for the $\text{Ce}^{3+}/\text{Ce}$ couple from both Tafel and LP methods regarding to Ce mole fraction in the LCC. The Ce solubility limit in Cd is 0.006 in mole fraction. ....	101
<b>Figure 5.1</b> Schematic design of electrode assembly and electrochemical cell in Muffle furnace. .....	107
<b>Figure 5.2</b> Cyclic voltammograms in LiCl-KCl-1.0 wt% $\text{UCl}_3$ at 773 K. The potential was swept at the scan rate from $50 \text{ mV s}^{-1}$ to $200 \text{ mV s}^{-1}$ . ....	109
<b>Figure 5.3</b> Cyclic voltammograms at concentrations of (a) 1.0 wt% $\text{UCl}_3$ , (b) 2.0 wt% $\text{UCl}_3$ , and (c) 4.0 wt% $\text{UCl}_3$ in LiCl-KCl eutectic salt at 773 K. The potential was swept at the scan rate from $50 \text{ mV s}^{-1}$ to $200 \text{ mV s}^{-1}$ . ....	110
<b>Figure 5.4</b> Diffusion coefficients of $\text{UCl}_3$ in LiCl-KCl as a function of temperature.....	112
<b>Figure 5.5</b> Cyclic voltammograms in LiCl-KCl-4wt% $\text{UCl}_3$ at 773 K with faster scan rates ranging from $700 \text{ mV s}^{-1}$ to $1500 \text{ mV s}^{-1}$ .....	112
<b>Figure 5.6</b> Diffusion coefficients of $\text{UCl}_3$ in LiCl-KCl. The values for 4wt% were measured by using Eq. (2-13) (black triangle) and Eq. (2-12) (red circle). ....	113
<b>Figure 5.7</b> Apparent standard potentials for $\text{U}^{3+}/\text{U}$ couple versus $\text{Cl}_2/\text{Cl}^-$ measured via CV techniques with Eq. (2-15). ....	114
<b>Figure 5.8</b> Potential plateaus results from OCP experiments in LiCl-KCl-0.5 wt% $\text{UCl}_3$ at temperature ranging 723 K to 798 K. ....	116
<b>Figure 5.9</b> Plots of the equilibrium potentials of $\text{U}^{3+}/\text{U}$ in LiCl-KCl versus (a) mole fraction and (b) logarithm of mole fraction.....	117
<b>Figure 5.10</b> The apparent standard potentials of $\text{U}^{3+}/\text{U}$ in LiCl-KCl salt measured via OCP and calculated in different methods. ....	118
<b>Figure 5.11</b> The averaged values of $\text{EU}_3 +/\text{U}_0 *$ via CV and OCP technologies, compared with literature values. ....	119
<b>Figure 5.12</b> The values of $\gamma\text{U}_3 +$ measured via OCP and CV methods compared with literature data. ....	120

<b>Figure 5.13</b> (a) Nyquist plots measured in $\text{UCl}_3$ -0.5 salt at 748 K. The applied potential was changed from -1.490 V to -1.510V to find the minimum overpotential. (b) Repetition with the applied potential amplitude ranging from 5 mV to 10 mV at -1.499 V.....	125
<b>Figure 5.14</b> The measured and fitted impedance spectra in the salt of (a) $\text{UCl}_3$ -0.5, (b) $\text{UCl}_3$ -1.0, (c) $\text{UCl}_3$ -2.0, and (d) $\text{UCl}_3$ -4.0 at temperature ranging from 723 K to 798 K. Applied potential amplitude was 7 mV, and the chi-square goodness of fit ( $\chi^2$ ) was less than 0.003.....	126
<b>Figure 5.15</b> (a) plots the $i_0$ of $\text{U}/\text{U}^{3+}$ against temperature for different concentrations, and (b) plots the $i_0$ of $\text{U}/\text{U}^{3+}$ versus mole fraction of the $\text{UCl}_3$ under different temperatures. ....	127
<b>Figure 5.16</b> (a) Current density versus potential at small overpotential region ( $< 5$ mV) in $\text{UCl}_3$ -0.5 salt; (b) Plot of $\log(i_0)$ versus overpotential in $\text{UCl}_3$ -0.5 salt; and (c) Plot of $\log(i_0)$ versus overpotential in $\text{UCl}_3$ -1.0, $\text{UCl}_3$ -2.0, and $\text{UCl}_3$ -4.0 at 748 K. The scan rate was used at $5 \text{ mV s}^{-1}$ . ....	130
<b>Figure 5.17</b> Plots of $i_0$ results measured by LP methods under different scan rates for (a) $\text{UCl}_3$ -0.5, (b) $\text{UCl}_3$ -1.0, (c) $\text{UCl}_3$ -2.0, and (d) $\text{UCl}_3$ -4.0. ....	131
<b>Figure 5.18</b> (a) Plots of $i_0$ values measured by LP and Tafel methods for concentrations of 0.5 wt%, 1.0 wt%, 2.0 wt%, and 4.0 wt% and (b) magnifying scale for the comparison of $i_0$ values between LP and Tafel methods at 0.5 wt% $\text{UCl}_3$ .....	132
<b>Figure 5.19</b> (a) Cyclic voltammogram at the scan rate of $50 \text{ mV s}^{-1}$ in $\text{UCl}_3$ -0.5 salt at 748 K, and (b) the magnifying scale of the small overpotential region (from (a)) for measuring the charge transfer resistance from the slope. ....	134
<b>Figure 5.20</b> Plots of $i_0$ by using CV method for $\text{U}/\text{U}^{3+}$ in $\text{UCl}_3$ -0.5, $\text{UCl}_3$ -1.0, $\text{UCl}_3$ -2.0, and $\text{UCl}_3$ -4.0 salt at the different temperatures with the standard deviations. ....	135
<b>Figure 5.21</b> (a) The $i_0$ values measured by the four different methods in the present study, and (b) the reported values of $i_0$ for $\text{U}/\text{U}^{3+}$ from different literature studies are being superimposed. ....	137
<b>Figure 5.22</b> Natural logarithm of $i_0$ against the inverse temperature. ....	139
<b>Figure 5.23</b> (a) $i_0/I_0$ versus $\exp(-E_a/RT)$ , and (b) $i_0/i_{0,\text{max}}$ versus mole fraction.....	140
<b>Figure 5.24</b> Cyclic voltammogram in $\text{LiCl-KCl-1wt\% UCl}_3\text{-1wt\% GdCl}_3$ at 773 K, measured at scan rate from $50 \text{ mV s}^{-1}$ to $200 \text{ mV s}^{-1}$ . ....	142
<b>Figure 5.25</b> Plots of diffusion coefficients measured in $\text{LiCl-KCl-UCl}_3\text{-GdCl}_3$ mixtures (No. 5 – 10), which were compared with original data sets (Section 5.3.1) at 773 K. ....	143

<b>Figure 5.26</b> The equilibrium potentials of $U^{3+}/U$ measured with presence of $GdCl_3$ , which were superimposed in the original trend of the equilibrium potential at 773 K. ....	143
<b>Figure 5.27</b> The exchange current densities measured in U-Gd samples, compared with the values measured with pure $UCl_3$ salts at 773 K. ....	145
<b>Figure B.1</b> Cyclic voltammogram in (a) sample no. 5, (b) sample no. 6, (c) sample no. 7, (d) sample no. 8, (e) sample no. 9, (f) sample no. 10 at temperature of 773 K. The scan rate was ranging from $50 \text{ mV s}^{-1}$ to $200 \text{ mV s}^{-1}$ . ....	177
<b>Figure B.2</b> The measured and fitted impedance spectra in the mixture salts (sample no. 5 – 10) at 773 K. ....	178
<b>Figure B.3</b> Equilibrium potentials of $U^{3+}/U$ in $LiCl-KCl-UCl_3-GdCl_3$ samples (no. 5 – 10), measured by OCP method. U metal was pre-deposited on the tungsten rod by applying potential at -1.6 V (vs. $Ag/AgCl$ ) for 30 seconds. ....	179
<b>Figure C.1</b> Nyquist plots of $Sm^{3+}/Sm^{2+}$ at 773 K at concentrations of (a) 1 wt% $SmCl_3$ (b) 2 wt% $SmCl_3$ (c) 3 wt% $SmCl_3$ . The electrode area was $0.911 \text{ cm}^2$ . ....	182
<b>Figure C.2</b> The equivalent circuit for the interface between the electrode and bulk salt, which is composed with resistances and CPEs. ....	182
<b>Figure C.3</b> Examples of the measured and fitted Nyquist plots at 773 K. $\chi^2 < 0.07$ . ....	183
<b>Figure C.4</b> Plot of $\ln(i_0)$ against $1/T$ to show the Arrhenius temperature dependence. ....	183



## LIST OF ABBREVIATIONS AND SYMBOLS

Abbreviations	Meaning
ANL	Argonne national laboratory
CPE	Constant phase element
CP	Chronopotentiometry
CV	Cyclic voltammetry
EBR-II	Experimental breeder reactor-II
EIS	Electrochemical impedance spectroscopy
ER	Electrorefiner
ICP-MS	Inductively coupled plasma-mass spectrometry
INL	Idaho national laboratory
LCC	Liquid cadmium cathode
LP	Linear polarization
MA	Minor actinide
OCC	Open circuit chronopotentiometry
OCP	Open circuit potential
PUREX	Plutonium uranium redox extraction
Redox	Reduction-oxidation
RSS	Radiation safety section
SNM	Special nuclear material
UNF	Used nuclear fuel
VCU	Virginia Commonwealth University

Symbols	Physical meaning	Unit
a	Activity	
$\alpha$	Transfer coefficient	
C	Concentration	mol cm <sup>-3</sup>
C <sub>p</sub>	Heat capacity	kJ mol <sup>-1</sup> K <sup>-1</sup>

D	Diffusion coefficient	$\text{cm}^2 \text{s}^{-1}$
$D_0$	Pre-exponential factor for diffusivity	$\text{cm}^2 \text{s}^{-1}$
E	Equilibrium potential	V
$E_a$	Activation energy	$\text{kJ mol}^{-1}$
$E^0$	Standard reduction potential	V
$E^{0*}$	Apparent standard reduction potential	V
$E_p$	Peak potential in CV	V
$E_{cp}$	Cathodic peak potential in CV	V
$E_{p/2}$	Half peak potential in CV	V
F	Faraday's constant	$\text{C mol}^{-1}$
$\Delta G^0$	Standard Gibbs free energy	$\text{J mol}^{-1} \text{K}^{-1}$
$\Delta G^{0*}$	Partial molar Gibbs free energy	$\text{J mol}^{-1} \text{K}^{-1}$
$\Delta G^{sc}$	Gibbs free energy at super cooled state	$\text{kJ mol}^{-1} \text{K}^{-1}$
$\Delta G^{\text{Formation}}$	Gibbs free energy for the formation	$\text{kJ mol}^{-1} \text{K}^{-1}$
$\Delta G^{\text{Fusion}}$	Gibbs free energy for fusion	$\text{kJ mol}^{-1} \text{K}^{-1}$
$\gamma$	Activity coefficient	
$\Delta H^{\text{Fusion}}$	Enthalpy of fusion	$\text{kJ mol}^{-1}$
i	Current	A
$i_p$	Peak current	A
$i_0$	Exchange current density	$\text{A cm}^{-2}$
$I_0$	Pre-exponential factor for exchange current density	$\text{A cm}^{-2}$
$k^0$	Rate constant	$\text{cm s}^{-1}$
n	Number of electrons transferred	
R	Universal gas constant	$\text{J mol}^{-1} \text{K}^{-1}$
$R_{ct}$	Charge transfer resistance	ohm
$R^2$	Coefficient of determination	
S	Working electrode surface area	$\text{cm}^2$
$\Delta S^{\text{Fusion}}$	Entropy of fusion	$\text{kJ mol}^{-1} \text{K}^{-1}$
T	Absolute temperature	K
$T_m$	Melting temperature	K

$v$	Scan rate in CV	$V\ s^{-1}$
$X$	Mole fraction	

## ABSTRACT

Understanding the characteristics of special nuclear materials in LiCl-KCl eutectic salt is extremely important in terms of effective system operation and material accountability for safeguarding pyroprocessing technology. By considering that uranium (U) is the most abundant and important element in the used nuclear fuel, measurements and analyses of U properties were performed in LiCl-KCl eutectic salt. Therefore, the electrochemical techniques such as cyclic voltammetry (CV), open circuit potential (OCP), Tafel, linear polarization (LP), and electrochemical impedance spectroscopy (EIS) were conducted under different experimental conditions to explore the electrochemical, thermodynamic, and kinetic properties of U in LiCl-KCl eutectic. The ultimate goal of this study was to develop proper methodologies for measuring and analyzing the exchange current density ( $i_0$ ) of  $U^{3+}/U$  reaction, which has not been fully studied and understood in literature.

In the preliminary study, cerium (Ce) was selected as a surrogate material for uranium and its behavior was being explored with the developments of experimental methods. CV was performed to evaluate Ce properties such as the diffusion coefficients (D), apparent standard reduction potential ( $E^{0*}$ ), Gibbs free energy ( $\Delta G$ ), and activity coefficient ( $\gamma$ ). In addition, EIS methods were adapted and specific experimental procedures were established for the proper  $i_0$  measurements providing repeatable and reproducible data sets. The  $i_0$  values for  $Ce^{3+}/Ce$  pair were ranging from  $0.0076 \text{ A cm}^{-2}$  to  $0.016 \text{ A cm}^{-2}$ , depending on the experimental conditions. These preliminary results give insight in developing the experimental setups and methods to evaluate the properties of U in LiCl-KCl. Plus, Ce is one of the lanthanide (Ln) fission products in electrorefiner (ER) system; therefore, the resulting data values yield useful information of the fundamental behaviors of Ln elements in the system.

Based on these developed methodologies, the experimental designs and routines were established to explore the main properties (e.g.,  $D$ ,  $E^{0*}$ , etc.) of  $\text{UCl}_3$  in  $\text{LiCl-KCl}$  eutectic salt under different concentrations (0.5 wt% to 4 wt%  $\text{UCl}_3$ ) and temperatures (723 K to 798 K). Specially, the  $i_0$  values of  $\text{U}^{3+}/\text{U}$  were evaluated via EIS, LP, Tafel, and CV methods. All  $i_0$  values had linear trends with the change of concentration and temperature; however, these values measured by LP, Tafel, and CV methods were greatly influenced by the change in electrode surface area. Overall, the  $i_0$  values agreed within 33% relative error range with the EIS method being the most consistent and accurate in comparison to reported literature values. The measured values of  $i_0$  were ranging from  $0.0054 \text{ A cm}^{-2}$  to  $0.102 \text{ A cm}^{-2}$ . Therefore, an extremely reliable database for  $i_0$  was provided and it is feasible to anticipate the  $i_0$  kinetics in other experimental conditions by using the provided equation models. Furthermore,  $\text{GdCl}_3$  was added to the  $\text{LiCl-KCl-UCl}_3$  system to explore the effects of other elements on the U properties such as the diffusion coefficients, thermodynamic properties, and  $i_0$  kinetics. The diffusion coefficient was generally decreased by 12 ~ 35% with addition of  $\text{GdCl}_3$  in  $\text{LiCl-KCl-UCl}_3$ ; however, the apparent standard potentials and exchange current density follow the same trends with data obtained without  $\text{GdCl}_3$  additions. Hence, the results indicate that the thermodynamic and kinetic values for  $\text{U}^{3+}/\text{U}$  reaction in  $\text{LiCl-KCl}$  eutectic salt are not greatly influenced by the presence of  $\text{GdCl}_3$ .

## Chapter 1 Introduction

Nuclear power produces a significant portion of electricity worldwide nowadays. The reported number of commercial nuclear power plants operating in 2014 was 438 with a global generating capacity of 376.2 GW(e) [1]. Seventy of reactors were under the construction [1] and continuous expansion of nuclear power is expected in the future with increasing demand of energy. As the nuclear power production has increased, the management of the used nuclear fuel (UNF) became an important issue due to the political, economic, and societal concerns in the nuclear industry [2]. The total amount of UNF cumulatively generated worldwide by 2014 was 204,421 tHM, and it increases from year to year [3]. The used fuel storage capacity in 2014 was 201,722 tHM and the global reprocessing capacity was only 3,800 tHM/year [3]. Therefore, in terms of saving fuel resources and solving the issue of storage capacity, the significance of recovering components from the used fuel will continue to grow in the future [2].

Reprocessing UNF can be more invaluable when it is considered that 96 percent of uranium remains after the fuel is permanently removed from reactor, which can be re-used after suitable retreatments [2, 4]. Two methods have been widely investigated and implemented for the reprocessing of the nuclear fuel, which are referred as aqueous reprocessing and pyroprocessing [4]. The aqueous reprocessing utilizes a method known as PUREX (Pu-U recovery extraction), which is the most common and well developed technique. In the PUREX process, pure U and Pu are separated through chemical adjustments and several cycles of solvent extractions by using highly concentrated nitric acid [4, 5, 6]. By experiencing the renaissance of nuclear energy worldwide, pure U and Pu productions gave rise to several concerns about proliferation of nuclear materials. From the safeguarding aspect of reprocessing UNF, pyroprocessing technology has been considered as an alternative method for future reprocessing [2, 4, 6, 7].

Pyroprocessing was originally developed by the Argonne National Laboratory (ANL) and currently is operated at Idaho National Laboratory (INL) to treat used metallic fuels from Experimental Breeder Reactor-II (EBR-II) [8-10]. This technology uses molten salt electrolytes as a media instead of using acid solutions or organic solvents [4, 9]. In these electrolytes, U, Pu, and minor actinides (MAs) can be recovered by electrochemical reduction on cathode electrodes. In comparison to the conventional aqueous methods which have superior maturity to date, pyroprocessing technology provides the following unique benefits: 1) intrinsic proliferation-resistant features by Pu recovery as a mixture, 2) compact facilities for fuel recovery and fabrication, 3) critically-safe condition for processing high enriched fuel, and 4) rapid on-site support for fast reactor fuel cycle [6, 11]. In addition, a low radiation sensitivity of the salt electrolyte allows the early reprocessing of UNF after discharge [2], which will minimize the chance of a loss of coolant accidents in the spent fuel pool [12]. With these noble features, the main purpose of pyroprocessing technology is not only to treat the irradiated nuclear fuels, but to reduce volume of the nuclear waste, recycle actinides, and close the fast reactor fuel cycle [13]. Therefore, there are considerable ongoing research and development on pyroprocessing technologies in many countries [4]. For example, the research teams in South Korea have constructed and operated an engineering scale demonstration facility with non-radioactive materials for the purpose of pyroprocessing research [14]. On another aspect, Russia has already demonstrated the production of mixed oxide fuels through pyroprocessing technology and plans to use the technology for the development of a closed fuel cycle by 2020 [4].

## 1.1 Pyroprocessing

Pyroprocessing technology, also known as electrochemical process, electrometallurgical reprocessing, or pyrochemical technology, has been considered as a promising way to treat metal/oxide form of UNF from the nuclear fuel cycle [8-10]. Figure 1.1 illustrates schematically the flow sheet of the process [5, 6]. Despite of its original development purpose, oxide form of used fuels from light water reactor can also be treated through the head-end process, known as electrolytic oxide reduction. In the electrolytic oxide reduction process, the used oxide fuel is loaded into a cathode basket in a molten  $\text{LiCl-Li}_2\text{O}$  salt at 923 K and chemically reduced into metal form by the reaction with Li metal, which is electrochemically deposited on the cathode [15]. In 2006, INL successfully converted 50 g of the used light water reactor (LWR) fuel into metal form in their hot cell facility [16]. Then, the metal fuels are transferred into the anode basket of an electrolyzer (ER). While U, Pu, MAs, and rare earth materials are anodically dissolved into the  $\text{LiCl-KCl}$  eutectic salt from the anode basket, only U is recovered on the solid cathode by controlling the voltage applied on the cathode. After that, the residual U, Pu, and MAs are simultaneously collected by using a liquid cadmium cathode (LCC) due to the fact that activity of the elements get very small in liquid metal [17, 18]. The deposits (U and U-Pu-MA mixtures) from the cathode electrodes go to the cathode processor. The process is basically in a high temperature vacuum furnace where the adhering salt or cadmium are evaporated and pure metal product are left [10]. The ingot products from the cathode processor are fabricated into new metal fuel in an injection casting furnace [8] which can be used in fast reactors. The electrolyte salt from the ER system is recycled by removing actinides through the ion exchange method and the separated fission products (Cs, Rb, Sr, Ba, Br, I, Y, Sm, Eu, etc.) are immobilized into ceramic waste forms



[10]. After operating the ER system, zirconium and noble metal fission products are left in the anode basket, which are processed into alloy metal waste form for the disposal [10].

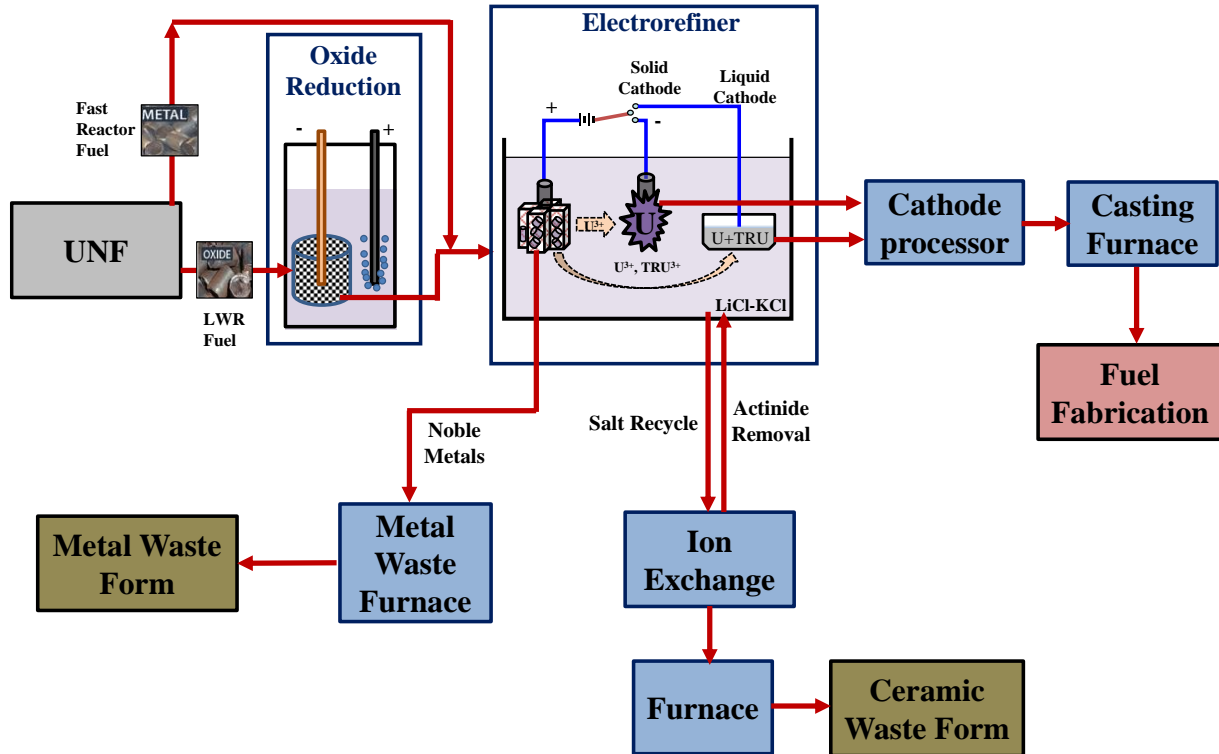


**Figure 1.1** Schematic flowchart of pyroprocessing based on spent fuel treatment.

## 1.2 Electrorefiner (ER)

The ER is the key component in pyroprocessing technology, in which the primary separation of U and MAs from fission products is being performed [18, 19]. The system contains a LiCl-KCl eutectic salt (44.2 wt% LiCl and 55.8 wt% KCl), and the operating temperature ranges from 723 K to 773 K [4]. There are two engineering scale ERs (Mark IV and Mark V) at INL (U.S.)

which are currently operated to treat the metallic used driver and blanket fuels, respectively, from EBR-II [19]. Figure 1.2 shows the drawings of both INL ERs, which have similar size but Mark V has an upgraded electrode design [19]. The Mark IV ER has been used to treat the driver fuels (highly enriched uranium at about 63% of U-235), whereas Mark V ER treats the blanket fuels (which contains depleted uranium) [20]. To date, 830 kg of heavy metals have been processed via Mark IV ER and numerous studies have been performed and reported in the literature [19]. Technical issues which are currently of concern include current efficiency, uranium recovery efficiency, zirconium recovery, and understanding of cadmium effects [19].

Here, UNFs are loaded in the anode basket and lowered into the LiCl-KCl molten salt. As current is applied through the cell, U metal is oxidized into  $U^{3+}$  ions from the anode basket [19]. Fission products, which have more negative redox potential than that of U, are being oxidized together (these products are referred as active products) whereas noble metals which have more positive redox potential than U stay in the anode basket [19]. The general contents of the driver fuel are summarized in Table 1.1 [21, 22-25]. Therefore, the main goal is to dissolve as much U as possible from the used fuels on the anodic side with minimal oxidation of the noble metals into the salt [19] and collect uranium metal on the cathode side. Li and Simpson in 2005 [20] reported that 99.7 % of U from fission products could be dissolved into the salt over several runs, but it caused Zr and noble metal co-dissolution into the salt. Table 1.2 lists the weight percent of dissolved fission products into the LiCl-KCl salt from EBR-II used fuel (loaded in anode basket). For the cathode electrodes, there are two types of electrode: 1) solid electrode (typically stainless steel) and the LCC. By using the solid electrode, selective deposition of pure U is possible by controlling the applied potential. On the other hand, reduction potentials of actinide elements including Pu and U become very close on the LCC, so that MAs are inevitably recovered along

with U and Pu into the LCC process [17]. The U has a tendency to be deposited in form of a dendrite [18, 19] which prevents the co-deposition of MA on LCC. Therefore, several studies have been performed to develop the LCC structures for avoiding dendrite formation on LCC [18, 26, 27]. Overall, the main reaction schemes in an electrorefiner can be described as follows [28]:

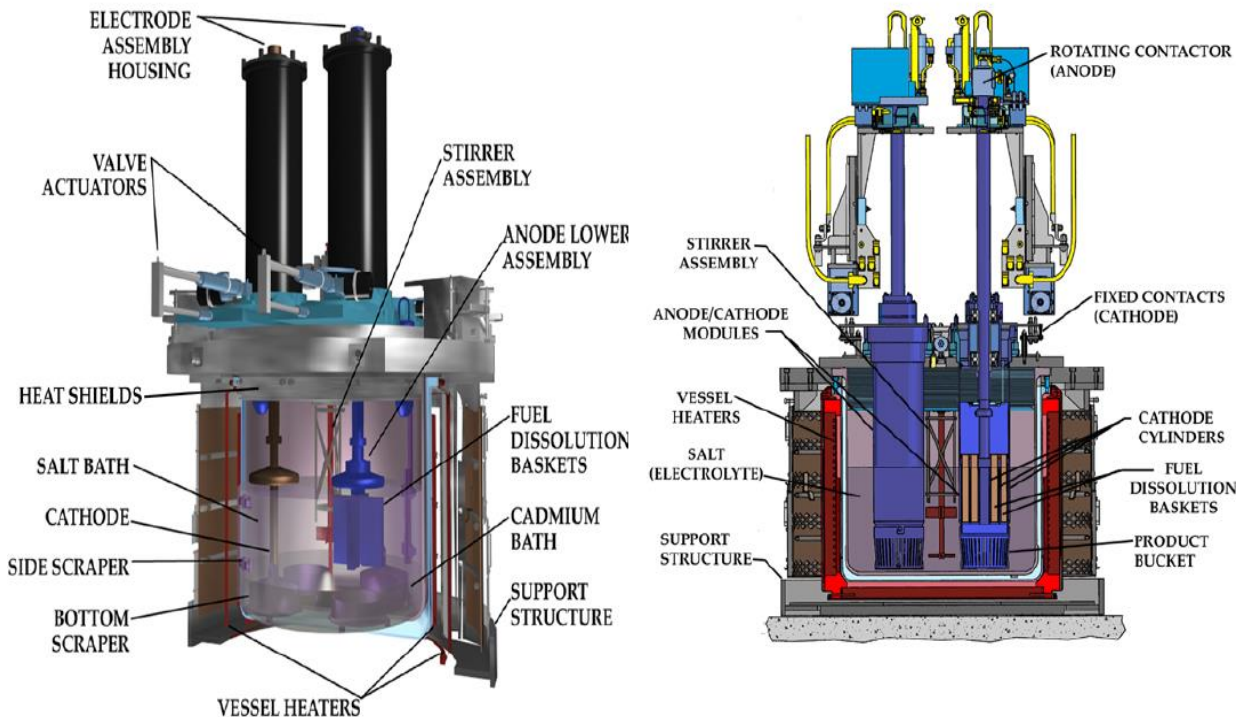
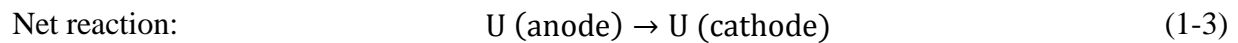
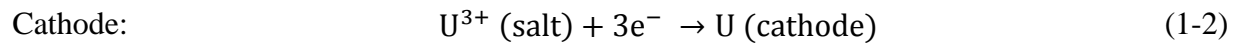
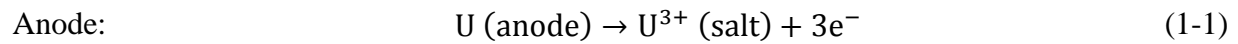


**Figure 1.2** Engineering scale electrorefiner at INL Fuel Conditioning Facility, Mark IV (left) and Mark V (right) [19].

**Table 1.1** Critical used driver fuel composition and equilibrium potential of the elements

Elements	Weight % in the used fuel [21]	$E^0$ (V vs. Ag/AgCl) at 723 K [22]	
Bromine (Br)	0.007	0.920 (723 K)	
Tellurium (Te)	0.112	0.64 (723 K)	
Ruthenium (Ru)	0.407	0.615 (723 K)	
Rhodium (Rh)	0.111	0.526 (723 K)	
Palladium (Pd)	0.090	0.513 (723 K)	
Iodine (I)	0.048	0.473 (723 K)	
Arsenic (As)	0.005	0.283 (723 K)	
Molybdenum (Mo)	0.771	0.119 (723 K)	Noble species (remain in anode basket)
Antimony (Sb)	0.004	0.087 (723 K)	
Silver (Ag)	0.004	0.000 (723 K)	
Copper (Cu)	0.003	0.295 (723 K)	
Tin (Sn)	0.015	-0.355 (723 K)	
Niobium (Nb)	0.002	-0.41 (723 K)	
Selenium (Se)	0.019	-0.459 (723 K)	
Cadmium (Cd)	0.007	-0.589 (723 K)	
Vanadium (V)	0.003	-0.806 (723 K)	
Titanium (Ti)	0.077	-1.010 (723 K)	
Zirconium (Zr)	10.81	-1.088 (723 K)	
Europium (Eu)	0.011	-1.471 (773 K)	
<b>Uranium (U)</b>	80.60	-1.496 (723 K)	
Neptunium (Np)	0.041	-1.519 (723K) [23]	
Plutonium (Pu)	0.413	-1.570 (723 K)	
Gadolinium (Gd)	0.005	-2.066 (723 K)	
Neodymium (Nd)	0.930	-2.097 (723 K)	Active species (dissolved into the salt)
Yttrium (Y)	0.126	-2.109 (723 K)	
Lanthanum (La)	0.284	-2.126 (723 K)	
Promethium (Pm)	0.011	-2.147 (773 K)	
Cerium (Ce)	0.542	-2.183 (723 K)	
Praseodymium (Pr)	0.269	-2.316 (773 K)	
Sodium (Na)	2.160	-2.5 (723 K)	
Samarium (Sm)	0.177	< -2.5 [24]	
Europium (Eu)	0.011	< -2.5 [25]	

**Table 1.2** The fission product dissolution (wt%) from used EBR-II driver fuel into LiCl-KCl salt [19]

Fission products dissolved into the salt	Weight percent in average
Uranium (U)	99.72
Lanthanum (La)	99.74
Cerium (Ce)	99.67
Neodymium (Nd)	99.96
Zirconium (Zr)	87.85
Technetium (Tc)	23.42
Molybdenum (Mo)	27.32
Ruthenium (Ru)	17.92

### 1.3 Motivation

As shown in Table 1.1, the used fuel contain a variety of fission products and active fission products are dissolved into the salt, which makes the system more complicated and difficult to be understood. Since U is the most abundant element in the ER, it is important to understand the fundamental properties of U in the salt in terms of effective system operation, and material accountability for safeguarding purposes. In these aspects, many studies have been conducted by several researchers to determine the electrochemical and kinetic properties of U in the salt. However, discrepancies through the literature survey can be observed due to many different experimental conditions; therefore, the general trends for the data sets can be hardly found. In addition, several properties have not been reported and fully understood due to the difficulty of the measurement, such as the exchange current density of U, which is necessary to be understood for near real time material detection and development of the kinetic model for pyroprocessing.

Furthermore, although the LCC in the ER plays an important role in the feasibility of pyroprocessing toward non-proliferation characteristic [29], only a few studies had been conducted to explore the properties of actinides on LCC in the salt [30-32]. Therefore, more reliable data sets of U in the salt system with a variety of experimental conditions are necessary to advance fundamental knowledge and gain new data library sets.

#### **1.4 Goal/Outcome**

The primary goal of this dissertation is to develop the experimental methods to evaluate electrochemical and kinetic properties of U in the LiCl-KCl salt based ER. Bench-scaled ER system have been developed in argon environment glovebox system. The main focus of this project is to perform electrochemical experiments including cyclic voltammetry (CV), open circuit potential (OCP), Tafel plot, linear polarization (LP), and electrochemical impedance spectroscopy (EIS) techniques for determining the parameters needed for modeling and developing a methodology for safeguards. Specially, the exchange current density ( $i_0$ ) of  $U/U^{3+}$  reaction will be intensively explored in LiCl-KCl eutectic salt. While  $i_0$  values are necessary for the kinetic models, these have not been fully understood in the system. In addition, the electrochemical and kinetic behaviors of U will be further examined in multi-component systems, which may occur in the ER. The approach in this dissertation will integrate the measurement of electrochemical data and the outcome will identify the various electrochemical and kinetic operating parameters. The resulting data base will provide an insight into fundamental understanding and signatures for material accountability for the ER process in pyroprocessing technology.

## 1.5 Approach

Three phases have been established in this research study. In phase I, pure argon environment ( $\text{O}_2/\text{H}_2\text{O}$  levels  $< 5$  ppm) was established in glovebox systems (RAM I and RAM II) for the treatment of the LiCl-KCl salt due to the fact that the salt is extremely hygroscopic and corrosive. Experimental setups including furnace, ceramic crucibles, and electrode assemblies were prepared in RAM I glovebox. Simultaneously, extensive literature review on fundamental properties of U in LiCl-KCl was conducted for understanding trends of the properties from the previously established data bases. In addition, the electrochemical techniques were studied for better understanding and reliable electrochemical measurements. The main purpose of phase II was to develop the experimental methods to determine the fundamental properties by using Ce as a surrogate material for U. All methods—CV, EIS, Tafel plot, LP, and OCP—were performed to determine the apparent standard potential, diffusion coefficient, exchange current density, and Gibbs free energy. The experiments were done at different concentrations (0.5 wt% to 4 wt% in LiCl-KCl) and temperatures (698 K to 823 K) in order to establish the data library and to understand the physical trends of Ce in LiCl-KCl. The studies focused on assessing the feasibility of EIS technique to measure the exchange current density in the salt system. Furthermore, the same experiments were carried out on the LCC in order to understand the Ce properties on a liquid cathode. A liquid cadmium surface was constructed with a design of an electrode vessel; therefore, electrochemical measurements could be performed on the surface. In Phase III, electrochemical studies of U were performed in LiCl-KCl salt at various concentrations (ranging from 0.5 wt% to 4 wt%  $\text{UCl}_3$ ) and temperatures (from 723 K to 798 K). Based on the methodologies developed in Phase II, the electrochemical and thermodynamic properties of U were evaluated. Additionally, the measurement of  $i_0$  for  $\text{U}/\text{U}^{3+}$  reaction was done via EIS, Tafel, LP, and CV methods for building

reliable data base. Plus, the same measurement procedures were followed to explore the U properties in LiCl-KCl-UCl<sub>3</sub>-GdCl<sub>3</sub> salt mixtures. These phases were planned, explored and accomplished at Virginia Commonwealth University (VCU) for the 3-year period. Specific timeframe is described in Table 1.3.

**Table 1.3** Estimated schedule and timeframe for the present project

Phase	Year 1 (2014)				Year 2 (2015)				Year 3 (2016)			
	1	2	3	4	1	2	3	4	1	2	3	4
I												
II												
III												

## 1.6 Organization of the Dissertation

This dissertation is composed of six chapters in total. In Chapter 2, thermodynamic and kinetic properties of uranium reported in the literature are reviewed and discussed. The significance of the properties with respect to pyroprocessing applications is pointed out, and methods of the electrochemical techniques used in the dissertation are described in detail. Chapter 3 contains basic information of equipment, experimental setups, and reagents. In addition, procedures for electrochemical preparations, sample collections, and sample analysis by inductively coupled plasma-mass spectrometry (ICP-MS) are being discussed with step-by-step illustrations. Chapter 4 presents the preliminary studies with Ce as a surrogate material for U in LiCl-KCl eutectic salt. Two studies are being described in this chapter: (i) measurements of Ce



properties with solid cathode and (ii) with liquid cadmium cathode. Since each study has different motivations and experimental procedures, an additional introductory information and experimental programs are briefly highlighted at the beginning of both studies. The main goal of this chapter is to develop experimental methods to measure the desired properties; therefore, specific methodologies are explained with corresponding equations associating with experimental results of Ce properties. Chapter 5 provides a detailed explanation and experimental procedures including discussion of the properties of U in LiCl-KCl eutectic salt under different effects—concentration, temperature, and additional species (that is, Gd). Here, the same experimental methods developed in Chapter 4 have been utilized; hence, discussions of resulting data are more focused in this chapter. The final chapter (Chapter 6) summarizes the resulting data sets in the present research and discusses necessary future steps. Data, figures, and tables further supporting the body of chapters are provided in Appendix sections at the end of this dissertation.

## Chapter 2 Literature Survey

A great number of studies have been performed as an effort of evaluating pyroprocessing systems as well as understanding the electrochemical and thermodynamic behavior of nuclear elements in salt based electrolytes (which is typically a LiCl-KCl eutectic salt). The electrochemical properties were explored at different operating conditions which may occur in the electrolyzer (ER) system. These data will be useful to understand a practical operation of the ER as well as to guide the development of kinetic models that can be utilized to detect the signal of special nuclear materials (SNM) in the process as a safeguard purpose. Therefore, the purpose of this chapter is to discuss the importance of the parameters and accumulate the values reported by researchers in the past. Also, several electrochemical techniques along with methodologies for the experimental measurements will be explored.

### 2.1 Molten salt in electrorefining and general electrochemistry

Molten salts have several advantages over aqueous solvents when serving as a medium for UNF reprocessing. The advantages include high radiation resistance, low criticality concern, low vapor pressure, low secondary wastes and high stability [33]. Thus, physical, chemical and electrochemical properties of the salts and its interactions with actinides and fission products must be considered. Currently, two chloride salt mixtures (LiCl–KCl and NaCl–KCl) and two fluoride salt mixtures (BeF<sub>2</sub>–LiF and CaF<sub>2</sub>–LiF) have been recognized as good candidates for pyroprocessing [34-36]. The compositions of these salts and their melting temperatures are given in Table 2-1. LiCl-KCl molten salt is widely selected as a candidate for electrorefining system because of its lower melting eutectic temperature. Typically, electrorefining system is operated at a temperature ranging between 723 K and 773 K.

**Table 2.1** Physical properties of the salt mixtures [34-36]

Properties	LiCl-KCl	NaCl-KCl	BeF <sub>2</sub> -LiF	CaF <sub>2</sub> -LiF
Composition (A-B, Mol % B)	40	50	67	77
Eutectic melting temperature (K)	623	931	733	1042
Molar mass (g mol <sup>-1</sup> )	55.25	66.50	32.89	37.93
Density at melting point (kg m <sup>-3</sup> )	1644.6	1604.1	2055.7	2066.8
Viscosity at melting point (Pa s)	0.2798	0.2128	0.1947	-
Electrical conductance (S m <sup>-1</sup> )	63.72	220.07	128.37	624.68

## 2.2 Uranium Studies

Since uranium (U) is the main element in the ER system, several researchers previously focused on understanding its electrochemical and kinetic behavior in the molten LiCl-KCl system. The most important parameters are the apparent standard potential ( $E^{0*}$ ), the activity coefficient ( $\gamma$ ), the diffusion coefficient ( $D$ ), and the exchange current density ( $i_0$ ). The values of  $E^{0*}$  and  $D$  for U have been reported widely by using different electrochemical techniques, such as cyclic voltammetry (CV), chronopotentiometry (CP), and open circuit potential (OCP) [37-47]. However, these data values are scattered due to the fact that the experiments have been done under different concentrations, temperatures, and experimental environments. Based on the  $E^{0*}$  values, several thermodynamic properties can be calculated including the Gibbs free energies of  $UCl_3$  formations and  $\gamma$ . Specially, only a few researchers reported the values of  $\gamma$ , which, however, show wide discrepancy [37, 39, 41]. These issues will be further discussed in Section 2.2.1. In addition, the properties have been poorly understood by using LCC electrode, which plays an important role in

the electrorefining process. Also, very few  $i_0$  values are available [48-51], which started to be explored and reported since 2009. Choi et al., Ghosh et al., and Rose et al. [48-50] reported the values of  $i_0$  at different concentrations (ranging from 3 wt % to 5 wt %) at 773 K. Lim et al. in 2016 [51] reported  $i_0$  for U at different concentrations and temperatures. Yet, there is a lack of understanding in the trend of  $i_0$  and a meaningful comparison is difficult among the literature studies due to the fact that the data were measured in different experimental conditions and scales. Also, none of the authors has mentioned the challenge of the electrode area growth during the measurements by using the Tafel or LP methods (this concern will be discussed in section 2.2.3). Detailed information on studies of U is summarized in Appendix I.

### 2.2.1 Redox process and Apparent Standard Potential ( $E^{0*}$ )

The electrochemical process of  $U/U^{3+}$  reduction-oxidation (which is called “redox”) reaction is governed by the Nernst equation exhibiting the equilibrium potential for the reaction with respect to temperature and concentrations of oxidant/reductant [52]:

$$E_{U^{3+}/U}^{eq} = E_{U^{3+}/U}^0 + \frac{RT}{nF} \ln \left( \frac{a_{U^{3+}}}{a_U} \right) \quad (2-1)$$

where  $E_{U^{3+}/U}^{eq}$  is the equilibrium potential between U metal and  $U^{3+}$  ions,  $E_{U^{3+}/U}^0$  is the standard reduction potential which is the theoretical potential when the cell is ideally reversible at equilibrium states with a solution concentration of 1 mol L<sup>-1</sup> at 1 atm and 298 K, R is the universal gas constant (8.314 J mol<sup>-1</sup>K<sup>-1</sup>), F is the Faraday’s constant (96485 C mol<sup>-1</sup>), and T is the absolute temperature (K). The  $a_{U^{3+}}$  is the activity of  $UCl_3$  which can be expressed by  $a_{U^{3+}} = \gamma_{U^{3+}} \times \chi_{U^{3+}}$

where  $\gamma_{U^{3+}}$  is the activity coefficient and  $\chi_{U^{3+}}$  is the mole fraction of U. Thus, the equation can be expressed using the mole fraction [52]

$$E_{U^{3+}/U}^{eq} = E_{U^{3+}/U}^{0*} + \frac{RT}{nF} \ln \left( \frac{\chi_{U^{3+}}}{\chi_U} \right) \quad (2-2)$$

where  $E_{U^{3+}/U}^{0*}$  is the apparent standard potential (this is often referred as a ‘formal potential’). The apparent standard potentials is the function of temperature and activity coefficient; therefore, it can be determined by plotting  $E_{U^{3+}/U}^{eq}$  against  $\ln(\chi_{U^{3+}})$ . This property gives an insight into the reduction potential that the operator will be able to apply for the U recovery in the ER. Therefore, several researchers have reported the values of  $E_{U^{3+}/U}^{0*}$ , in which they used different temperatures, concentrations, reference electrodes, and experimental methods [37-45], as shown in Figure 2.1. The reported data values show good agreement within 50 mV deviation from the average values, which are linearly dependent with temperature in general. The result reported by Hoover et al. [42] stands at more negative potential compared to the trend; this discrepancy may be due to the fact that they measured the  $E^{0*}$  at a high concentration range between 1 and 10 wt% of  $UCl_3$  in LiCl-KCl. Typically, the property of  $E^{0*}$  is considered as independent of concentration; however, this must be experimentally evaluated.

Once the  $E_{U^{3+}/U}^{0*}$  values were determined, the thermodynamic properties of  $UCl_3$  can be further investigated by combining Eq. (2-1) and (2-2); therefore,  $E_{U^{3+}/U}^{0*}$  can be defined as

$$E_{U^{3+}/U}^{0*} = E_{U^{3+}/U}^0 + \frac{RT}{nF} \ln(\gamma_{U^{3+}}) \quad (2-3)$$

where  $\gamma_{U^{3+}}$  is the activity coefficient of  $UCl_3$  in LiCl-KCl. Since  $E_{U^{3+}/U}^0$  is a theoretical value at the aforementioned ideal state, the value does not exist in reality. Therefore, super cooled liquid

state was commonly considered as ideal as possible in the real system [37, 39, 41], and the Eq. (2-3) can be re-written by using the basic thermodynamic equation as following,

$$\Delta G_{\text{UCl}_3}^{\text{SC}} - \Delta G_{\text{UCl}_3}^{0*} = RT \ln(\gamma_{\text{U}^{3+}}) \quad (2-4)$$

where  $\Delta G_{\text{UCl}_3}^{\text{SC}}$  is the Gibbs free energy at super cooled liquid state. The data for the pure substance can be found in several references [37, 53]. If  $\Delta G_{\text{UCl}_3}^{\text{SC}}$  is known,  $\gamma_{\text{U}^{3+}}$  can be calculated. Figure 2.2 plots the reported values of  $\gamma_{\text{U}^{3+}}$ , showing wide discrepancy up to  $10^1$  order of magnitude [37, 39, 41, 54]. This may be due to the challenges of obtaining  $\Delta G_{\text{UCl}_3}^{\text{SC}}$  from literatures, and calculating exponential term ( $\exp(\frac{\Delta G_{\text{UCl}_3}^{\text{SC}} - \Delta G_{\text{UCl}_3}^{0*}}{RT})$ ). Therefore, sufficient data sets need to be collected in order to understand thermodynamic properties of U in the salt system.

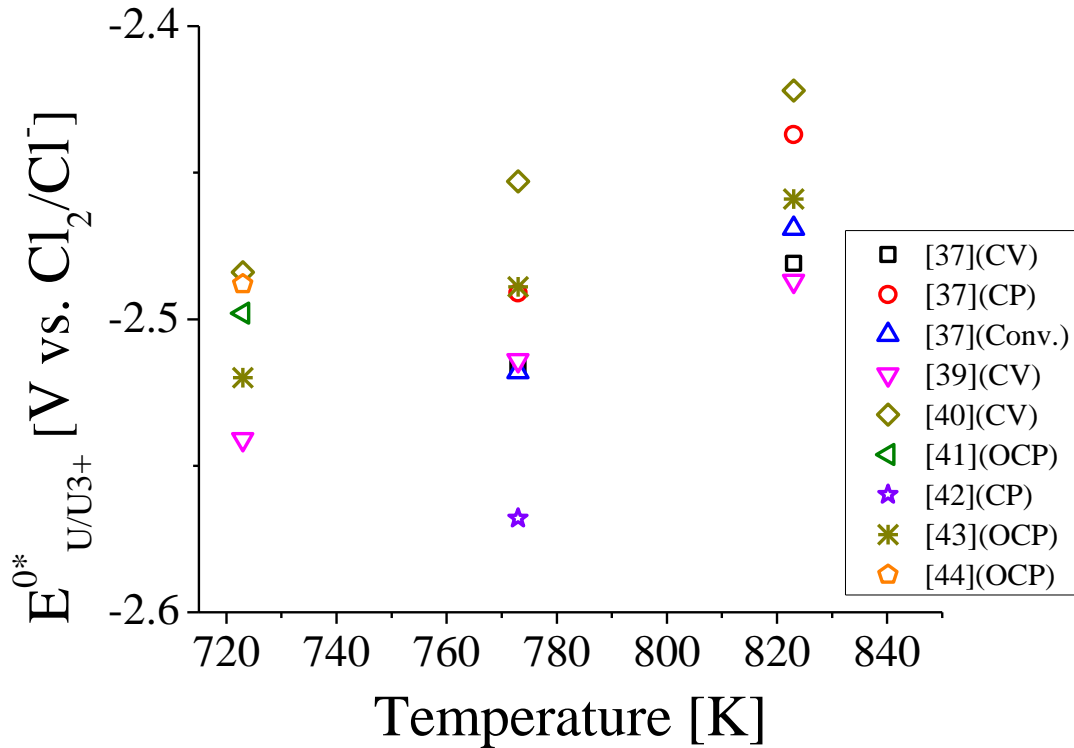


**Figure 2.1** Comparison of the apparent standard potential in LiCl-KCl salt reported by various researchers (Note: CV = cyclic voltammetry, CP = chronopotentiometry, and OCP = open circuit potential).

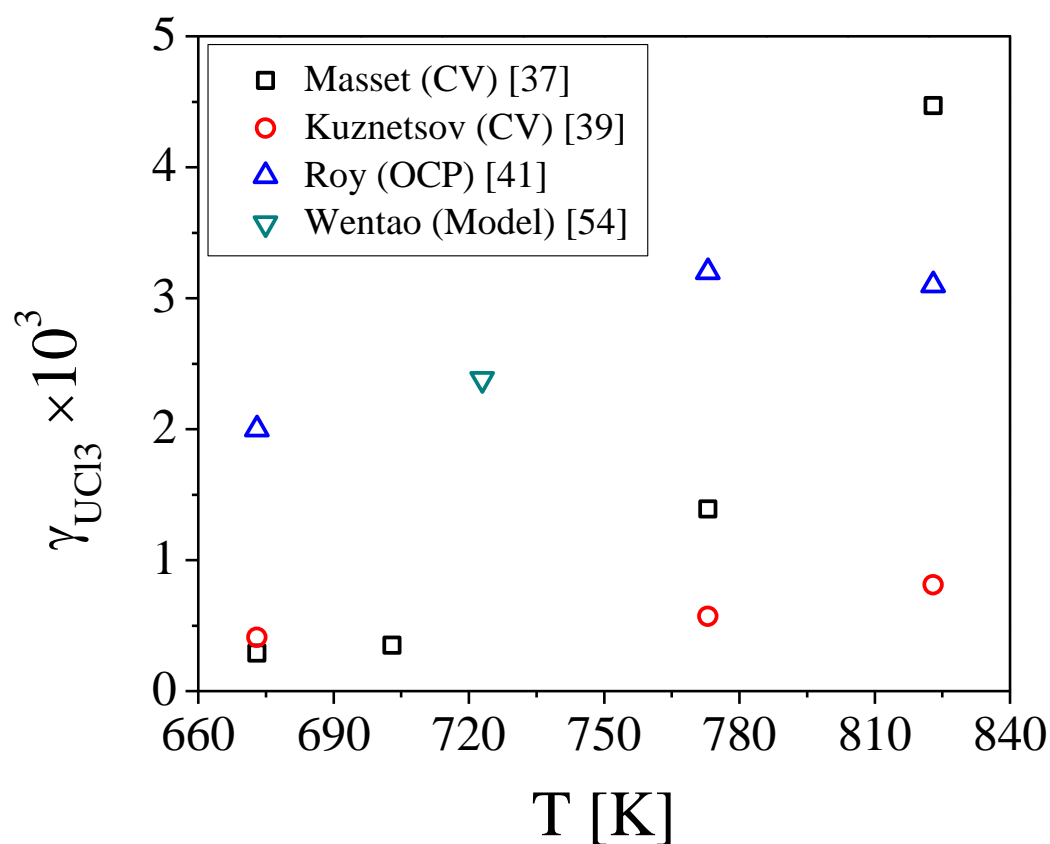


**Figure 2.2** Activity coefficients of  $\text{UCl}_3$  in  $\text{LiCl-KCl}$  reported by previous studies.

### 2.2.2 Diffusion coefficient

Mass transfer from and to the electrodes in an electrochemical cell can be expressed by diffusivity or diffusion coefficient which is constant between molar flux and concentration gradient [22]. The value of the diffusion coefficient affects the mass transport of the species in the molten salt, the efficiency of the system, and the maximum current that the system can support. Thus, knowledge on the diffusion coefficient of  $\text{UCl}_3$  in  $\text{LiCl-KCl}$  eutectic melt provides essential data for optimization of U electrorefining. The diffusion coefficients of  $\text{U}^{3+}$  have been electrochemically measured in the salt via CV and CP techniques. Several studies [37, 39, 42, 45-

47] have reported the values in LiCl-KCl which are plotted in Figure 2.3. It appears that the diffusion coefficient is linearly dependent to temperature; however, data are scattered specially at high temperature (for example, a standard deviation of  $D_{U^{3+}}$  is  $1.5 \times 10^{-5} \text{ cm}^2 \text{ s}^{-1}$  from the mean value ( $3.02 \times 10^{-5} \text{ cm}^2 \text{ s}^{-1}$ ) at 823 K). Also, the values reported by Masset and co-workers [37] are relatively higher than data from other sources. The CP method generally provides higher values than those from CV method. Therefore, the values of  $D_{U^{3+}}$  are necessary to be measured and collected in various experimental conditions for further comparison and understanding. In addition, concentration effects on the diffusion coefficient need to be evaluated in LiCl-KCl salt even though it is theoretically function of temperature and species.

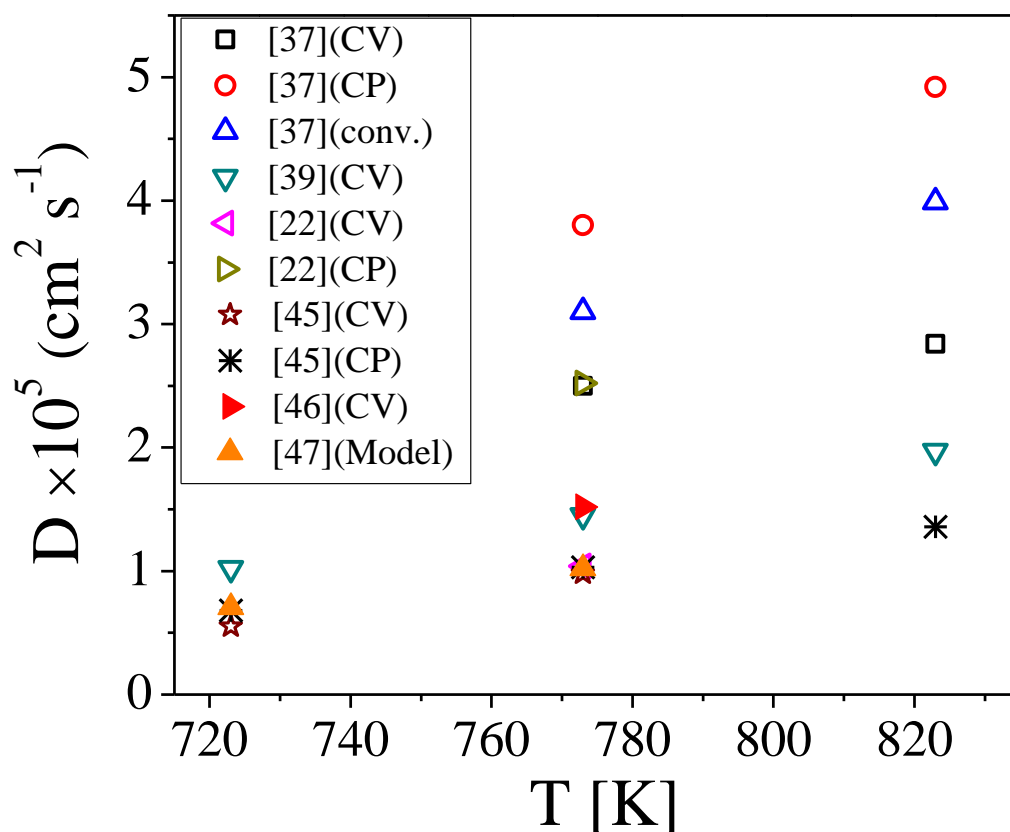


**Figure 2.3** Plot of the diffusion coefficients of  $UCl_3$  in LiCl-KCl salt reported by various researchers.



### 2.2.3 Exchange current density

Exchange current density ( $i_0$ ) is an important parameter to understand the kinetics of electrochemical reactions ( $U^{3+}/U$ ) on the electrode surface. Additionally, the values are essential to the physics-based model used in Butler-Volmer equation which shows fundamental relationship between current and overpotential applied on the electrode. The equation can be expressed as

$$i = i_0 \cdot \left\{ \exp \left[ \frac{\alpha_a n F \eta}{RT} \right] - \exp \left[ - \frac{\alpha_c n F \eta}{RT} \right] \right\} \quad (2-5)$$

where  $i_0$  is the exchange current density,  $i$  is the current,  $\alpha_a$  is the anodic charge transfer coefficient,  $\alpha_c$  is the cathodic charge transfer coefficient, and  $\eta$  is the activation overpotential. There are several methods to measure the value of  $i_0$ : Tafel plot, linear polarization (LP), and electrochemical impedance spectroscopy (EIS). However, the  $i_0$  of  $U^{3+}/U$  couple has not been well measured and understood due to challenges of the measurement. Choi et al. in 2009 [48] performed LP experiments in 3.3 wt%  $UCl_3$ -LiCl-KCl salt where Cd coexisted at the bottom of the vessel. The authors conducted the experiments by using different materials for the electrode and concluded that the different materials of electrodes result in different values of  $i_0$ , ranging from 0.0202 to 0.0584  $A\ cm^{-2}$ . Ghosh and co-workers [49] reported that the value is  $8 \pm 2 \times 10^{-3}$   $A\ cm^{-2}$ , by measurements of Tafel plot, which stands far from the trend of other literature studies. Rose et al. in 2015 [50] measured the  $i_0$  of  $U/U^{3+}$  in 5 wt%  $UCl_3$ -LiCl-KCl salt by using Tafel plot method. Tafel plots were analyzed by using the Oldham-Mansfeld model in a very small overpotential region, which is theoretically not a Tafel region. The value of  $i_0$  from that study was from 0.0695 to 0.220  $A\ cm^{-2}$ . Recently, Lim et al. [51] reported the  $i_0$  values of U via the Tafel and LP methods; this published study is the only source with reported  $i_0$  data at the different temperatures and concentrations. The values of  $i_0$  for  $U^{3+}/U$  are plotted and compared in Figure

2.4. From these literature results, there are still missing data sets for  $i_0$  of U in order to fully understand the general trend. Also, a meaningful comparison among the reported data is not possible due to the data discrepancy resulting from differences in the experimental conditions, the size of the system, and the data acquisition methods. Furthermore, the authors never mentioned the challenges and uncertainties in measuring the electrode surface area during the Tafel and LP measurements. Therefore, further studies must be conducted in the same experimental conditions and system sizes. The measurements at different concentrations and temperatures under the same experimental environments would be necessary in order to build up a meaningful data base for  $i_0$  of  $\text{U}/\text{U}^{3+}$  in LiCl-KCl salt.

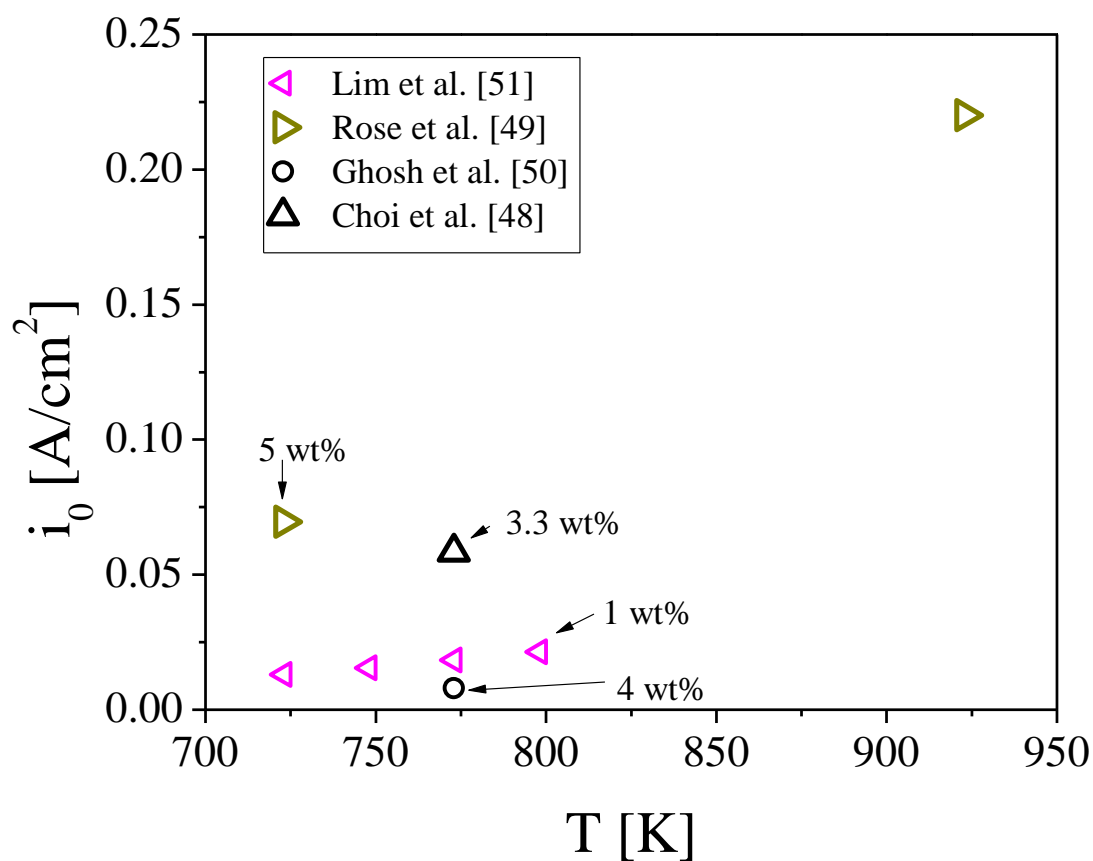


**Figure 2.4** Plot of  $i_0$  from literature studies (measuring with a tungsten electrode).

## **2.3 Review of the electrochemical techniques**

In this research, five electrochemical techniques have been considered for the measurement of parameters: CV, OCP, EIS, Tafel plot, and LP methods. CV is widely used to understand the redox process of the elements and determine diffusion coefficient and the apparent reduction potential. The equilibrium potential and the apparent reduction potential also can be easily extracted via OCP. In addition, kinetic parameters including the exchange current density and the rate constant can be calculated by conducting EIS, Tafel, and LP methods. In the following subsections, these five techniques and their associated equations to measure the electrochemical and thermodynamic properties will be discussed.

### **2.3.1 Cyclic voltammetry (CV)**

CV may be a most widely used technique among all methods available for studying electrode processes [52]. In this technique, linear scan voltammetry is carried out by switching the direction of the potential scan at a certain time, as shown in Figure 2.5 (a). This applied potential results in the reduction and oxidation of the species on the electrode surface. A current increase can be observed due to the electrode reaction, and peak current can be found because of the depletion of species on the electrode surface, as shown in Figure 2.5 (b).

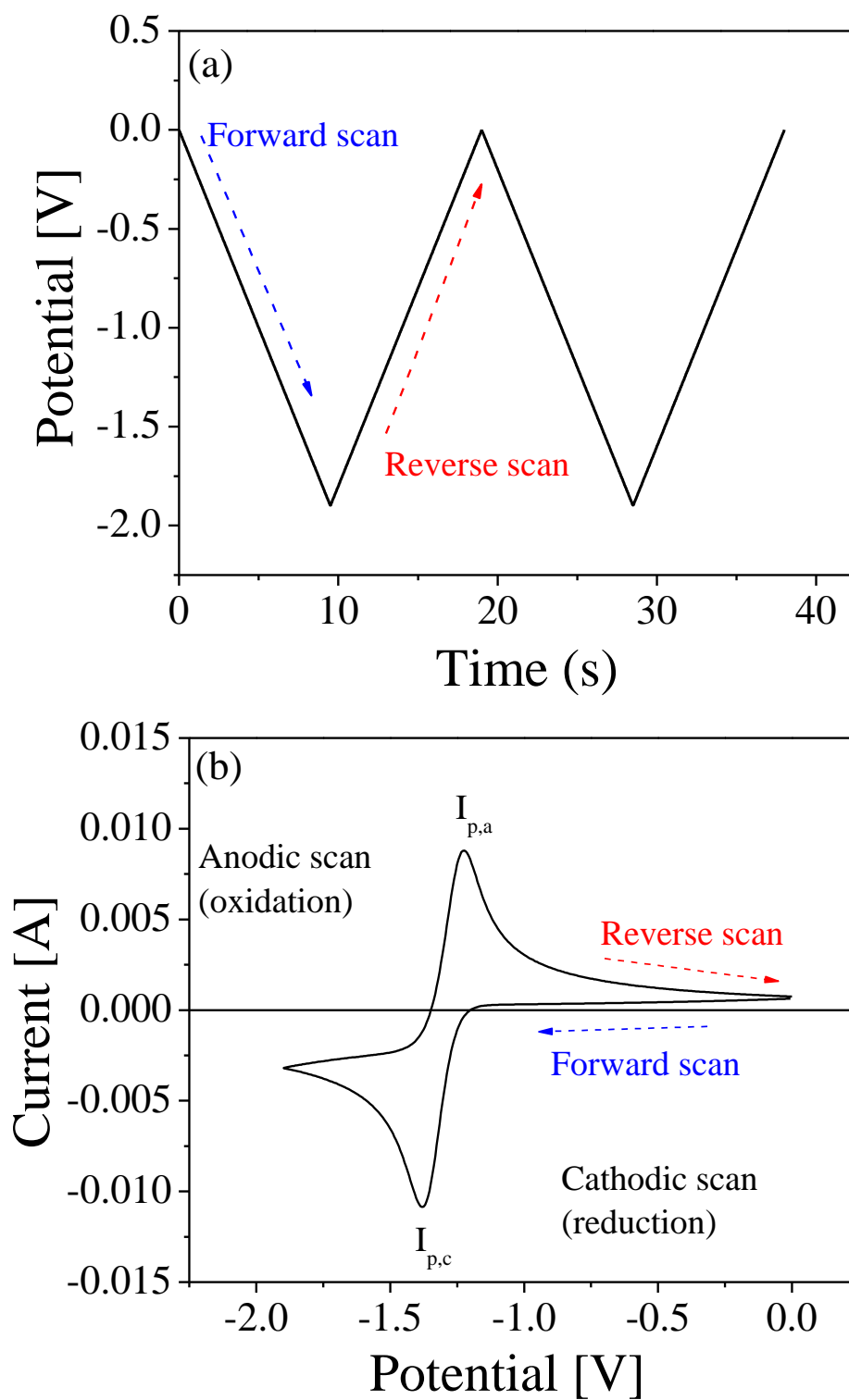


**Figure 2.5** (a) A typical potential waveform in CV, and (b) a typical reversible CV response with reduction and oxidation reactions.

From the results of the CV data, a reversibility of the redox reaction can be verified, which is a relationship between the redox reaction rate and the mass transfer rate. The reversible system is characterized by faster kinetic reaction than mass transfer of the species. In this case, the peak potential ( $E_p$ ) will remain at the same potential under different sweeping scan rates [52]. If the electrode reaction rate is slowly moving than the mass transfer, the system is irreversible; that is, the peak potential will shift toward a negative direction with an increasing scan rate [52]. The quasi-reversible system is intermediate between reversible and irreversible systems [55]. The condition for the reversibility is established at stationary planar electrode as [52, 55]:

$$\text{reversible system: } k^0 \geq 0.3 v^{1/2} \text{ cm s}^{-1} \quad (2-6)$$

$$\text{quasi – reversible system: } 0.3 v^{1/2} \geq k^0 \geq 2 \times 10^{-5} v^{1/2} \text{ cm s}^{-1} \quad (2-7)$$

$$\text{irreversible system: } k^0 \leq 2 \times 10^{-5} v^{1/2} \text{ cm s}^{-1} \quad (2-8)$$

where  $k^0$  is the rate constant for the electrode reaction ( $\text{cm s}^{-1}$ ) and  $v$  is the scan rate. The number of electrons transferred in the electrode reaction can be determined by the measurement of cathodic and anodic peak currents, which can be exhibited [37, 55] by

$$\text{For reversible system: } |E_{pc} - E_{pc/2}| = 0.77 \frac{RT}{nF} \quad (2-9)$$

$$\text{For irreversible system: } |E_{pc} - E_{p/2}| = 1.857 \frac{RT}{n\alpha F} \quad (2-10)$$

where  $E_{p/2}$  is the half peak potential, and  $E_{pc}$  and  $E_{pa}$  are the cathodic and anodic peak potentials, respectively. Dalahay solved the boundary value problem for soluble/soluble diffusional system, the peak current can be expressed [56] as

For reversible system:

$$i_p = 0.446nFSC_0 \sqrt{\frac{nFDv}{RT}} \quad (2-11)$$

For irreversible system:

$$i_p = 0.499nFSC_0 \sqrt{\frac{\alpha nFDv}{RT}} \quad (2-12)$$

where  $S$  is the electrode surface area ( $\text{cm}^2$ ),  $C_0$  is the bulk concentration of species ( $\text{mol cm}^{-3}$ ),  $v$  is the scan rate ( $\text{V s}^{-1}$ ), and  $D$  is the diffusion coefficient ( $\text{cm}^2 \text{s}^{-1}$ ). Model for the reversible soluble/insoluble diffusion system (electrodeposition on the electrode) was developed by Berzins and Delahay [57]. The model used the assumption that the deposited species (in metal form) has a constant activity at unity. The equation can be expressed as

$$i_p = 0.611 nFSC_0 \left( \frac{nFvD}{RT} \right)^{1/2} \quad (2-13)$$

Therefore, Eq. (2-11) – Eq. (2-13) allow to calculate diffusion coefficient by plotting  $i_p$  over the square root of the scan rate. In Eq. (2-12),  $\alpha n$  can be estimated by using Eq. (2-10) from CV measurements. The diffusivity generally follows Arrhenius temperature relationship, which can be expressed as

$$D = D_0 \exp\left(\frac{-E_a}{RT}\right) \quad (2-14)$$

where  $D_0$  is the pre-exponential factor, and  $E_a$  is then an activation energy ( $\text{kJ mol}^{-1}$ ) for the diffusion. Therefore, the activation energy for the diffusion can be calculated from the slope when  $\ln(D)$  is plotted versus  $1/T$ .

The measured peak potentials from the cyclic voltammogram can be used to calculate the apparent standard potential. For a reversible soluble/insoluble system, the cathodic peak potential can be expressed as [55, 56]

For reversible system:

$$E_p = E^{0*} + \frac{RT}{nF} \ln(X) - 0.854 \frac{RT}{nF} \quad (2-15)$$

For irreversible system:

$$E_p = E^{0*} - \frac{RT}{n\alpha F} \left[ 0.78 - \ln k_i + \ln \left( \sqrt{\frac{n\alpha F v D}{RT}} \right) \right] \quad (2-16)$$

(soluble/soluble)

where  $E_p$  is the peak potential (V) obtained from the cathodic side,  $X$  is the mole fraction, and  $E^{0*}$  is the apparent standard potential (V), and  $k$  is the rate constant ( $\text{cm s}^{-1}$ ). Using Eqs. (2-14) and (2-15), the apparent standard potential of species for the reversible and irreversible systems can be experimentally calculated via the CV measurements.

### 2.3.2 Open circuit potential (OCP)

The thermodynamic properties in terms of redox reaction can be readily measured by using the OCP method. During this measurement, a potential is measured with no appreciable current flowing through the cell; therefore, OCP is also known as ‘the zero-current potential’ or ‘the rest potential’ [55]. When the redox couple is present at an equilibrium state on the electrode, the OCP provide a steady potential between oxidant and reductant, which is the equilibrium potential. An example potential response is described in Figure 2.6, in which the equilibrium potential of U was measured at the concentration of 0.5 wt%  $\text{UCl}_3$ -LiCl-KCl at 773K. By providing the equilibrium potential, the apparent standard potential (typically referred as a formal potential) of the redox reaction can be calculated by plotting the equilibrium potential versus concentration of species. Also, the values of the equilibrium potential can be directly substituted in Eq. (2-2) to determine the apparent standard potential. Furthermore, the OCP measurement is useful in monitoring whether electrochemical cell/electrode is in equilibrium state; therefore, OCP should be checked

before or between electrochemical measurements to verify that the electrochemical cell is under the same condition at the equilibrium state.

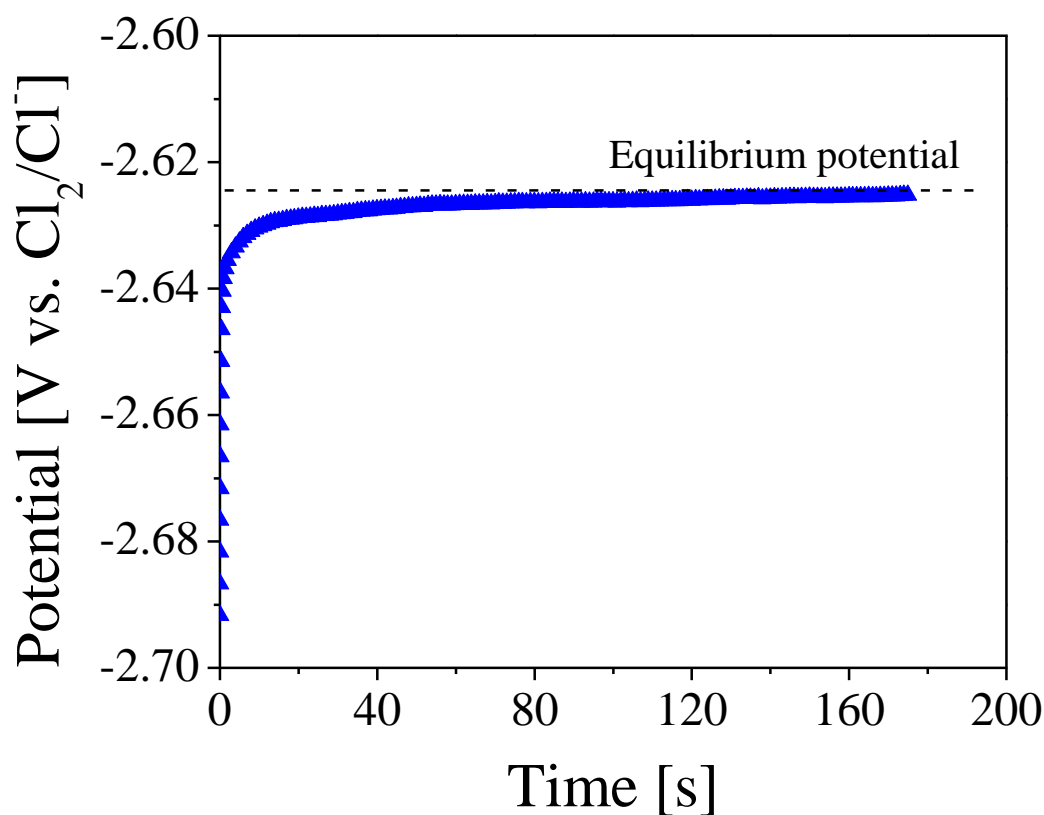


**Figure 2.6** An example of OCP measurement in 0.5 wt %  $\text{UCl}_3$ - $\text{LiCl}$ - $\text{KCl}$  at 773 K.

### 2.3.3 Electrochemical impedance spectroscopy (EIS)

EIS is a technique to measure the cell/electrode impedance as a function of the frequency [55]. This technique is useful to understand the electrode process with respect to contributions from diffusion, kinetics, double layer, and reactions; therefore, there are many broad applications that EIS can be used to yield insightful information, such as corrosion, membranes, batteries, etc. [52]. The impedance can be measured by applying a perturbation signal which results in a



corresponding response (i.e. solution resistance, double layer capacitance, and charge transfer resistance). The potential perturbation input can be expressed as a function of time: [55]

$$E(t) = E(0)\sin(\omega t) \quad (2-17)$$

where  $E(t)$  is the potential at time  $t$  (V),  $E(0)$  is the amplitude of the potential signal (V), and  $\omega$  is the angular frequency ( $\text{rad s}^{-1}$ ) which is  $2\pi$  times the conventional frequency in Hz. The current response can be expressed as [55, 58]

$$i(t) = i(0) \sin(\omega t + \phi) \quad (2-18)$$

where  $i(t)$  is the current at time  $t$  (A),  $i(0)$  is the amplitude of the current signal (A), and  $\phi$  is the phase angle which is illustrated in Figure 2.7. This current-voltage relation is analogous to Ohm's law; therefore, the impedance,  $Z$ , can be expressed as

$$Z(t) = \frac{E(t)}{i(t)} = \frac{E(0)\sin(\omega t)}{i(0)\sin(\omega t + \phi)} = Z(0) \frac{\sin(\omega t)}{\sin(\omega t + \phi)} \quad (2-19)$$

where  $Z(t)$  is the impedance ( $\Omega$ ) and  $Z(0)$  is the amplitude of the impedance. When the  $E(t)$  and  $i(t)$  are considered in complex plane, the equations can be described as

$$E(t) = E(0)\exp(j\omega t) \quad (2-20)$$

$$i(t) = i(0) \exp(j(\omega t - \phi)) \quad (2-21)$$

where  $j$  is the imaginary number,  $\sqrt{-1}$ . By applying complex function,  $\exp(j\phi) = \cos \phi + j\sin \phi$ , the impedance,  $Z$ , can be expressed in complex plane as

$$Z(t) = Z(0)(\cos \phi + j\sin \phi) = Z(\text{Re}) + Z(\text{Im}) \quad (2-22)$$

where  $Z(\text{Re})$  and  $Z(\text{Im})$  are the real and imaginary part of the impedance. The  $Z(\text{Re})$  and  $Z(\text{Im})$  can be plotted on x-axis and y-axis, respectively, which is called the 'Nyquist plot.'

The EIS can be interpreted with an equivalent circuit consisting of resistances, capacitances, diffusion related impedances (Warburg impedance), and so on. The simplest model for the electrode process is called Voigt model containing solution resistance ( $R_s$ ), charge transfer resistance ( $R_{ct}$ ), and double layer capacitance ( $C_{dl}$ ), as shown in Figure 2.8. The impedance of the Voigt model can be expressed by using following equation [55]:

$$Z(t) = R_s + \frac{1}{\frac{1}{R_{ct}} + j\omega C_{dl}} = R_s + \frac{R_{ct}}{1 + j\tau\omega} \quad (2-23)$$

where  $\tau$  is the time constant relating with RC circuit. The second term in Eq. (2-20) can be considered with two different scenarios. First, it becomes very small and is negligible at high frequency. Second, it approaches  $R_{ct}$  at very low frequency. Figure 2.9 shows the ideal Nyquist plot for the Voigt model where  $R_s$  and  $R_s + R_{ct}$  can be easily found on the x-axis. The  $R_{ct}$  is formed when an electrochemical reaction occurs on the electrode at the equilibrium state,  $R \leftrightarrow O + ne^-$ , and the exchange current density ( $i_0$ ,  $A\ cm^{-2}$ ) and rate constant ( $k^0$ ,  $cm\ s^{-1}$ ) for the charge transfer can be calculated by using [55]:

$$R_{ct} = \frac{RT}{nFSi_0} = \frac{RT}{n^2F^2Sk^0C_0^{1-\alpha}} \quad (2-24)$$

Since the polarization of the electrochemical system in reality can be non-ideal and more complex according to the interfacial formations, the constant phase element (CPE) is typically being utilized to fit the experimental EIS spectra through the following expression: [59]

$$Z_{CPE} = \frac{1}{T(j\omega)^\Phi} \quad (2-25)$$

where  $T$  is a constant in  $F \text{ cm}^{-2} \text{ s}^{\phi-1}$  is the constant,  $\phi$  is the number constant between -1 and 1, and  $\omega$  is the frequency. Here, CPE can easily become double-layer capacitance, Warburg resistance, or pure resistance by changing the number of  $\phi$  in Eq. (2-25).

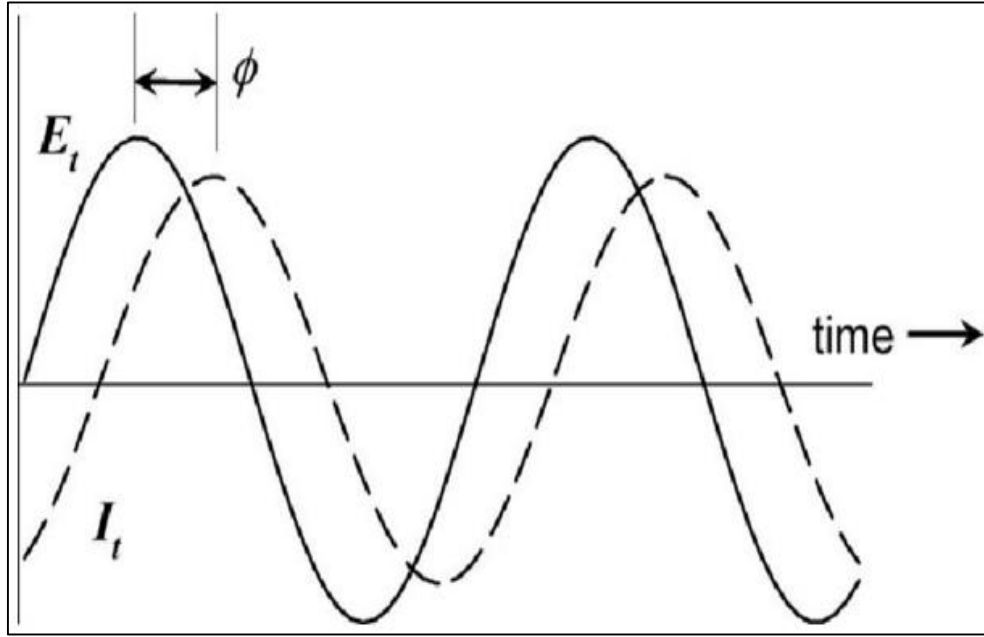


**Figure 2.7** Sinusoidal potential input and sinusoidal current response in typical EIS measurements [58].

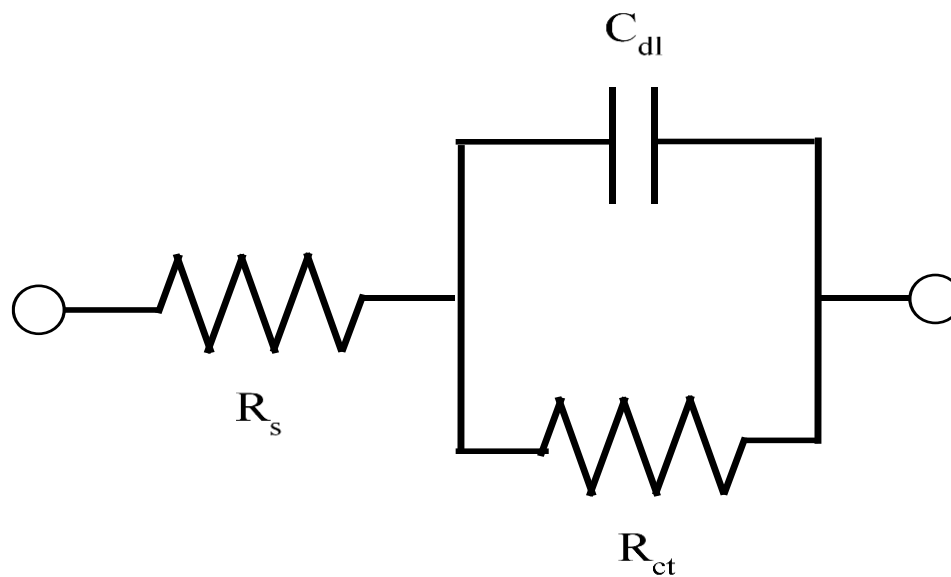


**Figure 2.8** An equivalent circuit for Voigt model which is composed with resistance and capacitance.

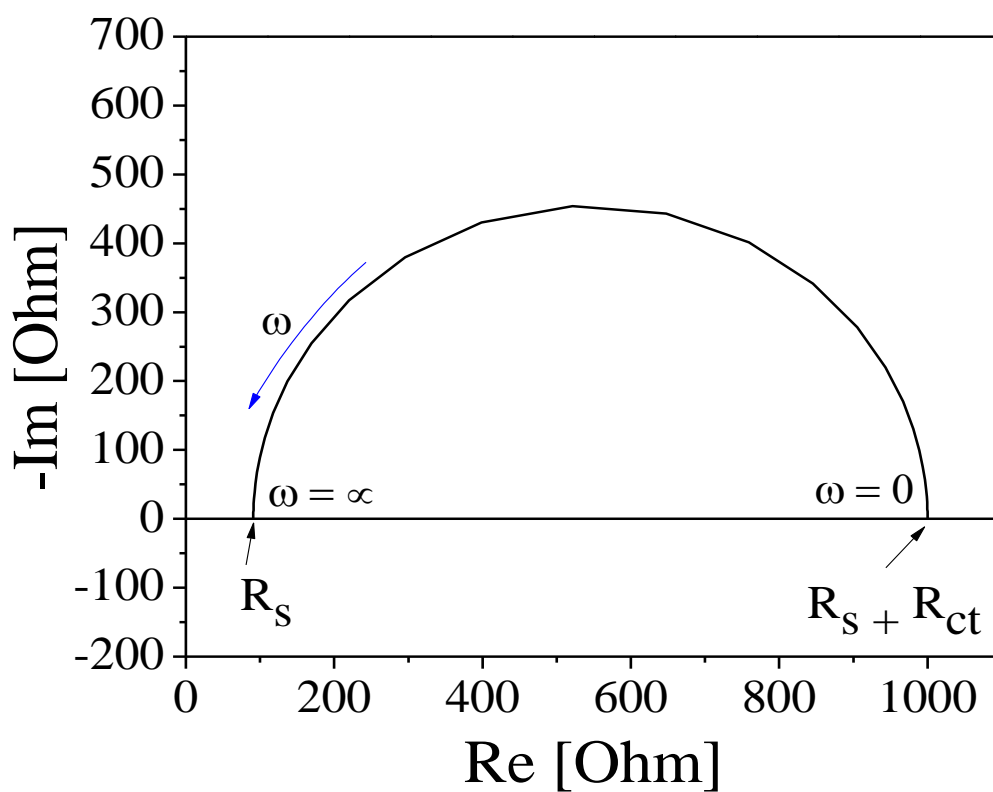


**Figure 2.9** An ideal Nyquist curve for the Voigt model.  $R_s$  is bulk solution resistance and  $R_{ct}$  is the charge transfer resistance on electrode surface.

### 2.3.4 Tafel and linear polarization (LP) methods

Considering a single step electrode reaction,  $R \leftrightarrow O + e^-$ , the rate of reaction controlled by the electron transfer can be examined via Tafel and linear polarization (LP) methods. The electrode reaction can be derived using current and overpotential relation under the assumption of fast mass transfer of the species, which can be expressed in another form of Eq. (2-5) as

$$i = i_0 \left[ \exp\left(\frac{-\alpha n F}{RT} \eta\right) - \exp\left(\frac{(1 - \alpha) n F}{RT} \eta\right) \right]. \quad (2-26)$$

When  $\eta$  is large, the second term on the RHS will be negligible and Eq. (2-25) becomes [55]

$$\log(i) = \log(i_0) + \frac{\alpha n F}{2.303 RT} \eta, (\eta < 0). \quad (2-27)$$

The plot of  $\log(i)$  versus  $\eta$ , known as the ‘Tafel plot,’ is useful in determining the value of  $i_0$  by extrapolating to an intercept of  $\log(i)$ . Figure 2.10 shows an example the Tafel plot [55] in which linear Tafel region can be obtained at large overpotential region. Here, the value of  $i_0$  can be determined at y-intercept. In the case that small  $\eta$  is applied to the cell, the Butler-Volmer equation can be further simplified to [55]

$$i = i_0 \left( \frac{n F}{RT} \right) \eta. \quad (2-28)$$

By plotting current-overpotential in very small overpotential region (Figure 2.11 shows an example of current-overpotential curve and the overpotential is typically less than 10 mV),  $R_{ct}$  can be obtained from the slope. Then, the value of  $i_0$  can be calculated by using the Eq. (2-28).

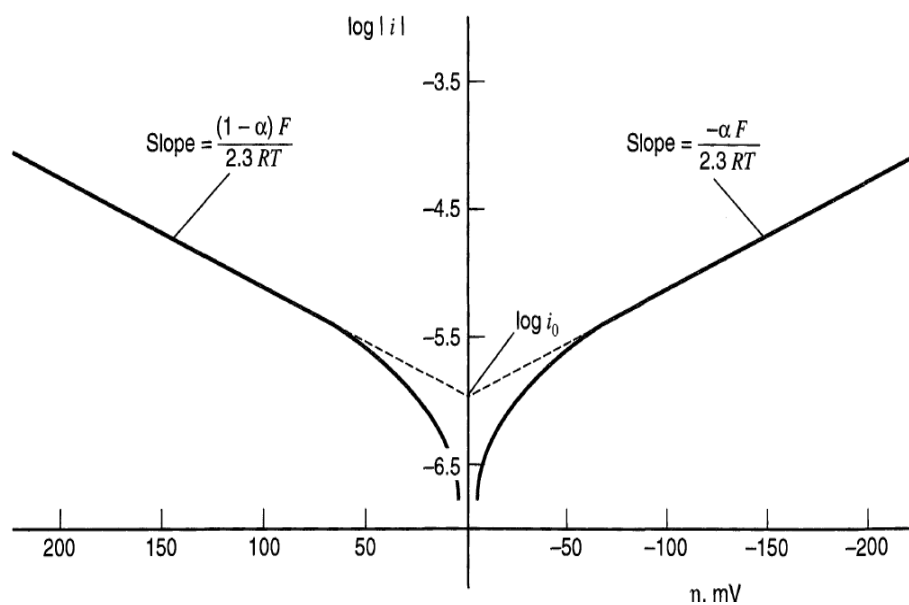


**Figure 2.10** An example of Tafel plot for anodic and cathodic branches [55].

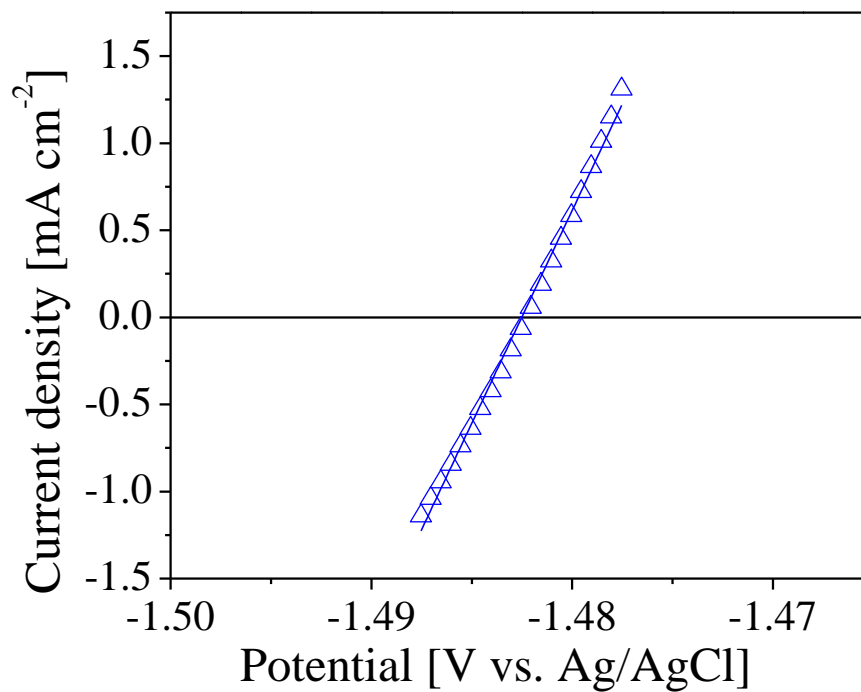


**Figure 2.11** An example of current-potential curve at small overpotential region.

**Table 2.2** Summary of electrochemical techniques used in each chapter and measured properties

Experiments	Elements	Electrode	Electrochemical methods				
			CV	OCP	EIS	Tafel/LP	OCC
Chapter 4.1	Ce	W	O		O		
Chapter 4.2	Ce	LCC	O			O	O
Chapter 5.1	U	W	O	O	O	O	
Chapter 5.2	U-Gd	W	O	O	O		
			D	E	$R_{ct}$	$i_0$	$\Delta G$
Measured			$E0^*$	$E0^*$	$i_0$	$k^0$	$\Delta H$
Properties			$\Delta G$	$\Delta G$	$k^0$		$\Delta S$
			$\gamma$	$\gamma$			

## 2.4 Summary

Literature surveys were performed to understand the available properties of nuclear elements previously reported. It was discussed that some data sets are scattered and not fully understood due to challenges in experimental measurements. In addition, electrochemical techniques and methods used in this project were investigated based on the literatures and textbooks. For the proper evaluation of uranium properties including diffusion coefficient, apparent standard potential, Gibbs free energy, activity coefficient, and exchange current density, specific techniques and equations must be applied to obtain accurate data sets. Table 2.2 summarizes the selected techniques and specific design to be used for each experiment in Chapters 4 and 5.

## Chapter 3 Experimental setup and procedures

To elucidate the fundamental characteristics of UNF, it is important to carefully prepare and design the experiments in a controlled environment. As an example, the salt chemicals including LiCl and KCl have a hygroscopic characteristic; hence, the chemicals need to be prepared in free oxygen and water environment, or need to be purified. Therefore, the main purpose of this Chapter is to provide detailed description of the experimental program used in the present research—installments of the equipment, reagents, materials, and sample preparation methods for performing all experimental runs. These steps are extremely critical in order to obtain reliable and repeatable results from the electrochemical measurements. It should be noted that this Chapter will only provide general experimental setups and materials conducted in the laboratory. More detailed setups, designs, and experimental procedures specific to each experiment will be provided and discussed in Chapters 4 and 5.

### 3.1 Equipment

Two glovebox systems (Innovative Technology) were established in the Radiochemistry laboratory (E4262 School of Engineering at VCU) as shown in Figure 3.1. The O<sub>2</sub> and H<sub>2</sub>O levels are being monitored by oxygen and water sensors preinstalled on the glovebox system as shown in Figure 3.2(a). Occasionally, O<sub>2</sub> level was analyzed with a portable O<sub>2</sub> sensor (Advanced Instruments Inc. (see Figure 3.2(b))) to confirm the accuracy of the O<sub>2</sub> sensor on glovebox. All the electrochemical experiments were prepared and conducted when the O<sub>2</sub> level is less than 5 ppm. RAM II glovebox was designed to utilize radioactive materials; therefore, all researchers working



in RAM II must take radiation safety training through VCU radiation safety section (RSS) and pass a test. When working in RAM II glovebox, researchers monitor hands, arms, and any materials moving in and out the glovebox by using hand-held monitors or Friskers as seen in Figure 3.3. Within the glovebox systems, commercial furnaces were installed to heat and maintain the salt samples at desired temperature. During preliminary studies, Kerrlab melting furnace was mainly utilized (see Figure 3.4(a)); however, this furnace had an issue in failing to control the temperature after a continuous intensive use (e.g., 1-2 weeks duration). This may be due to failure of heating coil or temperature controller. After experiencing this issue several times during the preliminary studies, another commercial furnace (Muffle furnace) was purchased from Thermo Scientific and redesigned for the electrochemical experiments, as shown in Figure 3.4(b). Therefore, all the uranium studies (Chapter 5) were performed using Muffle furnace, which has been working remarkably well until now.

All the salt samples were handled, and precisely prepared by using the Mettler Toledo balance ( $< 1 \mu\text{g}$  tolerance, see Figure 3.5) installed in the glovebox systems. Here, it should be noted that further errors can be introduced by build-up of static charges on the weighting plates or pressure difference in the glovebox system. When the sample preparations and electrodes setup were completed, VSP-300 potentiostat/galvanostat (purchased from Biologic Science Instrument as shown in Figure 3.6) were connected through the isolated feed through ports on the glovebox wall. For collecting and processing the measured data, EC-Lab software released from Biologic-Science Instruments was utilized for all electrochemical experiments in the present research. During the data measurements, the salt samples were taken using a tungsten rod and analyzed by an Agilent 7900 inductively coupled plasma-mass spectrometry (ICP-MS), as shown in Figure 3.7.



**Figure 3.1** Glovebox systems (RAMI (top) and RAMII (bottom)) for electrochemical experiments.

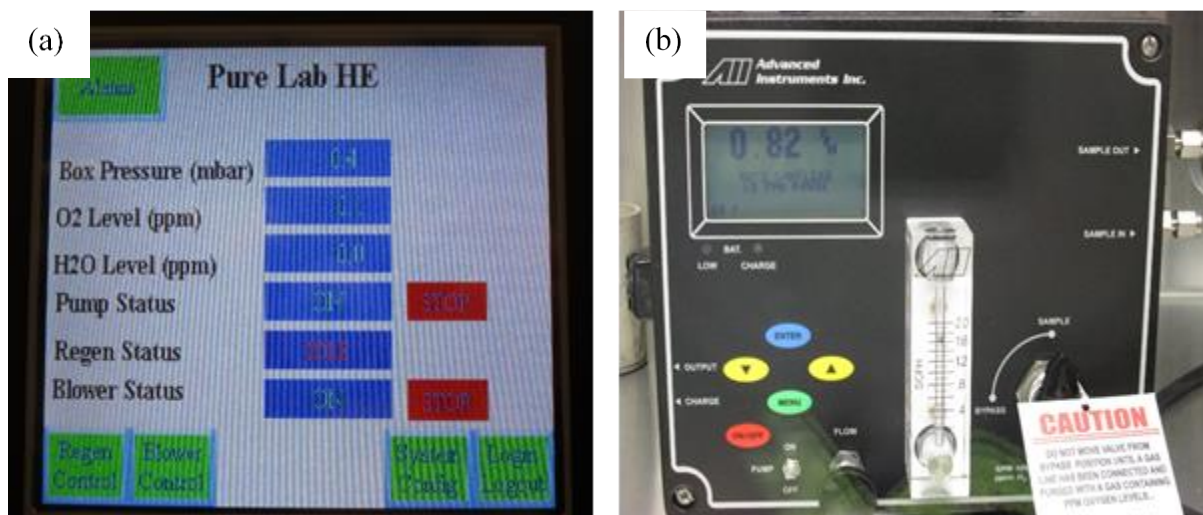


**Figure 3.2** (a) Digital control panel on the glovebox systems reading oxygen and water levels and (b) a portable oxygen analyzer from Advanced Instruments Inc.



**Figure 3.3** Pancake detector frisking meter (left) and hand survey meter (right) from Atlantic Nuclear Corporation.

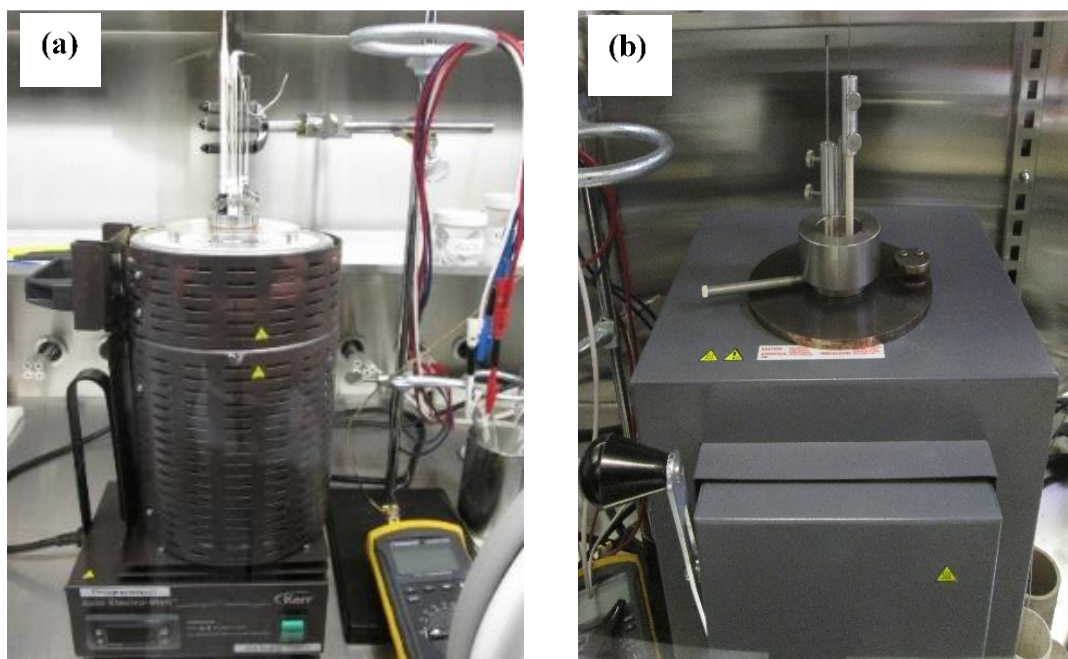


**Figure 3.4** (a) Kerrlab melting furnace, and (b) Muffle furnace from Thermo Scientific.



**Figure 3.5** Mettler Toledo balance placed in the glovebox systems.





**Figure 3.6** VSP-300 potentiostat/galvanostat, Biologic Science Instrument.



**Figure 3.7** Agilent 7900 ICP-MS instrument installed in the Radiochemistry laboratory.

## 3.2 Experimental preparation

### 3.2.1 Reagents and crucibles

Anhydrous lithium chloride ( $\text{LiCl}$ , 99.995%, bead type) and potassium chloride ( $\text{KCl}$ , 99.95%) were purchased from Alfa Aesar. The beads of  $\text{LiCl}$  and  $\text{KCl}$  were well mixed in quartz crucible to prepare a  $\text{LiCl-KCl}$  (58.2:41.8 in mol%) eutectic salt. The prepared mixtures were loaded in a vessel and heated in furnace (melting temperature of  $\text{LiCl-KCl}$  eutectic salt is 623 K). Once  $\text{LiCl-KCl}$  eutectic salt was prepared, target elements including cerium chloride ( $\text{CeCl}_3$ ), uranium chloride ( $\text{UCl}_3$ ), and gadolinium chloride ( $\text{GdCl}_3$ ) were added in the vessel. The depleted  $\text{UCl}_3$  powders (73 wt%  $\text{UCl}_3$  in  $\text{LiCl-KCl}$ ) provided by INL (see Figure 3.8(a)) were used for the uranium studies in Chapter 5. It should be noted that all the salt samples were dried at 523 K for 5 hours to remove possible moisture contents despite having the salt in sealed glass ampoules under argon prior the melting processes. Prior to the electrochemical measurements, few more hours (3 to 5 hours) were given for the salt system to reach the equilibrium state at the desired temperature.

In preliminary studies, alumina ( $\text{Al}_2\text{O}_3$ ) crucible was generally used as the vessel, which was washed/sonicated with ultra-pure water and dried in an oven at 473 K for 2 hours. All the uranium studies were performed with Inconel® crucible (Inconel 601 alloy, nickel-chromium-iron alloy from Alfa Aesar) owing to the reactions happening between uranium chloride and oxygen/adhesives from the alumina crucibles. These main vessels were placed in a secondary crucible to contain any molten salt upon possible failure of the primary crucible as can be seen in Figure 3.9. The specific information of the reagents and crucibles can be found in Table 3.1.

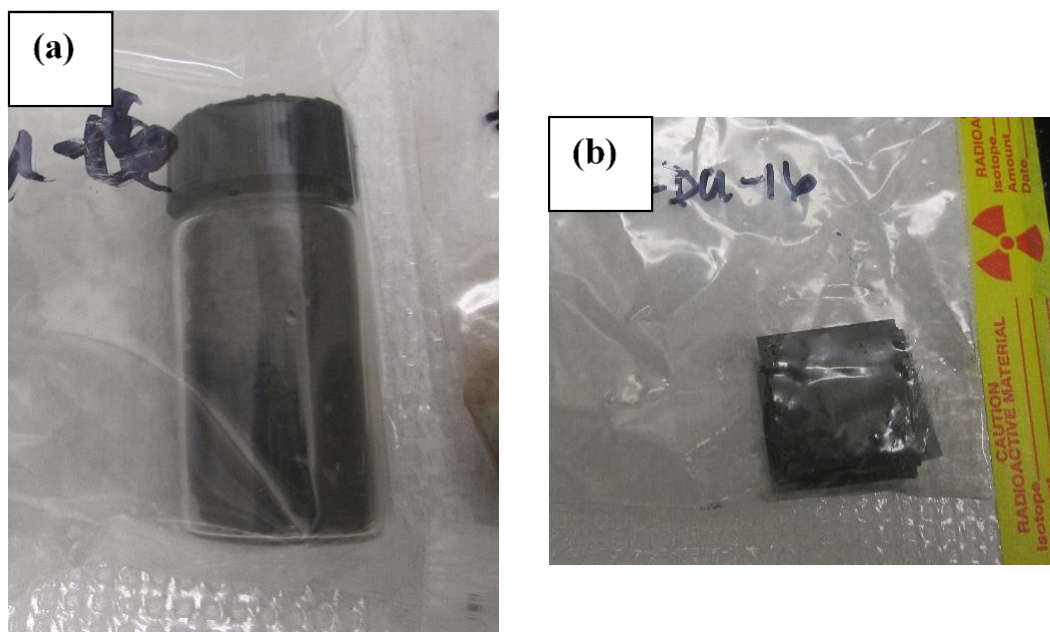


**Figure 3.8** Depleted uranium samples: (a) LiCl-KCl - 73 wt%  $\text{UCl}_3$  eutectic, and (b) uranium plates provided by INL.



**Figure 3.9** Alumina crucible (left) and Inconel crucible (right) placed in safety crucible for preliminary and uranium studies, respectively.

**Table 3.1** Material summaries for reagents and crucibles used in the present study

Materials	Detailed data	Manufacturers	Applications
<b>LiCl</b>	99.995%, bead type	Alfa Aesar	Prepare LiCl-KCl electrolyte
<b>KCl</b>	99.95%, bead type	Alfa Aesar	Prepare LiCl-KCl electrolyte
<b>AgCl</b>	99.998%, bead type	Alfa Aesar	Reference electrode
<b>CeCl<sub>3</sub></b>	99.9%, bead type	Alfa Aesar	Preliminary study
<b>CdCl<sub>2</sub></b>	99.999%, powder	Alfa Aesar	Preliminary study
<b>Ce metal</b>	99.9%, metal chips	Sigma-Aldrich	Preliminary study
<b>Cd</b>	99.999%, shots	Alfa Aesar	Preliminary study
<b>UCl<sub>3</sub></b>	73% in LiCl-KCl, powder	INL	Uranium study
<b>GdCl<sub>3</sub></b>	99.99%, powder	Alfa Aesar	Uranium study
<b>U metal</b>	Depleted U metal plate	INL	Uranium study
<b>Al<sub>2</sub>O<sub>3</sub></b>	99.8%, OD: 48, H: 47 mm		Vessel in Preliminary study
<b>crucible</b>	OD: 28, H: 40 mm	Coorstek	Vessel in Preliminary study
	OD: 40, H: 165 mm		Safety crucible in Preliminary study
	OD: 54, H: 91 mm		Safety crucible in Uranium study
<b>Inconel®</b>	OD: 47 mm, H: 41 mm	Alfa Aesar	Vessel in Uranium study
<b>crucible</b>			

### 3.2.2 Electrodes: Working, Counter, and Reference Electrode

All electrode rods were preinstalled in alumina sheath for the prevention of a shortage in the electrical circuit as indicated in Figure 3.10(a). Tungsten rods (99.95%, 1.5 mm – 2.0 mm in



diameter, Alfa Aesar) were typically used as a working electrode. The geometric surface area was determined by measuring the immersed length of the working electrode into the molten salt as shown in Figure 3.10(b). A glassy carbon rod (HTW, 3mm in diameter), Ce metal chips (Sigma-Aldrich 99.9%), and U metals (see Figure 3.8(b) provided by INL) were used for a counter electrode according to the experimental runs. Since designs and configurations of the working/counter electrodes vary with the different tasks, specific information can be found in the experimental section of each chapter (see Chapters 4 and 5). In contrast, all the experiments utilized the Ag/AgCl reference electrode, so that the preparation of reference will be discussed in this section. Specific procedure of the preparation is as follows:

- Prepare the LiCl-KCl eutectic salt in a closed-end Quartz tubing (22 mm in OD, Research Glass),
- Add a certain amount of AgCl in the Quartz crucible and melt the salt at 773 K,
- Stir the LiCl-KCl-AgCl salt and leave it for 3 hours for homogeneity of the salt,
- Insert a Pyrex tube (4 mm in OD, Research Glass) into the salt solution, and draw the salt into the tube by using a syringe,
- Leave the drawn salt under a room temperature to solidify the salt, and
- Obtain the solid rod of LiCl-KCl-AgCl salt as shown in Figure 3.11.

The prepared AgCl salt rod was loaded in a 7 mm diameter Pyrex tube (Research Glass), which is closed at one end. At the tip of the tube, the thickness of the wall was made thin enough (less than 0.5 mm in thickness, see Figure 3.12(a)) allowing ionic conduction between the solution and electrolyte. As shown in Figure 3.12(b), the prepared AgCl salt rod is loaded in the Pyrex tube, which is melted at high temperature and contacted with Ag wire (99.99%, 1 mm in diameter, Alfa

Aesar). Therefore, the equilibrium potential between Ag metal and AgCl solution was established and used as a standard potential for all electrochemical measurements in the present researches.

In the preliminary study (Chapter 4), 5 mol% AgCl reference was prepared and used as a reference electrode, while Ag/AgCl (1 mol%) reference was utilized for the uranium studies in Chapter 5. Since various concentrations of AgCl solution were utilized for electrochemical research in literature, the results data should be converted into  $\text{Cl}_2/\text{Cl}^-$  scale for meaningful comparison. Therefore, the conversions from Ag/AgCl (1 mol% and 5 mol %) to  $\text{Cl}_2/\text{Cl}^-$  reference electrode were being performed by the interpolation/extrapolation of the data reported by Yang and Hudson [60]. The potential differences between Ag/AgCl and  $\text{Cl}_2/\text{Cl}^-$  used in the present study are summarized in Table 3.2.

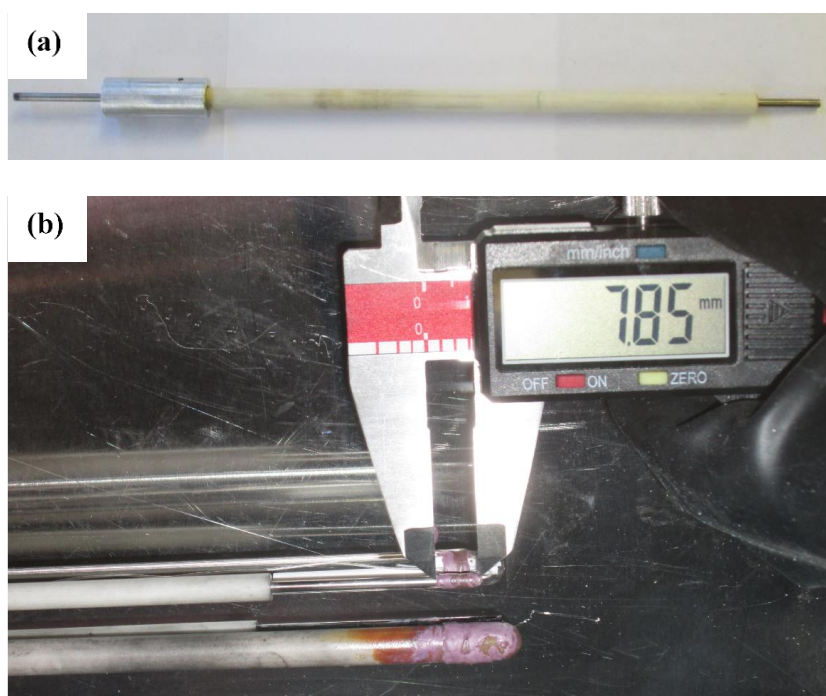


**Figure 3.10** (a) Tungsten rod sheathed with alumina tube, (b) measurement of submerged electrode area in the salt by using digital caliper.

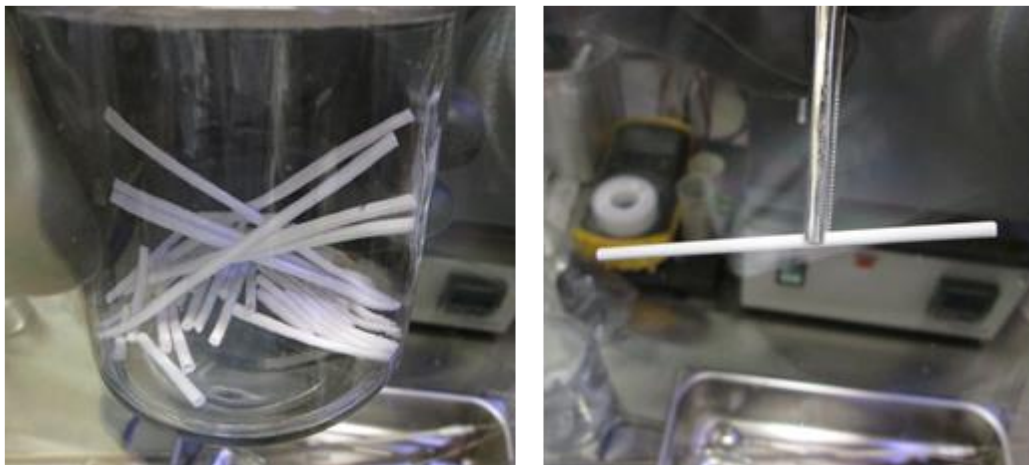


**Figure 3.11** Prepared AgCl salt rods.

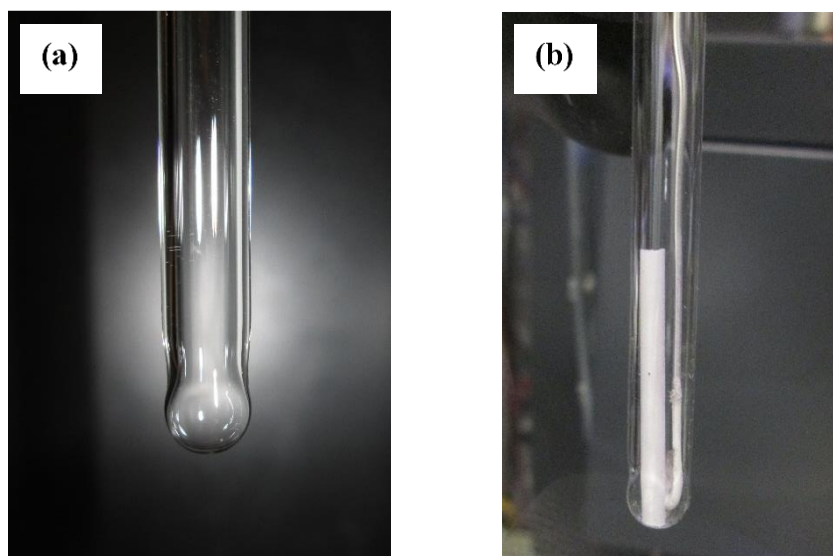


**Figure 3.12** (a) Pyrex tube with thin end for ionic conductivity, (b) Ag/AgCl reference built in Pyrex tube.

**Table 3.2** Potential differences between Ag/AgCl reference electrodes and Cl<sub>2</sub>/Cl reference at different temperatures [60]

T [K]	$\Delta E$ between Ag/AgCl and Cl <sub>2</sub> /Cl references [V]	
	1 mol% Ag/AgCl	5 mol% Ag/AgCl
698	1.155	1.069
723	1.157	1.068
748	1.159	1.067
773	1.161	1.067
798	1.161	1.066
823	1.163	1.065

### 3.2.3 Electrode assembly

For securely placing the electrodes and thermocouple under the molten salt at high temperature, an electrode assembly was designed and manufactured in VCU School of Engineering machine shop, which is indicated in Figure 3.13. Main purpose of the design was to 1) assemble the electrode as a single body for easy access into the furnace from the top lid, 2) place the electrodes at demanding vertical position, and 3) take the salt sample during experiments. Figure 3.14 shows the parts of the electrode assembly and its specific diagram. There are three main bodies made with stainless steel where four holes (two holes are designed for 5 mm OD cylinder and the other holes are for 7 mm OD cylinder). On top of the Part (c) in Figure 3.14, high temperature rubber O-rings were placed which the electrodes were slid in. When Parts (a) and (c) are tighten by using the threads, the O-rings are squeezed and therefore tightly holding the electrodes without breaking the alumina sheath. In this manner, the electrodes are securely

assembled in a single body; hence, an access of the assembly can be easily made into the furnace at high temperatures. In addition, electrode rods inside the alumina sheath can be separately removed from the assembly body. Thus, electrode cleaning and salt sampling can be readily conducted during the electrochemical measurements.



**Figure 3.13** Electrode assembly for electrochemical applications.

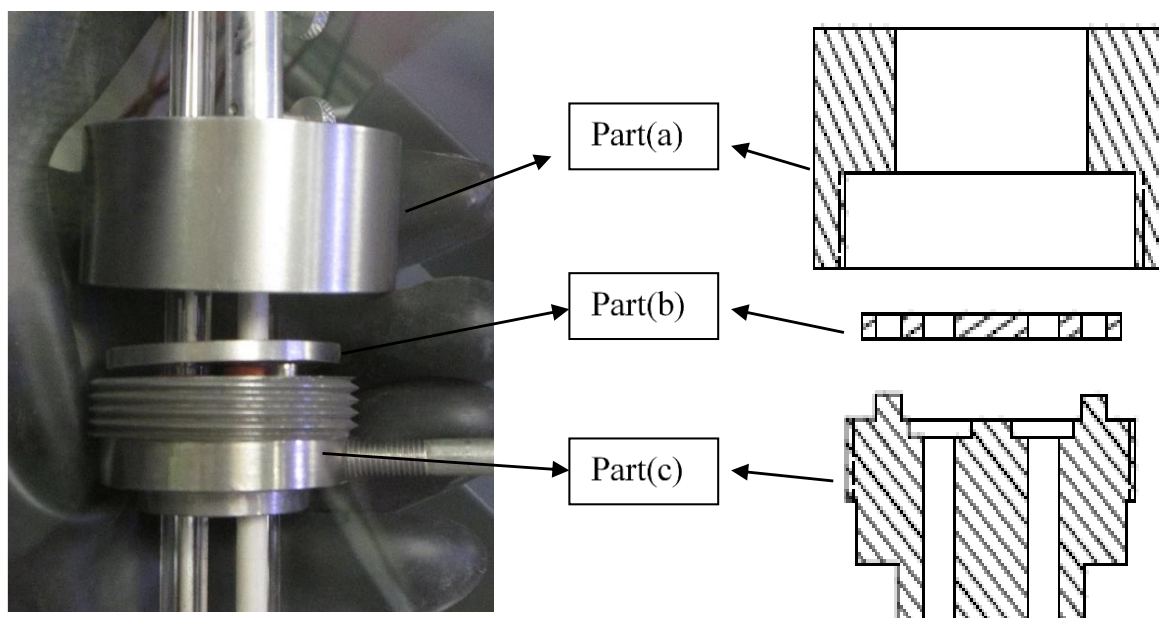


**Figure 3.14** Electrode assembly parts and its diagram.

### 3.2.4 Sample preparations for ICP-MS Analysis

In particular, all uranium salt samples provided by INL may be non-homogenous and contain oxide formations, which will have an influence on the chemical compositions. Therefore, the concentration of the prepared  $\text{UCl}_3$  salts were demonstrated by using an ICP-MS analysis. Due to the hygroscopic feature of the salt sample, the following sample preparation procedures were used:

- Prepare the nitric acid (2%  $\text{HNO}_3$ ) with the ultrapure (Type 1) water,
- Prepare 6 – 9 standard samples using multi-element blends: CCS1 and CCS4 (Inorganic Ventures),
- Prepare different internal standards at  $\sim 5000 \mu\text{g/L}$ ,

- Take 15 mL centrifuge tubes into the glovebox,
- Measure the weight of salt sample (be careful of static and pressure effects),
- Load salt samples in the centrifuge tubes and close the lid,
- Take out the centrifuge tubes from the glovebox,
- Open the lid and quickly fill out the tubes with 10 mL  $\text{HNO}_3$  in order to minimize water absorption from an environment,
- Wait for the solid salts to be fully dissolved into the  $\text{HNO}_3$  solution,
- Dilute the stock samples with 500 - 5000 times for running uranium samples lower than EPA regulation (U.S. EPA regulation for drinking water is less than  $30 \mu\text{g/L}$ ), and
- Run the ICP-MS with the diluted samples and calculate concentrations with the used dilution factors.

### 3.3 Summary

In this chapter, general experimental preparations generally were described. Apparatus including the glovebox systems, the furnaces, and the potentiostat were first presented. Then, the reagents and crucibles used in the present study were introduced and their specifications and preparation methods were discussed. It was followed by the explanation of electrodes. While the working and counter electrodes are particularly designed for achieving goals of each experiment, the Ag/AgCl reference electrode was commonly used for all electrochemical measurements; therefore, Ag/AgCl reference construction and the potential difference from  $\text{Cl}_2/\text{Cl}^-$  reference electrode were mainly focused. In addition, the electrode assembly were designed and built based on the concept for easy access into the molten salt at high temperature. Lastly, all sample

preparations and procedures for the ICP-MS quantitative analysis were provided. This given information will be useful to understand other experimental setups and conditions in following chapters discussing the electrochemical measurements and results.



## Chapter 4 Experimental Development with Ce as a Surrogate Material for U (Preliminary studies)

The main purpose of this chapter is to provide the information on a development of experimental methodologies, and electrochemical techniques with a non-radioactive material, which can be applied toward uranium. Cerium chloride ( $\text{CeCl}_3$ ) was selected as a surrogate material for  $\text{UCl}_3$  because the  $\text{Ce}^{3+}$  has similar electrochemical characteristic and ionic size of  $\text{U}^{3+}$  [61]. The ionic sizes are about 115 pm and 117 pm, for  $\text{Ce}^{3+}$  and  $\text{U}^{3+}$ , respectively [62], and diffusion coefficients of both elements are in order of  $10^{-5} \text{ cm s}^{-1}$  [37, 45, 61, 63, 64]. Therefore, electrochemical measurements were performed to evaluate Ce properties such as diffusion coefficient, apparent standard potential, thermodynamic properties, and exchange current density in LiCl-KCl eutectic salt. Section 4.1 will discuss the measurements of Ce properties using solid working electrode while Section 4.2 discuss the Ce behaviors on LCC electrode, which will elucidate the fundamental properties of actinide (An) and lanthanide (Ln) in ER process with LCC operations.

### 4.1 Electrochemical properties and analyses of $\text{CeCl}_3$ in LiCl-KCl eutectic salt<sup>1</sup>

#### 4.1.1 Introduction

Several studies on the electrochemical behaviors of cerium in the molten salt at high temperatures have been previously conducted. In 1998, Iizuka [7] conducted CP to determine

---

<sup>1</sup> Contents in Section 4.1 are cited from the author's publication:  
D. Yoon and S. Phongikaroon, "Electrochemical properties and analyses of  $\text{CeCl}_3$  in LiCl-KCl eutectic salt," *Journal of The Electrochemical Society*, **162** (10), E237-E243 (2015).

diffusion coefficient of  $\text{CeCl}_3$  at different temperatures. Marsden and Pesic in 2011 [61] measured apparent standard potentials and diffusion coefficients of  $\text{CeCl}_3$  by CV technique. They also determined the exchange current densities of  $\text{CeCl}_3$  using the LP method. While the diffusion coefficients and apparent standard potentials of Ce elements were well evaluated from many researchers with various techniques, only LP method was used for the measurement of  $i_0$ . Due to the difficulties in measuring the  $i_0$  with LP method, Marsden and Pesic [61] provided wide ranges of  $i_0$  values for  $\text{Ce}^{3+}/\text{Ce}$ .

Thus, the main goal of the Section 4.1 is to provide measurement and analyses of electrochemical and kinetic properties of  $\text{CeCl}_3$  in LiCl-KCl eutectic salt at different concentrations and temperatures using two methods: (1) CV for measuring the diffusion coefficients and apparent standard potentials and (2) EIS for determining the  $i_0$  values. The outcomes will provide useful insight into these properties with a unique feature of EIS technique by reducing uncertainty of electrode area measurement because very small current is applied at around an open circuit potential.

#### **4.1.2 Particular experimental setup and routine**

For the preparation of chemicals, crucibles, and reference electrode, general procedures as discussed in Section 3.2 were followed. Figure 4.1 indicates the schematic design of the electrochemical cell placed in the Kerrlab furnace. Tungsten rods (1.5 mm and 2 mm in diameter) were used as the working electrode. The length of the working electrode submerged into the salt was measured, and the surface areas were ranging from  $0.32 \text{ cm}^2$  to  $0.63 \text{ cm}^2$  depending on experimental runs. The cerium chips were loaded in a molybdenum basket and lowered into the

prepared salt, which works as the counter electrode. Prior to using the counter electrode, an oxide layer on the cerium chips was eliminated using sand paper under argon environment. Ag/AgCl (5 mol%) was used as a reference electrode. Table 4.1 summarizes the experimental program developed in this study. Prior to each experiment, the working electrode was anodically cleaned by stripping at a potential of -0.1 V versus the reference electrode for 3 minutes. Then, OCP was checked to ensure the equilibrium condition has reached in the system. This was repeated for each electrochemical measurement, and anodic stripping and OCP were carried out longer in case of higher concentrations.

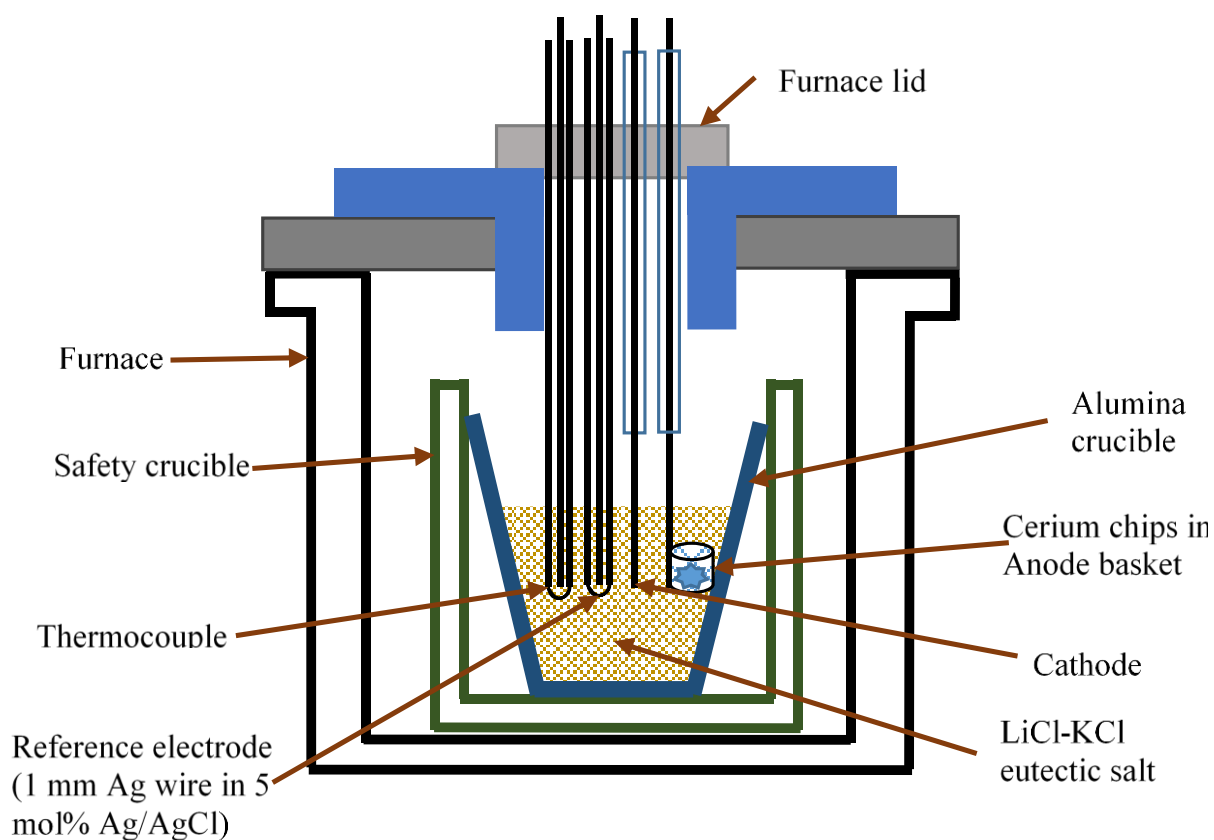


**Figure 4.1** Schematic sketch of the experimental setup of all electrochemical experiments.

**Table 4.1** Detailed experimental program for electrochemical measurements of  $\text{CeCl}_3$ 

Experimental runs	Temperature [K]	Electrode area [cm <sup>2</sup> ]	CeCl <sub>3</sub> concentration		
			[wt%]	[mol%]	[mole/cm <sup>3</sup> ] $\times 10^5$
Ce_S_1	698 – 798	0.559	0.507	0.115	3.33 – 3.44
Ce_S_2		0.685	0.498	0.113	3.27 – 3.37
Ce_S_3		0.597	2.06	0.473	13.7 – 14.1
Ce_S_4		0.324	4.03	0.944	27.4 – 28.3

### 4.1.3 Results and Discussion

#### 4.1.3.1 Cyclic voltammetry (CV) of the LiCl-KCl-CeCl<sub>3</sub> system

The CV technique was first applied to the pure LiCl-KCl system to identify that no other reactions occurring in the range between 0 V and -2.5 V versus Ag/AgCl reference. The voltammogram of pure LiCl-KCl (in Figure 4.2) shows that Li reduction starts at -2.55 V (vs. Ag/AgCl). No redox reaction between 0 to -2.4 V was observed and residual current in that region was less than 2 mA. Therefore, it was safe to perform the CV experiments over that potential range without interference from other reactions. Figure 4.3 shows the cyclic voltammograms of  $\text{CeCl}_3$  (0.5 wt%, 2 wt%, and 4 wt%) in LiCl-KCl at 773 K. It was extremely important to obtain repeatable and reproducible CV data. Table 4.2 provide the summary of the methods for the CV measurements and data acquisition in detail. Cerium reduction and oxidation peaks were observed at around -2.2 and -2.09 V versus the Ag/AgCl reference electrode, respectively. For 0.5wt%  $\text{CeCl}_3$ ,

the peak potentials stay at the same potential under different scan rates representing the reversibility of the reaction in the range of the scan rate. However, the peak potentials move slightly in the negative direction according to the scan rate when the concentration of  $\text{CeCl}_3$  was being increased to 4 wt%. This may be considered as a quasi-reversible reaction.

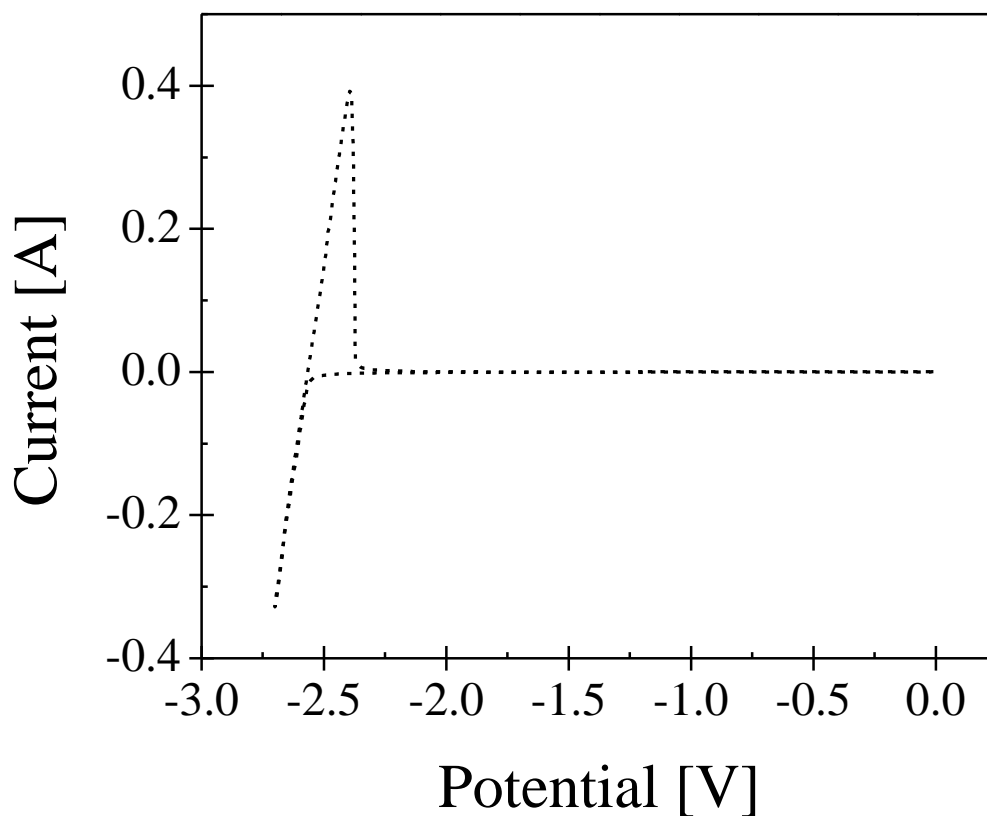


**Figure 4.2** Cyclic-voltammogram of pure LiCl-KCl eutectic salt at 773 K at the scan rate of  $0.1 \text{ V s}^{-1}$ . Tungsten rod (2 mm in diameter) was used as cathode electrode, and the surface area was  $0.471 \text{ cm}^2$ .

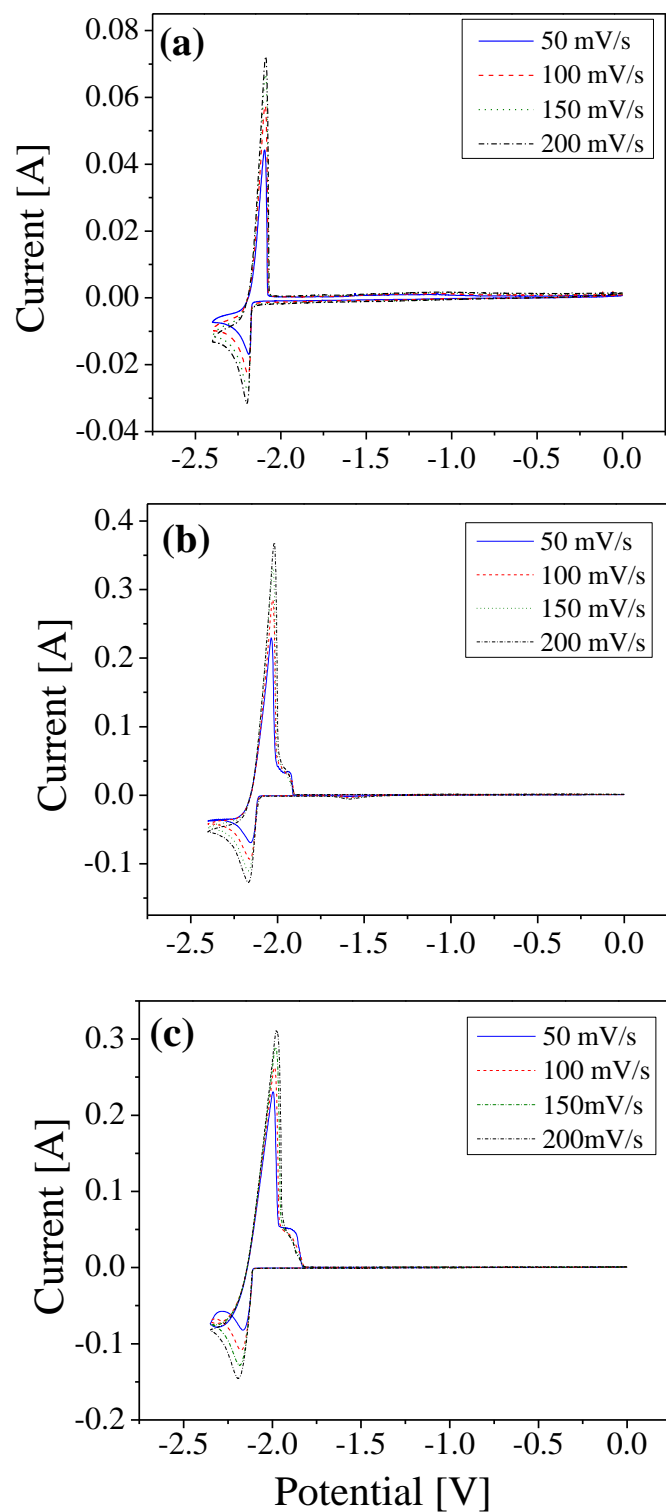


**Figure 4.3** Cyclic-voltammogram of  $\text{CeCl}_3$  in  $\text{LiCl-KCl}$  at 773 K at scan rates of 0.05, 0.1, 0.15, and 0.2  $\text{V s}^{-1}$ : (a) 0.5 wt %  $\text{CeCl}_3$ , (b) 2 wt %  $\text{CeCl}_3$  (c) 4 wt %  $\text{CeCl}_3$ .

**Table 4.2** Steps of CV measurements and data acquisition

Step	Description
1	Clean the working electrode by applying an oxidative potential (-0.1 V vs. Ag/AgCl) for 3 minutes,
2	Wait for 1 ~ 3 minutes until the OCP becomes stable,
3	Perform CV measurements at least 5 cycles,
4	Obtain the data if the CV curves are repeatable,
5	Repeat Steps 1 – 4 for next CV measurement,
6	Measure peak current, peak potential, and half peak current using the EC-LAB software, and
7	Calculate the values of D and $E^{0*}$ using Eq. (2-13) and Eq. (2.15), respectively.

The difference between peak potential and half peak potential can be used to calculate the number of electron transferred by using Eq. (2-9). The calculated number of electron transferred,  $n$ , was ranging from 2.5 to 3.1 agreeing with the expected value for the reduction process of  $Ce^{3+}/Ce$ . The cathodic peak currents were plotted with respect to the square root of the scan rate to calculate diffusion coefficient of  $CeCl_3$  in LiCl-KCl using Eq. (2-13). The diffusion coefficient of  $CeCl_3$  was determined at different concentrations, as indicated in Figure 4.4. Small decrease of the values could be observed by increasing concentration from 0.5 wt% to 2 wt%; however, the diffusion coefficients of  $CeCl_3$  in LiCl-KCl salt were approximately the same between the concentrations of 2 and 4 wt%. Present study shows smaller values for the diffusion coefficients comparing with those from Marsden and Pesic [61] and Iizuka [7]. But these values possess a similar trend.

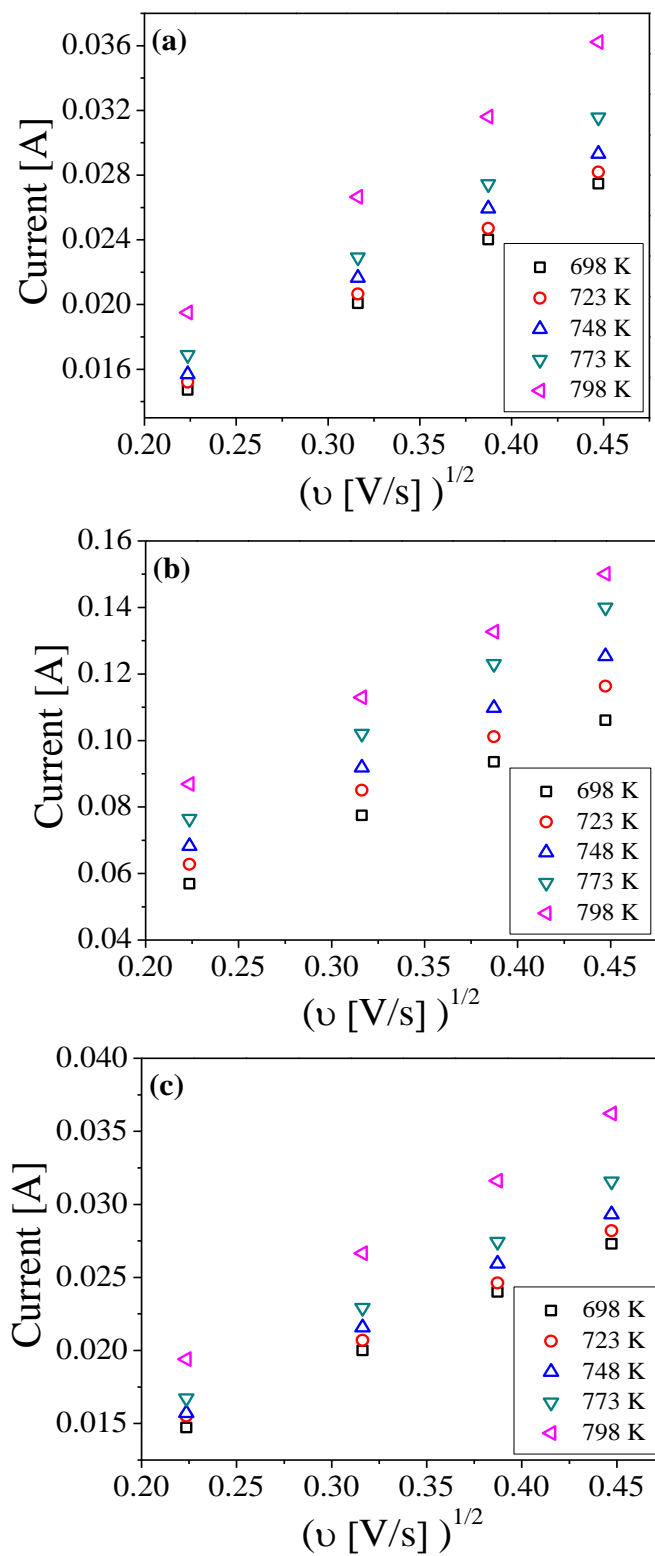


**Figure 4.4** Plots of the peak currents versus the square roots of the scan rates at (a) 0.5 wt%, (b) 2 wt%, (c) 4 wt%  $\text{CeCl}_3$ .



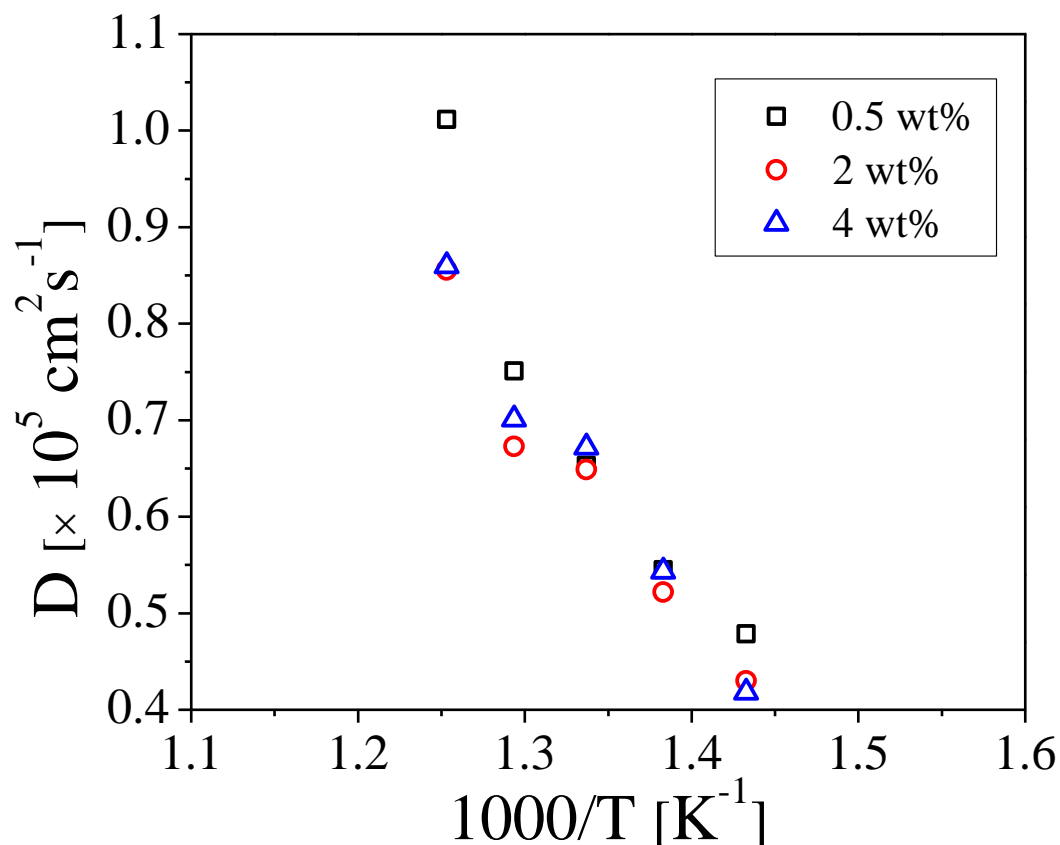


**Figure 4.5** Plots of diffusion coefficient of  $\text{Ce}^{3+}$  versus inverse temperature at different  $\text{CeCl}_3$  concentrations (0.5, 2, and 4 wt %).

The square root of the diffusion coefficients were plotted against inverse temperature, allowing calculation of the activation energy for  $\text{CeCl}_3$  diffusion by using the Arrhenius relationship in Eq. (2-14). The  $R^2$  values between the fitted regression lines and experimental points were all greater than 0.96 indicating a good fit to the data sets. Table 4.3 lists the diffusion coefficients of  $\text{CeCl}_3$  and the average activation energies with different temperatures and concentrations.

**Table 4.3** Diffusion coefficients (D) measured from CV experiments and activation energy ( $E_a$ ) at different concentrations and temperatures

CeCl <sub>3</sub>	0.5 wt %		2 wt %		4 wt %	
T [K]	D	$E_a$	D	$E_a$	D	$E_a$
	$[\times 10^5 \text{ cm}^2 \text{ s}^{-1}]$	$[\text{kJ mol}^{-1}]$	$[\times 10^5 \text{ cm}^2 \text{ s}^{-1}]$	$[\text{kJ mol}^{-1}]$	$[\times 10^5 \text{ cm}^2 \text{ s}^{-1}]$	$[\text{kJ mol}^{-1}]$
698	0.479		0.430		0.418	
723	0.545		0.547		0.544	
748	0.653	30.7	0.675	31.6	0.672	33.4
773	0.751		0.690		0.700	
798	1.012		0.875		0.860	

From the cathodic peak potentials in the cyclic voltammogram, the apparent standard potential of CeCl<sub>3</sub> was calculated by using Eq. (2-15). The calculated apparent standard potentials are plotted in Figure 4.6 showing a proportional relationship with respect to an increase in temperature. The apparent standard potentials for the concentration of 0.5 wt% and 2 wt% agree with each other (staying within similar ranges of values), but the apparent standard potential for 4 wt% of CeCl<sub>3</sub> was slightly more negative. Once the apparent standard potentials were determined, thermodynamic properties can be further investigated using Eq. (2-4). Although the melting temperature ( $T_m$ ) of CeCl<sub>3</sub> salt is 1080 K in nature, CeCl<sub>3</sub> is dissolved in LiCl-KCl eutectic salt under a liquid phase; therefore, the fusion energy between solid and liquid phases need to be considered as well. Several literature studies mistakenly use the Gibbs energy for the formation at super cooled state ( $\Delta G^{\text{Formation}}$ ) as an ideal Gibbs free energy without considering the fusion

energy [61, 65]. Thus,  $\Delta G^{SC}$  can be re-written with considering the fusion energy between liquid and solid state through the following relationship:

$$\Delta G^{SC} = \Delta G^{Formation} + \Delta G^{Fusion} \quad (4-1)$$

where  $\Delta G^{Formation}$  is the Gibbs free energy for the formation ( $\text{kJ mol}^{-1}$ ) and  $\Delta G^{Fusion}$  is the Gibbs energy for the fusion between liquid and solid phases. This second term can be expressed as

$$\Delta G^{Fusion} = \Delta H^{Fusion} - T\Delta S^{Fusion} + \int_{T_m}^T \Delta C_p dT - T \int_{T_m}^T \frac{\Delta C_p}{T} dT \quad (4-2)$$

where  $\Delta H^{Fusion}$  is the enthalpy of fusion ( $\text{kJ mol}^{-1}$ ),  $\Delta S^{Fusion}$  is the entropy of the fusion at  $T_m$  ( $\text{kJ mol}^{-1} \text{ K}^{-1}$ ), and  $\Delta C_p$  is the heat capacity between  $T_m$  and  $T$  ( $\text{kJ mol}^{-1} \text{ K}^{-1}$ ). These thermodynamic values for  $\text{CeCl}_3$  at desired temperatures were obtained from the literature published by Barin [53], which are listed in Table 4.4 with the calculated thermodynamic data values ( $\Delta G^{Fusion}$ ,  $\Delta G^{SC}$ ). The values of  $\Delta G_{\text{CeCl}_3}^{0*}$  were calculated from the apparent standard potentials using the thermodynamic equation ( $\Delta G = -nF\Delta E$ ); therefore, the values of  $\gamma_{\text{CeCl}_3}$  could be calculated using Eq. (2-4). Results from Figure 4.7 show that values increase as temperature rises. However, these values need to be further evaluated to provide an overall trend with temperature. Compared with literature values [61, 65], the activity coefficients in the present study are smaller with an order from  $10^1$  to  $10^2$ . This deviation may be because previous researcher used only the Gibbs free energy for the formation to represent  $\Delta G^{SC}$  as mentioned above. Detailed calculated values are summarized in Table 4.4.

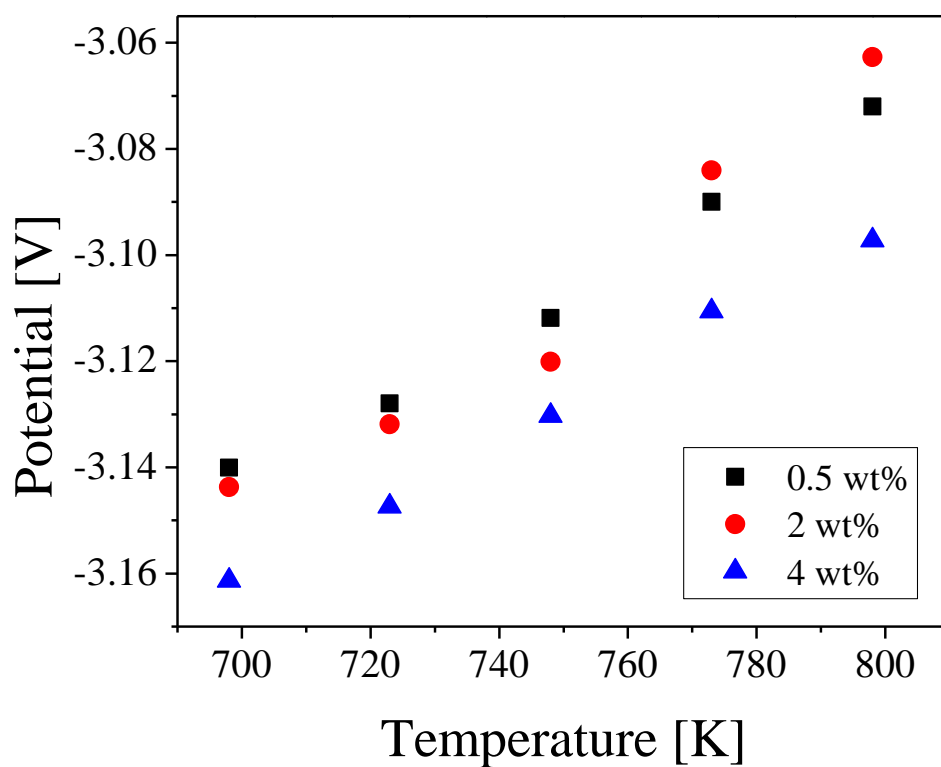


**Figure 4.6** Plot of apparent standard potentials versus temperature.

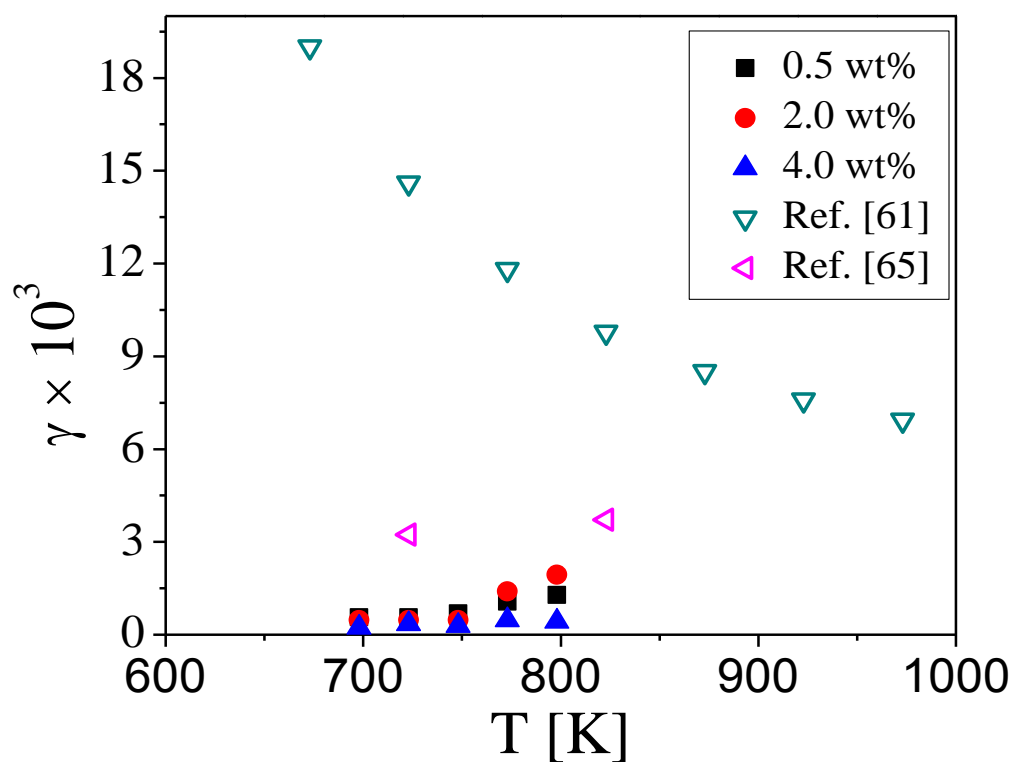


**Figure 4.7** Activity coefficients of  $\text{CeCl}_3$  in  $\text{LiCl-KCl}$ , compared with literature values.

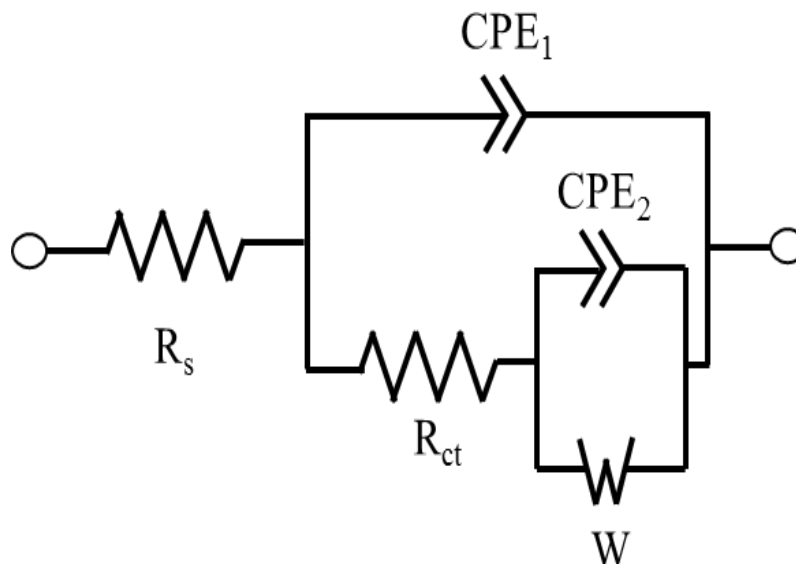
**Table 4.4** Thermodynamic information from the literature [53] and calculated values

		698 K	723 K	748 K	773 K	798 K	T <sub>m</sub> (1080 K)
$\Delta G_{\text{CeCl}_3}^{\text{Formation}}$ (kJ mol <sup>-1</sup> )		-880.90	-875.1	-869.31	-863.53	-857.28	
$\Delta H_{\text{CeCl}_3}^{\text{Fusion}}$ (kJ mol <sup>-1</sup> )							53.14
$\Delta S_{\text{CeCl}_3}^{\text{Fusion}}$ (J mol <sup>-1</sup> K <sup>-1</sup> )							49.20
$C_p$ (J mol <sup>-1</sup> K <sup>-1</sup> )		115.93	116.6	117.20	117.84	118.47	
$\Delta G_{\text{CeCl}_3}^{\text{Fusion}}$ (kJ mol <sup>-1</sup> )		15.40	14.67	13.90	13.07	12.20	
$\Delta G_{\text{CeCl}_3}^{\text{SC}}$ (kJ mol <sup>-1</sup> )		-865.5	-860.4	-855.4	-850.5	-845.1	
$\Delta G_{\text{CeCl}_3}^{0*}$ (kJ mol <sup>-1</sup> )	0.5 wt%	-908.9	-905.4	-900.7	-894.4	-899.2	
	2.0 wt%	-910.0	-906.5	-903.1	-892.7	-886.5	
	4.0 wt%	-914.1	-908.4	-906.1	-899.6	-896.5	
$\gamma_{\text{CeCl}_3}$ $\times 10^3$	0.5 wt%	0.56	0.56	0.68	1.07	1.29	
	2.0 wt%	0.47	0.47	0.47	1.40	1.94	
	4.0 wt%	0.23	0.34	0.29	0.48	0.43	

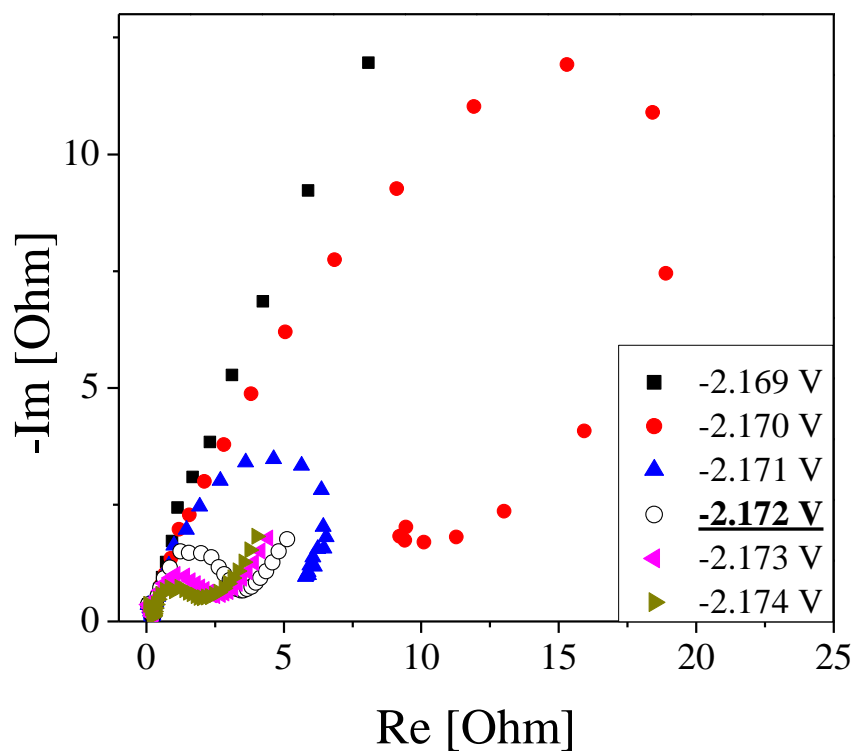
#### 4.1.3.2 Electrochemical impedance spectroscopy (EIS)

The EIS technique was selected and performed to calculate exchange current density ( $i_0$ ) of  $\text{Ce}^{3+}/\text{Ce}$  couple in LiCl-KCl salt. Compared to the LP and Tafel techniques, EIS has an advantage that the electrode surface area is almost maintained the same due to an extremely small current that is being applied at OCP or in that proximity. Therefore, uncertainty of electrode area can be reduced significantly in determining  $i_0$ . For analyzing impedance spectra, a simple equivalent circuit was proposed as shown in Figure 4.8 where CPE was used instead of double

layer capacitance and Warburg impedance. It is important to point out that  $R_s$  is the solution resistance,  $R_{ct}$  is the charge transfer resistance on the electrode surface,  $C_{dl}$  is the double-layer capacitance and  $W$  is the diffusion related resistance (Warburg). A frequency ranging from 50 kHz to 50 mHz was used, and the applied potential amplitude was set at 10 mV. Figure 4.9 shows impedance spectra for 0.5 wt% of  $CeCl_3$  in which the potential was gradually increased from the equilibrium potential (-2.169 V). In general, an impedance should be measured at an equilibrium potential to properly calculate  $i_0$ . However, at the equilibrium potential, the impedance swiftly increases at the high frequency and downward distortion was observed at low frequency as shown in Figure 4.9 because no ion transfer can occur between the tungsten electrode and cerium ions. Therefore, minimum overpotentials ( $\eta = 1 - 5$  mV) was applied to the cell for the cerium reduction to occur at the electrode surface. For an example, in Figure 4.9, by increasing  $\eta$  from equilibrium potential, a transition point can be observed at -2.172 V (open circles in Figure 4.9) with a noticeable behavior that, a diffusion related impedance (Warburg impedance) starting to occur at low frequency region. This occurrence implies that electrons transfer and diffusion from the bulk salt to the electrode surface starts to occur at that potential. In this case, current density flows through the EIS experiment was only less than  $1.5 \text{ mA cm}^{-2}$ . The electron exchange was confirmed by OCP measured right after the EIS experiments. After performing EIS at the potential of -2.172 V, OCP was maintained at the equilibrium potential for 500 s while OCP was released from the equilibrium potential when the applied potential was lower than -2.172 V. Therefore, minimum  $\eta$  for  $Ce^{3+}/Ce$  reduction to occur could be found and  $R_{ct}$  values were measured at those voltages by fitting the Nyquist plot to an equivalent circuit.



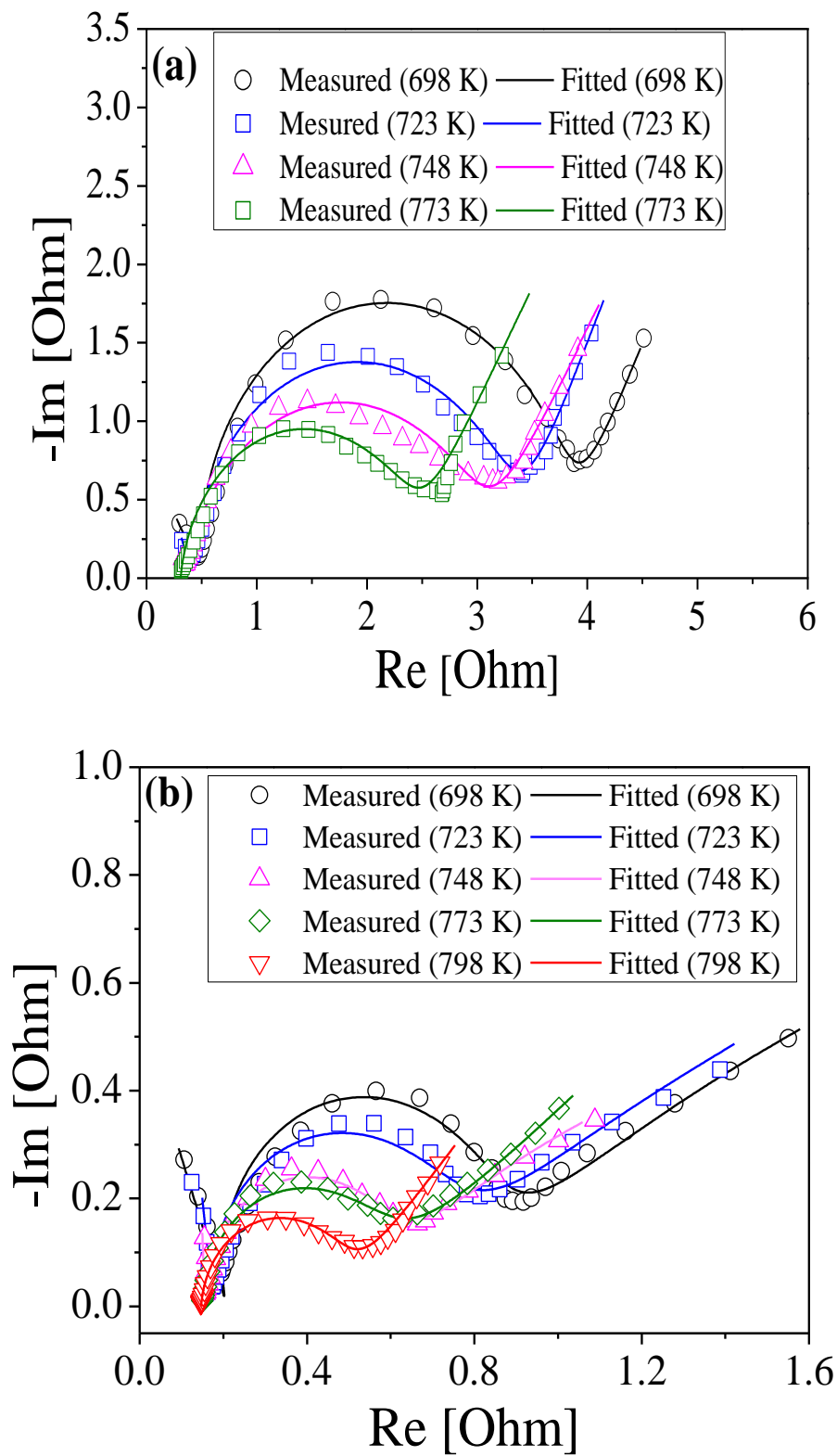
**Figure 4.8** Equivalent circuit for the electrochemical cell showing bulk solution resistance, charge transfer resistance, CPEs and Warburg impedance.



**Figure 4.9** Nyquist plot for 0.5 wt % of  $\text{CeCl}_3$  in  $\text{LiCl-KCl}$  at 723 K on a tungsten electrode. The frequency was from 50 kHz to 50 mHz, and the amplitude of applied sinus potential was 10 mV. Applied potentials were ranging from -2.169 to -2.174 V with an equilibrium potential of -2.169 V.

The measured and fitted impedance spectra of  $\text{Ce}^{3+}/\text{Ce}$  for the three different concentrations of  $\text{CeCl}_3$  at various temperatures are shown in Figure 4.10. First, the measured spectra were automatically fitted by using randomize and simplex method in Z-fit software (Bio-Logic), then a manual adjustment was done by changing the values of the equivalent circuit components. As the manual curve fitting was performed, the relative error could be minimized below a fraction of  $10^{-1}$ . Table 4.5 describes the methods to obtain EIS spectra and curve fittings as aforementioned. As a result of the curve fittings, the product of electrode surface area ( $S$ ) and  $R_{ct}$  and  $\eta$  were being measured; these values are summarized in Table 4.6. From the measured  $R_{ct}$ ,  $i_0$  can be readily computed by using Eq. (2-24). In addition,  $k^0$  can be calculated by assuming  $\alpha$  is 0.5 based on the observation from CV experiments that  $\text{Ce}^{3+}/\text{Ce}$  reaction follows reversible behaviors with a weak diffusion effect (at slow scan rates). Table 4.7 provides a list of  $i_0$  and  $k^0$  calculated from  $R_{ct}$ . Figure 4.11 plots the exchange current densities of  $\text{Ce}^{3+}/\text{Ce}$  reaction which can be characterized with concentrations and temperatures. The results indicate that  $i_0$  values with 0.5 wt% of  $\text{CeCl}_3$  are in between  $0.0076 \text{ A cm}^{-2}$  and  $0.016 \text{ A cm}^{-2}$ , agreeing well with repeated experimental runs. By increasing the concentration of  $\text{CeCl}_3$  to 4 wt%, the exchange current density appears to increase up to  $0.18 \text{ A cm}^{-2}$ . Marsden and Pesic [61] reported the exchange current density of  $\text{CeCl}_3$  at 4 wt% concentration using the linear polarization method, ranging from  $0.01 \text{ A cm}^{-2}$  to  $0.2 \text{ A cm}^{-2}$ . The values of  $i_0$  from this study are slightly higher, but both studies show similar range of values for the  $i_0$  of  $\text{CeCl}_3$  in LiCl-KCl salt.





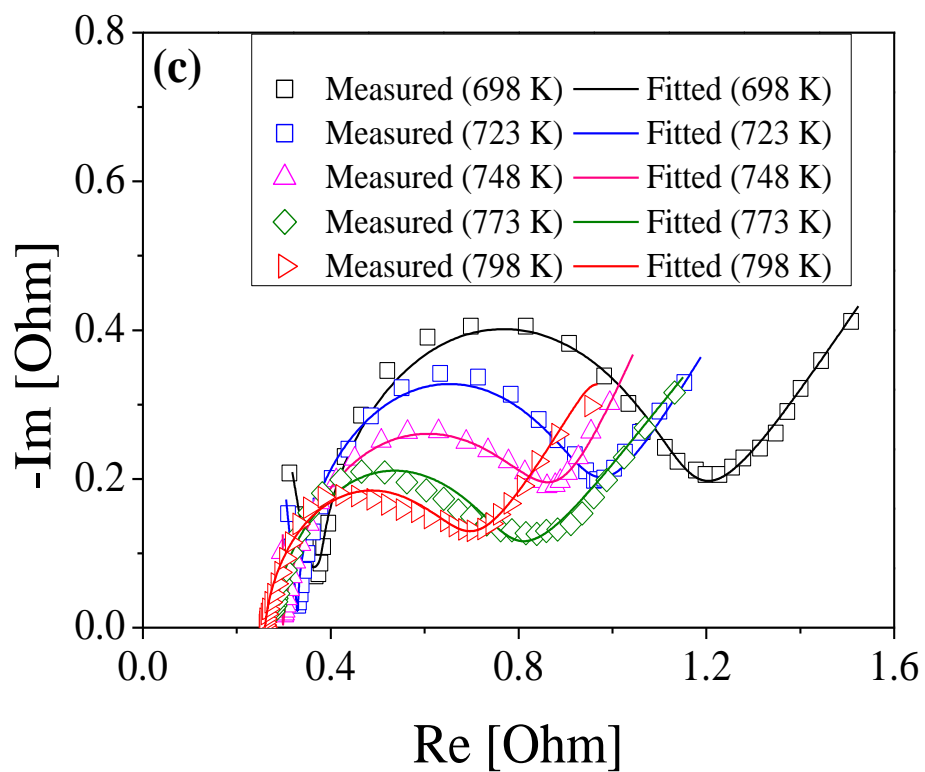


**Figure 4.10** Measured and fitted Nyquist plots at temperatures of 698, 723, 748, 773, and 798 K: (a) 0.5 wt %  $\text{CeCl}_3$ ; (b) 2 wt %  $\text{CeCl}_3$ ; and (c) 4 wt %  $\text{CeCl}_3$ .

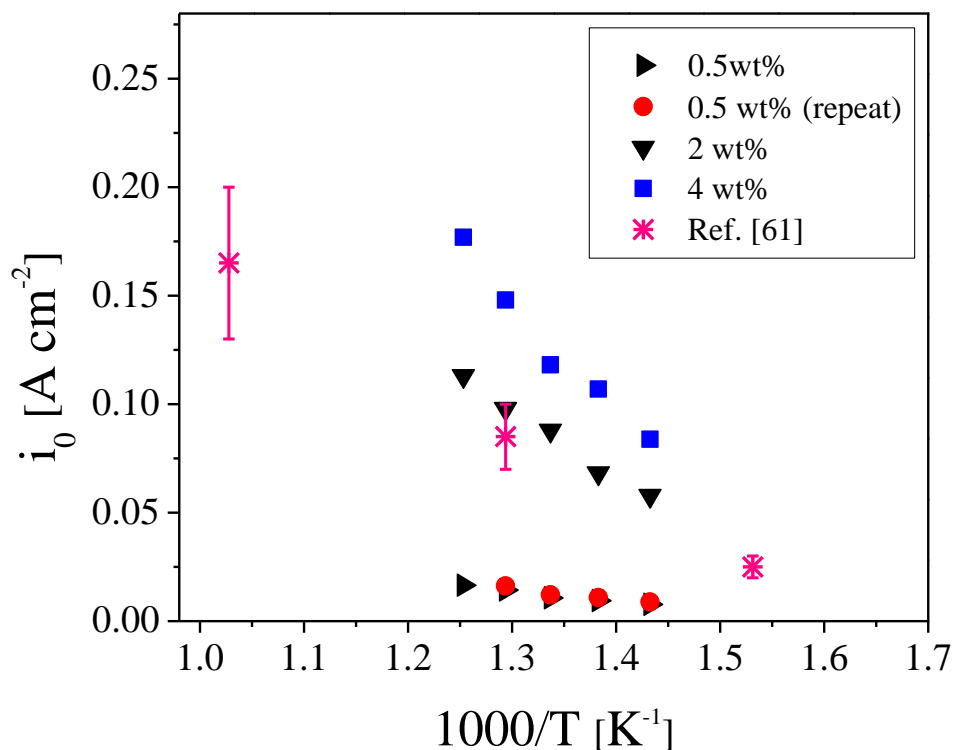


**Figure 4.11** Plots of exchange current densities versus inverse temperature from various experiment sets at  $\text{CeCl}_3$  concentrations of 0.5 wt%, 2wt%, and 4 wt%, compared with values measured by Marsden and Pesic [61].

**Table 4.5** Steps for the measurements of EIS spectra and curve fitting

Step	Description
1	Clean the working electrode by applying an oxidative potential (-0.1 V vs. Ag/AgCl) for 3 minutes and wait until OCP becomes stable,
2	Measure EIS at equilibrium potential,
3	If spectra start showing the double layer capacitance and Warburg impedance, move next step. If not, move to Step 1 and increase the applied overpotential,

4	Find the minimum overpotential and repeat the measurements 3 times at the same overpotential,
5	Fit the measured curve by Randomize and Simplex method in Z-fit software (Bio-Logic),
6	Adjust values in the equivalent parameters for the best fit and obtain $R_{ct}$ and
7	Calculate $i_0$ and $k_0$ by using Eq. (2-24).

**Table 4.6** The applied overpotential ( $\eta$ ) and measured charge transfers ( $R_{ct}$ ) times electrode surface area ( $S$ ) values at different concentrations and temperatures

CeCl <sub>3</sub>	0.5 wt %		2 wt %		4 wt %	
T [K]	$\eta$ [V]	$R_{ct} S$	$\eta$ [V]	$R_{ct} S$	$\eta$ [V]	$R_{ct} S$
		[ $\Omega$ cm <sup>2</sup> ]		[ $\Omega$ cm <sup>2</sup> ]		[ $\Omega$ cm <sup>2</sup> ]
698	0.006	2.63	0.004	0.34	0.003	0.24
723	0.006	2.29	0.004	0.30	0.003	0.19
748	0.006	2.09	0.004	0.24	0.002	0.18
773	0.006	1.62	0.004	0.22	0.002	0.15
798	0.005	1.45	0.004	0.20	0.001	0.13

**Table 4.7** Calculated exchange current density ( $i_0$ ) and rate constant ( $k^0$ ) for the charge transfer at different concentrations and temperatures

CeCl <sub>3</sub>	0.5 wt %		2 wt %		4 wt %	
T [K]	$i_0$	$k^0$	$i_0$	$k^0$	$i_0$	$k^0$
	[A cm <sup>-2</sup> ]	[ $\times 10^5$ cm s <sup>-1</sup> ]	[A cm <sup>-2</sup> ]	[ $\times 10^5$ cm s <sup>-1</sup> ]	[A cm <sup>-2</sup> ]	[ $\times 10^5$ cm s <sup>-1</sup> ]
698	0.0076	0.450	0.058	1.71	0.086	1.69
723	0.0091	0.536	0.068	1.99	0.107	2.20
748	0.0103	0.610	0.088	2.57	0.112	2.44
773	0.0137	0.817	0.098	2.88	0.146	3.03
798	0.0158	0.944	0.113	3.33	0.177	3.69

Based on the given data sets, Arrhenius temperature dependence form can be applied to further looking into temperature effects on the exchange current density using the expressing  $i_0 = I_0 \exp(-E_a/RT)$  where  $I_0$  is the pre-exponential factors (often referred to as an exchange current density at an infinite temperature). Figure 4.12 shows a plot of the natural logarithm of  $i_0$  against the inverse temperature. Here, a straight line can be seen for all three different CeCl<sub>3</sub> concentrations.  $E_a$  and  $I_0$  were calculated from the slope of the straight lines and the intercept of  $\ln i_0$ , respectively.  $E_a$  values for Ce<sup>3+</sup>/Ce were 34.5, 30.9, and 32.4 kJ mol<sup>-1</sup> ( $R^2 > 0.98$ ) for 0.5 wt%, 2 wt% and 4 wt%, respectively. These values are similar to the activation energy for U<sup>3+</sup>/U measured by Rose et al. [50], which is 34.5 kJ mol<sup>-1</sup>. As expected, higher activation energy is required for the charge transfer at lower concentration of CeCl<sub>3</sub>. Interestingly, the activation energy values from the diffusion coefficients shown in Table 4.2 are within similar range in comparing to those for the charge transfer, but behave in an opposite trend. That is, the activation energy for the diffusion increases with increasing CeCl<sub>3</sub> concentration, suggesting that it would be due to

interaction between particles at high concentration. Dimensionless quantities of  $i_0/I_0$  are plotted versus  $\exp(-E_a/RT)$  in Figure 4.13. Marsden and Pesic [61] reported the values of  $i_0$  in a broad range, so that values were averaged, calculated, and superimposed onto Figure 4.13 for comparison. All exchange current density values from three different concentrations are laid on a single straight line. Although the data point at 773 K in the study by Marsden and Pesic [61] is slightly off from the trend line, it is shown here that the exchange current densities from both studies exhibit a similar trend on temperature effect.

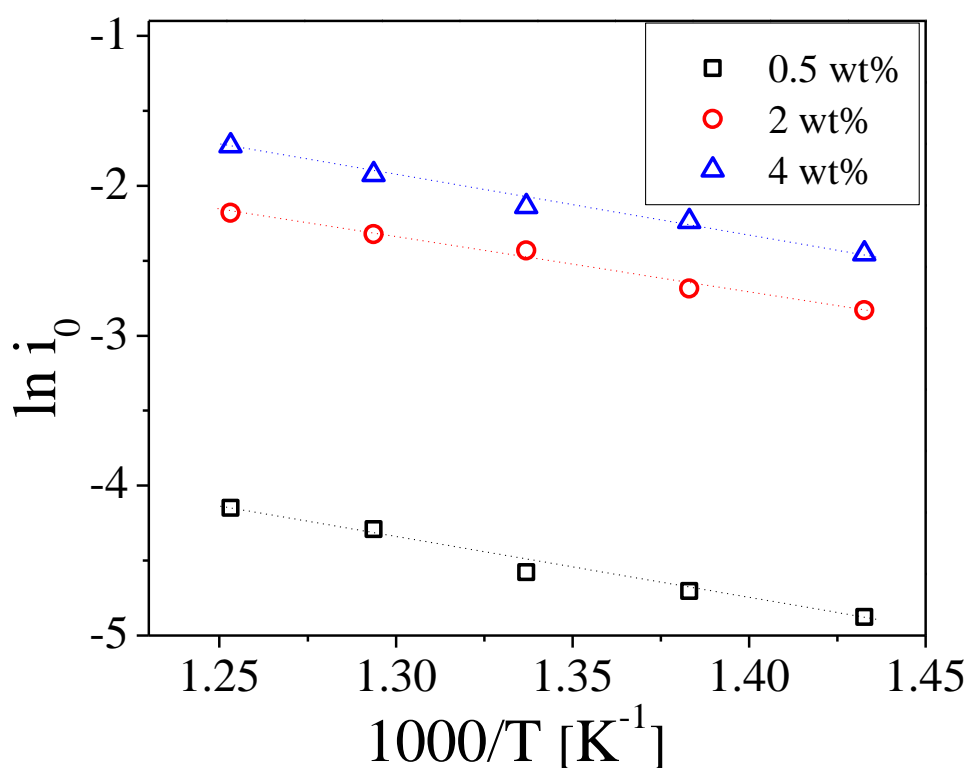


**Figure 4.12** Plot of  $\ln(i_0)$  versus inverse temperature showing Arrhenius dependency.

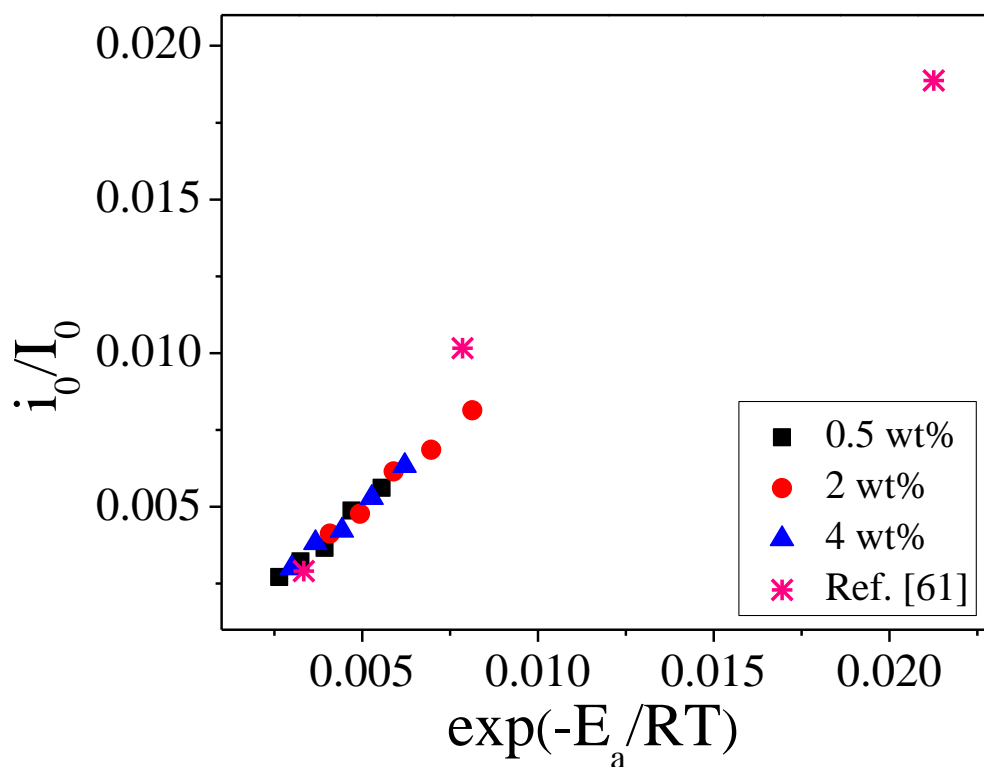


**Figure 4.13** Plot of  $i_0/I_0$  versus  $\exp(-E_a/RT)$ .

#### 4.1.3.3 Analysis on practical application

The results of this work provide the fact that cerium is a good surrogate material for uranium since they show similar electrochemical and thermodynamic behaviors in LiCl-KCl eutectic salt. By comparing the properties of cerium with those of uranium reported in the literatures, both are very stable in the trivalent form in LiCl-KCl salt and are reduced to metal form by gaining three electrons at certain potentials. However, the standard reduction potential of  $UCl_3$  is ranging from -2.4 to -2.6 V versus  $Cl_2/Cl^-$  reference electrode [37-39, 42], which is about 0.7 V more positive than the standard reduction potential for  $CeCl_3$ . The diffusion coefficients for  $UCl_3$  in LiCl-KCl molten salt have been reported by many researchers [30, 37-39, 42, 48, 66], which

are shown in the Figure 4.14. Although the values for  $\text{UCl}_3$  are generally higher than those for  $\text{CeCl}_3$ , the diffusion coefficients for both  $\text{UCl}_3$  and  $\text{CeCl}_3$  are in the same order of magnitude and can be correlated with the temperature. The activation energies for the diffusion of  $\text{UCl}_3$  have been reported, ranging from 24.2 to 34.4  $\text{kJ mol}^{-1}$  [37, 39], which is in a good agreement with the activation energy for  $\text{CeCl}_3$ . The similarity between both the activation energies for the diffusion may be owing to the similar ionic size of uranium and cerium.

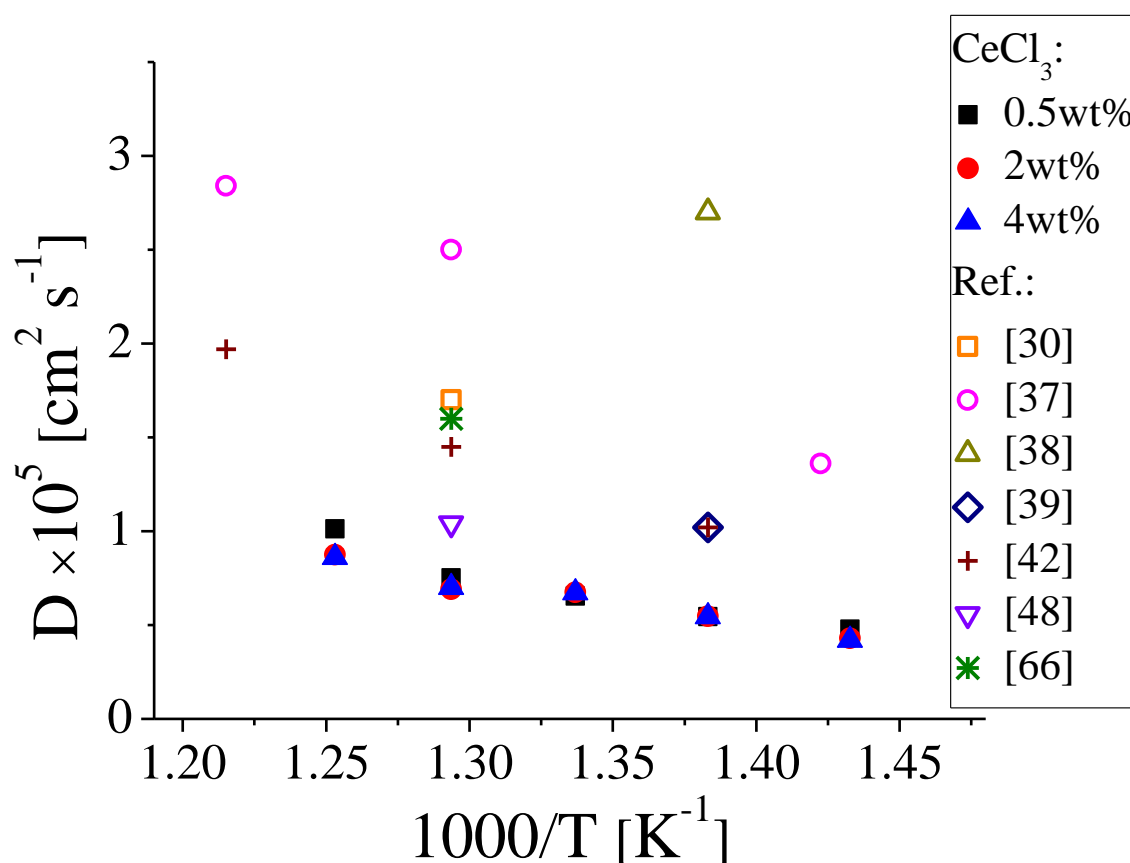


**Figure 4.14** Plot of diffusion coefficients for  $\text{UCl}_3$  from other studies, comparing with the diffusion coefficients of  $\text{CeCl}_3$  in this study.



The exchange current densities of uranium in the molten salt have been reported with few different methods [48-50]. As shown in Figure 4.15, the reported  $i_0$  values for  $U^{3+}/U$  reaction are scattered in the order from  $10^{-2}$  to  $10^{-1}$ ; thus, it is difficult to compare each data or observe its trend. The main reason of the deviation could be that the authors performed the different methods to measure  $i_0$  at different temperatures and concentrations (including other aforementioned challenges). Therefore, further study is necessary to determine the exchange density for  $U^{3+}/U$  reaction, and observe its trend regarding the concentration and temperature. EIS technique in this study shows an alternative method in determining  $i_0$  of  $CeCl_3$  and can also be an important tool to investigate the exchange current density of  $UCl_3$  in LiCl-KCl eutectic salt.

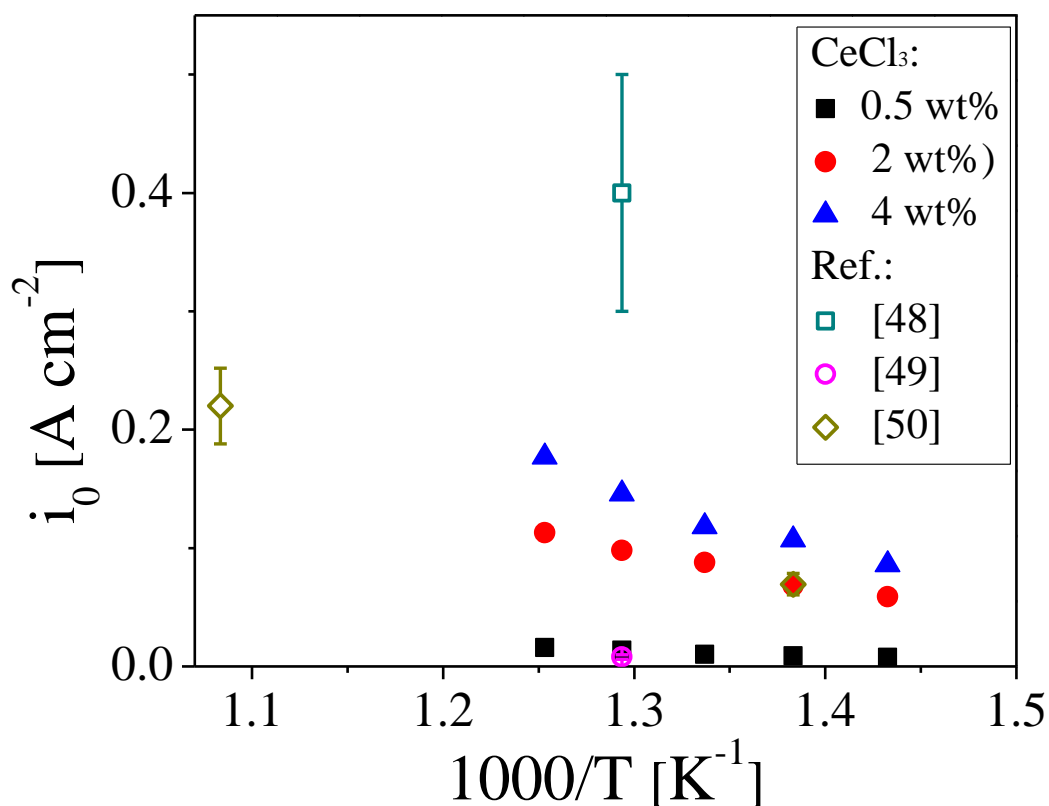


**Figure 4.15** Plot of the exchange current densities for  $U^{3+}/U$  reaction from other research studies comparing with those of  $Ce^{3+}/Ce$  measured in this study.

#### 4.1.4 Conclusions

Electrochemical properties of  $\text{CeCl}_3$  in LiCl-KCl eutectic salt at different concentrations and temperatures have been studied by using CV and EIS techniques. From the CV experiments, three-electron exchange was observed for the  $\text{Ce}^{3+}/\text{Ce}$  reaction. The diffusion coefficients of  $\text{CeCl}_3$  in LiCl-KCl were measured and calculated to be from  $0.48 \times 10^{-5}$  to  $1.01 \times 10^{-5} \text{ cm}^2 \text{ s}^{-1}$ , which can be correlated with temperature using Arrhenius expression. The results reveal that the concentration of  $\text{CeCl}_3$  has a weak effect on the diffusion coefficients. Comparing with the resulting values for  $\text{UCl}_3$ , the diffusion coefficients of  $\text{CeCl}_3$  are slightly smaller than those of  $\text{UCl}_3$ . Apparent standard potentials were also computed by using peak potentials from the CV experiments, which were linearly dependent on temperature. EIS experiments were performed to determine exchange current density of  $\text{Ce}^{3+}/\text{Ce}$  couple in LiCl-KCl molten salt system. Minimum  $\eta$  was applied for Ce reduction to happen and the charge transfer resistance was measured to calculate the exchange current density. The exchange current densities range from  $0.0076 \text{ A cm}^{-2}$  and  $0.18 \text{ A cm}^{-2}$ , which can be related to temperature and concentration. From Arrhenius temperature dependence, the activation energy for  $\text{Ce}^{3+}/\text{Ce}$  exchange was determined though EIS data, which is in the same range obtaining through CV data sets and in similar range with the activation energy for  $\text{U}^{3+}/\text{U}$  [50]. By plotting dimensionless quantities of the exchange current density, the exchange current densities of  $\text{Ce}^{3+}/\text{Ce}$  reaction in this work are in good agreement with those measured by linear polarization method [61]. In comparison with the exchange current densities of  $\text{U}^{3+}/\text{U}$  measured by other researchers, the values for  $\text{Ce}^{3+}/\text{Ce}$  are in a similar order, but a meaningful comparison is hard to be made due to the dispersed data for uranium.

## 4.2 Electrochemical and Thermodynamic Properties of $\text{CeCl}_3$ on Liquid Cadmium Cathode (LCC) in LiCl-KCl Eutectic Salt<sup>2</sup>

### 4.2.1 Introduction

The biggest advantage of pyroprocessing is to provide a strong resistance for nuclear proliferation, which is because of the production of mixed fuel including U, Pu, and MA. This mixed fuel is produced in the ER system by using LCC electrode because the activity of the fission products become very small in LCC. Therefore, the operation of the LCC plays an important role in the feasibility of electrochemical processes toward material accountability and safeguarding of ER [29]. Several studies have been done to understand electrochemical and thermodynamic features of U, Pu, and MAs on the LCC. Shirai and co-workers [32, 67] investigated the reaction of  $\text{U}^{3+}/\text{U}$  and  $\text{Pu}^{3+}/\text{Pu}$  couples on the LCC. The redox reaction for both couples were almost reversible, and the reduction potential on the LCC showed more positive values than that at the molybdenum electrode. Murakami and co-workers [31] measured diffusion coefficients of actinides and rare earth elements with LCC by performing chronopotentiometry (CP) in LiCl-KCl at temperature ranging from 723 K to 823 K. Castrillejo et al. [29, 68, 69] investigated the activities and Gibbs energy of rare earth materials in both Cd and Bi liquid electrodes.

However, only few elements in the electrorefiner have been examined with LCC, and there are still many actinides and lanthanides need to be explored in terms of electrochemical and thermodynamic properties on the interface between the LiCl-KCl molten salt and the LCC. In addition, the  $i_0$  of the elements, which is necessary for the kinetic model, has not been reported.

---

<sup>2</sup> Contents in Section 4.2 are cited from the author's publication:

D. Yoon and S. Phongikaroon, and Jinsuo Zhang, "Electrochemical and Thermodynamic Properties of  $\text{CeCl}_3$  on Liquid Cadmium Cathode (LCC) in LiCl-KCl Eutectic Salt," *Journal of The Electrochemical Society*, **163**(3), E97-E103 (2016).

Therefore, Ce was selected as a surrogate material in this study for a purpose of accumulating electrochemical and thermodynamic data sets which can be meaningfully compared with those from other researchers and developing an experimental method to measure the  $i_0$  of actinides on the LCC. Few electrochemical and thermodynamic properties of Ce have been reported on the LCC in the LiCl-KCl eutectic salt. Kim et al. [64] explored Ce reduction process and large potential difference were observed between tungsten electrode and LCC due to the Ce activity change with intermetallic compound formations in LCC. Shibata and co-workers [70] measured the Gibbs free energies and other thermodynamic properties of the Ce-Cd intermetallic compounds using an open circuit chronopotentiometry. These values will provide useful insight into features of Cd distillation from Cd-MA alloys. However, electrochemical behaviors of  $\text{CeCl}_3$  on the LCC have not been well explored and understood. In addition, there is not enough data on the thermodynamic properties of the intermetallic compounds to be compared.

The characteristic of  $i_0$  were studied on the solid cathode in LiCl-KCl salt by Marsden and Pesic [61] as mentioned in Chapter 4.1. However, significant differences would be expected using LCC since the properties of actinides are dramatically changed in the LCC (for an example, an activity of Ce and formation of intermetallic compounds in Cd). In this section, Tafel plot and LP methods were selected to estimate the value of  $i_0$  on the LCC. For soluble-insoluble reactions, the main disadvantage of those techniques is the measurement of apparent electrode surface area when the metal elements are deposited on the solid cathode. However, identical surface condition of liquid cadmium was observed with the naked eye after Ce metal was deposited on the LCC due to the fact that deposited metal was readily diffused into the LCC. Therefore, the steady surface area can be expected on the LCC during the Tafel and LP measurements.

The main goal of this section is to explore the electrochemical methods to estimate the electrochemical and thermodynamic properties of  $\text{CeCl}_3$  on the LCC in  $\text{LiCl-KCl}$  molten salt. CV experiments were performed to investigate the electrode reaction of the  $\text{Ce}^{3+}/\text{Ce}$  couple, and determine diffusion coefficient of  $\text{Ce}^{3+}$  on the LCC. The cyclic voltammogram of  $\text{LiCl-KCl-CeCl}_3\text{-CdCl}_2$  was obtained to confirm the intermetallic compound formations of Ce with Cd. Then, the open circuit chronopotentiometry was performed to measure the Gibbs free energy and other thermodynamic properties of the Ce-Cd intermetallic compounds. Finally, Tafel and LP plots were obtained with increasing Ce concentration in Cd to determine  $i_0$  of Ce on the LCC regarding to Ce-Cd phase formation.

#### 4.2.2 Detailed Experimental Setup and Preparation

The amount of cerium chloride ( $0.26 \text{ g} \pm 0.1 \text{ mg}$ ) was weighed and added into  $25 \text{ g} \pm 0.18 \text{ mg}$  of the  $\text{LiCl-KCl}$  salt, which is equivalent to 1 wt% of  $\text{CeCl}_3$  in the  $\text{LiCl-KCl}$  salt. For the experiment of Ce-Cd intermetallic compounds,  $0.022 \text{ g} \pm 0.1 \text{ mg}$  of cadmium chloride was added to the  $\text{LiCl-KCl-1wt\% CeCl}_3$  yielding  $\text{CeCl}_3$  and  $\text{CdCl}_2$  mole fractions of  $2.36 \times 10^{-3}$  and  $2.68 \times 10^{-4}$ , respectively. The prepared sample was loaded in the high purity alumina crucible (25 mm ID  $\times$  40 mm H). Figure 4.16 shows a schematic design of the electrode assembly in the cell. The glassy carbon rod was immersed as the counter electrode.  $\text{Ag/AgCl}$  (1 mol%) reference was used as the reference electrode. As the working electrode, liquid Cd was used. The Cd metal shots were delivered in a regular polyethylene bottle; thus, the surface of Cd shots were partially oxidized. For purification of the oxidized Cd prior to the experiments, Cd shots were melted in a closed-end Pyrex tube to separate the pure Cd from the oxidized layer. When Cd was melted, the oxide form

of Cd (yellow color) floated on the surface of liquid Cd. A Pyrex tube (4 mm in OD) was inserted into the Cd below the oxide layer and a syringe was used to draw the pure liquid Cd up into the tube. The Cd in the tube was cooled to room temperature. As a result, a pure Cd rod was obtained from the tube indicated by observing clean silver color of the Cd rod as shown in Figure 4.17.

For utilizing the liquid Cd in the electrochemical experiments, the pure Cd rods were contained in a Pyrex tube (8 mm ID  $\times$  18 mm H, see the inserted photo in Figure 4.16), which was contacted with molybdenum wire (Alfa Aesar, 0.5 mm in diameter). When the Cd was melted in the furnace, the surface of the LCC was observed in the shape of a dome owing to high surface tension of liquid cadmium (600 dynes  $\text{cm}^{-1}$  at 773 K [71]) in the Pyrex tube crucible. As shown in Figure 4.18(a), the surface shape was conserved when liquid cadmium was cooled quickly to room temperature. The diameter and the height of the half elliptical shape were measured as 8 mm and 2.25 mm, respectively (see Figure 4.18(b)). By assuming that the surface of the LCC is an ideal oblate spheroid, the surface area can be computed by the following formula [72],

$$S = \pi a^2 \left( 1 + \frac{\left(\frac{c}{a}\right)^2}{2\sqrt{1 - \frac{c^2}{a^2}}} \ln \left( \frac{1 + \sqrt{1 - \frac{c^2}{a^2}}}{1 - \sqrt{1 - \frac{c^2}{a^2}}} \right) \right) \quad (4-3)$$

where  $S$  is the surface area of the LCC,  $a$  is the radius of spheroid, and  $c$  is the height of the half spheroid. The surface areas of Cd were calculated ranging from 0.729  $\text{cm}^2$  to 0.733  $\text{cm}^2$  depending on experimental runs.

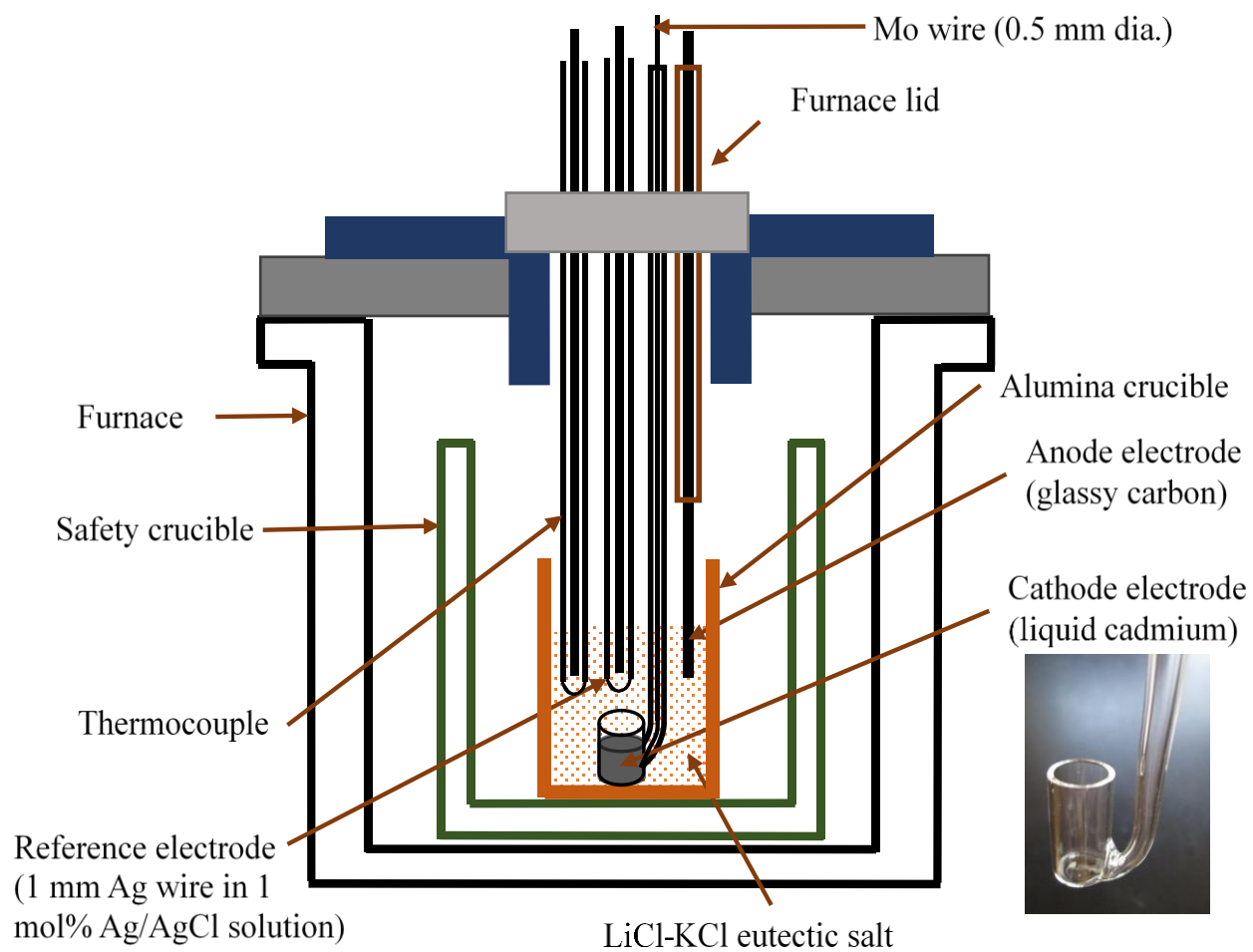


**Figure 4.16** A schematic design of the experimental setup for electrochemical experiments.



**Figure 4.17** Purified Cd rods under argon environment.

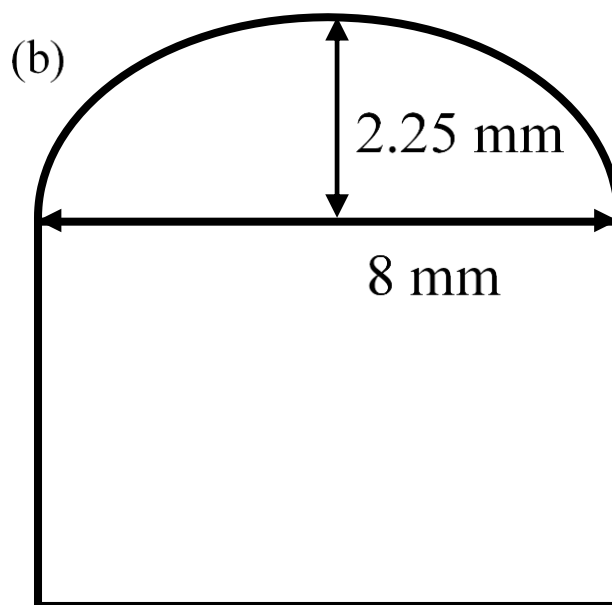
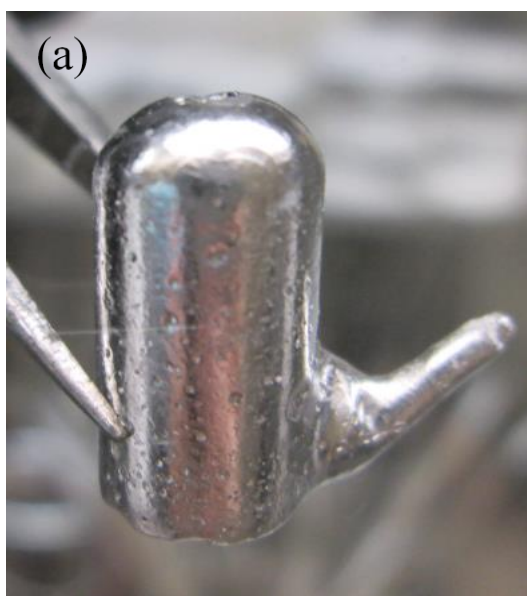


**Figure 4.18** Solid cadmium cooled fast to room temperature in a Pyrex crucible and (b) a sketch showing measured dimensions of half elliptical dome.



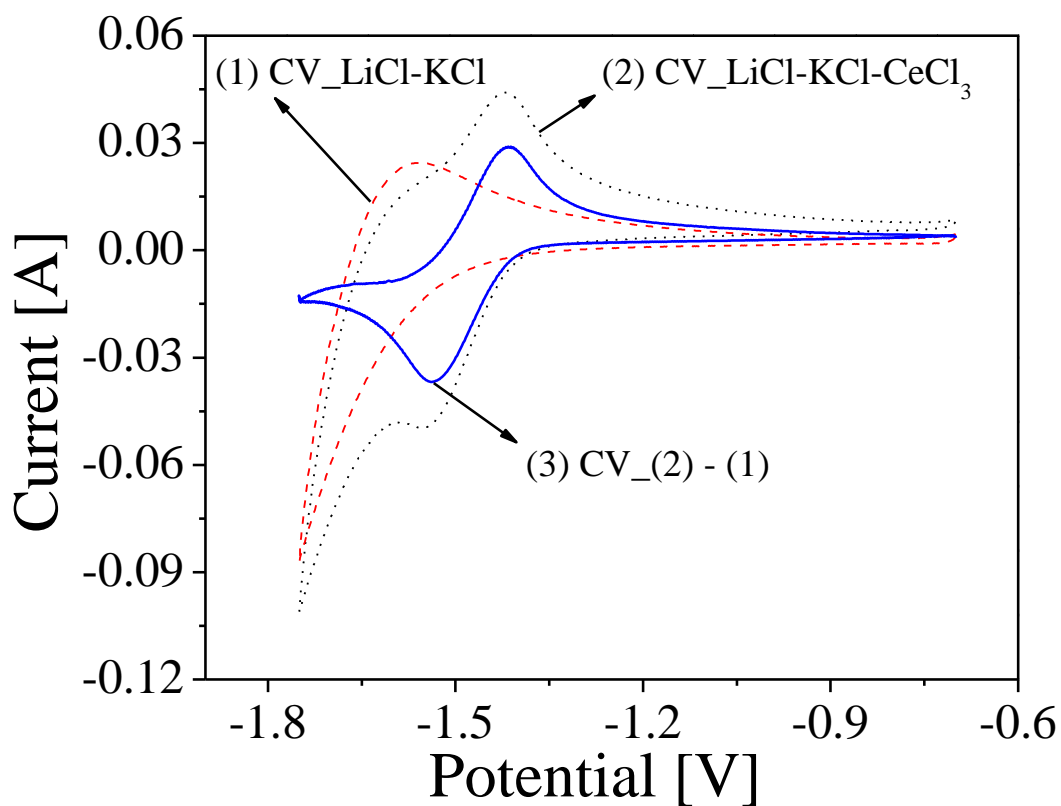
### 4.2.3 Results and Discussion

#### 4.2.3.1 Cyclic voltammetry (CV) of the LiCl-KCl-CeCl<sub>3</sub> on the LCC

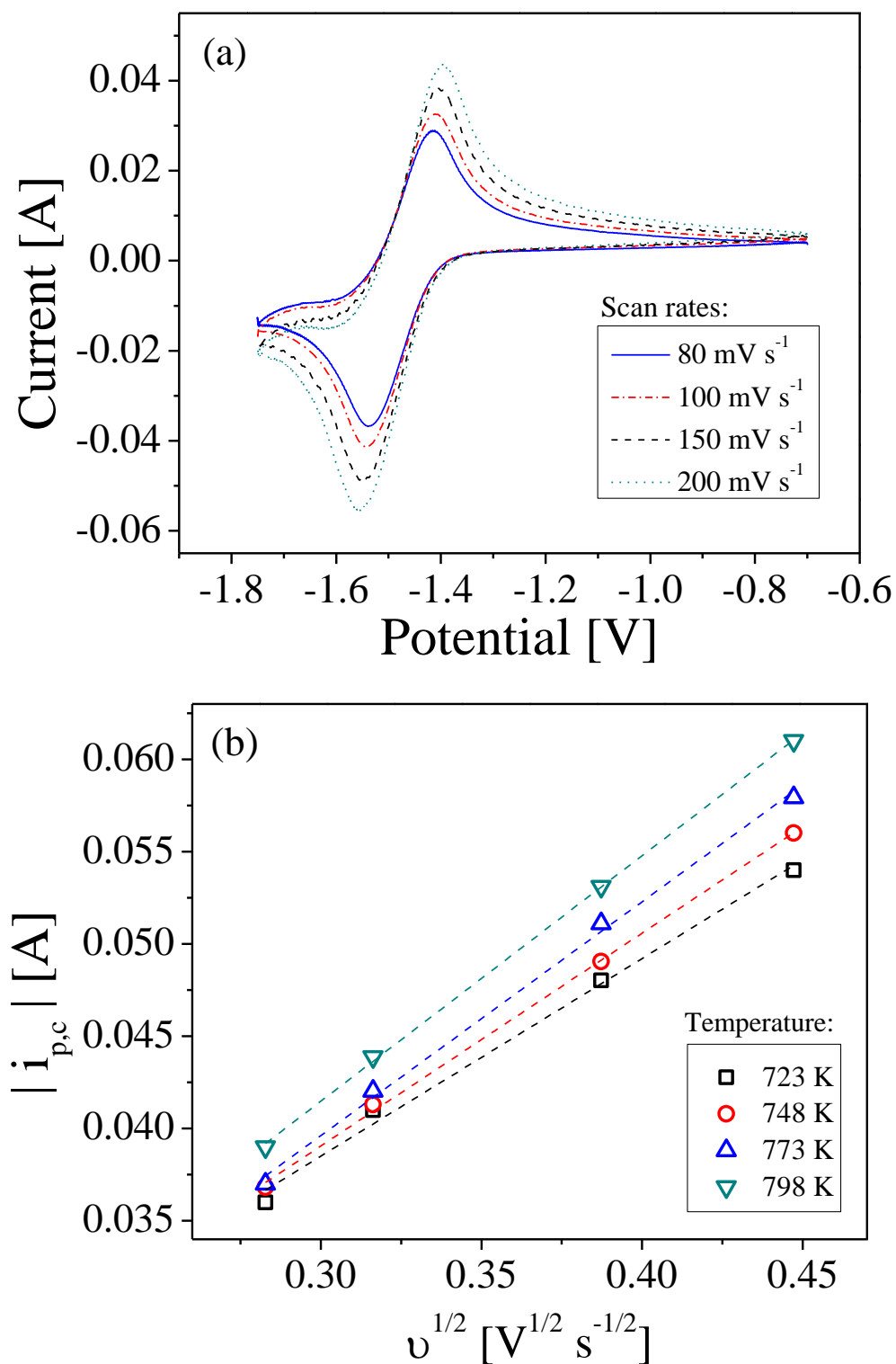
CV experiments were conducted in a LiCl-KCl-1 wt% CeCl<sub>3</sub> system at temperatures from  $723 \pm 1\text{ K}$  to  $798 \pm 1\text{ K}$ . Figure 4.19 shows representative CV curves of CeCl<sub>3</sub> with a  $100\text{ mV s}^{-1}$  scan rate at 748 K. Curve (1) was obtained in a pure LiCl-KCl salt, in which Li reduction starts approximately from -1.3 V versus 1 mol% Ag/AgCl reference electrode. This is mainly due to very small activity coefficient of metals in Cd. Lewis and Johnson [73] reported activity coefficients of Li in Cd, ranging from  $1.8 \times 10^{-3}$  to  $2.6 \times 10^{-3}$  over a concentration range of 0.06 – 7.0 atom% in Cd. Therefore, Li co-deposition can be expected in reduction process with the LCC. Curve (2) is cyclic voltammogram for CeCl<sub>3</sub>, but Li was deposited simultaneously. Therefore, curve (1) (background current) needs to be subtracted from curve (2), so that Li deposition effect can be removed from the curve (2). This is shown by curve (3) attributing only to Ce reduction and oxidation on the LCC. This background subtraction method has been widely used by several researchers [29, 64, 68], and can be utilized based on the assumption that the interaction between Li and Ce is weak and can be neglected. Table 4.8 briefly summarizes the procedure of the CV experiments on LCC electrode in LiCl-KCl eutectic salt.

Figure 4.20(a) combines the cyclic voltammograms of CeCl<sub>3</sub> on the LCC with increasing scan rate from  $0.08\text{ V s}^{-1}$  to  $0.2\text{ V s}^{-1}$ . The cathodic peak potential stays at near the same potential below the scan rate of  $0.2\text{ V s}^{-1}$  while the peak potential starts shifting toward negative potential when the scan rate was faster than  $0.2\text{ V s}^{-1}$ , representing the reversibility of Ce<sup>3+</sup>/Ce reaction below the  $0.2\text{ V s}^{-1}$  scan rate. Figure 4.20(b) shows linear dependence between the cathodic peak current and the square root of the scan rate. The diffusion coefficient of CeCl<sub>3</sub> in LiCl-KCl salt

can be calculated from the slope by using the Berzins-Delahay relationship, Eq. (2-13), which is applicable for a diffusion controlled process with a soluble-insoluble reversible system.



**Figure 4.19** Cyclic voltammograms of a LiCl-KCl-1 wt% CeCl<sub>3</sub> solution on the LCC at 748 K with the surface area of 0.729 cm<sup>2</sup>.



**Figure 4.20** (a) The cyclic voltammogram of a LiCl-KCl-1 wt%  $\text{CeCl}_3$  after subtraction of background current of LiCl-KCl, and (b) peak cathodic currents as a function of the square root of the scan rate. The surface area was  $0.729 \text{ cm}^2$ .

**Table 4.8** Steps for the measurements of CV data using LCC

Step	Description
1	Load the pure Cd rods into the Pyrex crucible,
2	Lower the electrode assembly into the salt and wait until Cd is melted,
3	Clean the LCC surface by applying an oxidative potential (-0.7 V vs. Ag/AgCl for avoiding Cd oxidation) for 3 minutes,
4	Wait for 1 ~ 3 minutes until the OCP becomes stable,
5	Perform CV measurements at least 5 cycles,
6	Obtain the data if the CV curves are repeatable,
7	Repeat Steps 1 – 6 for next CV measurement,
8	Subtract LiCl-KCl base line in order to eliminate Li reduction effect, and
9	Measure the peak currents and calculate the values of D using Eq. (2-13).

The diffusion coefficients of  $\text{Ce}^{3+}$  ranged from  $2.9 \times 10^{-6} \text{ cm}^2 \text{ s}^{-1}$  to  $5.1 \times 10^{-6} \text{ cm}^2 \text{ s}^{-1}$  at temperatures from 723 to 798 K. Figure 4.21 shows the diffusion coefficients of  $\text{CeCl}_3$  on the LCC versus  $1000/T$ , which are superimposed on the diffusion coefficients of  $\text{Ce}^{3+}$  on tungsten electrode measured in Section 4.1. The diffusion coefficients on the LCC were almost half of the values of the diffusion coefficients on the tungsten electrode. Gha-Young and co-workers [30] also had a similar trend with uranium chloride. That is, diffusion coefficient of uranium on LCC was about one tenth of the diffusion coefficient on solid cathode. This reduced values may be attributed from Li co-deposition and mass transfer limit from the LCC structure. It is assumed that as Li is reduced along with Ce on LCC, diffusion of  $\text{Ce}^{3+}$  is interfered by the interaction between Ce and Li ions.

In addition, to utilize LCC, the liquid cadmium was loaded in a Pyrex crucible having an upward surface area exposure to the molten salt LiCl-KCl. Therefore, mass transfers caused by electric force and convection are being restricted only through that exposure liquid cadmium surface. These speculated observations may be the main reasons for the small diffusion coefficient values. To date, the value of diffusion coefficient on LCC has not been measured well by researchers. Thus, diffusion coefficient on LCC needs to be further explored and understood in various experimental conditions. Generally, diffusivity is dependent on temperature change, which can be examined by Arrhenius temperature relationship. By plotting logarithm of diffusion coefficient against inverse temperature,  $E_a$  can be readily calculated from the slope. The activation energy for diffusion process of  $CeCl_3$  on the LCC was  $36.12 \text{ kJ mol}^{-1}$ , which is slightly higher than the activation energies for Ce diffusion on the tungsten electrode reported by several researchers [61, 74]. This result also supports the idea of the slower diffusion process on the LCC as mentioned previously. The results of the diffusion coefficient on LCC in the present study motivate further investigations on understanding the difficulty of mass transfer onto LCC. Theoretically, diffusion coefficient is only function of temperature and species.

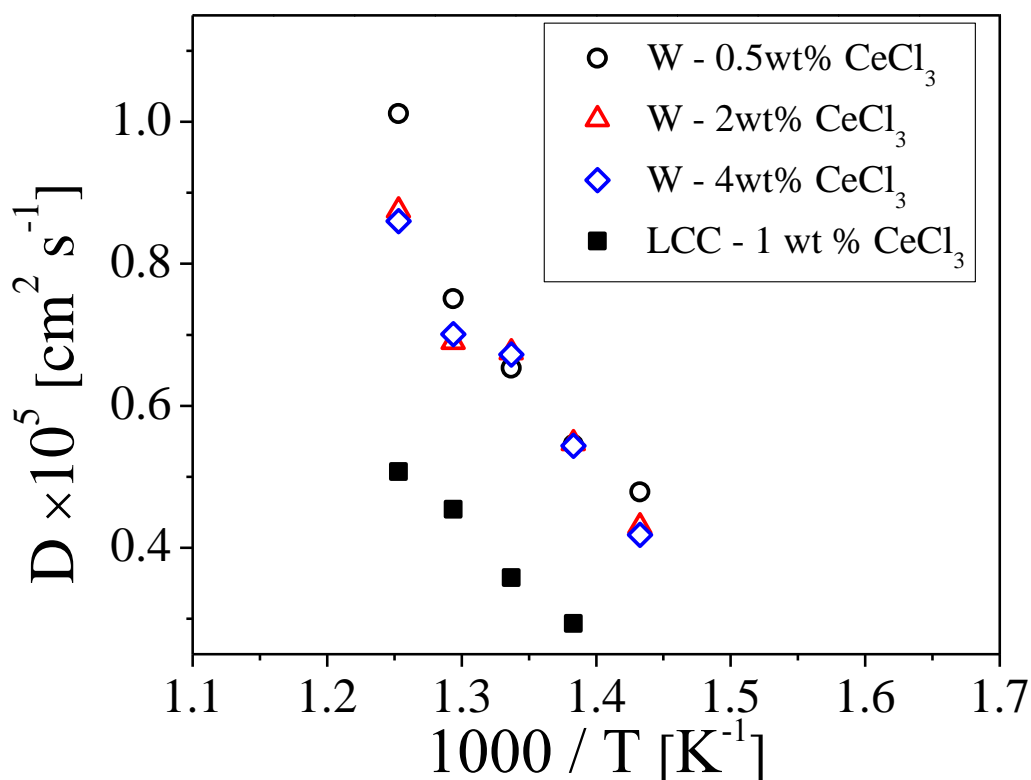


**Figure 4.21** Plot of the diffusion coefficients of  $\text{Ce}^{3+}$  on the LCC versus inverse temperature, comparing with values on the tungsten cathode measured in Section 4.1.

#### 4.2.3.2 Open circuit chronopotentiometry in $\text{LiCl-KCl-CeCl}_3\text{-CdCl}_2$

It has been known that Ce forms six different intermetallic compounds with Cd ( $\text{CeCd}$ ,  $\text{CeCd}_2$ ,  $\text{CeCd}_3$ ,  $\text{Ce}_{13}\text{Cd}_{58}$ ,  $\text{CeCd}_6$ , and  $\text{CeCd}_{11}$ ) [75], which could be readily observed by performing CV experiments in  $\text{LiCl-KCl-CeCl}_3\text{-CdCl}_2$  molten salt. Figure 4.22 shows a cyclic voltammogram of  $\text{CeCl}_3$  deposited on a Cd film at a  $50 \text{ mV s}^{-1}$  scan rate at 773 K. During the reduction process from 0 V to -2.2 V versus Ag/AgCl reference electrode, the Cd film was formed first on the tungsten electrode and then Ce starts to be deposited on top of the Cd film. In this

process, Ce-Cd intermetallic compounds have been gradually formed. When potential was swept in the oxidation direction, Ce metal in the intermetallic compounds was dissolved back into the salt. By decreasing the amount of Ce metal on the film, the formation of Ce-Cd intermetallic compound varies subsequently from CeCd to CeCd<sub>11</sub>, which can be clearly observed as oxidation peaks from P<sub>1</sub> to P<sub>6</sub> in Figure 4.22. However, P<sub>3</sub> was combined with P<sub>2</sub> due to the relatively fast scan rate making it difficult to be identified. Thus, it was considered that at slower scan rate than 50 mV s<sup>-1</sup>, all six peaks corresponding to Ce-Cd intermetallic compounds would be separately shown in a cyclic voltammogram.

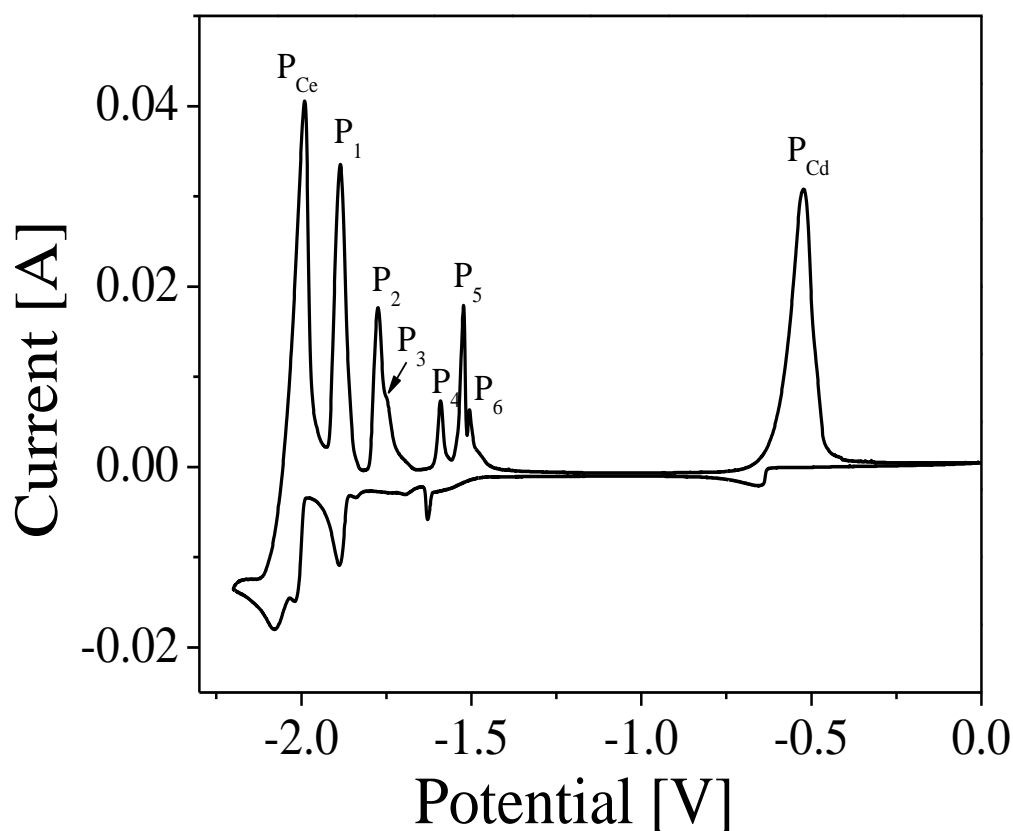


**Figure 4.22** A cyclic voltammogram of LiCl-KCl-CeCl<sub>3</sub>-CdCl<sub>2</sub> with the scan rate of 50 mV s<sup>-1</sup>. Concentrations of CeCl<sub>3</sub> and CdCl<sub>2</sub> were  $6.86 \times 10^{-5}$  mol cm<sup>-3</sup> and  $7.81 \times 10^{-6}$  mol cm<sup>-3</sup>, respectively.

The thermodynamic properties of these Ce-Cd intermetallic compounds can be examined by performing the open circuit chronopotentiometry (OCC), which has been considered as a suitable technique to determine thermodynamic properties of intermetallic compound formations [29, 64, 68-70]. Figure 4.23 is an example of the chronopotentiogram, showing a transient potential curve with respect to the Ce-Cd binary phase. In advance, the tungsten electrode was coated with Cd and Ce metals by applying potential at -2.2 V for 25 second. Then, the chronopotentiometry was conducted with positive current applied at 1  $\mu$ A. By dissolving Ce metal from Cd film to the bulk salt, cathodic potential was shifted toward the positive direction. The routine methods for measuring the OCC are explained in Table 4.9. Regarding variation of the Ce-Cd phase formation, totally six potential plateaus were observed. These potential plateaus can correspond to two-phase coexisting state: CeCd-CeCd<sub>2</sub>, CeCd<sub>2</sub>-CeCd<sub>3</sub>, CeCd<sub>3</sub>-Ce<sub>13</sub>Cd<sub>58</sub>, Ce<sub>13</sub>Cd<sub>58</sub>-CeCd<sub>6</sub>, CeCd<sub>6</sub>-CeCd<sub>11</sub>, and CeCd<sub>11</sub>-Cd. When two phases are coexisting on the electrode surface, the activity of Ce is fixed by equilibrium [29]. Therefore, potential difference at each plateau was measured based on an OCP of a Ce electrode, then the relative partial molar Gibbs free energies and activities of Ce in binary phase state were calculated by using the following equations;

$$\Delta G_{\text{Ce}} = -3F\Delta E \quad (4-4)$$

$$\text{emf} = \Delta E = -\frac{RT}{3F} \ln \alpha_{\text{Ce,Cd}} \quad (4-5)$$

where  $\Delta G_{\text{Ce}}$  is the relative partial molar Gibbs free energy of Ce ( $\text{kJ mol}^{-1}$ ),  $\Delta E$  is the potential difference between OCP and each plateau (V), and  $\alpha_{\text{Ce,Cd}}$  is the activity of Ce in Cd. The chronopotentiometry was repeated several times with same experimental conditions for confirming the reproducibility of the data, and the uncertainty was verified by using standard deviation for each experiment. Table 4.10 provides a summary of  $\Delta G_{\text{Ce}}$  and  $\alpha_{\text{Ce,Cd}}$ . The values of metal activity in Cd becomes smaller when Cd is more prevalent in LCC. For instance, activity of



Ce in the phase of Ce-CeCd<sub>11</sub> has its value in the order of  $10^{-11}$  while that in the CeCd-CeCd<sub>2</sub> coexisting phase is in the order of  $10^{-2}$ . It should be mentioned that the reduction potentials of actinide and lanthanide elements come together closely on the LCC at the beginning of the electrorefining process, and will be gradually detached by depositing more elements in the LCC. This result will give an insight into determining a proper rate and time of LCC electrorefining process considering non-proliferation feature of pyroprocessing technology.

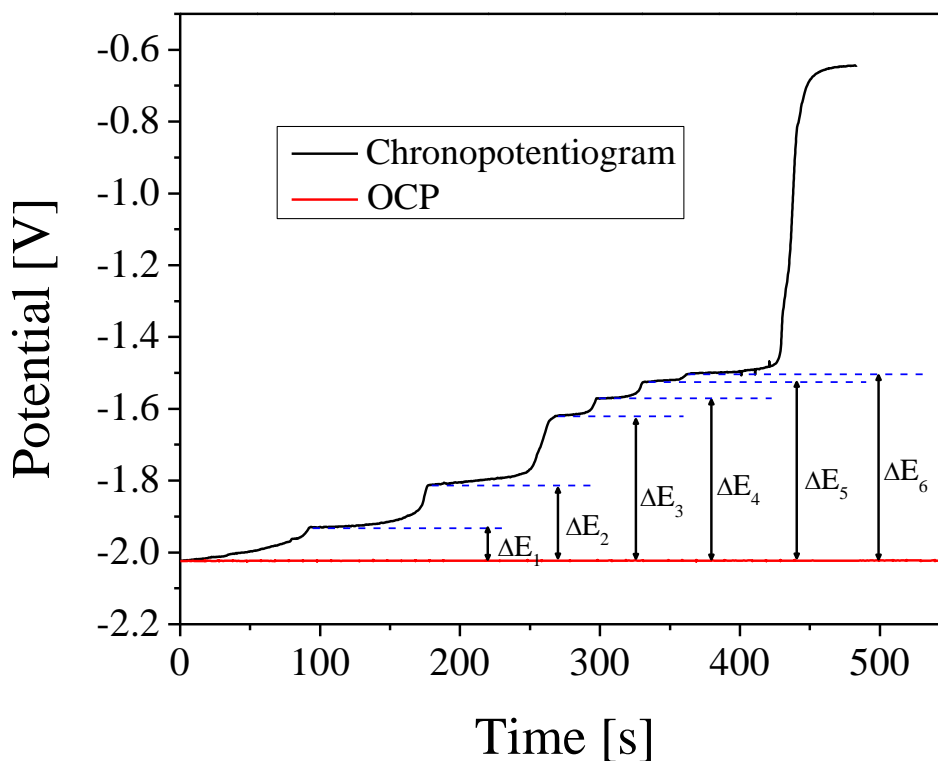


**Figure 4.23** An example of the open circuit chronopotentiogram of Ce at Cd-coated tungsten electrode at 773 K. The applied current was 1  $\mu$ A.

**Table 4.9** Summary of the measurement step for OCC method

Step	Description
1	Prepare LiCl-KCl-1wt% CeCl <sub>3</sub> -0.09wt% CdCl <sub>2</sub> ,
2	Lower the electrode assembly (working: tungsten, counter: glassy carbon),
3	Apply constant potential at -2.2 V vs. Ag/AgCl for 25 seconds,
4	Perform apply positive current a 1 $\mu$ A (OCC),
5	Obtain plateaus corresponding to the Ce-Cd intermetallic compounds,
6	Measure the potential difference between the plateaus and OCP, and
7	Calculate thermodynamic data of the Ce-Cd intermetallic compounds

**Table 4.10** The partial molar Gibbs free energies and activities of Ce in two-phase coexisting state at various temperatures

T [K]	$\Delta E_{\text{Ce-Cd}}$ [V vs Ce <sup>3+</sup> /Ce]	$\Delta G_{\text{Ce}}$ [kJ mol <sup>-1</sup> ]	$\alpha_{\text{Ce, Cd}}$
In the region of the co-existing CeCd and CeCd <sub>2</sub> phases			
698	$0.097 \pm 0.0008$	$-28.2 \pm 0.23$	$7.73 \pm 0.03 \times 10^{-3}$
723	$0.092 \pm 0.002$	$-26.2 \pm 0.45$	$1.19 \pm 0.008 \times 10^{-2}$
748	$0.090 \pm 0.002$	$-26.0 \pm 0.42$	$1.53 \pm 0.009 \times 10^{-2}$
773	$0.092 \pm 0.003$	$-26.7 \pm 0.84$	$1.57 \pm 0.02 \times 10^{-2}$
798	$0.088 \pm 0.001$	$-25.4 \pm 0.36$	$2.17 \pm 0.01 \times 10^{-2}$
823	$0.081 \pm 0.002$	$-23.3 \pm 0.43$	$3.30 \pm 0.02 \times 10^{-2}$
In the region of the co-existing CeCd <sub>2</sub> and CeCd <sub>3</sub> phases			
698	$0.218 \pm 0.0007$	$-63.1 \pm 0.21$	$1.91 \pm 0.03 \times 10^{-5}$
723	$0.210 \pm 0.001$	$-60.9 \pm 0.49$	$4.06 \pm 0.07 \times 10^{-5}$

748	$0.209 \pm 0.002$	$-60.7 \pm 0.55$	$5.73 \pm 0.1 \times 10^{-5}$
773	$0.211 \pm 0.003$	$-61.0 \pm 0.83$	$7.53 \pm 0.2 \times 10^{-5}$
798	$0.207 \pm 0.006$	$-59.9 \pm 0.16$	$1.20 \pm 0.06 \times 10^{-4}$
823	$0.203 \pm 0.002$	$-58.3 \pm 0.51$	$1.98 \pm 0.03 \times 10^{-4}$

In the region of the co-existing  $\text{CeCd}_3$  and  $\text{CeCd}_{58/13}$  phases

698	$0.413 \pm 0.001$	$-119.6 \pm 0.36$	$1.11 \pm 0.03 \times 10^{-9}$
723	$0.414 \pm 0.002$	$-119.8 \pm 0.83$	$2.19 \pm 0.04 \times 10^{-9}$
748	$0.407 \pm 0.003$	$-117.8 \pm 0.87$	$5.97 \pm 0.4 \times 10^{-9}$
773	$0.405 \pm 0.003$	$-117.2 \pm 0.76$	$1.19 \pm 0.06 \times 10^{-8}$
798	$0.398 \pm 0.006$	$-115.2 \pm 0.16$	$2.89 \pm 0.3 \times 10^{-8}$
823	$0.391 \pm 0.004$	$-112.9 \pm 0.54$	$6.83 \pm 0.2 \times 10^{-8}$

In the region of the co-existing  $\text{CeCd}_{58/13}$  and  $\text{CeCd}_6$  phases

698	$0.471 \pm 0.0007$	$-136.3 \pm 0.21$	$6.30 \pm 0.1 \times 10^{-11}$
723	$0.458 \pm 0.0006$	$-132.4 \pm 0.19$	$2.67 \pm 0.04 \times 10^{-10}$
748	$0.453 \pm 0.002$	$-131.0 \pm 0.67$	$7.08 \pm 0.3 \times 10^{-10}$
773	$0.451 \pm 0.003$	$-130.6 \pm 0.89$	$1.47 \pm 0.09 \times 10^{-9}$
798	$0.448 \pm 0.009$	$-129.6 \pm 0.25$	$3.30 \pm 0.06 \times 10^{-9}$
823	$0.439 \pm 0.002$	$-126.8 \pm 0.48$	$8.98 \pm 0.3 \times 10^{-9}$

In the region of the co-existing  $\text{CeCd}_6$  and  $\text{CeCd}_{11}$  phases

698	$0.544 \pm 0.001$	$-157.4 \pm 0.30$	$1.65 \pm 0.05 \times 10^{-12}$
723	$0.529 \pm 0.00$	$-153.2 \pm 0.31$	$8.54 \pm 0.2 \times 10^{-12}$
748	$0.515 \pm 0.002$	$-149.1 \pm 0.45$	$3.86 \pm 0.1 \times 10^{-11}$
773	$0.499 \pm 0.003$	$-144.5 \pm 0.91$	$1.72 \pm 0.1 \times 10^{-10}$

798	$0.483 \pm 0.002$	$-139.7 \pm 0.47$	$7.12 \pm 0.3 \times 10^{-10}$
823	$0.469 \pm 0.001$	$-135.4 \pm 0.41$	$2.52 \pm 0.07 \times 10^{-9}$

In the region of the co-existing  $\text{CeCd}_{11}$  and Cd phases

698	$0.573 \pm 0.0007$	$-165.7 \pm 0.21$	$3.95 \pm 0.08 \times 10^{-13}$
723	$0.555 \pm 0.001$	$-160.5 \pm 0.29$	$2.53 \pm 0.07 \times 10^{-12}$
748	$0.540 \pm 0.001$	$-156.4 \pm 0.16$	$1.20 \pm 0.03 \times 10^{-11}$
773	$0.521 \pm 0.003$	$-150.7 \pm 0.76$	$6.52 \pm 0.1 \times 10^{-11}$
798	$0.502 \pm 0.001$	$-145.4 \pm 0.42$	$3.02 \pm 0.03 \times 10^{-10}$
823	$0.487 \pm 1.4 \times 10^{-3}$	$-140.7 \pm 0.41$	$1.18 \times 10^{-9}$

---

The standard Gibbs free energy of Ce-Cd intermetallic compound formation can be calculated by the given relation [29, 68]:

$$\Delta G_f^0(\text{Ce}_{x_2}\text{Cd}) = \int_{x_1}^{x_2} \Delta E(x) dx + \Delta G_f^0(\text{Ce}_{x_1}\text{Cd}) \quad (4-6)$$

where  $\Delta G_f^0$  is the standard Gibbs free energy of formation of Ce-Cd intermetallic compounds. The  $x_1$  and  $x_2$  are stoichiometric coefficients of Ce ( $x_1, x_2 = 1, 1/2, 1/3, 13/58, 1/6, 1/11, x_1 > x_2$ ). Based on the calculations, Figure 4.24 displays the variation of the Gibbs free energy for the formation of six different intermetallic compounds with the temperature changing from 698 K to 823 K. The molar enthalpy and entropy for the formation can be calculated from the linear dependence of Gibbs free energy, which is expressed as

$$\Delta G_{\text{Ce}}^0 = \Delta H_{\text{Ce}}^0 - T\Delta S_{\text{Ce}}^0 \quad (4-7)$$

where  $\Delta H_{\text{Ce}}^0$  and  $\Delta S_{\text{Ce}}^0$  are the enthalpy ( $\text{kJ mol}^{-1}$ ) and entropy ( $\text{J mol}^{-1} \text{K}^{-1}$ ) for the formation, respectively. The  $R^2$  values were all greater than 0.986 indicating that the fitted regression lines

agree well with points of Gibbs free energies. Summary of the enthalpy and entropy of Ce-Cd intermetallic compound formations with equations used for the calculations is listed in Table 4.11. The results obtained for the Ce-Cd intermetallic compounds in the present study show slightly smaller values compared with those reported by Kim et al. [64] and Shibata et al. [70], but follow similar linear trends for each intermetallic compound.

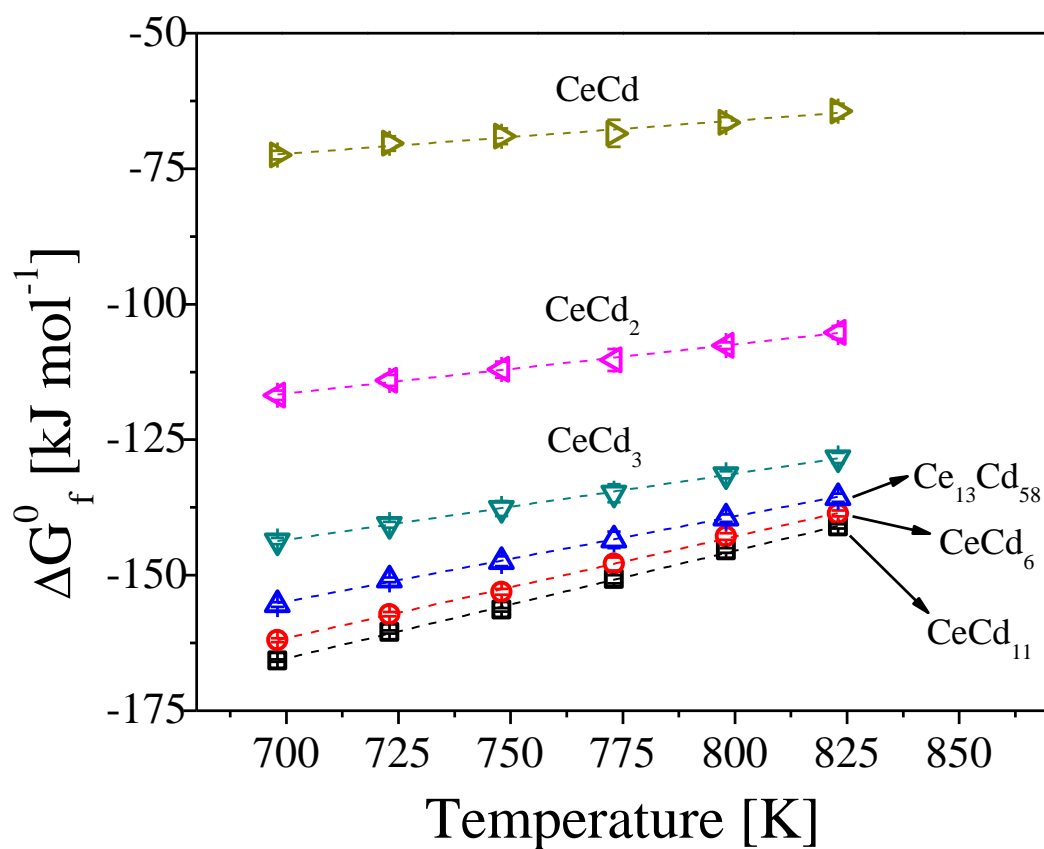


**Figure 4.24** Variation of the Gibbs free energies of Ce-Cd intermetallic compound formations as a function of temperature.

**Table 4.11** The enthalpies and entropies of Ce-Cd intermetallic compound formations

Formation reaction of intermetallic compounds	Equation for $\Delta G_f^0$	$\Delta H_f^0$ [kJ mol <sup>-1</sup> ]	$\Delta S_f^0$ [J mol <sup>-1</sup> K <sup>-1</sup> ]
$\text{Ce} + 11\text{Cd} \rightarrow \text{CeCd}_{11}$	$-3F\Delta E_6$	$-304.3 \pm 2.7$	$-198.6 \pm 3.6$
$\text{Ce} + 6\text{Cd} \rightarrow \text{CeCd}_6$	$\frac{5}{11} \left[ \frac{6}{5} \Delta G_{f,\text{CeCd}_{11}}^0 - 3F\Delta E_5 \right]$	$-293.1 \pm 1.9$	$-187.8 \pm 2.5$
$\text{Ce} + \frac{58}{13}\text{Cd} \rightarrow \text{CeCd}_{58/13}$	$\frac{20}{78} \left[ \frac{58}{20} \Delta G_{f,\text{CeCd}_6}^0 - 3F\Delta E_4 \right]$	$-264.7 \pm 2.1$	$-157.0 \pm 2.9$
$\text{Ce} + 3\text{Cd} \rightarrow \text{CeCd}_3$	$\frac{19}{58} \left[ \frac{39}{19} \Delta G_{f,\text{CeCd}_{\frac{58}{13}}}^0 - 3F\Delta E_3 \right]$	$-228.9 \pm 0.6$	$-122.1 \pm 0.8$
$\text{Ce} + 2\text{Cd} \rightarrow \text{CeCd}_2$	$\frac{1}{3} \left[ 2\Delta G_{f,\text{CeCd}_3}^0 - 3F\Delta E_2 \right]$	$-179.8 \pm 1.5$	$-90.5 \pm 1.9$
$\text{Ce} + \text{Cd} \rightarrow \text{CeCd}$	$\frac{1}{2} \left[ \Delta G_{f,\text{CeCd}_2}^0 - 3F\Delta E_1 \right]$	$-115.3 \pm 2.5$	$-61.4 \pm 3.3$

#### 4.2.3.3 Linear polarization (LP) and Tafel methods on LCC in LiCl-KCl-CeCl<sub>3</sub>

Tafel plot and LP methods were conducted for the measurement of the  $i_0$  of  $\text{Ce}^{3+}/\text{Ce}$  couple on LCC in LiCl-KCl molten salt. All experiments were done with an incremental increase in mole fraction of Ce by adding pure Ce metal in liquid Cd. The mole fraction was varied from 0.0013 to 0.0303 (from 0.0016 to 0.0375 in weight fraction). For both techniques, a very slow scan rate (0.5 mV s<sup>-1</sup>) was used for the purpose of obtaining the pure charge transfer kinetic which is directly related to the nature of  $i_0$ . The measurement methods for both LP and Tafel are described in Table 4.12.

**Table 4.12** Description for data acquisition from LP and Tafel methods

Step	Description
1	Load the pure Cd rods into the Pyrex crucible,
2	Lower the electrode assembly into the salt and wait until Cd is melted,
3	Lift the electrode assembly and add Ce metal chip into the LCC,
4	Lower the assembly and wait until OCP become stable,
5	Sweep potential from 0.2 V to -0.2 V based on OCP with 0.5 mV s <sup>-1</sup> scan rate,
6	Obtain linear LP and Tafel regions,
7	Calculate $i_0$ of Ce <sup>3+</sup> /Ce on LCC by using Eq. (2-27) and Eq. (2-28), and
8	Repeat Steps 3 – 7 for next LP and Tafel measurements.

Eqs. (2-27) and (2-28) can be used to estimate the  $i_0$  of Ce on the LCC from the Tafel and LP methods, respectively. Figure 4.25 shows Tafel plots for the reduction and oxidation of Ce<sup>3+</sup>/Ce couple on LCC in LiCl-KCl salt at 773 K. Significant asymmetry was observed between reduction and oxidation regions. In reduction region, Tafel curves are approaching the mass-transfer-limited current by an extreme reduction of Ce metal on the LCC while curves in oxidation region follow Tafel behavior. Thus, only oxidation regions of Tafel results were used for  $i_0$  measurements. Once the desired amount of Ce metal was dissolved into the liquid cadmium, Tafel measurements were started from oxidation region. In the oxidation part of the Tafel plots, linear dependences of current-overpotential were observed at overpotential ranging from 50 mV to 110 mV. Therefore, linear fits were done at the overpotential range, and the intercepts of log (i) were determined for

the calculation of  $i_0$ . Figure 4.26 plots current-potential curves in very small overpotential regions ( $< 10$  mV). The  $\text{Ce}^{3+}/\text{Ce}$  redox potential was shifted toward negative direction with increasing Ce concentration in Cd, but maintained at similar potential when Ce was saturated. The current shows linear dependence to the potential representing charge transfer resistance; therefore, Eq. (2-28) was used to calculate the  $i_0$  of Ce. Figure 4.27 compares the results of  $i_0$  with respect to increasing mole fraction of Ce in Cd from both Tafel and LP methods, and the values are listed in Table 4.13. The results from both methods show the relative difference less than 20%, but their trends of  $i_0$  against mole fraction of Ce in Cd are in good agreement. Interestingly, when Ce concentration is lower than its solubility in Cd,  $i_0$  of Ce is linearly dependent on Ce concentration (Ce solubility limit in Cd is 0.006 in mole fraction [76]). That is,  $i_0$  linearly increases with increasing concentration of Ce in Cd until Ce mole fraction is less than 0.006. However, as Ce fraction exceeds its solubility limit in Cd, a nearly steady  $i_0$  of Ce was observed. This may be attributed to the equilibrium state in the phase ( $\text{Cd-CeCd}_{11}$ ), which can be explained along with the flat plateaus obtained in the Gibbs free energy study in the present study. The activity of Ce is fixed in the two phases co-existing state; therefore, this results in the constant values of  $i_0$  beyond the Ce solubility limit in Cd (two phases co-existing between  $\text{Cd-CeCd}_{11}$ ). It could be considered that the value of  $i_0$  will increase with phase change to  $\text{CeCd}_6$ ,  $\text{Ce}_{13}\text{Cd}_{58}$ ,  $\text{CeCd}_3$ , and so on, due to the increase in the activity of Ce in Cd. However, the amount of each element deposited into the LCC is not expected to be more than 10 wt% in the electrorefining process. Therefore, the value of  $i_0$  should follow the general trend after the concentration exceeds the solubility limit in liquid Cd. In the case of Ce, the  $i_0$  of Ce stays at around  $0.012 \text{ A cm}^{-2}$  after its solubility in Cd. Unfortunately, there is no reported data of  $i_0$  on the LCC for any meaningful comparison.



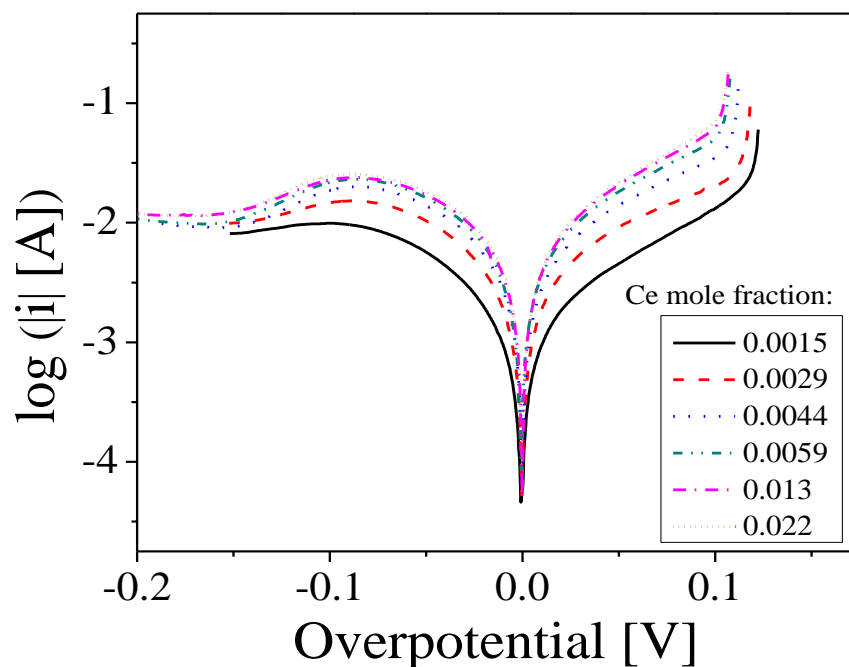


**Figure 4.25** Tafel plots for  $\text{Ce}^{3+}/\text{Ce}$  on the LCC with respect to incremental change of Ce mole fraction in Cd. The scan rate was  $0.5 \text{ mV s}^{-1}$ , and the surface area was  $0.731 \text{ cm}^2$ .

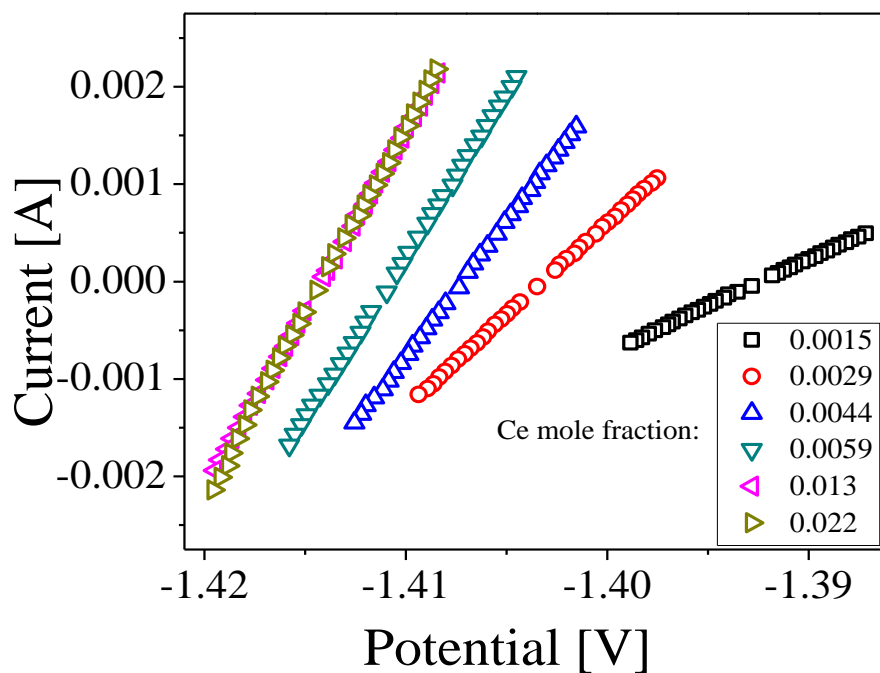


**Figure 4.26** Plots of current versus potential in the region of small overpotential for  $\text{Ce}^{3+}/\text{Ce}$  redox in the LiCl-KCl at 773 K at different mole fractions of Ce in Cd. The scan rate of  $0.5 \text{ mV s}^{-1}$  and the surface area of  $0.731 \text{ cm}^2$  were used for all measurements.

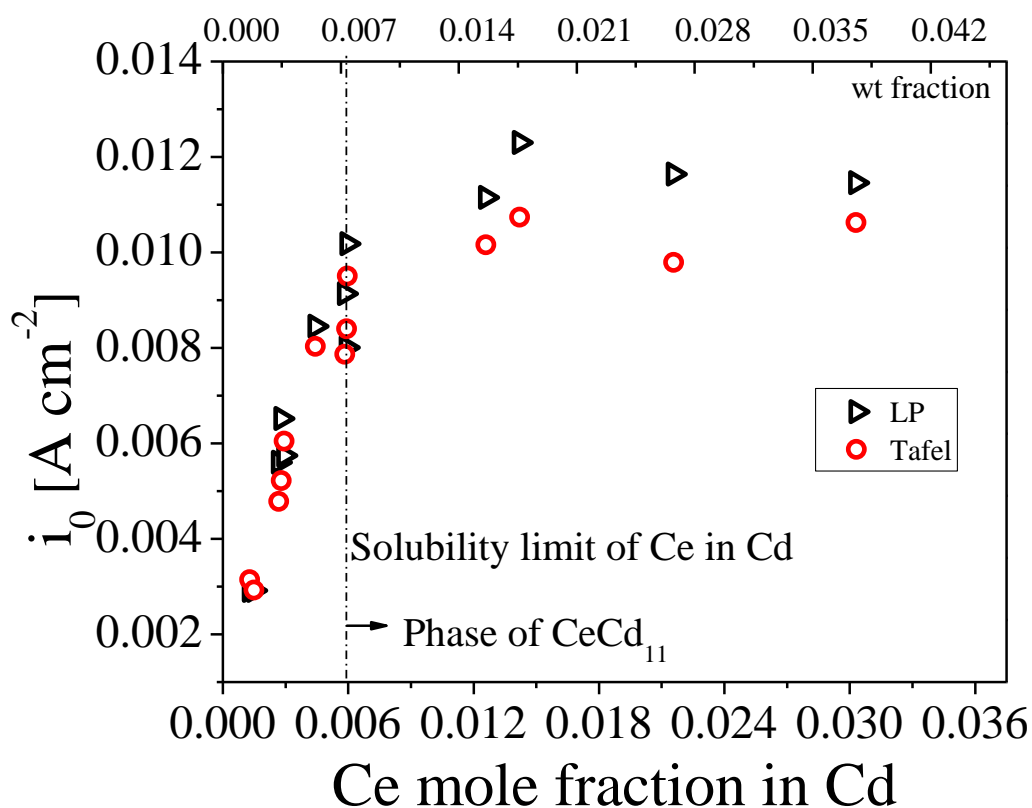


**Figure 4.27** Plots of  $i_0$  for the  $\text{Ce}^{3+}/\text{Ce}$  couple from both Tafel and LP methods regarding to Ce mole fraction in the LCC. The Ce solubility limit in Cd is 0.006 in mole fraction.

**Table 4.13** The values of  $i_0$  of Ce on Cd measured by both Tafel and LP methods

Mole fraction of Ce in liquid Cd	$i_0$ [A cm <sup>-2</sup> ]		
	Tafel method	LP method	Relative % difference
0.0013	0.00292	0.00315	7.8 %
0.0015	0.00291	0.00293	0.4 %
0.0027	0.0056	0.0048	14.7 %
0.0028	0.0065	0.0052	18.4 %

0.0029	0.0057	0.0060	5.2 %
0.0044	0.0084	0.0080	4.9 %
0.0058	0.0091	0.0079	13.9 %
0.0059	0.008	0.0084	4.9 %
0.006	0.01	0.0095	6.6 %
0.0126	0.011	0.010	8.9 %
0.0142	0.012	0.011	12.7 %
0.0216	0.012	0.0098	15.9 %
0.0303	0.0115	0.011	7.3 %

#### 4.2.4 Conclusions

Electrochemical properties of Ce on LCC were investigated in LiCl-KCl eutectic salt via CV, OCC, Tafel, and LP techniques. The effect of Li co-deposition could be removed by subtracting CV curve of pure LiCl-KCl from the curve of LiCl-KCl-CeCl<sub>3</sub>. Therefore cyclic voltammograms only attributed to Ce<sup>3+</sup>/Ce redox reaction were obtained. The cathodic peak potential stays at almost the same potential within 0.2 V s<sup>-1</sup> of scan rate, which reveals the redox reaction on the LCC is nearly reversible in the range of scan rates used. The diffusion coefficient of Ce on the LCC was measured by using the Berzins-Delahay equation. The values of the diffusion coefficient of Ce on the LCC were found to be in the range from  $2.9 \times 10^{-6} \text{ cm}^2 \text{ s}^{-1}$  to  $5.1 \times 10^{-6} \text{ cm}^2 \text{ s}^{-1}$ ; these values are almost half compared with those on the tungsten solid electrode. The slow diffusion rate of Ce on the LCC may result from the special structure of the LCC. In the cyclic voltammogram of LiCl-KCl-CeCl<sub>3</sub>-CdCl<sub>2</sub>, the Ce-Cd intermetallic compound formations

were verified by obtaining the different anodic peaks. The OCC was performed to determine the thermodynamic properties of Ce for Ce-Cd intermetallic compounds, including the Gibbs free energy, enthalpy, and entropy of the formation. Furthermore, activity of Ce showed the smallest value in phase of Cd-CeCd<sub>11</sub>, and become larger when Ce fraction increases in Cd. The Tafel and LP techniques were conducted to determine  $i_0$  of Ce on the LCC. The results from Tafel and LP methods agree well each other and show an interesting trend regarding to the Ce mole fraction in Cd. Within the solubility limit of Ce in Cd, the  $i_0$  of Ce increases with increasing mole fraction of Ce in Cd. However, the  $i_0$  of Ce was almost unchanged with increasing mole fraction of Ce beyond the solubility limit of Ce in Cd. Thus, it can be concluded that the  $i_0$  of Ce is also dependent on the state of Ce-Cd intermetallic compound phase, and identical  $i_0$  could be expected in the same phase formation.

### 4.3 Summary

This chapter focuses the developments of the suitable setups and measurement methods to understand the behaviors of SNM. Ce was chosen as a surrogate element for the U. Its electrochemical, thermodynamic, and kinetic properties were explored in LiCl-KCl eutectic salts. In Section 4.1, CV and EIS techniques were being performed with solid cathode in LiCl-KCl-CeCl<sub>3</sub> salts. Peak currents and potentials from CV measurements were employed to calculate the diffusion coefficients of CeCl<sub>3</sub> and the apparent standard potentials of Ce<sup>3+</sup>/Ce in the salt. Compared to previous literature, EIS technique was applied to determine the exchange current density. Minimum overpotentials for Ce<sup>3+</sup>/Ce reaction to occur on the electrode surface were applied and EIS spectra were measured at that potential. By fitting the EIS spectra to the proposed

equivalent circuit, the charge transfer impedances for  $\text{Ce}^{3+}/\text{Ce}$  could be measured, which were used to calculate the  $i_0$  values. Therefore, the values of  $i_0$  for  $\text{Ce}^{3+}/\text{Ce}$  reaction were examined at different temperatures and concentrations, indicating that the EIS method is feasible to determine the  $i_0$  kinetics in LiCl-KCl eutectic salt. The EIS method was further used to understand the  $i_0$  kinetics for the soluble/soluble reaction ( $\text{Sm}^{3+}/\text{Sm}^{2+}$ ) in LiCl-KCl eutectic salt, which can be found in Appendix.

Section 4.2 further explored the Ce behaviors on LCC electrode to understand behaviors of MA and Ln materials on liquid cathodes in ER system. When CV is performed with the LCC, Li metal is simultaneously deposited along with Ce; therefore, the CV baselines of pure LiCl-KCl were subtracted to obtain CV curves only attributed to the Ce redox reactions. From the processed CV curves, the diffusion coefficients of  $\text{CeCl}_3$  were calculated revealing that the diffusivity was relatively weak by using LCC compared to usage of a solid electrode. For elucidation in thermodynamic behaviors of MA in LCC, the OCC method was performed by building Ce-Cd thin layer on tungsten electrode in LiCl-KCl- $\text{CeCl}_3$ - $\text{CdCl}_2$ . It was verified that the Ce forms the intermetallic compounds in liquid Cd, and thermodynamic characters were evaluated including the Gibbs free energies, enthalpies, entropies for the Ce-Cd intermetallic compound formations. The LP and Tafel methods were utilized to estimate the exchange current densities of  $\text{Ce}^{3+}/\text{Ce}$  on LCC.

This chapter investigates various Ce properties with solid/liquid cathodes in LiCl-KCl salts, which will be useful database not only for anticipating U behavior, but also understanding and accumulating the fundamental features of the Ln elements in ER system. In each section, the specific steps and methods were specifically described for the electrochemical measurements and the data acquisitions, which will be used or improved in following chapter for uranium experiments (Chapter 5).

## Chapter 5 Uranium Electrochemical Studies in Molten LiCl-KCl

### Eutectic<sup>3</sup>

Based on the surrogate experiments and methodologies accumulated discussed in the previous chapter, the experimental setups and programs were established to explore the electrochemical, thermodynamic, and kinetic properties of U in LiCl-KCl salt system via CV, OCP, LP, Tafel, and EIS techniques. The resulting data sets are provided in Sections 5.3.1 to 5.3.4. Here, the  $i_0$  of  $U^{3+}/U$  were intensively investigated via EIS, LP, Tafel, and CV techniques and being delivered in Sections 5.3.4.1 to 5.3.4.3. The discussion and further analyses on these results are given in the following subsection. In addition, LiCl-KCl- $UCl_3$ - $GdCl_3$  salt systems were investigated and the same electrochemical measurements were carried out to gain insight on the effect of other elements on U properties which could be happening in ER system. The results and discussion can be found in Section 5.3.5.

### 5.1 Introduction

For the advancement of the safeguard technologies in pyroprocessing, it is necessary to build fundamental database for SNM, which will enhance the developments of kinetic models and the real-time monitoring technologies. Particularly, uranium is the most abundant element in reprocessing paths (UNF contains ~96 % of U [6]); thus, the assessment of fundamental features must be accurately done. For the pyroprocessing applications, kinetic, thermodynamic, and electrochemical properties of uranium should be known and documented under different conditions. Despite numerous studies on kinetic, thermodynamic, and electrochemical features in

---

<sup>3</sup> Contents in Chapter 5 are cited from the author's publication:  
D. Yoon and S. Phongikaroon, "Measurement and Analysis of Exchange Current Density for  $U/U^{3+}$  Reaction in LiCl-KCl Eutectic Salt via Various Electrochemical Techniques," **submitted** to *Electrochimica Acta*.

LiCl-KCl eutectic salt, the  $i_0$  values of uranium have not been fully explored and understood as discussed in Chapter 2. The  $i_0$  is a criterion of the reaction rate on the electrode, which plays a significant role in electrochemical equations and expressions; hence, the measurement and collection of  $i_0$  for  $U^{3+}/U$  reaction in LiCl-KCl are extremely crucial for developing the kinetic models and near-real time monitoring system for pyroprocessing technology. In addition, ER salt system contains a number of fission products including actinide An and Ln components [21]; therefore, effects of multi-elements on the U behavior should be explored in LiCl-KCl eutectic salt system.

In the present study, electrochemical, thermodynamic, and kinetic properties of U were investigated by using CV, OCP, LP, Tafel and EIS methods. The properties were determined at different concentrations ranging from 0.5 wt% to 4 wt% and temperatures from 723 K to 798 K in order to understand the concentration and temperature effects on U behaviors. For the confidence of the  $i_0$  evaluation, four different electrochemical methods including LP, Tafel plot, EIS, and CV were performed, and the result values were compared and discussed. In addition,  $GdCl_3$  under different concentrations was added into LiCl-KCl- $UCl_3$  eutectic salt at 773 K, and the effects of  $GdCl_3$  co-existence were explored on the properties of U such as diffusion coefficient, equilibrium potential, and exchange current density. The resulting data in this work will help elucidating the U behaviors in multi-components salt system.

## 5.2 Detailed Experimental Setup and Program

Figure 5.1 illustrates the schematic design of the electrochemical cell in the Muffle furnace. The salt samples were prepared in the Inconel® crucible, which is located in the furnace with the alumina secondary safety crucible. The tungsten rod (2 mm in diameter) was used as the working

electrode. The U metal plates were chopped and loaded in a molybdenum basket, which were used as a counter electrode; therefore, the salt concentration could be maintained the same during the electrochemical measurements. The Ag/AgCl (1 mol%) reference was used for all experiments in this chapter. The specifications can be found in Table 3.1 and the same methods for salt preparations and electrode preparations were followed as mentioned in Section 3.2. For exploring the U characteristics and the effect of  $\text{GdCl}_3$  on U properties, the experimental program was developed as being summarized in Table 5.1. Concentration information based on the ICP-MS quantitative analyses and the electrode surface area for each run were obtained for verification and analysis.

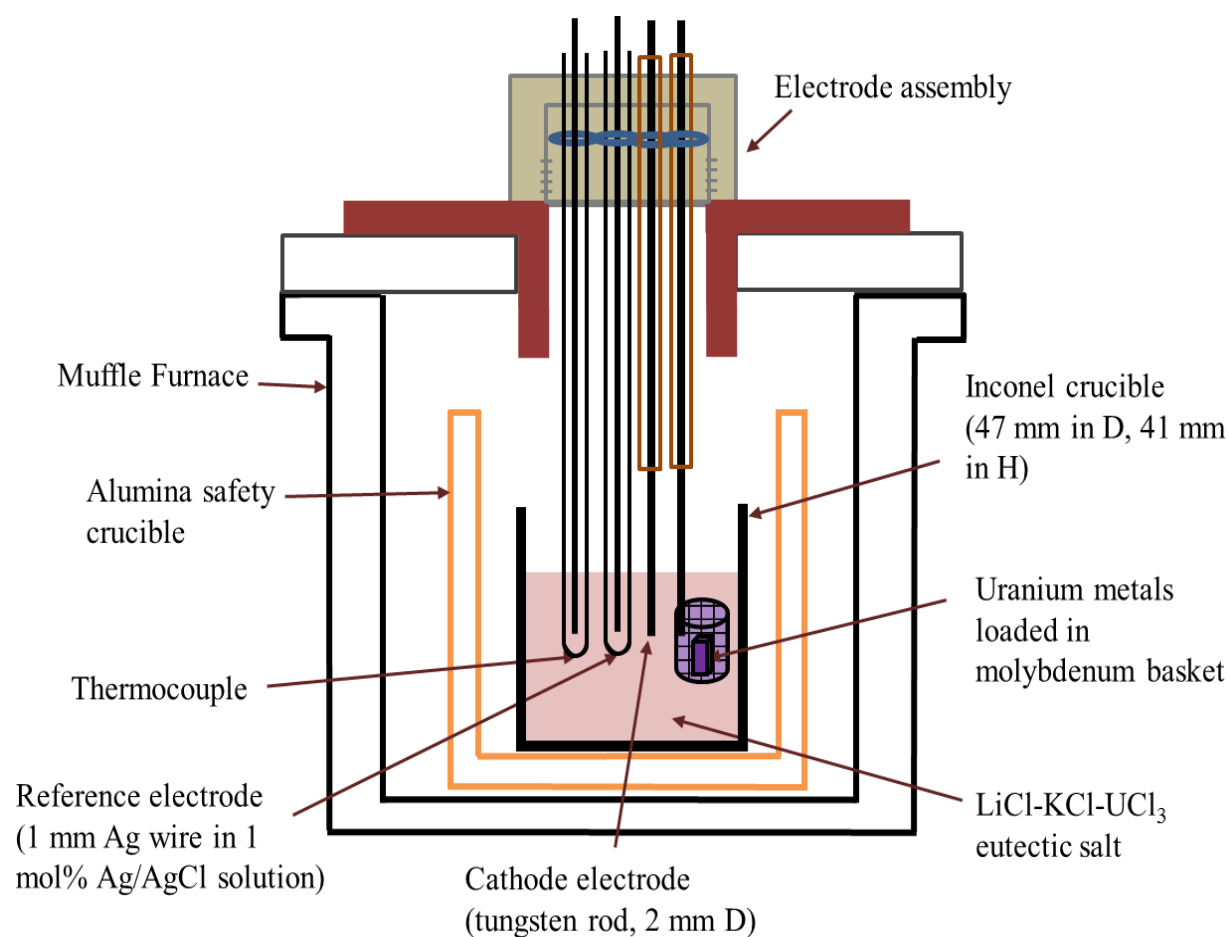


**Figure 5.1** Schematic design of electrode assembly and electrochemical cell in Muffle furnace.



**Table 5.1** Electrolyte concentration and the working electrode surface area for each experimental run

No.	Samples	UCl <sub>3</sub> (wt%)	GdCl <sub>3</sub> (wt%)	Electrode surface area (cm <sup>2</sup> )
1	UCl <sub>3</sub> -0.5	0.559		0.621
2	UCl <sub>3</sub> -1.0	1.06		0.723
3	UCl <sub>3</sub> -2.0	2.04		0.471
4	UCl <sub>3</sub> -4.0	4.04		0.396
5	U0.5_Gd0.5	0.59	0.49	0.565
6	U1.0_Gd0.25	1.04	0.29	0.584
7	U1.0_Gd0.5	1.45	0.47	0.503
8	U1.0_Gd1.0	1.09	0.95	0.522
9	U2.0_Gd1.0	1.71	0.96	0.471
10	U2.0_Gd2.0	1.94	2.09	0.452

### 5.3 Results and discussion

#### 5.3.1 Diffusion coefficient of UCl<sub>3</sub> in LiCl-KCl

CV curves were obtained by sweeping the potential from 0 V to -2.35 V with different scan rates to determine the diffusion coefficient of UCl<sub>3</sub> in LiCl-KCl eutectic salt. The same procedure for the measurement was used as developed in Table 4.2; however, the cleaning process was done by applying potential at -0.45 V (vs. Ag/AgCl) for avoiding oxidation of U<sup>3+</sup> to U<sup>4+</sup>. Figure 5.2 is an example of CV curves in LiCl-KCl-1wt% UCl<sub>3</sub> salt at 773 K. Reduction and oxidation peaks

for  $U^{4+}/U^{3+}$  and  $U^{3+}/U$  were observed at  $I_a/I_c$  and  $III_a/III_c$ , respectively; no other reaction was found beyond the  $U^{3+}/U$  reduction potential. In addition, small pre-peaks were observed on the reduction and oxidation processes at  $II_a$  and  $II_c$  respectively. These pre-peaks were also observed at different concentrations up to 4 wt%  $UCl_3$  as shown in Figure 5.3, which has been also reported by many researchers [40-41, 45-46, 77]. Reddy et al. [45] and Serrano and Taxil [77] further studied the pre-peaks by observing the peak current at different scan rates and concentrations, concluding that the peaks were being attributed by an adsorption and desorption of uranium monolayer on the working electrode.

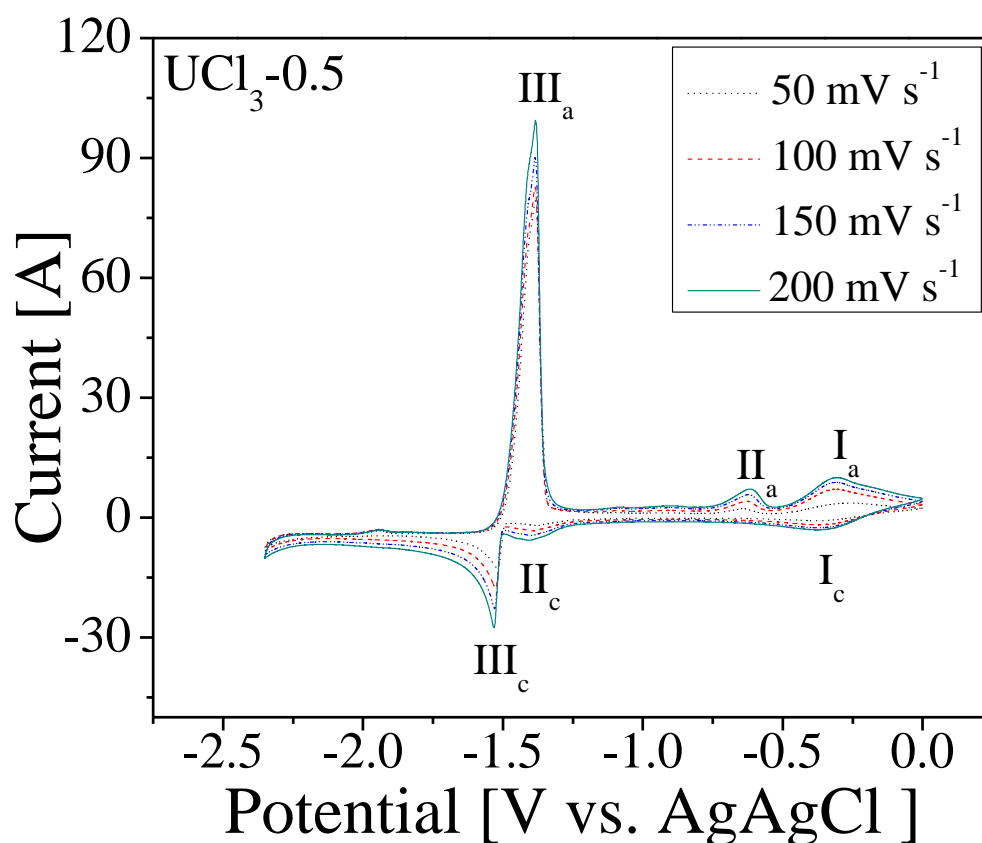


**Figure 5.2** Cyclic voltammograms in LiCl-KCl-1.0 wt%  $UCl_3$  at 773 K. The potential was swept at the scan rate from  $50 \text{ mV s}^{-1}$  to  $200 \text{ mV s}^{-1}$ .

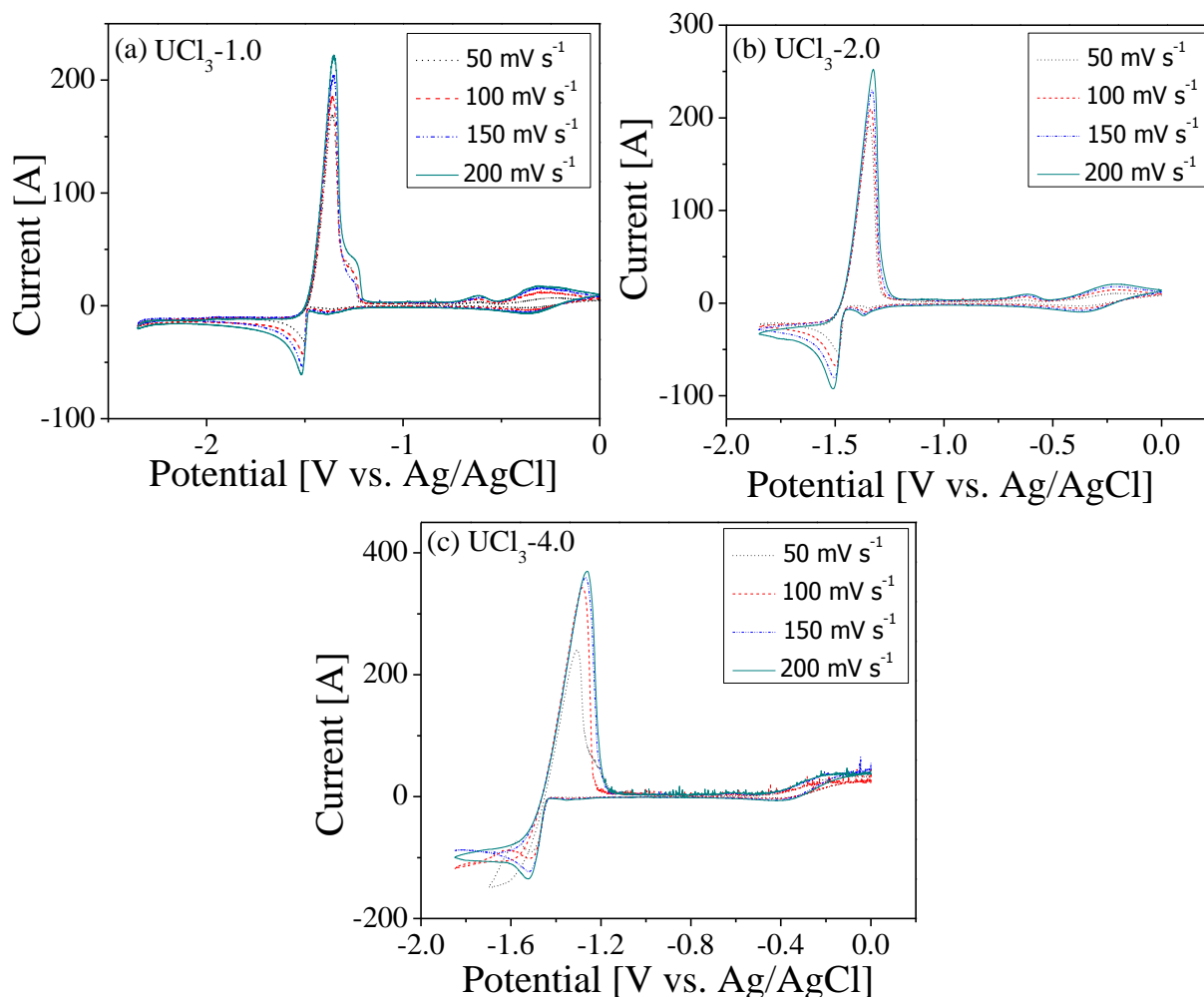


**Figure 5.3** Cyclic voltammograms at concentrations of (a) 1.0 wt%  $\text{UCl}_3$ , (b) 2.0 wt%  $\text{UCl}_3$ , and (c) 4.0 wt%  $\text{UCl}_3$  in  $\text{LiCl-KCl}$  eutectic salt at 773 K. The potential was swept at the scan rate from 50  $\text{mV s}^{-1}$  to 200  $\text{mV s}^{-1}$ .

The reduction peaks for  $\text{U}^{3+}/\text{U}$  ( $\text{III}_c$ ) stay at the same potential with the scan rate change between 50  $\text{mV s}^{-1}$  and 200  $\text{mV s}^{-1}$ ; thus, the redox reactions were considered as a reversible system under the experimental conditions. The height of peak currents were measured from the base line, which were linearly proportional to the square root of the scan rate. The linear slopes were employed through the use of Berzin-Delahay equation (Eq. (2-13)) for the  $\text{UCl}_3$  diffusion

calculation in LiCl-KCl. Figure 5.4 plots the calculated diffusion coefficients of  $\text{UCl}_3$ , showing the linear trend over temperature. It seems that the values are weakly affected by the concentration change up to 2 wt% of  $\text{UCl}_3$ ; however, the diffusion coefficient begins decreasing at 4 wt% of  $\text{UCl}_3$  (see red circles in Figure 5.4). This may be owing to a challenge of the CV measurement at high concentration with the lower scan rate as shown in Figure 5.3(c) where the reduction peaks can be hardly obtained due to the massive U reduction on the working electrode. When the CV were measured in LiCl-KCL-4wt%  $\text{UCl}_3$  at scan rate ranging from  $700 \text{ mV s}^{-1}$  to  $1500 \text{ mV s}^{-1}$ , distinct peaks were obtained and massive U reduction was diminished as shown in Figure 5.5. However, the relationship between the peak current and the diffusion coefficient need to be derived for irreversible soluble-insoluble system to determine the diffusion coefficient. Despite of incompatibility, Eq. (2-12) was used to estimate the diffusion coefficients of  $\text{UCl}_3$  at 4 wt% by using the peak currents at faster scan rate (in Figure 5.5). The values of  $n\alpha$  were calculated by using Eq. (2-10). The resulting data are illustrated in Figure 5.6 indicating that the diffusion coefficients (4 wt%  $\text{UCl}_3$ ) measured by the irreversible relationship (Eq. (2-12)) were moved in the same trend line observed at lower concentrations (0.5 wt%, 1 wt%, and 2 wt%  $\text{UCl}_3$ ). This phenomenon (decrease of diffusion coefficient at higher concentration) were also observed in a previous literature [46]; however, further studies are necessary to explain this issue. The effect could be due to the attractive interaction among the particles or that the reversible equation (Berzin-Delahay, Eq. (2-13)) is not likely applicable at a high concentration.

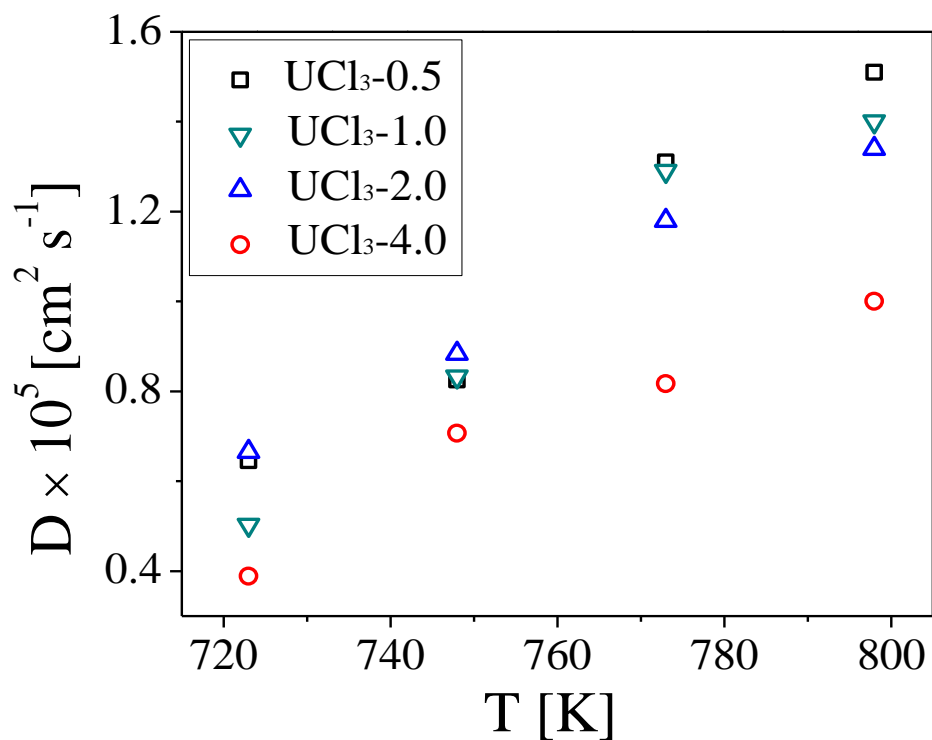


**Figure 5.4** Diffusion coefficients of  $\text{UCl}_3$  in  $\text{LiCl-KCl}$  as a function of temperature.

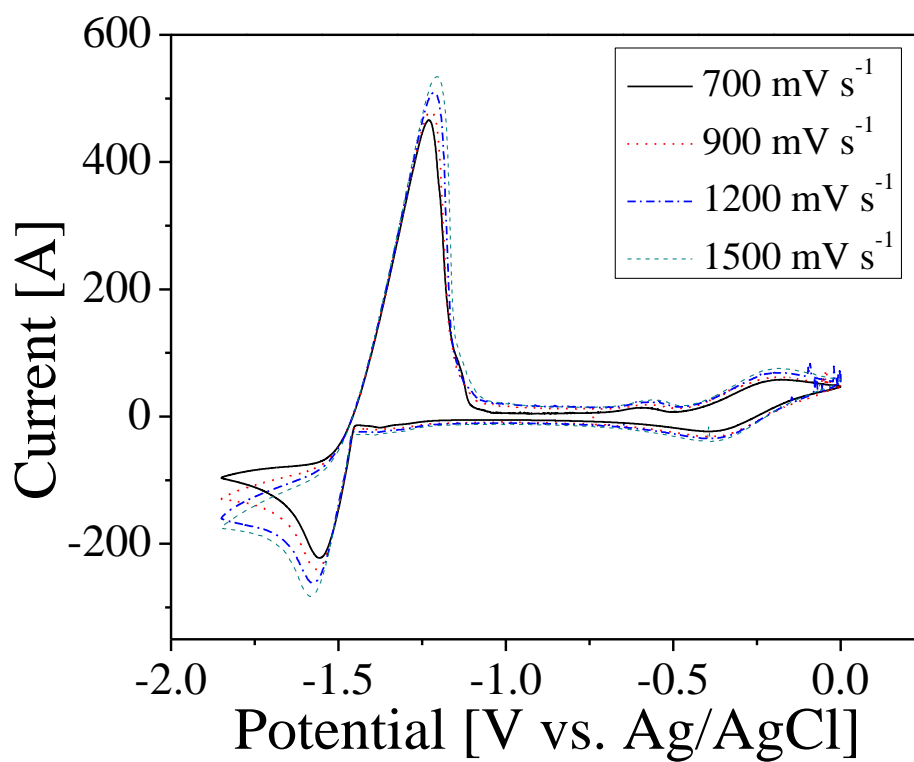


**Figure 5.5** Cyclic voltammograms in  $\text{LiCl-KCl-4wt\% UCl}_3$  at 773 K with faster scan rates ranging from  $700 \text{ mV s}^{-1}$  to  $1500 \text{ mV s}^{-1}$ .

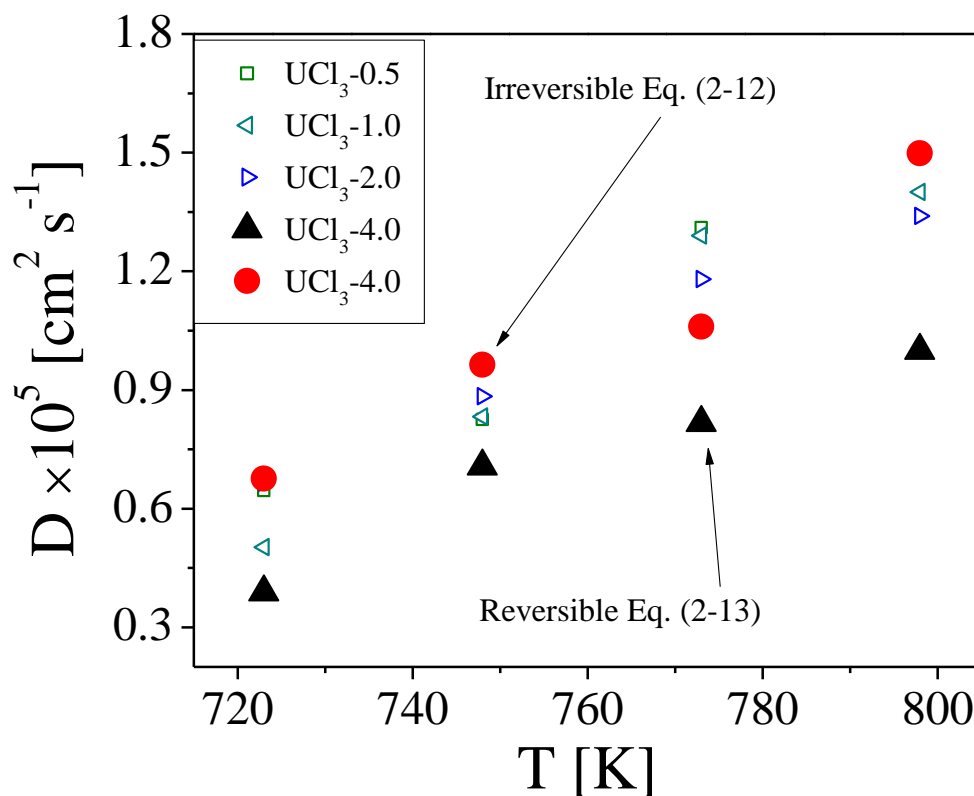


**Figure 5.6** Diffusion coefficients of  $\text{UCl}_3$  in  $\text{LiCl-KCl}$ . The values for 4wt% were measured by using Eq. (2-13) (black triangle) and Eq. (2-12) (red circle).

### 5.3.2 Apparent standard potentials of $\text{U}^{3+}/\text{U}$ via CV and OCP

The cathodic peak potentials were obtained from the CV results in Section 5.3.1 to calculate the values of  $E_{\text{U}^{3+}/\text{U}}^{0*}$  using Eq. (2-15). The resulting values are plotted in Figure 5.7 and showing proportional increase with rising temperature. The values of  $E_{\text{U}^{3+}/\text{U}}^{0*}$  seem to be independent on concentration change up to 2 wt%  $\text{UCl}_3$ , but start shifting toward negative direction at 4 wt%  $\text{UCl}_3$ .

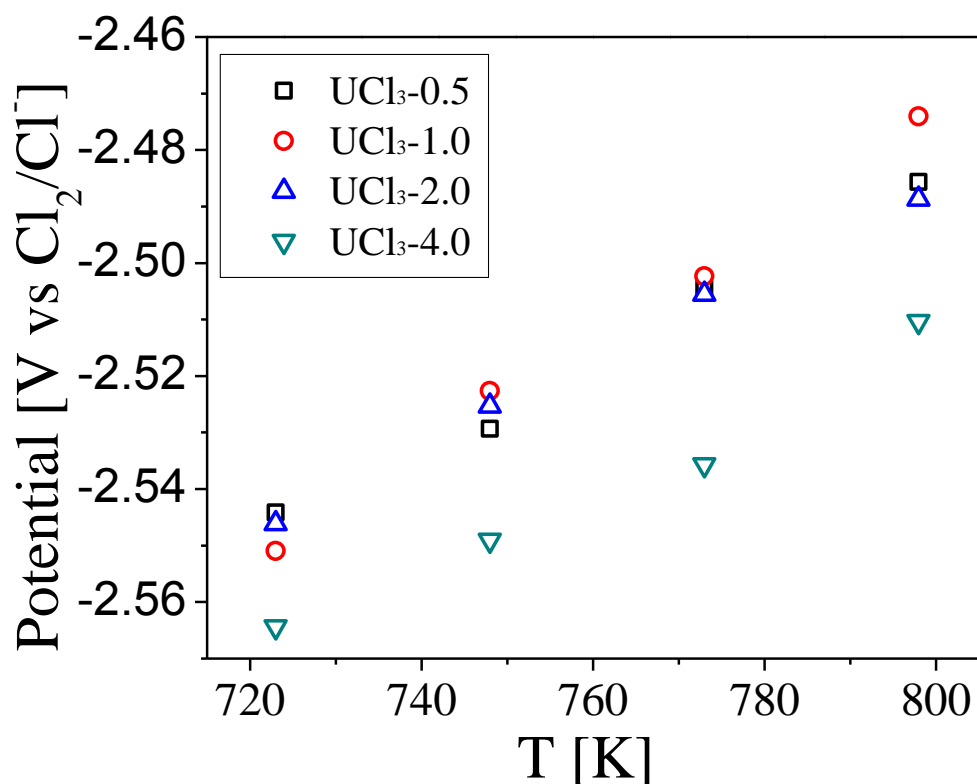


**Figure 5.7** Apparent standard potentials for  $U^{3+}/U$  couple versus  $Cl_2/Cl^-$  measured via CV techniques with Eq. (2-15).

In addition, OCPs were measured between U metal and  $U^{3+}$  ions in LiCl-KCl, which can be employed to calculate  $E_{U^{3+}/U}$  and  $E_{U^{3+}/U}^{0*}$ . Prior to the OCP measurements, U was deposited on the tungsten electrode by applying potential at -1.6 V (vs. Ag/AgCl reference) for 30 seconds, which was repeated at least three times. Figure 5.8 shows the representative OCP data which were obtained in LiCl-KCl-0.5 wt%  $UCl_3$  at temperature range (723 K to 798 K). Flat plateaus were observed within 30 seconds, which is due to the fact that the charge transfer between U metal on the electrode and  $U^{3+}$  ions in bulk salt reached the equilibrium state. The deviations of the measured equilibrium potentials were less than 1 mV, and the average values are plotted in Figure

5.9(a). The equilibrium potential of  $U^{3+}/U$  proportionally increases with increasing  $UCl_3$  concentration up to  $3.3 \times 10^{-3}$  mole fraction (2 wt % of  $UCl_3$  in LiCl-KCl); however, the rate of increase starts decreasing at  $6.6 \times 10^{-3}$  mole fraction. It seems that the equilibrium potential is more correlated at higher concentration ( $> 4$  wt%  $UCl_3$ ); however, this should be experimentally demonstrated in future works. The apparent standard potentials of  $U/U^{3+}$  can be determined using Nernst equation (Eq. (2-2)) with the assumption that the U metal activity is unity. Here, the measured  $E_{U^{3+}/U}$  in Figure 5.9(a) can be directly substituted in Eq. (2-3) to calculate  $E_{U^{3+}/U}^{0*}$  according to the  $UCl_3$  mole fractions. In addition,  $E_{U^{3+}/U}^{0*}$  can be evaluated by plotting  $E_{U^{3+}/U}$  versus  $\ln(X_{U^{3+}})$ . Within the concentration range in the present work, values of  $E_{U^{3+}/U}$  show linear correlations with  $\ln(X_{U^{3+}})$ , as can be seen in Figure 5.9(b). The linear regressions show good  $R^2$  values greater than 0.991, and  $E_{U^{3+}/U}^{0*}$  can be determined at y-intercept. The slopes of the linear lines equal to  $RT/nF$ ; therefore, the number of charge transferred can be experimentally evaluated (which is referred as  $n_{exp.}$ ). The calculated values of  $n_{exp.}$  varied from 2.46 to 2.55, which are slightly smaller than the ideal number of the charge transferred for the  $U^{3+}/U$  reaction ( $n_{ideal} = 3$ ). This may be due to lower probability of the charge transfer in reality, and the number becomes smaller with increasing concentration. Figure 5.10 plots the results from both the direct substitution and linear regression methods with Nernst equation. If the  $n_{ideal}$  is used in Eq. (2-3) for the direct substitution methods, the result values are approximately 30 mV more negative. However, the data sets would fall on top of the values determined by the linear regression method when  $n_{exp}$  values were being used through the direct substitution method. Comparing to values from literatures, Figure 5.11 plotted the resulting data from CV and OCP measurement along with the literature values, revealing that the values are close and follow a similar trend to temperature. However, it can be noticed that  $E_{U^{3+}/U}^{0*}$  values measured by CV and CP are generally



more negative than the values measured by OCP. This may be because of the characteristics of CV and CP methods by applying overpotential to the working electrode for  $U^{3+}/U$  reaction to occur. The applied overpotential depends on the used scan rates and currents used in CV and CP, respectively.

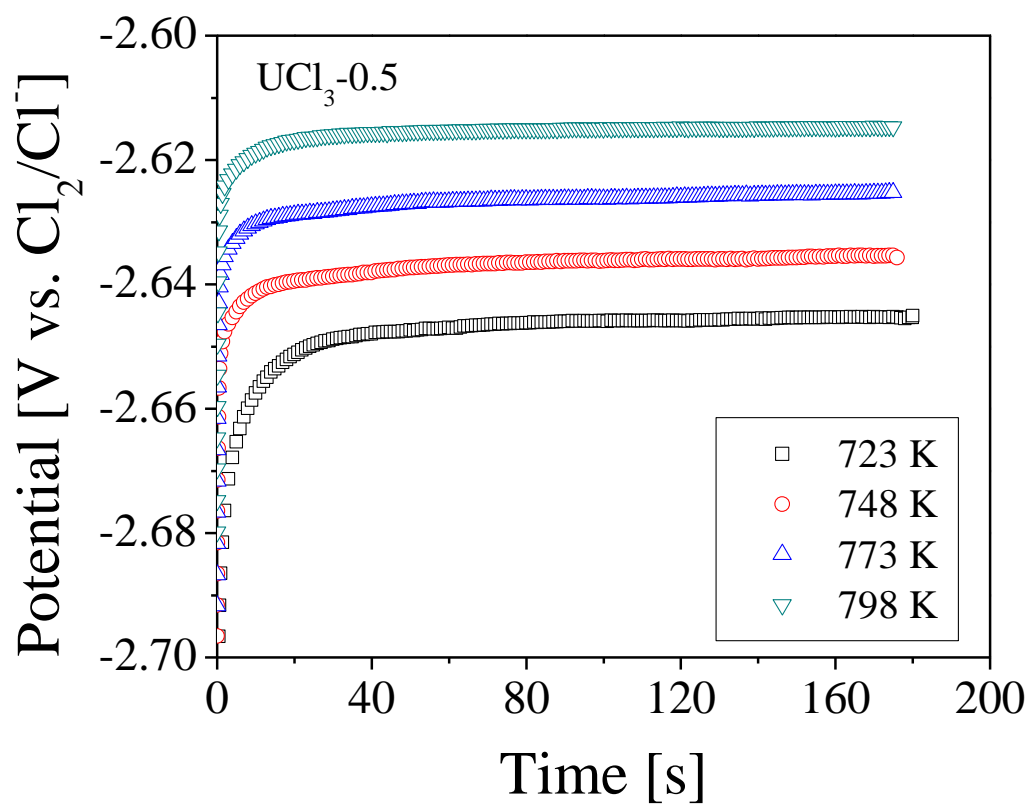


**Figure 5.8** Potential plateaus results from OCP experiments in LiCl-KCl-0.5 wt%  $UCl_3$  at temperature ranging 723 K to 798 K.

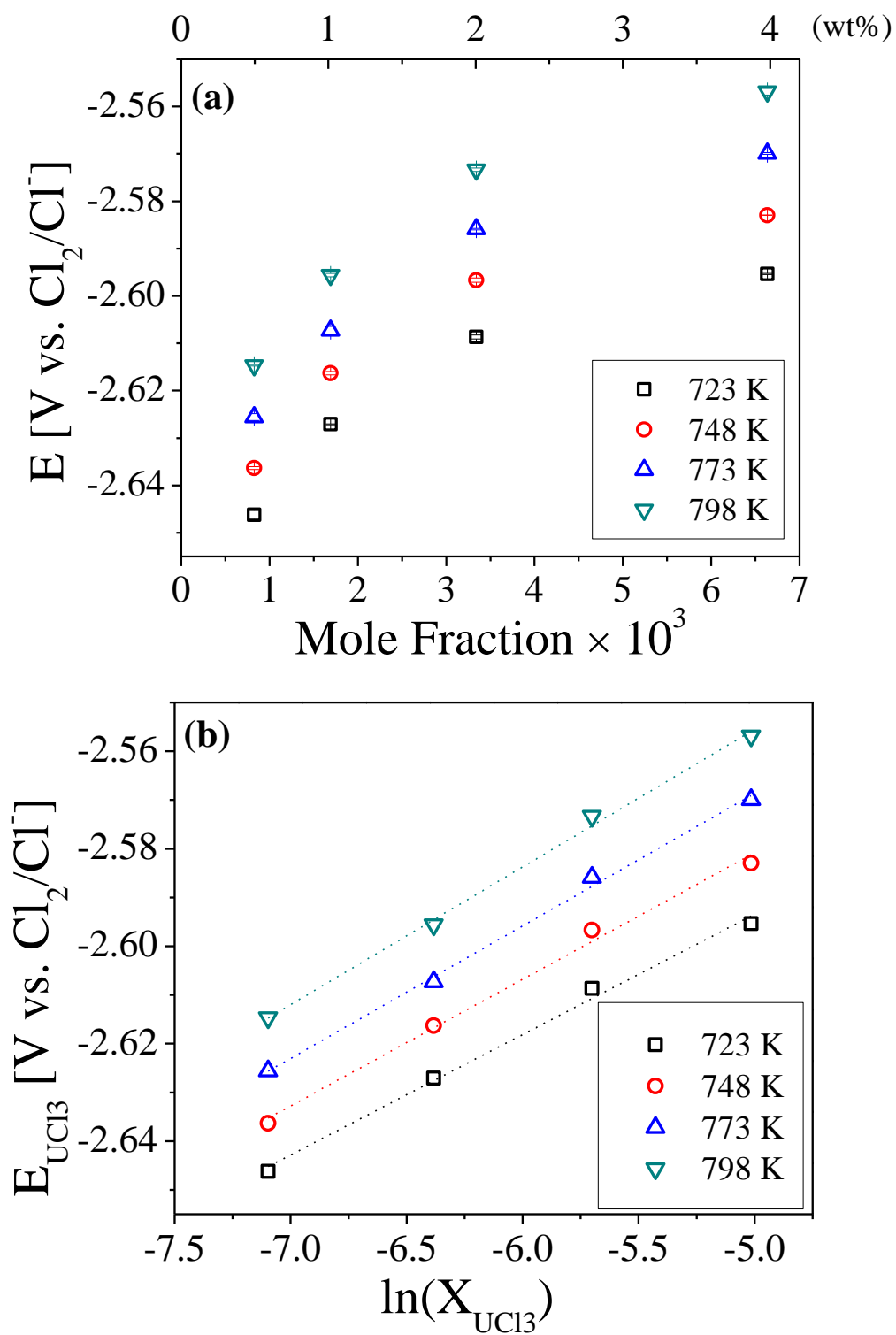


**Figure 5.9** Plots of the equilibrium potentials of  $\text{U}^{3+}/\text{U}$  in  $\text{LiCl-KCl}$  versus (a) mole fraction and (b) logarithm of mole fraction.

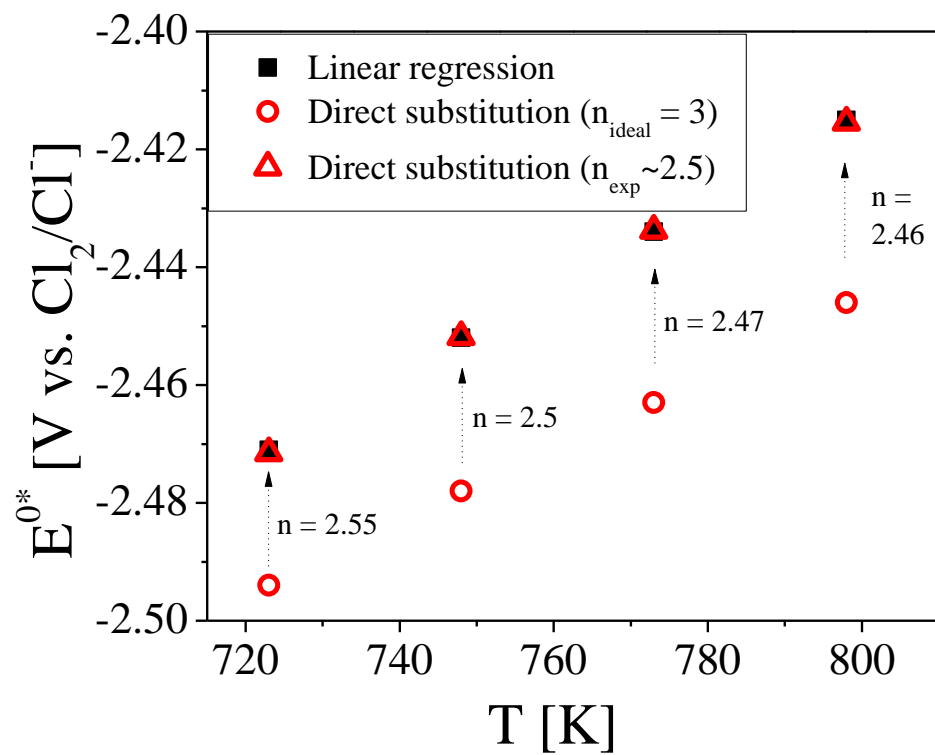


**Figure 5.10** The apparent standard potentials of  $\text{U}^{3+}/\text{U}$  in LiCl-KCl salt measured via OCP and calculated in different methods.

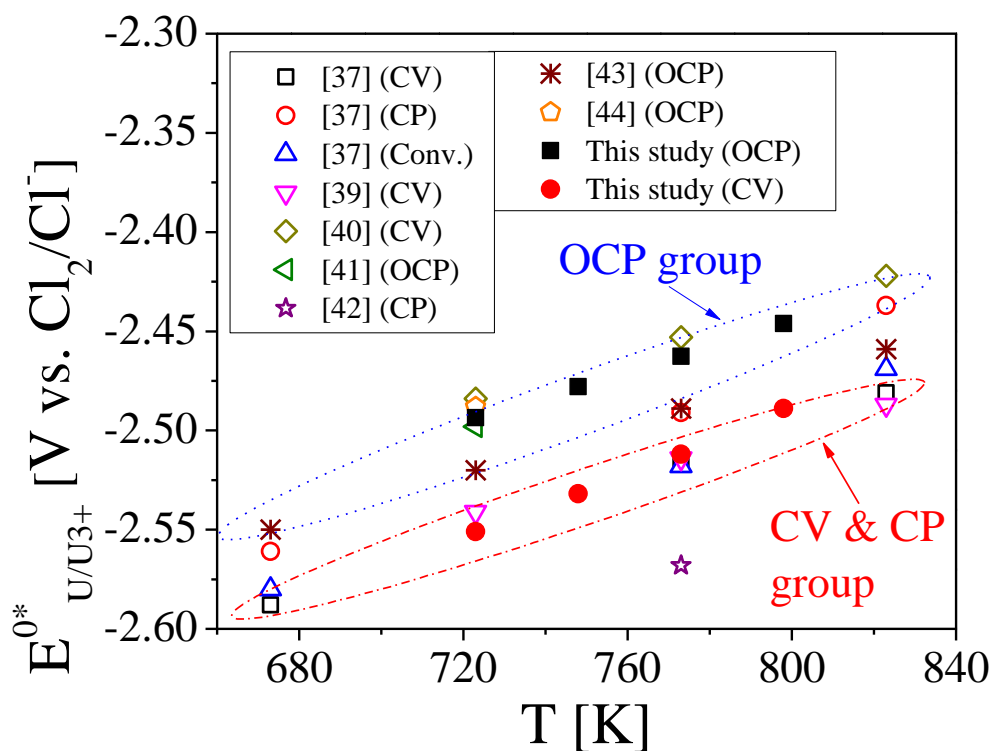


**Figure 5.11** The averaged values of  $E_{U^{3+}/U}^{0*}$  via CV and OCP technologies, compared with literature values.

### 5.3.3 Activity coefficient of $UCl_3$

The previously determined values of  $E_{U^{3+}/U}^{0*}$  were utilized to calculate thermodynamic properties of  $UCl_3$  in LiCl-KCl eutectic salt. The partial molar Gibbs free and activity coefficient of  $UCl_3$  were calculated with the same calculation methods developed in Section 4.1.3.1. In addition, the pure thermodynamic data for  $UCl_3$  were found at the super cooled liquid state [53]. Using Eq. (4-1) and Eq. (4-2),  $\Delta G_{UCl_3}^{Fusion}$  and  $\Delta G_{UCl_3}^{SC}$  were calculated. The super cooled thermodynamic information and calculated values are summarized in Table 5.2. The values of  $\Delta G_{UCl_3}^{0*}$  were calculated using the thermodynamic equation ( $\Delta G = -nF\Delta E$ ), and therefore, the  $\gamma_{U^{3+}}$

was readily calculated using Eq. (2-4). The resulting values are listed in Table 5.3 and  $\gamma_{U^{3+}}$  data sets are compared with the reported values from literatures as shown in Figure 5.12. Here, the similar trend can be observed as seen in the results of the apparent standard potentials (Figure 5.11). The values of  $\gamma_{U^{3+}}$  measured by CV and OCP are being divided into two different trends according to temperature. Between CV and OCP methods, significant discrepancies were found up to  $10^2$  order of magnitude, and OCP method generally provides higher values and show a steep increase rate when temperature rises.

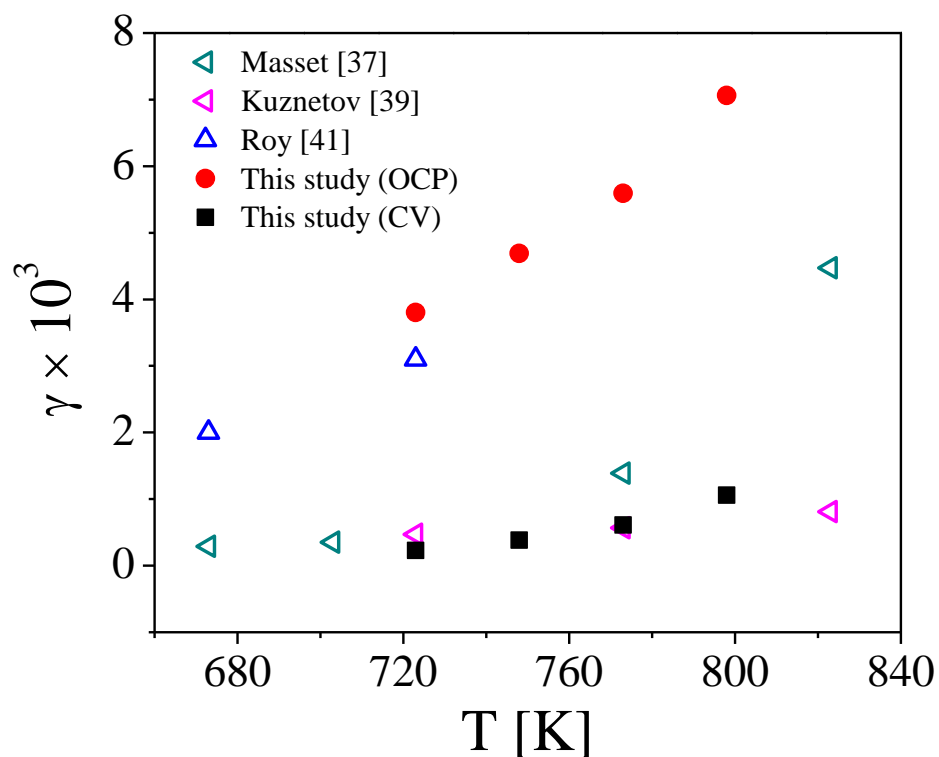


**Figure 5.12** The values of  $\gamma_{U^{3+}}$  measured via OCP and CV methods compared with literature data.

**Table 5.2** Thermodynamic information from the literature [53] and calculated values

	723 K	748 K	773 K	798 K	T <sub>m</sub> (1100 K)
$\Delta G_{\text{UCl}_3}^{\text{Formation}}$ (kJ mol <sup>-1</sup> )	-703.03	-697.83	-692.64	-687.45	
$\Delta H_{\text{UCl}_3}^{\text{Fusion}}$ (kJ mol <sup>-1</sup> )					46.44
$\Delta S_{\text{UCl}_3}^{\text{Fusion}}$ (J mol <sup>-1</sup> K <sup>-1</sup> )					41.84
C <sub>p</sub> (J mol <sup>-1</sup> K <sup>-1</sup> )	111.22	111.94	112.66	113.38	129.70
$\Delta G_{\text{UCl}_3}^{\text{Fusion}}$ (kJ mol <sup>-1</sup> )	14.76	13.96	13.12	12.26	
$\Delta G_{\text{UCl}_3}^{\text{SC}}$ (kJ mol <sup>-1</sup> )	-688.26	-683.87	-679.52	-675.19	

**Table 5.3** Thermodynamic data evaluated by OCP and CV methods

	T (K)	Masset [37] (CV)	Kuznetsov [39] (CV)	Roy [41] (OCP)	This study (OCP)	This study (CV)
$\Delta G_{\text{UCl}_3}^{0*}$ (kJ mol <sup>-1</sup> )	673	-745.1		-731.7		
	723			-723.1	-721.8	-738.5
	748				-717.2	-732.8
	773	-726.2			-712.9	-727.1
	798				-708.1	-720.7
	823	-712.9				
$\gamma_{\text{U}^{3+}} \times 10^3$	673	0.29		2.0		
	723		0.47	3.1	3.80	0.23

748			4.69	0.38
773	1.39	0.57	5.59	0.61
798			7.06	1.06
823	4.47	0.81		

### 5.3.4 Exchange current density of $U^{3+}/U$

The EIS, LP, Tafel, and CV methods were conducted to investigate the  $i_0$  kinetics of  $U^{3+}/U$  couple at  $UCl_3$  concentrations ranging from 0.5 wt% to 4 wt% and temperature from 723 K to 798 K. The detailed results from the four different techniques are provided in following sections and the comparisons among the data was made in Section 5.3.4.5. Further dimensionless analyses will be also provided as well.

#### 5.3.4.1 EIS

The same EIS measurement procedures and minimum over potential method developed in Section 4.1.3.2 were used in this section. Figure 5.13(a) illustrates the example procedure for finding minimum overpotential for  $U/U^{3+}$  reaction for  $UCl_3$ -0.5 salt at 748 K. At about -1.499 V, the minimum overpotential was obtained and the EIS measurements were repeated with the different potential amplitudes ranging from 5 mV to 10 mV. As shown in Figure 5.13(b), the impedance spectra display a good agreement with the potential amplitudes, which indicate the stable charge transfer kinetic at the minimum overpotential. The obtained impedance spectra were

fitted to the same equivalent circuit as shown in Figure 4.8. Figure 5.14 illustrates the measured and fitted impedance spectra in the complex plane for all four samples under the different temperature conditions. Small current values were applied during the EIS measurement ( $< 3 \text{ mA cm}^{-2}$ ), so that the surface area change by uranium deposition is expected to be negligible. After the manual curve fitting, the goodness of fittings ( $\chi^2$ ) was further checked by using an equation expressed as

$$\chi^2 = \frac{1}{N - m} \sum_{i=1}^N \frac{(\bar{V}_r - V_r)^2 + (\bar{V}_j - V_j)^2}{(V_r^2 + V_j^2)} \quad (5-1)$$

where  $N$  is the number of data points,  $m$  is the number of equivalent circuit parameters,  $\bar{V}_r$  is the fitted real values,  $\bar{V}_j$  is the fitted imaginary values,  $V_r$  is the measured real values, and  $V_j$  is the measured imaginary values. The values of  $\chi^2$  were lower than 0.003, indicating a good fit to the measured data sets. From the results of curve fitting, charge transfer resistances were measured, which were being employed to calculate the value of  $i_0$  and  $k^0$  for  $\text{U}^{3+}/\text{U}$  reaction in  $\text{LiCl-KCl}$  molten salt. Figures 5.15(a) and 5.15(b) show plots of the calculated  $i_0$  values versus temperature (K) and concentration ( $\text{UCl}_3$  mole fraction), respectively. The EIS experiments were repeated three to four times with the same experimental conditions to confirm the reproducibility of the results; the variations of the value are represented as the standard deviations (error bars). The values of  $i_0$  for  $\text{U}/\text{U}^{3+}$  reaction are ranging from  $0.0054 \text{ A cm}^{-2}$  to  $0.102 \text{ A cm}^{-2}$  under different concentration and temperature conditions, as listed in Table 4. The values were almost linearly proportional to an increase in the concentration and temperature, slight deviations were observed when the  $\text{UCl}_3$  concentration is over 4 wt% in  $\text{LiCl-KCl}$ . For further understanding of the rate constant ( $k^0$ ) and the charge transfer coefficient, the following equation was considered [55]:



$$i_0 = nFk^0 C_{\text{UCl}_3}^{(1-\alpha)} C_{\text{U}}^{\alpha} \quad (5-2)$$

Figure 5.15(b) shows linear relationships between  $i_0$  and concentration; therefore, the experimental results imply that either  $\alpha$  is zero or  $C_{\text{UCl}_3}$  is the same to  $C_{\text{U}}$  at the electrode surface (that is,  $C_{\text{UCl}_3} \sim C_{\text{U}}$  at equilibrium condition). In general, the parameter  $\alpha$  was incorporated directly into Eq. (2-24) for determining the  $i_0$  values in the EIS, LP, and CV methods, but the Tafel method was the available technique for gaining an insight into this parameter by calculating from the obtaining slope of the overpotential (see Eq. (2-27)). Data sets at 0.5 wt%  $\text{UCl}_3$  from the Tafel experiments were available and slopes were obtained to calculate  $\alpha$  values, ranging from 0.015 to 0.04, which were slightly less than the value of 0.22 reported by Lim et al. [51]. Ghosh et al. [49] reported extremely low  $\alpha$  value of U ( $\alpha \sim 0.01$ ) in LiCl-KCl salt. Although their systems were different, it provided that the system in this study might have small charge transfer coefficient at low concentrations. This general analysis led to the assumption that  $\alpha$  values are close to zero; thus, Eq. (5-2) could be simplified to

$$i_0 = nFk^0 C_{\text{UCl}_3}. \quad (5-3)$$

The  $k^0$  values were calculated from the slopes of the  $i_0$  linear trends on the concentrations and summarized in Table 5.4.

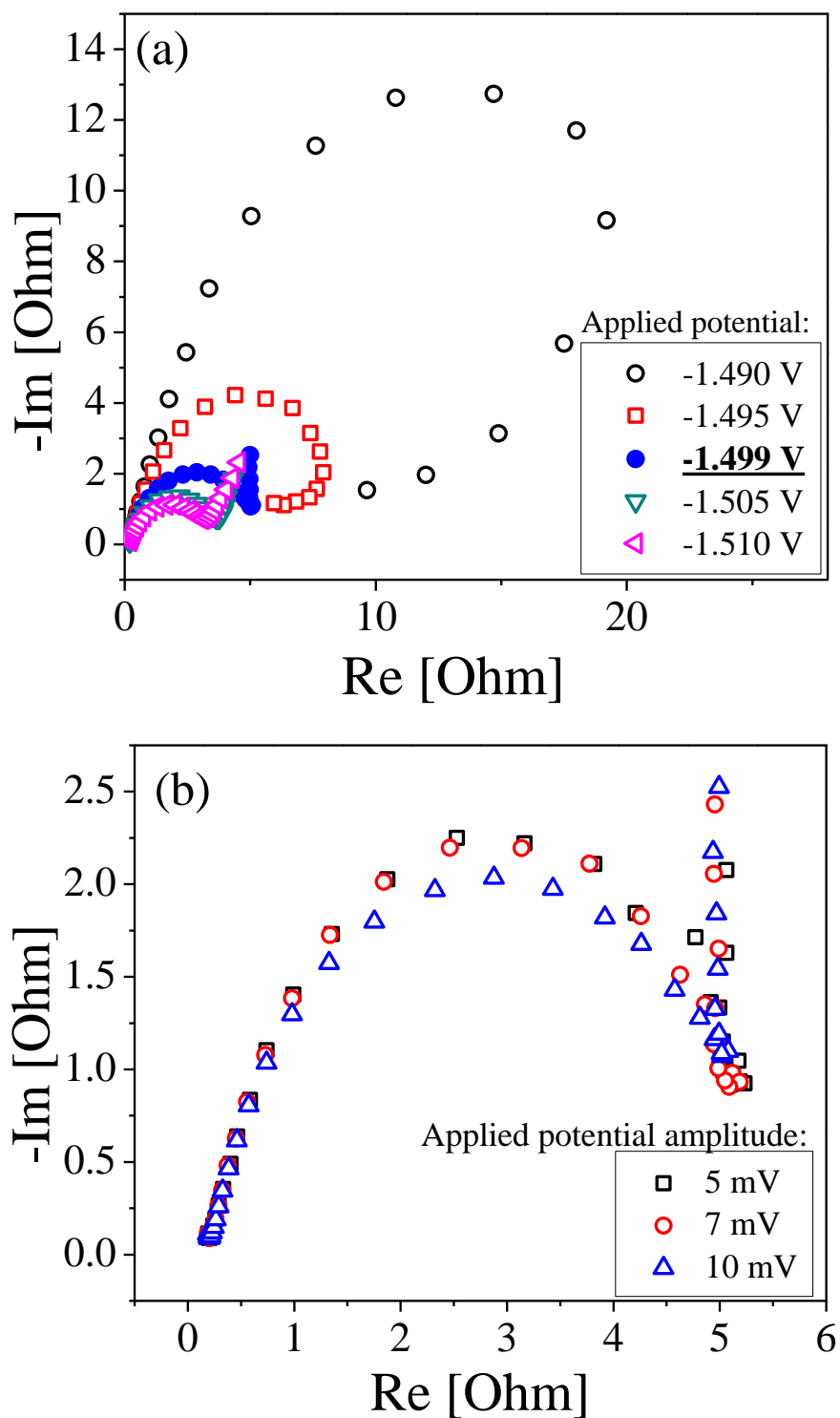


**Figure 5.13** (a) Nyquist plots measured in  $UCl_3$ -0.5 salt at 748 K. The applied potential was changed from -1.490 V to -1.510V to find the minimum overpotential. (b) Repetition with the applied potential amplitude ranging from 5 mV to 10 mV at -1.499 V.

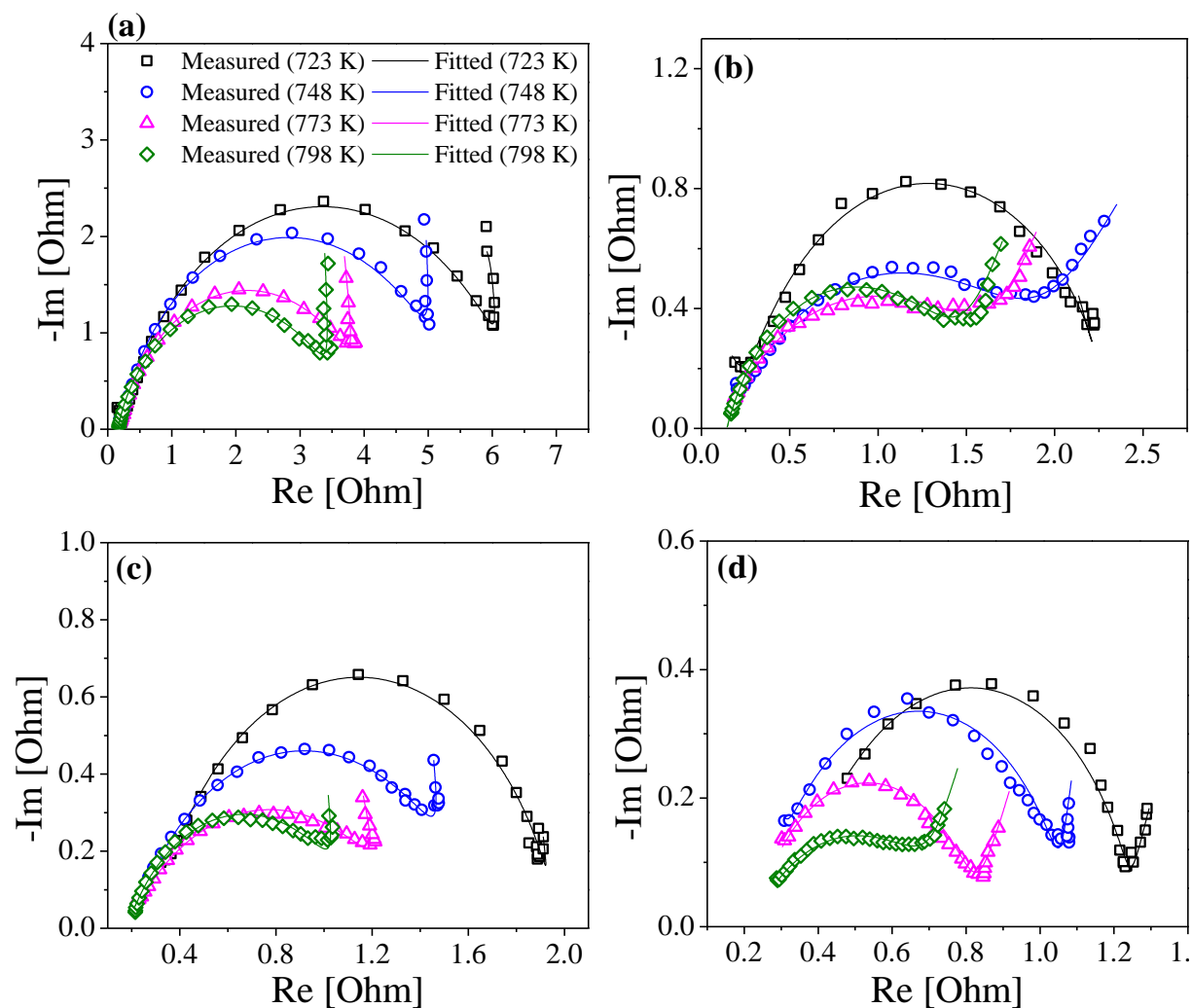


**Figure 5.14** The measured and fitted impedance spectra in the salt of (a)  $\text{UCl}_3\text{-}0.5$ , (b)  $\text{UCl}_3\text{-}1.0$ , (c)  $\text{UCl}_3\text{-}2.0$ , and (d)  $\text{UCl}_3\text{-}4.0$  at temperature ranging from 723 K to 798 K. Applied potential amplitude was 7 mV, and the chi-square goodness of fit ( $\chi^2$ ) was less than 0.003.

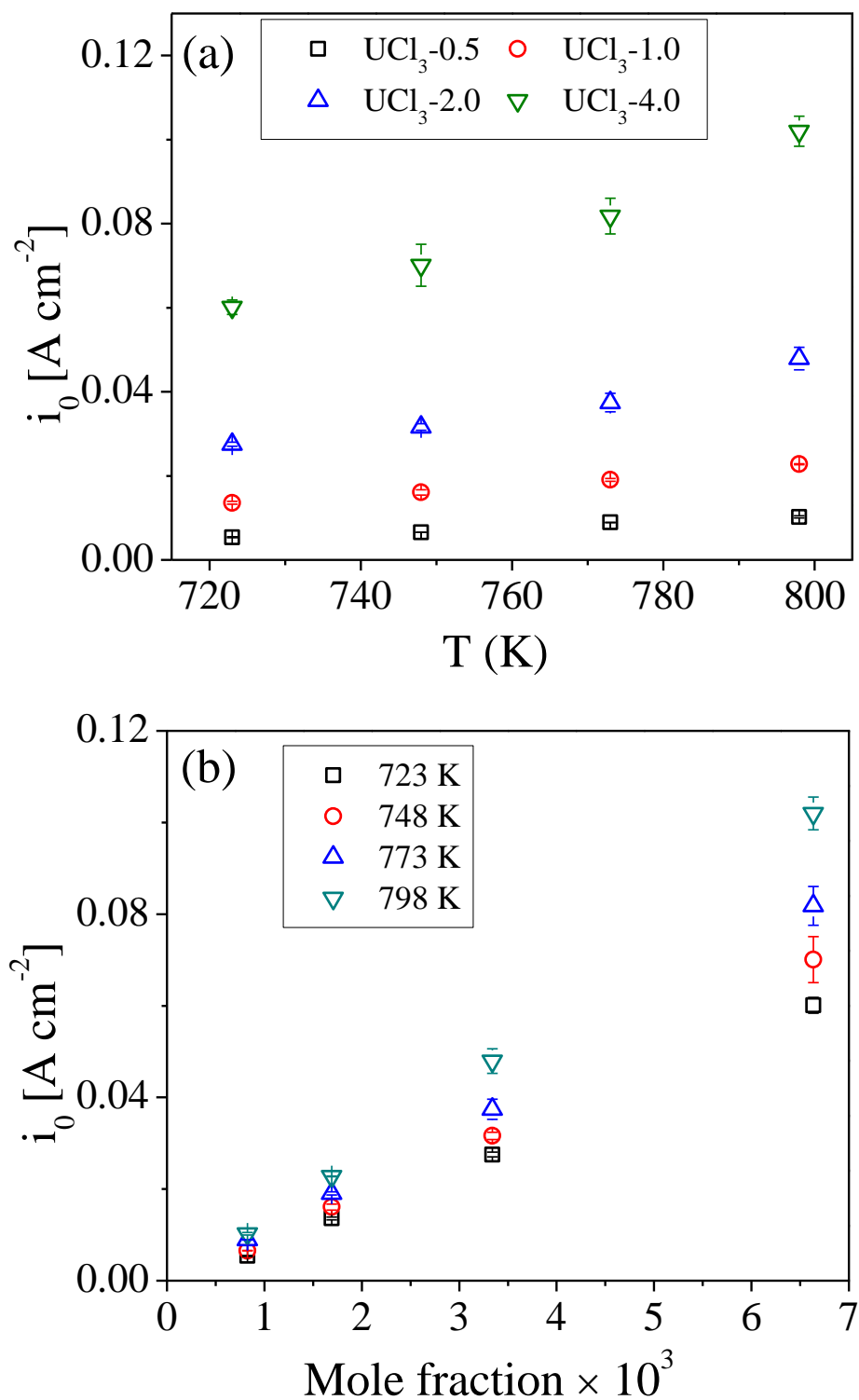


**Figure 5.15** (a) plots the  $i_0$  of  $\text{U}/\text{U}^{3+}$  against temperature for different concentrations, and (b) plots the  $i_0$  of  $\text{U}/\text{U}^{3+}$  versus mole fraction of the  $\text{UCl}_3$  under different temperatures.

**Table 5.4** Summary of  $i_0$  and  $k^0$  for  $U/U^{3+}$  reaction measured by the EIS method

		Temperature, T (K)			
		723	748	773	798
	$k^0 \times 10^3 [\text{cm s}^{-1}]$	1.048	1.230	1.454	1.827
		( $R^2 = 0.993$ )	( $R^2 = 0.993$ )	( $R^2 = 0.995$ )	( $R^2 = 0.996$ )
UCl <sub>3</sub> -0.5	$i_0 \times 10^3 [\text{A cm}^{-2}]$	$5.4 \pm 0.09$	$6.55 \pm 0.03$	$8.91 \pm 0.06$	$10.2 \pm 0.25$
UCl <sub>3</sub> -1.0		$13.6 \pm 0.32$	$16.1 \pm 0.64$	$19.0 \pm 0.35$	$22.8 \pm 0.09$
UCl <sub>3</sub> -2.0		$27.5 \pm 0.5$	$31.6 \pm 0.77$	$37.4 \pm 2.2$	$47.9 \pm 2.7$
UCl <sub>3</sub> -4.0		$60.1 \pm 1.7$	$70.1 \pm 5.0$	$81.8 \pm 4.2$	$102 \pm 3.6$

### 5.4.3.2 LP and Tafel methods

For both LP and Tafel measurements, the potential was swept from -350 mV to 250 mV based on the equilibrium potentials. Figure 5.16(a) shows an example of current-potential curve in UCl<sub>3</sub>-0.5 salt. The slopes were obtained in the overpotential ranging from -5 mV to 5mV at the different temperatures, which were employed to calculate  $i_0$  of  $U/U^{3+}$ . As Eq. (2-26) is valid with no diffusion effect; thus, very slow scan rate should be applied for the proper exploration of the charge transfer kinetics. However, at extremely slow scan rates ( $< 3 \text{ mV s}^{-1}$ ), the electrode surface area continuously increases due to the deposition of U metals on the electrode. Therefore, LP method was examined with the different scan rates ranging  $3 \text{ mV s}^{-1}$  to  $100 \text{ mV s}^{-1}$ . Figure 5.16(b) illustrates Tafel curves in UCl<sub>3</sub>-0.5 salt at the same temperature range. Here, the linear Tafel regions can be observed at the overpotential from -100 mV to -230 mV, which were fitted to measure the value of  $i_0$ . Unfortunately, the linear Tafel region cannot be acquired at the concentration higher than 1 wt% UCl<sub>3</sub> as shown in Figure 5.16(c). This issue is mainly owing to

the vigorous U deposition with the high bulk concentrations. Therefore, Tafel plot method was only applied with the scan rates of  $3 \text{ mV s}^{-1}$ ,  $5 \text{ mV s}^{-1}$ , and  $7 \text{ mV s}^{-1}$  in  $\text{UCl}_3$ -0.5 salt for determining the  $i_0$  of  $\text{U}/\text{U}^{3+}$  pair.

Figure 5.17 shows the measured values of  $i_0$  by LP method with different scan rates. For  $\text{UCl}_3$ -0.5 and  $\text{UCl}_3$ -1.0 (Figures 5.17(a) and 5.17(b), respectively), the  $i_0$  values rapidly decrease when the scan rates increase from  $3 \text{ mV s}^{-1}$  to  $15 \text{ mV s}^{-1}$  while they increase sharply at the scan rate faster than  $20 \text{ mV s}^{-1}$ . This result signifies that the diffusion limits caused by an increase in the scan rate can dominantly affect the kinetic measurements. In contrary, steady decreases can be observed with increasing the scan rate in  $\text{UCl}_3$ -2.0 and  $\text{UCl}_3$ -4.0 salts as shown in Figures 5.17(c) and 5.17(d), respectively. The latter results indicate that the variation of the electrode surface area may contribute an effect on the resulting  $i_0$  due to the U deposition. Therefore, having these challenges, the measured  $i_0$  values appear dispersed with varying scan rates. Figure 5.18(a) shows all measured  $i_0$  values from LP and Tafel methods. In general, the  $i_0$  values of  $\text{U}/\text{U}^{3+}$  follow the linear relationship with temperature. While the relative errors from the averaged  $i_0$  were less than 10% in both  $\text{UCl}_3$ -0.5 and  $\text{UCl}_3$ -1.0, these errors rose up to 24% in  $\text{UCl}_3$ -4.0 salt due to the aforementioned challenges. The effect of the change on surface area becomes problematic on the LP and Tafel measurements. Tafel curves were measured in  $\text{UCl}_3$ -0.5 salt, and the  $i_0$  calculated from y-intercept was varying for the scan rates of  $3 \text{ mV s}^{-1}$  to  $7 \text{ mV s}^{-1}$  (see Figure 5.18(b)). Tafel results also show a linear trend with the temperature and agree with the LP result within 20% of relative error range.

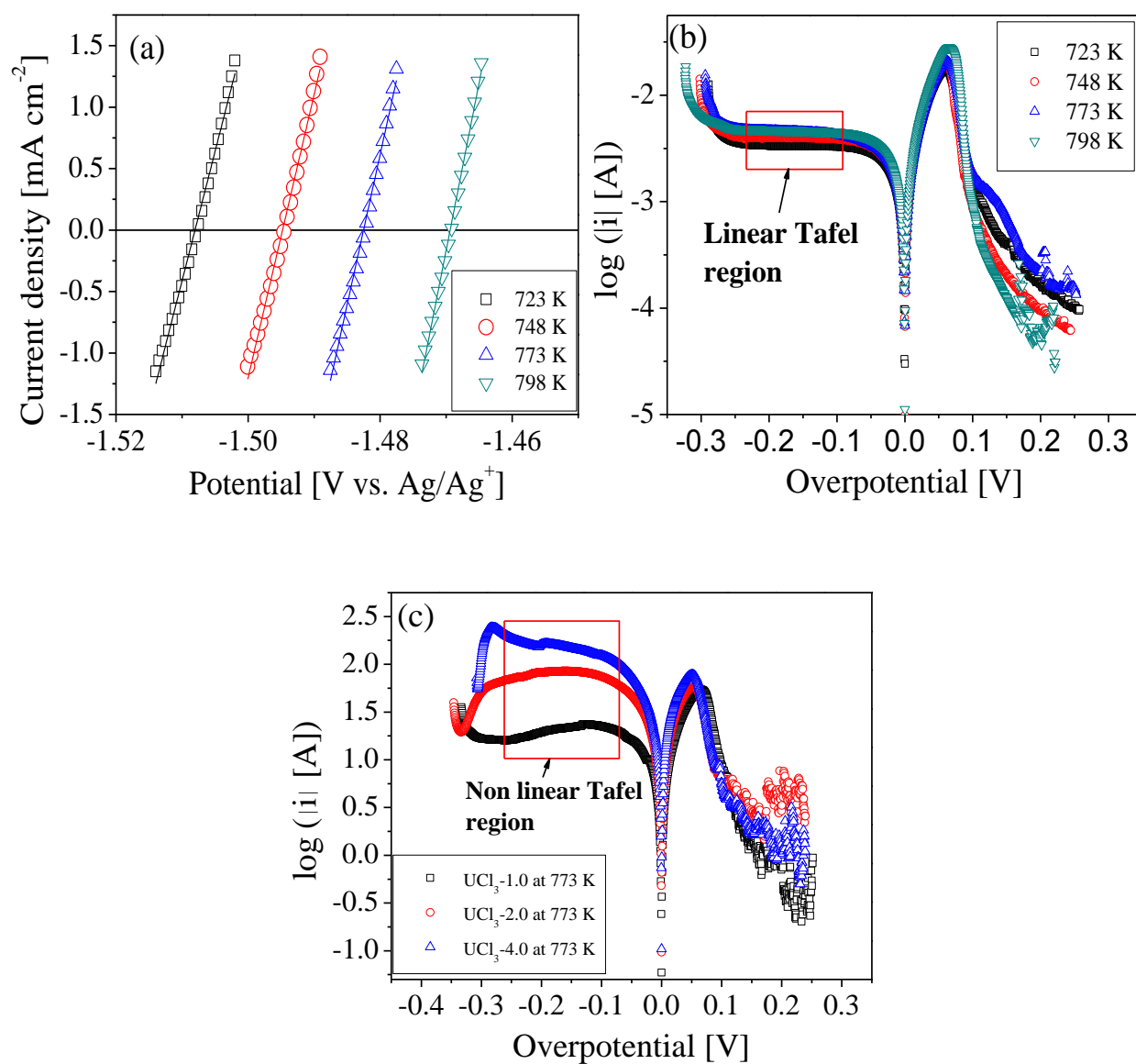


**Figure 5.16** (a) Current density versus potential at small overpotential region ( $< 5$  mV) in  $\text{UCl}_3$ -0.5 salt; (b) Plot of  $\log(i_0)$  versus overpotential in  $\text{UCl}_3$ -0.5 salt; and (c) Plot of  $\log(i_0)$  versus overpotential in  $\text{UCl}_3$ -1.0,  $\text{UCl}_3$ -2.0, and  $\text{UCl}_3$ -4.0 at 748 K. The scan rate was used at  $5 \text{ mV s}^{-1}$ .

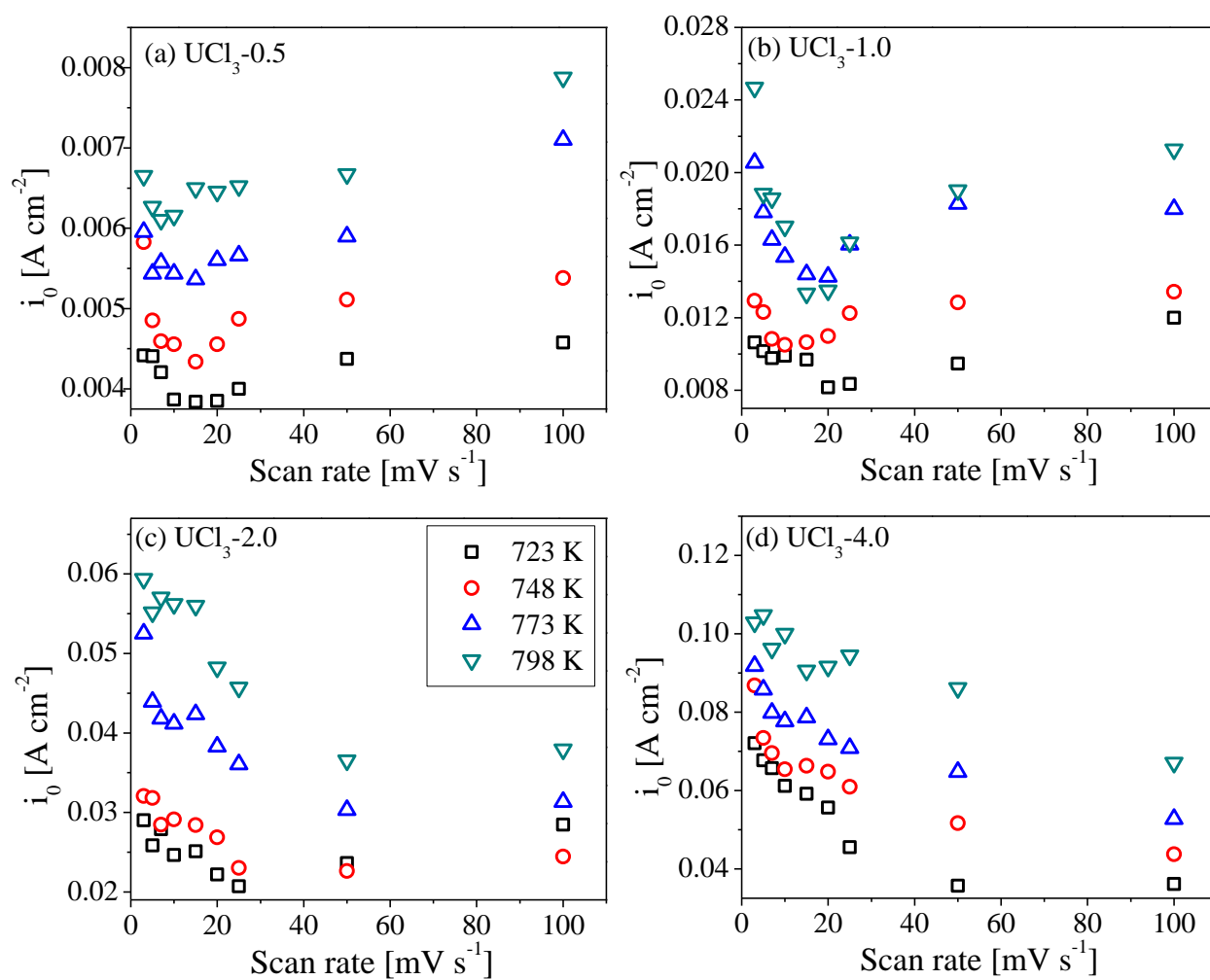


**Figure 5.17** Plots of  $i_0$  results measured by LP methods under different scan rates for (a) UCl<sub>3</sub>-0.5, (b) UCl<sub>3</sub>-1.0, (c) UCl<sub>3</sub>-2.0, and (d) UCl<sub>3</sub>-4.0.



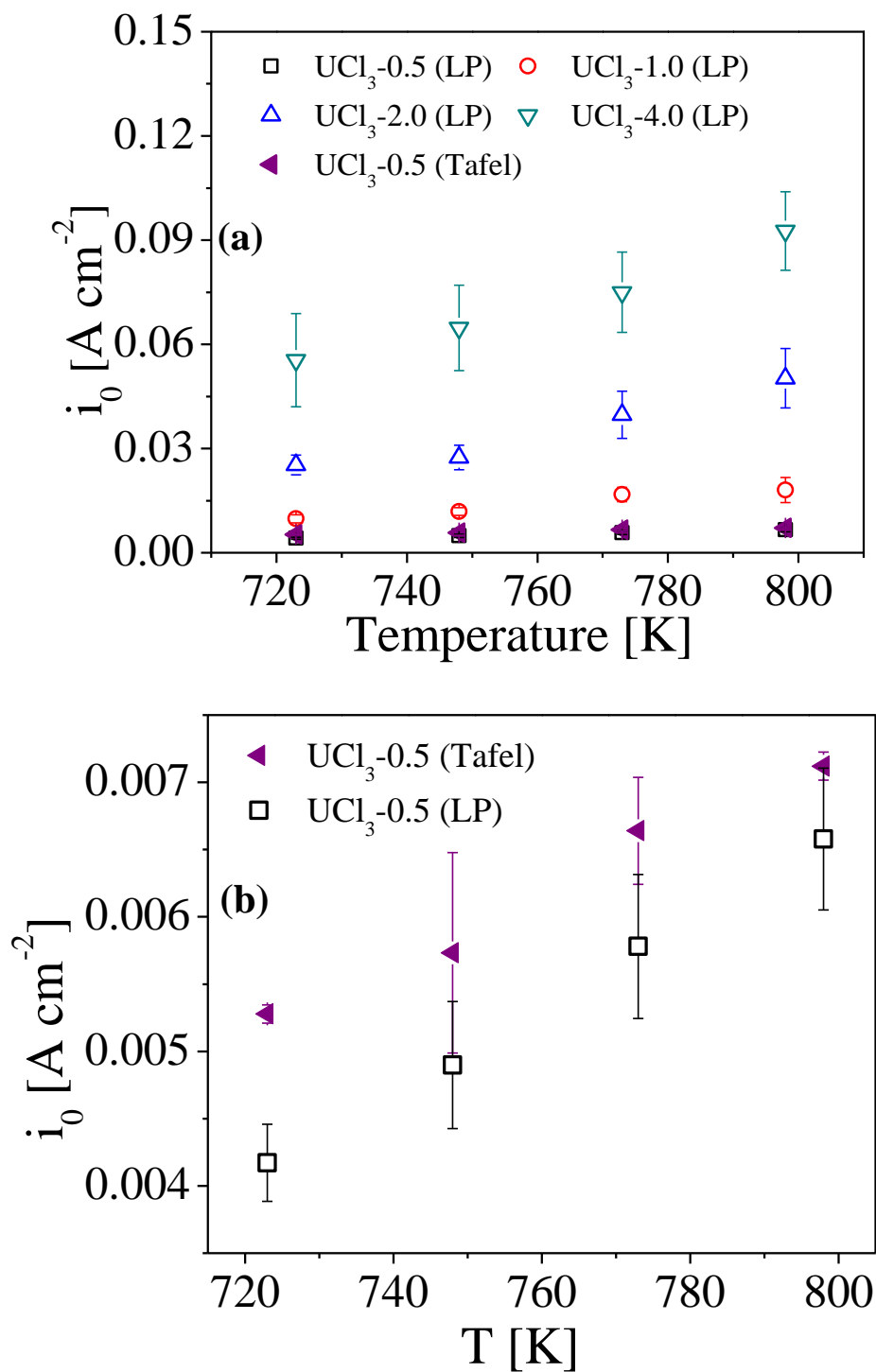


**Figure 5.18** (a) Plots of  $i_0$  values measured by LP and Tafel methods for concentrations of 0.5 wt%, 1.0 wt%, 2.0 wt%, and 4.0 wt% and (b) magnifying scale for the comparison of  $i_0$  values between LP and Tafel methods at 0.5 wt%  $\text{UCl}_3$ .

### 5.4.3.3 Cyclic voltammetry (CV)

CV is powerful and the most widely practiced among the electrochemical methods [52]. The CV method is analogous to the LP measurement because CV observes current based on the potential change. Only difference from the LP method is that CV is a reversal method executed by higher scan rates. As mentioned in Section 5.4.3.2, the results from LP method show the agreement within 24% relative error range under the different scan rates (from  $3 \text{ mV s}^{-1}$  to  $100 \text{ mV s}^{-1}$ ). Therefore, CV curves at the scan rate of  $50 \text{ mV s}^{-1}$  and  $100 \text{ mV s}^{-1}$  was used, and the charge transfer resistance in very small overpotential region was obtained to estimate the values of  $i_0$  for  $\text{U}/\text{U}^{3+}$ . It should be mentioned that this selected scan rate is not considered fast in the CV application; however, this method was explored in order to compare with LP method and assess the applicability for the estimation of  $i_0$ . Figure 5.19 shows an example procedure on a CV curve in  $\text{UCl}_3\text{-0.5}$  salt at 748 K. The potential where the deposited U starts to be oxidized (indicated by red circle in Figure 5.19 (a)) can be found, and the slope from current-potential curve within 10 mV overpotential can be measured as described in Figure 5.19(b), which is the charge transfer resistance. Then, the value of  $i_0$  for  $\text{U}/\text{U}^{3+}$  reaction would be calculated by using Eq. (2-28). Figure 5.20 reveals that the value increases when both the concentration and temperature increase; however, it was difficult to observe the linearity from these results. The advantage of the CV method is the rapid data acquisition through an instant scan rate; hence, this technique would be useful in development of the near-real time technique for the material detection and accountability in the ER system.

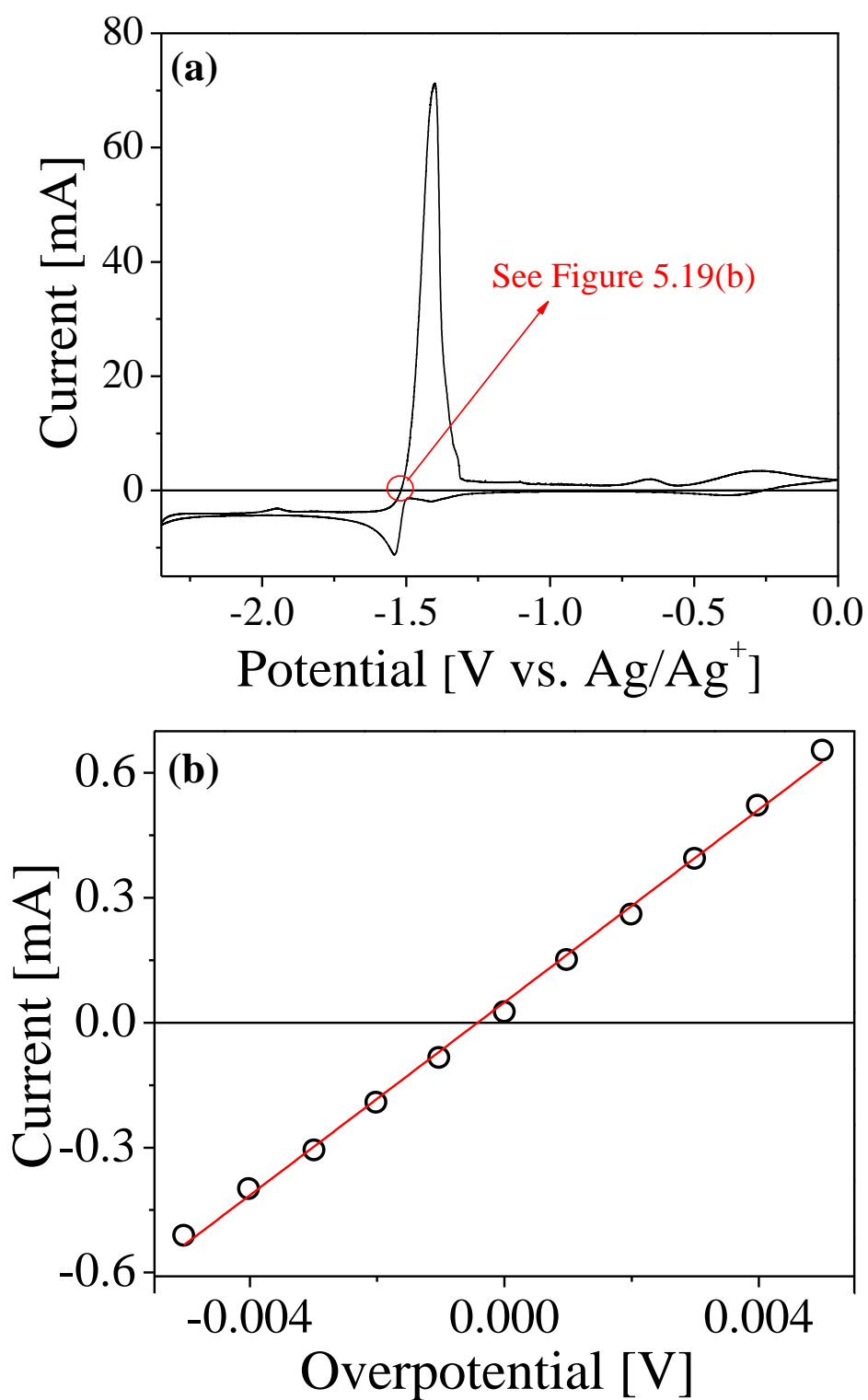


**Figure 5.19** (a) Cyclic voltammogram at the scan rate of  $50 \text{ mV s}^{-1}$  in  $\text{UCl}_3\text{-}0.5$  salt at  $748 \text{ K}$ , and (b) the magnifying scale of the small overpotential region (from (a)) for measuring the charge transfer resistance from the slope.

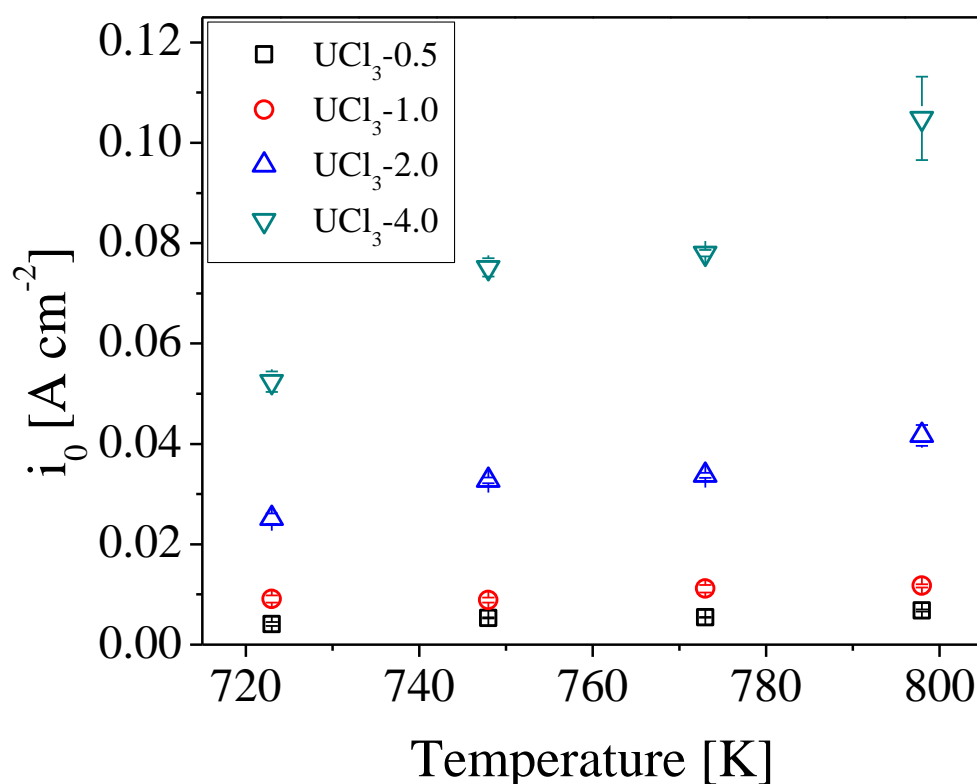


**Figure 5.20** Plots of  $i_0$  by using CV method for  $U/U^{3+}$  in  $UCl_3$ -0.5,  $UCl_3$ -1.0,  $UCl_3$ -2.0, and  $UCl_3$ -4.0 salt at the different temperatures with the standard deviations.

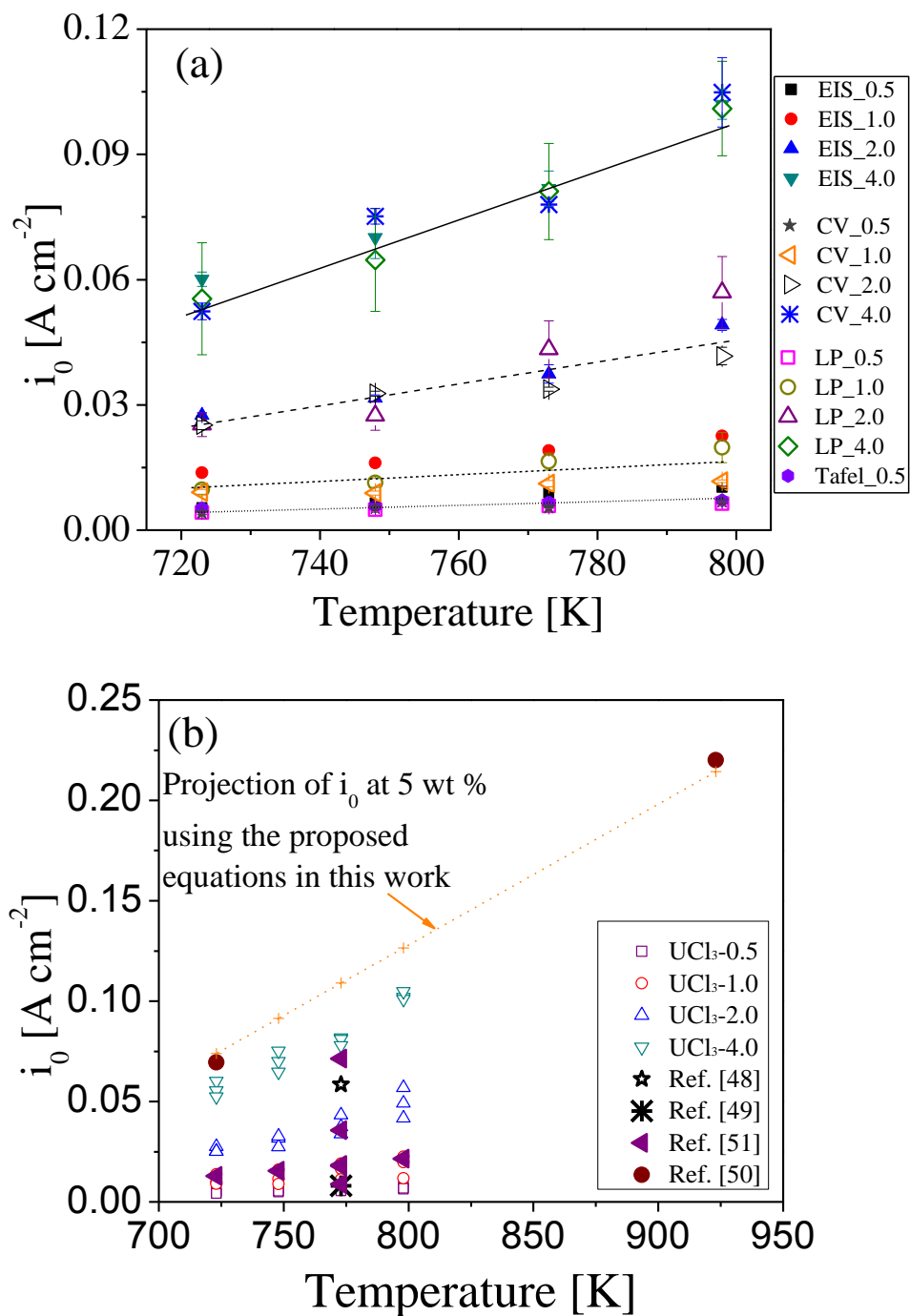
#### 5.4.3.4 Data comparison and practical analysis

Figure 5.21(a) shows the results from the four techniques being explored. The  $i_0$  values from EIS measurements show the most linear trends regarding to the concentration and temperature whereas the values measured by CV method are much scattered and do not have a strong linear correlation with the concentration and temperature. Overall, the results from the four methods are in a moderate agreement within 33% relative difference from their average values. Figure 5.21(b) shows  $i_0$  results from this work in comparison to the reported  $i_0$  values. Lim et al.

[51] provided the equations of the  $i_0$  as a function of the concentration and temperature. By plotting the equations from the literature, the results reside within the range of  $i_0$  from this study. Particularly, EIS measurements for 1 wt%  $\text{UCl}_3$  in the present study agree moderately well with those from Lim and co-workers [51]. However, LP results in this study are significantly influenced by the scan rate, which repudates the conclusion from the study of Lim et al. [51] that the scan rate ( $5 \text{ mV s}^{-1}$  -  $100 \text{ mV s}^{-1}$ ) has no significant effect on the  $i_0$  value. Choi et al. [48] measured  $i_0$  of  $\text{U/U}^{3+}$  at ~3.3 wt% concentration at 773 K and reported that the  $i_0$  value measured with a tungsten electrode was  $0.0584 \text{ A cm}^{-2}$  which located in the vicinity of  $i_0$  measured in this study.

Because the EIS method provides the most linear trends and agreements with other literature data, the results from EIS measurements have been selected for further analysis without considering the deviations (error bars) of the data. The linear relationships of  $i_0$  in Figures 5.15(a) and 5.15(b) were modeled by using a linear equation,  $y = ax + b$  (these fitted values are summarized in Table 5.5). Here, the equations in Table 5.5 can be used to determine any desired  $i_0$ . These equations were being extrapolated to estimate the  $i_0$  of  $\text{U/U}^{3+}$  at the 5 wt% concentration under 723 K and 923 K reported by Rose and co-workers [50]. The resulting calculations reveal that the values of the  $i_0$  are  $0.0739 \text{ A cm}^{-2}$  ( $C = 5 \text{ wt\%}$  (0.00848 mole fraction) and  $T = 723 \text{ K}$ ) and  $0.214 \text{ A cm}^{-2}$  ( $C = 5 \text{ wt\%}$  (0.00848 mole fraction) and  $T = 923 \text{ K}$ ) agreeing well with the values of  $i_0$  reported by Rose et al. [50]. The projection for  $i_0$  value at 5 wt%  $\text{UCl}_3$  can be checked in Figure 5.21(b) (see a line of orange dot). Although literature  $i_0$  values were being measured under different electrochemical scales and cell configurations, the results are in a good agreement (see Figure 5.21(b)). Thus, it can be postulated that the effect of system scale and configuration has a weak influence on the  $i_0$  kinetics. In order to confirm this argument, a large number of data collections will be required in different electrochemical environments. Also, the  $i_0$  value reported by Ghosh

et al. [49] does not follow the general trends of this work. This discrepancy may be coming from their study on the anodic dissolution by using a uranium rod as an anode.



**Figure 5.21** (a) The  $i_0$  values measured by the four different methods in the present study, and (b) the reported values of  $i_0$  for  $\text{U}/\text{U}^{3+}$  from different literature studies are being superimposed.

**Table 5.5** Linear models for concentration (mole fraction) and temperature (K) dependence

		Equations	R <sup>2</sup>
Temperature (T) dependence of $i_0$	UCl <sub>3</sub> -0.5:	$6.752 \times 10^{-5} T - 0.0436$	0.973
	UCl <sub>3</sub> -1.0:	$1.221 \times 10^{-4} T - 0.0750$	0.987
	UCl <sub>3</sub> -2.0:	$2.682 \times 10^{-4} T - 0.1678$	0.932
	UCl <sub>3</sub> -4.0:	$5.494 \times 10^{-4} T - 0.3393$	0.956
Concentration (C)* relationship of $i_0$	723 K:	8.823 C	0.993
	748 K:	10.274 C	0.993
	773 K:	12.047 C	0.995
	798 K:	15.012 C	0.996

Based on the EIS data sets, additional temperature and concentration dependence were further investigated. Here, the temperature relationship of kinetic parameters can typically be expressed by Arrhenius equation (as discussed in Section 4.1.3.2)  $i_0 = I_0 \exp(-E_a/RT)$ . Figure 5.22 shows  $\ln(i_0)$  versus  $1/T$  for all concentrations where the slopes and y-intercepts can be used to tabulate  $I_0$  and  $E_a$ , respectively; the calculated values are being summarized in Table 5.6. The dimensionless relationship between  $i_0/I_0$  and  $\exp(-E_a/RT)$  can be plotted (see Figure 5.23(a)); therefore, the  $i_0$  can be easily estimated when  $I_0$  and  $-E_a$  are known. Furthermore, the concentration dependency of  $i_0$  are being explored in Figure 5.23(b). The dimensionless quantity of  $i_0/i_{0, \max}$  were plotted against mole fraction. Here,  $i_{0, \max}$  is the  $i_0$  value at 4 wt% UCl<sub>3</sub> which can be found in Table 5.6. Thus,  $i_0$  quantity can be estimated by simply knowing  $i_{0, \max}$  at 4 wt% UCl<sub>3</sub> reported in the

present study. The equations for the dimensionless relationships ( $i_0/I_0=1.0046 \exp(-E_a/RT)$  and  $i_0/i_{0, \max}=155.2 \times$ ) in Figures 5.23(a) and 5.23(b) are shown in each figure, respectively. The concentration is valid from 0.00083 to 0.00664 in mole fraction. The fitted equation of  $i_0/I_0=1.0046 \exp(-E_a/RT) \approx \exp(-E_a/RT)$  with the  $R^2$  of 0.997 confirms the Arrhenius behaviors within the system. Overall, these correlations can be used at the concentration less than 4 wt% of  $\text{UCl}_3$  in LiCl-KCl eutectic salt.

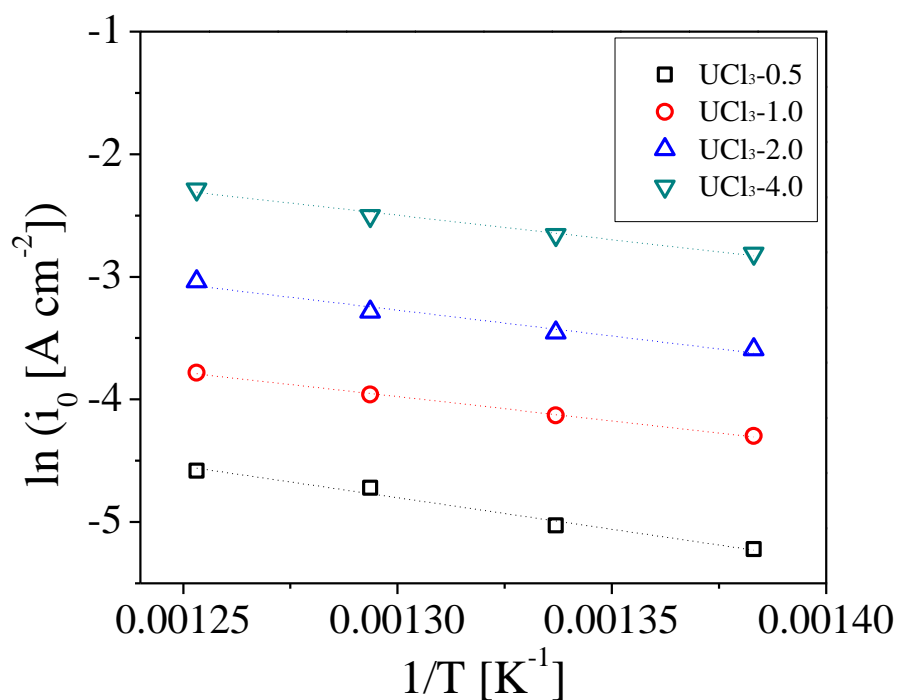


**Figure 5.22** Natural logarithm of  $i_0$  against the inverse temperature.



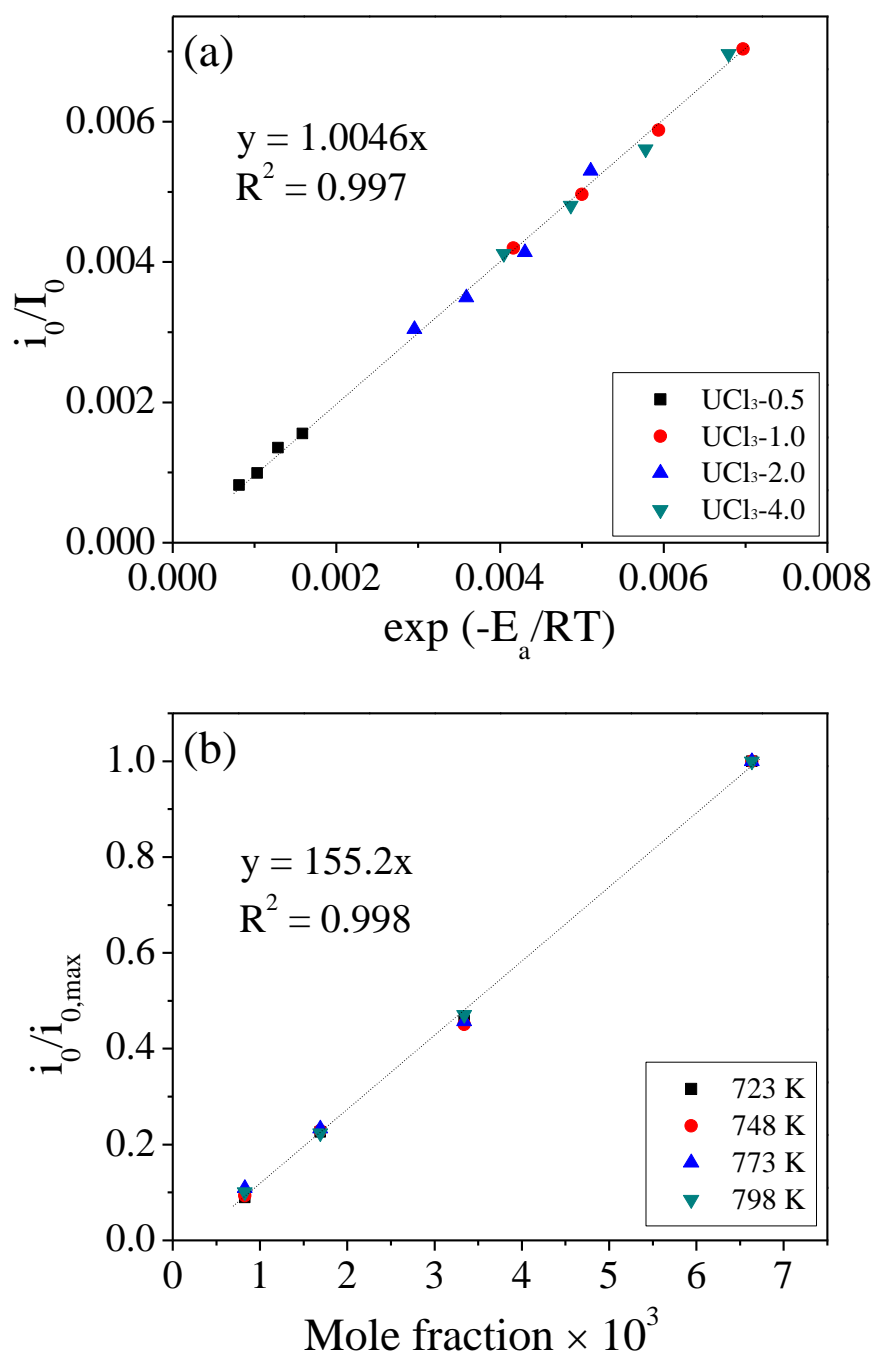


**Figure 5.23** (a)  $i_0/I_0$  versus  $\exp(-E_a/RT)$ , and (b)  $i_0/i_{0,max}$  versus mole fraction.

**Table 5.6** The pre-exponential factors and activation energies for  $U/U^{3+}$  based on the data from EIS measurements

UCl <sub>3</sub> -0.5		UCl <sub>3</sub> -1.0		UCl <sub>3</sub> -2.0		UCl <sub>3</sub> -4.0	
I <sub>0</sub>	E <sub>a</sub>	I <sub>0</sub>	E <sub>a</sub>	I <sub>0</sub>	E <sub>a</sub>	I <sub>0</sub>	E <sub>a</sub>
[A cm <sup>-2</sup> ]	[kJ mol <sup>-1</sup> ]	[A cm <sup>-2</sup> ]	[kJ mol <sup>-1</sup> ]	[A cm <sup>-2</sup> ]	[kJ mol <sup>-1</sup> ]	[A cm <sup>-2</sup> ]	[kJ mol <sup>-1</sup> ]
6.5883	-42.468	3.2368	-32.948	9.0449	-35.011	14.595	-33.119

### 5.3.5 Effects of GdCl<sub>3</sub> on U properties

The effects of GdCl<sub>3</sub> on UCl<sub>3</sub> behaviors were explored at 773 K by adding certain amounts of GdCl<sub>3</sub> into LiCl-KCl-UCl<sub>3</sub> salt (Sample No. 5 – 10 in Table 5.1). The concentration ratio of UCl<sub>3</sub>/GdCl<sub>3</sub> varies from 1 to 4 through the samples. For measuring the diffusion coefficients, equilibrium potentials, and exchange current densities in the salt samples, the same procedures and data analyses were used. Figure 5.24 shows the measured CV data in LiCl-KCl-1wt% UCl<sub>3</sub> - 1 wt% GdCl<sub>3</sub> at scan rate ranging from 50 mV s<sup>-1</sup> to 200 mV s<sup>-1</sup>. Redox peaks for Gd<sup>3+</sup>/Gd couple (IV<sub>c</sub> and IV<sub>a</sub>, respectively) were observed at potentials more negative than U<sup>3+</sup>/U redox peaks; therefore, it can be considered that the U<sup>3+</sup>/U reaction occurs independently whereas Gd<sup>3+</sup>/Gd reaction is happening along with U deposition on the electrode. Since peaks of P<sub>3c</sub> stays at the same potential even with addition of GdCl<sub>3</sub>, Eq. (2-13) was utilized to determine the diffusion coefficient of UCl<sub>3</sub> in the salt mixtures. Figure 5.25 shows the diffusion coefficients of UCl<sub>3</sub> measured in Sample 5 – 10 along with the results reported in Section 5.3.1 at 773 K. By adding GdCl<sub>3</sub> to the LiCl-KCl-UCl<sub>3</sub> system, the diffusion coefficient of UCl<sub>3</sub> becomes smaller by  $0.2 \times 10^{-5} \sim 0.3 \times 10^{-5} \text{ cm}^2 \text{ s}^{-1}$ . The values decreases slightly with increasing concentrations of UCl<sub>3</sub> and GdCl<sub>3</sub>, but UCl<sub>3</sub>-GdCl<sub>3</sub> mixtures need to be examined at concentrations higher than 4 wt%. At lower concentration of UCl<sub>3</sub>

(Sample No. 5),  $\text{GdCl}_3$  co-existence significantly affects the diffusion behavior of  $\text{UCl}_3$ , which reveals that diffusivity of  $\text{UCl}_3$  in ER system may be considerably affected by the concentration of other elements (e.g. actinide and lanthanide elements). However, further studies need to be done with different elements and multi-elements in order to understand the evidence of decreasing diffusivity. This may be affected by the physical and chemical interactions among the particles.

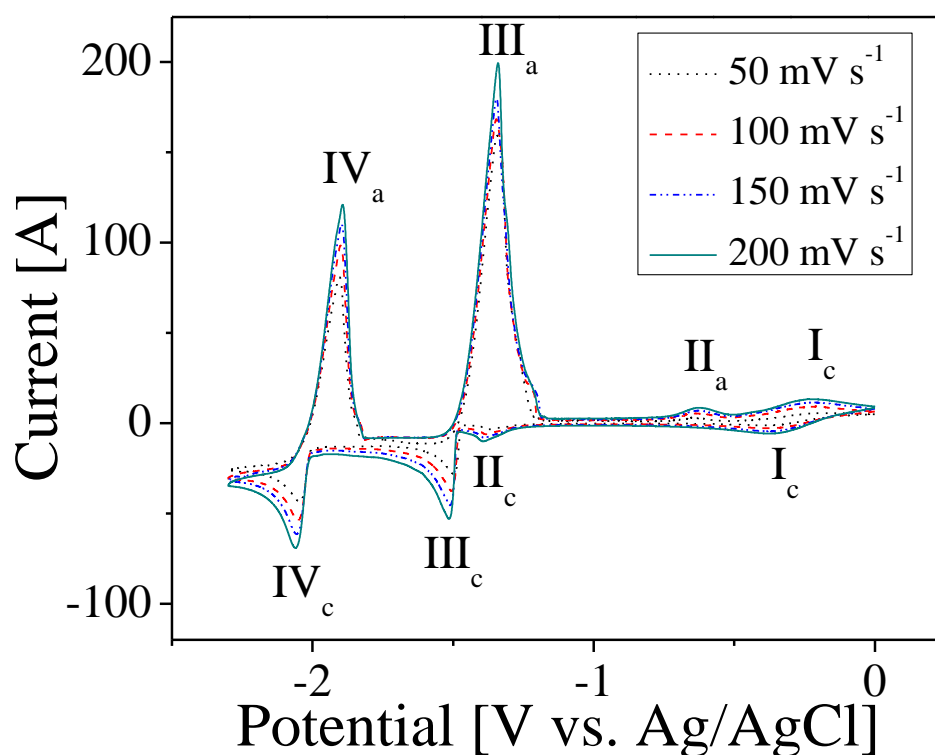


**Figure 5.24** Cyclicvoltammogram in  $\text{LiCl-KCl-1wt\% UCl}_3\text{-1wt\% GdCl}_3$  at 773 K, measured at scan rate from  $50 \text{ mV s}^{-1}$  to  $200 \text{ mV s}^{-1}$ .

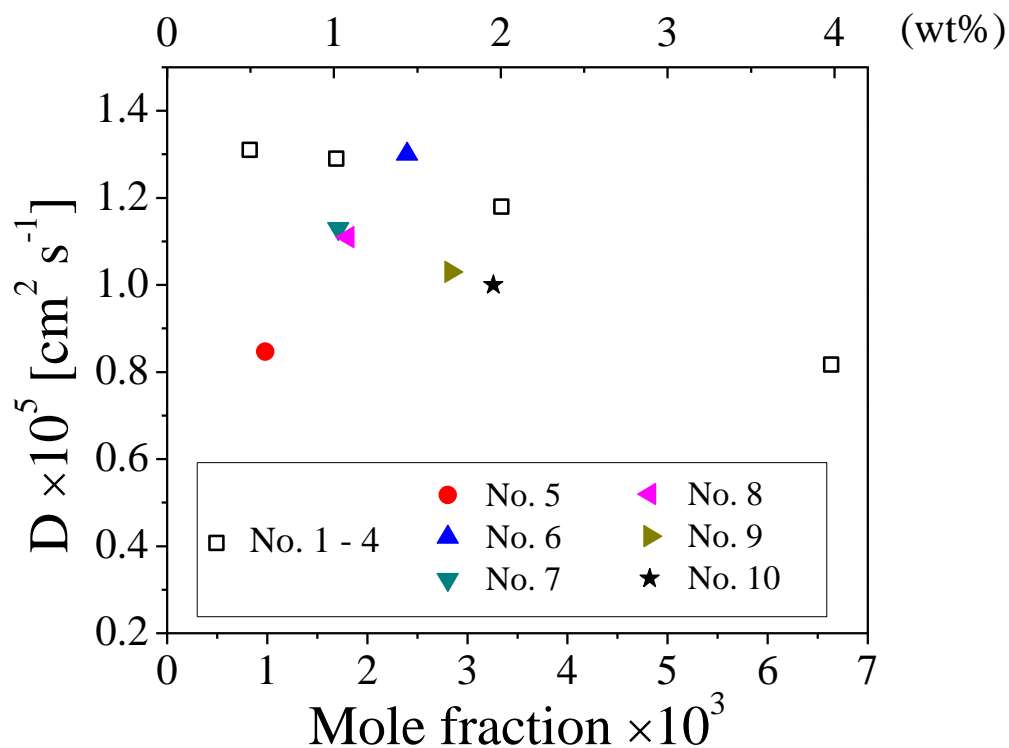


**Figure 5.25** Plots of diffusion coefficients measured in LiCl-KCl-UCl<sub>3</sub>-GdCl<sub>3</sub> mixtures (No. 5 – 10), which were compared with original data sets (Section 5.3.1) at 773 K.

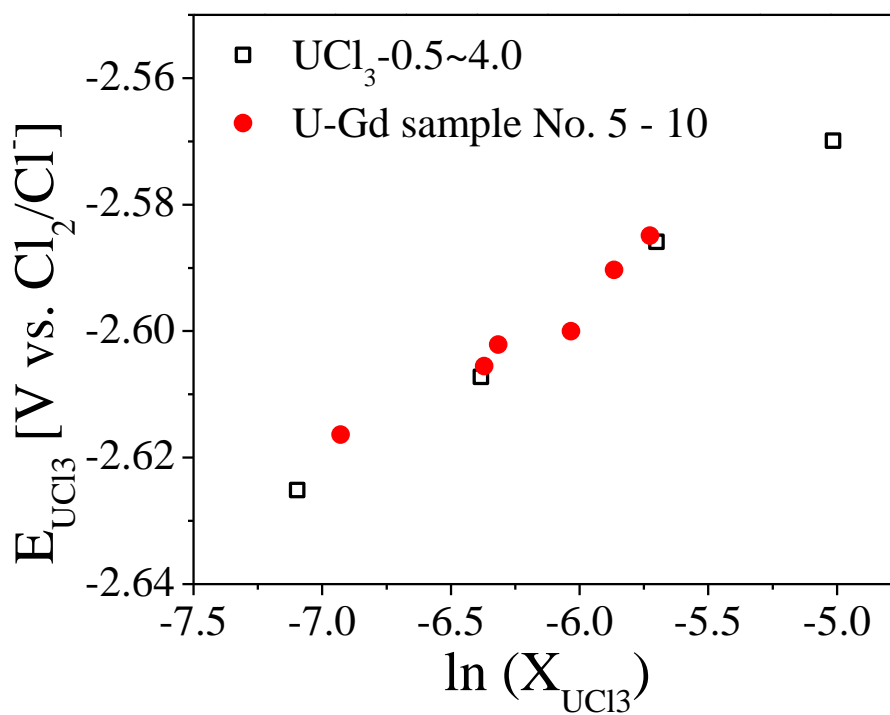


**Figure 5.26** The equilibrium potentials of U<sup>3+</sup>/U measured with presence of GdCl<sub>3</sub>, which were superimposed in the original trend of the equilibrium potential at 773 K.

Figure 5.26 shows the equilibrium potentials as function of concentration in Sample No. 5 – 10 at 773 K which are superimposed on the pure  $\text{UCl}_3$  data as seen in Section 3.1.2. The resulting values follow the linear dependence line within 0.2% relative difference. This indicates that the results of  $E_{\text{U}^{3+}/\text{U}}^{0*}$  and  $\gamma_{\text{U}^{3+}}$  also show good agreement with the original data with pure  $\text{UCl}_3$ ; therefore, it could be believed that thermodynamic properties of  $\text{UCl}_3$  is scarcely dependent on the presence of  $\text{GdCl}_3$  in  $\text{LiCl-KCl-UCl}_3$  salt system. The calculations of  $E_{\text{U}^{3+}/\text{U}}^{0*}$  and  $\gamma_{\text{U}^{3+}}$  are summarized in Table 5.7, and showing good consensus with the data sets measured with pure  $\text{UCl}_3$  salts (reported in Table 5.3). Furthermore, the exchange current densities of  $\text{U}^{3+}/\text{U}$  were measured with the  $\text{GdCl}_3$  additions and the resulting data are plotted in Figure 5.27. The values are laid along with the linear model, indicating that the kinetic parameters of  $\text{U}^{3+}/\text{U}$  are also independent on  $\text{GdCl}_3$ . The resulting data and trends from the experiments with the mixture salts provide a useful insight into behaviors of U such as electrochemical, thermodynamic, and kinetic behaviors with  $\text{GdCl}_3$  existence in  $\text{LiCl-KCl}$ ; however, further experimental database should be accumulated to understand U behavior among the various fission products which is occurring in real ER system. Unfortunately, the thermodynamic and kinetic properties of U in multi-components have not been explored in previous publications.

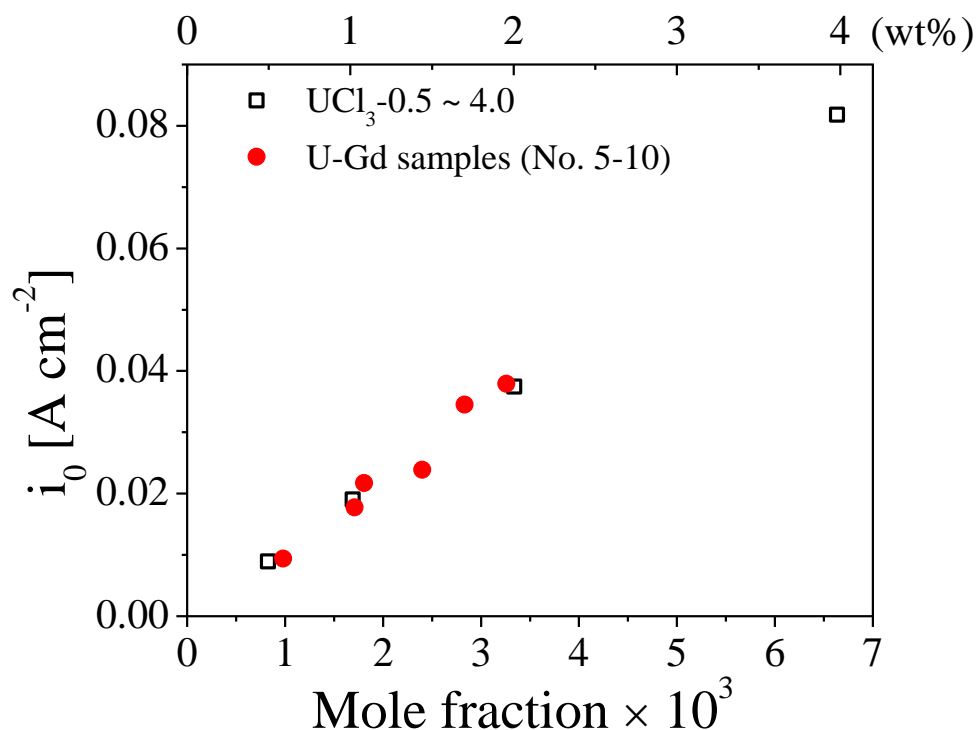


**Figure 5.27** The exchange current densities measured in U-Gd samples, compared with the values measured with pure UCl<sub>3</sub> salts at 773 K.

## 5.4 Summary

The properties of U were investigated via various electrochemical techniques at different UCl<sub>3</sub> concentrations and temperatures. This chapter starts with evaluating the diffusion coefficients of UCl<sub>3</sub>, which were done by using CV technique. Although the reversible equation was used to calculate the values, the irreversible equation was also employed to develop a measurement method at high concentrations. However, the equation will need to be revised for the soluble-insoluble system. The equilibrium potentials of U<sup>3+</sup>/U couple were measured using OCP, indicating that it shows a linear trend within 2 wt% UCl<sub>3</sub> concentration while the values reach to certain level at concentrations higher than 4 wt% UCl<sub>3</sub>. From the measured equilibrium potential,

**Table 5.7** Thermodynamic properties of  $\text{UCl}_3$  in  $\text{LiCl-KCl-UCl}_3\text{-GdCl}_3$  mixture salts

No	Sample	$E_{\text{U}^{3+}/\text{U}}^{0*}$	$\Delta G_{\text{UCl}_3}^{0*}$	$\gamma_{\text{U}^{3+}}$
		(V vs. $\text{Cl}_2/\text{Cl}$ )	( $\text{kJ mol}^{-1}$ )	$\times 10^3$
5	U0.5_Gd0.5	-2.46	-712.8	5.64
		$\pm 6.0 \times 10^{-3}$	$\pm 17.4$	$\pm 1.53 \times 10^{-1}$
6	U1.0_Gd0.25	-2.46	-713.2	5.26
		$\pm 4.2 \times 10^{-4}$	$\pm 1.2$	$\pm 9.8 \times 10^{-2}$
7	U1.0_Gd0.5	-2.47	-713.8	4.80
		$\pm 4.5 \times 10^{-5}$	$\pm 1.3$	$\pm 9.7 \times 10^{-3}$
8	U1.0_Gd1.0	-2.46	-712.6	5.80
		$\pm 4.0 \times 10^{-4}$	$\pm 11.6$	$\pm 1.1 \times 10^{-1}$
9	U2.0_Gd1.0	-2.46	-712.1	6.30
		$\pm 2.7 \times 10^{-4}$	$\pm 7.6$	$\pm 7.5 \times 10^{-2}$
10	U2.0_Gd2.0	-2.46	-711.4	6.98
		$\pm 1.2 \times 10^{-4}$	$\pm 3.5$	$\pm 3.8 \times 10^{-2}$

the apparent standard potentials of  $\text{U}^{3+}/\text{U}$  were determined, which were used for further calculations of thermodynamic properties of  $\text{UCl}_3$ . The partial molar Gibbs free energies were calculated at the different temperatures, and activity coefficients of  $\text{UCl}_3$  in  $\text{LiCl-KCl}$  were evaluated with the consideration of super cooled liquid state as an ideal salt state. Next, the exchange current densities of  $\text{U}^{3+}/\text{U}$  couple were focused by using four different techniques such as EIS, LP, Tafel, and CV methods. In general, the measured data sets via the four methods agree within 33% relative error range. The EIS method provided the most reproducible results which are

linearly dependent on the concentration and temperature. LP and Tafel methods show large deviations with the different scan rates due to the change of electrode surface area. For the CV method, the results were similar to that from LP method, but the data sets did not show the linear relationship with either the concentration or temperature. This low to moderate discrepancies between data from CV and EIS measurements indicate that CV may be used as a rapid data acquisition and analysis providing advantage toward the real time material detection and accountability.

Based on the  $i_0$  data measured via EIS technique, further analyses were performed. The dependences with the concentration and temperature were linearly modeled and the equations were provided. Arrhenius temperature relationship was used to fit these data sets, from which the maximum value of  $i_0$  at infinite temperature and activation energy for  $U/U^{3+}$  reaction were obtained. Also, dimensionless equations were provided, which can be utilized to estimate the  $i_0$  properties for  $U/U^{3+}$  reaction in various experimental conditions.

Lastly, the same experiments were performed with  $GdCl_3$  addition to the salt. The diffusion coefficient was affected by the addition of  $GdCl_3$ : 12 ~ 35 % of declines in diffusion coefficient values were observed by adding  $GdCl_3$  in  $LiCl-KCl-UCl_3$  (ratio of  $UCl_3$  was ranging from 1 to 4). The equilibrium potentials shows the similar values even when  $GdCl_3$  was added in the salt which indicates that thermodynamics of  $UCl_3$  in  $LiCl-KCl$  are hardly affected by co-existence of  $GdCl_3$ . In addition, having the additional  $GdCl_3$  in the salts, the  $i_0$  values follow the same trends with no  $GdCl_3$ ; hence, this indicates that the kinetics for  $U^{3+}/U$  reaction on the electrode surface are not significantly being influenced by the presence of  $GdCl_3$ .



## Chapter 6 Summary and Future Work

### 6.1 Background

Pyroprocessing technology has been examined in several countries including the United State, Russia, France, Japan, South Korea, and India. The purpose of this technology is not only to treat the irradiated nuclear fuel, but also to reduce volume of the nuclear waste, recycle actinides, and close the fast reactor fuel cycle. The heart of this technology is the ER where pure U and An elements are being recovered in LiCl-KCl eutectic salt at 773 K. This recovery can be accomplished by using an electrolysis; therefore, many studies have been done to understand the electrochemical, thermodynamic, and kinetic behaviors of those products. However, several datasets reported in the past have been scattered and obscure due to challenges in the experimental measurements. Therefore, in this dissertation, the main goal was to develop methods to provide reliable and repeatable data for U properties in LiC-KCl salt system, which will give fundamental understanding and signatures for material accountability in ER process.

### 6.2 Literature Data for U and Electrochemical Techniques

Literature survey was delivered in Chapter 2. The main focus was uranium properties in LiCl-KCl eutectic such as diffusion coefficients, apparent standard potential, activity coefficient, and exchange current density. Summarized information and discussion can be found below:

- Molten salts have several advantages over aqueous solvents: high radiation resistance, low criticality concern, low vapor pressure, low secondary wastes and high stability. Typically,

LiCl-KCl molten salt is selected as a candidate for electrorefining system with the benefit of low melting temperature (623 K).

- The apparent standard potential can be measured via CV and OCP methods, which gives an insight into the reduction potential that need to be applied for the U recovery in the ER. The reported data values show good agreement within 50 mV deviation, which are linearly dependent with temperature in general. It has been reported that the properties are independent on concentration variation; however, this needs to be experimentally evaluated at high concentrations.
- Several values of activity coefficient were reported, showing wide discrepancy up to  $10^2$  order of magnitude. This is because of the challenges of obtaining pure Gibbs free energy data.
- The diffusion coefficient data will provide an idea on the mass transport of U in the system; hence, the efficiency and the maximum current for the system can be optimized. The reported values are scattered depending on the techniques, ranging from  $5.5 \times 10^{-6} \text{ cm}^2 \text{ s}^{-1}$  to  $4.9 \times 10^{-5} \text{ cm}^2 \text{ s}^{-1}$ . Recent trend is that the resulting data sets from various research teams are agreeing well by the CV technique.
- Exchange current density ( $i_0$ ) is an important parameter to understand kinetics of electrochemical reactions ( $\text{U}^{3+}/\text{U}$ ) on the electrode surface, which will enhance the development of kinetic models and the real-time monitoring technologies. Only few data sets are available since 2009, from which meaningful comparison and trend are hardly understood. Most of the literature sources used linear polarization (LP) method, which seems to be limited to be used at high concentrations.

- In this dissertation, five different electrochemical techniques including CV, OCP, EIS, Tafel, and LP were selected to obtain the significant datasets.

### 6.3 Experimental setup and procedure

All experimental preparations and measurement were carefully performed under argon environment due to the hygroscopic and corrosive characteristics of salt chemicals. Chapter 3 provide information on instrumental setups and materials generally used in the experiments. As each experiment require different setups and preparations, detailed descriptions were also provided and discussed in later chapters. Here are the summarizing points:

- Two glovebox systems for non-radioactive and radioactive materials (RAM I and RAM II, respectively) were installed in Radiochemistry laboratory at VCU. All experiments were done in these gloveboxes with O<sub>2</sub> and H<sub>2</sub>O levels controlled less than 5 ppm.
- Commercial furnaces were used in the gloveboxes to heat and maintain the salt samples at desired temperature. Kerrlab melting furnace and Muffle furnace were utilized for the preliminary studies and uranium studies, respectively.
- LiCl-KCl eutectic salt was prepared by mixing LiCl (58.2 mol%) and KCl (41.8 mol%). Specifications of chemicals used in the present study are listed in Table 3.1.
- Prior to the melting the salts, the salt samples were dried at 523 K for 5 hours to remove possible water contents. In addition, when the salts were prepared at desired temperature, 3 – 5 hours were given for reaching the equilibrium state.
- Typically, alumina crucibles and Inconel crucibles were used as a main vessel. These are placed in a secondary alumina crucible for the safety purpose.

- All electrode rods were preinstalled in alumina sheaths for avoiding a shortage. Ag/AgCl (5 mol%) and Ag/AgCl(1 mol%) were used as a reference electrode. In the data analysis, the potentials were converted into  $\text{Cl}_2/\text{Cl}$  reference for providing comparable data.
- The electrodes are assembled into one body by designing electrode assembly, which provides security of electrodes at desired position, easy access into the molten salt, and salt sampling during the experiments.
- During uranium experiments, the salt samples were taken out from the vessel, and analyzed by ICP-MS. Detailed procedures for ICP-MS analysis are provided in Section 3.2.4.

## 6.4 Preliminary studies with Ce surrogate

The main objective of this preliminary study is to develop experimental methodologies and electrochemical techniques, which can be further applied to uranium studies. Cerium was selected as a surrogate material for uranium, and electrochemical measurements were performed to evaluate Ce properties in LiCl-KCl eutectic. The Ce behaviors were investigated with various electrochemical techniques on a solid and liquid cathodes.

### 6.4.1 Measurement of Ce properties by using a solid cathode in LiCl-KCl

The Ce properties were explored by using CV and EIS methods in LiCl-KCl- $\text{CeCl}_3$  salt at concentrations and temperatures ranging 0.5 wt% to 4 wt% and 698 K to 798 K, respectively. The following results were observed.

- The peak currents were obtained from CV measurements, and used into Berzin-Delahay relationship to calculate the diffusion coefficients of  $\text{CeCl}_3$  in LiCl-KCl salt. The diffusion

coefficient stays approximately the same over concentration change up to 4 wt%, while it shows a nearly proportional trend to temperature.

- The peak potentials from CV curves were used to calculate the apparent standard potentials of  $\text{Ce}^{3+}/\text{Ce}$  reaction. The resulting data sets are ranging from -3.16 V to -3.06 V versus  $\text{Cl}_2/\text{Cl}^-$  reference, which proportionally increase with rising temperature. From the calculated apparent standard potential, thermodynamic properties were calculated. Particularly, activity coefficients of  $\text{CeCl}_3$  were calculated based on the pure Gibbs energy data at super cooled state. Here, the fusion energy was considered due to the nature of  $\text{CeCl}_3$  ( $T_m=1080$  K). The values of the diffusion coefficients and activity coefficients for  $\text{CeCl}_3$  are summarized in Table 6.1.
- EIS spectra were measured at minimum overpotentials for  $\text{Ce}^{3+}/\text{Ce}$  reaction to be occurring, which were fitted to the equivalent circuit illustrated in Figure 4.8. The charge transfer resistances were obtained from the fitted curves, which were used to calculate the  $i_0$  and  $k^0$  for  $\text{Ce}^{3+}/\text{Ce}$  couple. The resulting data shows the linear correlation with temperature within concentration at 4 wt%  $\text{CeCl}_3$ , which was expressed as a linear equation in Table 6.2.
- The data measured by EIS in the present study show a good agreement with data reported by Marsden and Pesic [61]. The authors used the LP method to measure the  $i_0$  of  $\text{Ce}^{3+}/\text{Ce}$ , however, they reported the broad range of data due to the electrode surface area change during the LP methods.

**Table 6.1** Diffusion coefficients and activity coefficients of  $\text{UCl}_3$  in  $\text{LiCl-KCl}$  salt

$\text{CeCl}_3$	0.5 wt %		2 wt %		4 wt %	
T [K]	D	$\gamma_{\text{CeCl}_3}$	D	$\gamma_{\text{CeCl}_3}$	D	$\gamma_{\text{CeCl}_3}$
	$[\times 10^5 \text{ cm}^2 \text{ s}^{-1}]$	$\times 10^3$	$[\times 10^5 \text{ cm}^2 \text{ s}^{-1}]$	$\times 10^3$	$[\times 10^5 \text{ cm}^2 \text{ s}^{-1}]$	$\times 10^3$
698	0.479	0.56	0.430	0.47	0.418	0.23
723	0.545	0.56	0.547	0.47	0.544	0.34
748	0.653	0.68	0.675	0.47	0.672	0.29
773	0.751	1.07	0.690	1.40	0.700	0.48
798	1.012	1.29	0.875	1.94	0.860	0.43

**Table 6.2** Linear relationships of the exchange current densities against the inverse temperature based on the experimental data

$\text{CeCl}_3$	$i_0 [\text{A cm}^{-2}]$	$R^2$
0.5 wt%	$-46.284 \frac{1}{T} + 0.0733$	0.954
2 wt%	$-306.4 \frac{1}{T} + 0.4957$	0.987
4 wt%	$-488.93 \frac{1}{T} + 0.7818$	0.960

- The practical analysis was performed to compare the measured properties cerium with those of uranium reported from previous literatures. The diffusion coefficients for both  $\text{UCl}_3$  and  $\text{CeCl}_3$  are in the same order of magnitude and showing the similar correlation with the temperature. The activation energies for the diffusion of  $\text{UCl}_3$  have been reported,

ranging from 24.2 to 34.4 kJ mol<sup>-1</sup> [37, 39], which is in a good agreement with the activation energy for CeCl<sub>3</sub>.

- The similarity between both the activation energies for the diffusion may be owing to the similar ionic size of uranium and cerium. In contrast, the standard reduction potential of CeCl<sub>3</sub> was about 0.7 V more negative than the standard reduction potential for UCl<sub>3</sub>. Due to the dispersion of the reported  $i_0$  for U<sup>3+</sup>/U reaction, it was difficult to compare the  $i_0$  values between cerium and uranium.

#### 6.4.2 Measurement of Ce properties on liquid cadmium cathode

In Section 4.2, further electrochemical measurements were performed to estimate the electrochemical and thermodynamic properties of CeCl<sub>3</sub> on liquid cathode. Liquid cadmium was loaded in a Pyrex crucible (see Figure 4.16), which was used as a working electrode. CV, OCC, LP, and Tafel methods were conducted to explore the diffusion coefficient, Gibbs energies for the intermetallic formations, and exchange current densities of CeCl<sub>3</sub> on the liquid cadmium cathode (LCC).

- CV curves measured in LiCl-KCl obtained at concentration of 1 wt% CeCl<sub>3</sub> and temperature ranging from 723 K to 798 K. The CV results show the Li co-deposition; therefore, background CV curves (for pure LiCl-KCl salt) were subtracted. Then, CV curves only attributed to the Ce redox on LCC were obtained. From the peak currents, the same calculation with Berzin-Delahay relationship was done to determine the diffusion coefficients of CeCl<sub>3</sub> on LCC.

- The diffusion coefficients of  $\text{CeCl}_3$  ranged from  $2.9 \times 10^{-6} \text{ cm}^2 \text{ s}^{-1}$  to  $5.1 \times 10^{-6} \text{ cm}^2 \text{ s}^{-1}$  at temperatures from 723 to 798 K, which are almost half values of the diffusion coefficients on the tungsten electrode. The diffusion of  $\text{Ce}^{3+}$  may be interfered by deposition of  $\text{Li}^+$  or LCC structure. To utilize LCC, the liquid cadmium was loaded in a Pyrex crucible having an upward surface area exposure to the molten salt  $\text{LiCl-KCl}$ . Therefore, mass transfers caused by electric force and convection are being restricted only through that exposure liquid cadmium surface.
- OCC experiments were performed to understand thermodynamic properties of Ce-Cd intermetallic compounds in LCC. In advance, Ce and Cd were deposited together on tungsten working electrode by applying reductive potential at -2.2 V (vs.  $\text{Ag/AgCl}$ ) for 25 seconds. Then, the OCC were measured by applying the positive current at 1  $\mu\text{A}$ . By changing Ce contents in liquid Cd film, Ce-Cd intermetallic formation also changes, which is indicated as a plateau on OCC curves. There were six different intermetallic compounds observed, and each potential of plateau was measured based on OCP. The potential differences were employed to calculate the partial molar Gibbs energy for the formations and activity of  $\text{CeCl}_3$  in  $\text{LiCl-KCl}$ , which are summarized in Table 4.10.
- By observing the calculated values of activity, it can be implied that the reduction potentials of An and Ln elements come together closely on the LCC at the beginning of the ER process, and will be gradually detached by depositing more elements in the LCC.
- Using Eq. (4-6), the standard Gibbs free energy for Ce-Cd intermetallic formations were calculated. The resulting data sets are listed in Table 4.11, which helps understanding thermodynamic energies of MA-Cd intermetallic formations in ER-LCC system and cathode processor where Cd separation is conducted by a distillation at high temperatures.



- Tafel plot and LP methods were conducted for the measurement of the  $i_0$  of  $\text{Ce}^{3+}/\text{Ce}$  couple on LCC in LiCl-KCl molten salt by incrementally adding Cd metals in liquid Cd (mole fraction was varied from 0.0013 to 0.0303). The results from both methods (summarized in Table 4.13) show the relative difference less than 20%, but their trends of  $i_0$  against mole fraction of Ce in Cd are in good agreement. When Ce concentration is lower than its solubility in Cd,  $i_0$  of Ce is linearly dependent on Ce concentration (Ce solubility limit in Cd is 0.006 in mole fraction). However, as Ce fraction exceeds its solubility limit in Cd, a nearly steady  $i_0$  of Ce is being observed. These phenomena are well illustrated in Figure 4.27, which may be attributed to the equilibrium state in the phase ( $\text{Cd-CeCd}_{11}$ ) obtained in the Gibbs free energy study.

## 6.5 Measurements of uranium properties

Based on the methodologies developed in the preliminary studies, the experimental designs and programs were established to explore the electrochemical, thermodynamic, and kinetic properties of U in LiCl-KCl salt system via CV, OCP, LP, Tafel, and EIS techniques. In addition, LiCl-KCl- $\text{UCl}_3$ - $\text{GdCl}_3$  salt systems were being investigated and the same electrochemical measurements were carried out to give insight on an effect of other elements on U properties which could be happening in ER system. The results and discussion are summarized as follows:

- The diffusion coefficients of  $\text{UCl}_3$  in LiCl-KCl eutectic were measured by plotting the peak currents versus the square roots of the scan rate with the Berzin-Delahay relationship. The result values are ranging from  $3.9 \times 10^{-6} \text{ cm}^2 \text{ s}^{-1}$  to  $1.51 \times 10^{-5} \text{ cm}^2 \text{ s}^{-1}$ , showing a good linearity with temperature, but weak influence by the concentration change up to 2 wt%

UCl<sub>3</sub>. The diffusion coefficients begin decreasing at 4 wt% of UCl<sub>3</sub>, which may be due to the interaction among the particles or invalidity of the Berzin-Delahay equation at high temperatures. When the irreversible equation (Eq. (2-12)) was used with fast scan rates up to 1500 mV s<sup>-1</sup>, the diffusion coefficients at 4 wt% matched with the results at lower concentrations (from 0.5 wt% to 2 wt%).

- The apparent standard potential of U<sup>3+</sup>/U pair was evaluated by using CV and OCP methods. The peak potentials from CV curves were used along with the Eq. (2-15). The result values were ranging from -2.474 V to -2.564 V versus Cl<sub>2</sub>/Cl<sup>-</sup> reference depending on temperature, which were almost irrelevant to concentration changes up to 2 wt% UCl<sub>3</sub>.
- In addition, OCPs were measured to calculate the apparent standard potentials. Both results show similar values of the apparent standard potentials, which also follow a similar trend to temperature. However, it can be noticed that values measured by CV are generally more negative than the values measured by OCP, which can be also observed from literatures. The results from both CV and OCP are summarized in Table 6.3
- Based on the results of the apparent standard potentials, the activity coefficients of UCl<sub>3</sub> in LiCl-KCl were calculated by considering the difference between ideal and actual Gibbs free energies. For understanding the ideal energies, thermodynamic data at super cooled state were utilized as listed in Table 5.2. Here, the resulting values of the activity coefficient from CV and OCP methods are being divided into two different trends according to temperature. The discrepancies were found up to 10<sup>2</sup> order of magnitude, and OCP method generally provides higher values and show a steep increase rate when temperature rises. Detailed data of the activity coefficients are listed in Table 6.3.

**Table 6.3** Summary of apparent standard, Gibb free energy, and activity coefficient of  $\text{UCl}_3$ 

Apparent standard potential [V vs. $\text{Cl}_2/\text{Cl}$ ]			Gibbs free energy of $\text{UCl}_3$ formation [ $\text{kJ mol}^{-1} \text{K}^{-1}$ ]		Activity coefficient $\times 10^3$	
T (K)	OCP	CV	OCP	CV	OCP	CV
723	-2.494	-2.551	-721.8	-738.5	3.80	0.23
748	-2.478	-2.532	-717.2	-732.8	4.69	0.38
773	-2.463	-2.512	-712.9	-727.1	5.59	0.61
798	-2.446	-2.490	-708.1	-720.7	7.06	1.06

- The EIS, LP, Tafel, and CV methods were conducted to investigate the  $i_0$  kinetics of  $\text{U}^{3+}/\text{U}$  couple at  $\text{UCl}_3$  concentrations ranging from 0.5 wt% to 4 wt% and temperature from 723 K to 798 K.
- The values of  $i_0$  for  $\text{U}/\text{U}^{3+}$  reaction are ranging from  $0.0054 \text{ A cm}^{-2}$  to  $0.102 \text{ A cm}^{-2}$  under different concentration and temperature conditions, showing the linear dependences on the concentration and temperature.
- For both LP and Tafel measurements, the potential was swept from -350 mV to 250 mV based on the equilibrium potentials.
- LP method was examined with the different scan rates ranging  $3 \text{ mV s}^{-1}$  to  $100 \text{ mV s}^{-1}$ . The result values were deviated up to 24 % depending on the applied scan rates, which is mainly due to the diffusion limits and electrode surface area changes.
- In case of Tafel analysis, the linear Tafel region cannot be acquired at the concentration higher than 1 wt% of  $\text{UCl}_3$  owing to the vigorous U deposition with the high bulk

concentrations. Therefore, Tafel measurements were done only at concentration of 0.5 wt%  $\text{UCl}_3$ .

- In general, the  $i_0$  values from LP and Tafel methods follow the linear trends to concentration and temperature; however, the poor repeatability were obtained at the concentration of 4 wt%  $\text{UCl}_3$ .
- CV data were processed in analogous methods to LP, The charge transfer resistance were measured at small overpotential region where the deposited U starts to be oxidized. Then the  $i_0$  values were calculated. The calculated values increase when both the concentration and temperature increase; however, it is difficult to observe the linearity from these results.
- The advantage of the CV method is the rapid data acquisition through an instant scan rate; hence, this technique is useful in development of the near-real time technique for the material detection and accountability in the ER system.
- Figure 5.21(a) plots the results from the four techniques which show a moderate agreement within 33% relative difference from their average values. EIS measurements show the most linear trends regarding to the concentration and temperature whereas the values measured by CV method are much scattered and do not have a strong linear correlation with the concentration and temperature.
- As EIS measurements show the most linear trends regarding to the concentration and temperature, the linear relationships of  $i_0$  with temperature and concentration can be modeled by using a linear equation ( $y = ax + b$ ). The equations (listed in Table 5.5) are being extrapolated to estimate the  $i_0$  at 5 wt%  $\text{UCl}_3$ , showing a good agreement with reported literature values.

- Dimensionless relationships ( $i_0/I_0 \approx \exp(-E_a/RT)$  and  $i_0/i_{0,\max} = 155.2x$ ) were provided; therefore, estimation of the  $i_0$  properties for  $U^{3+}/U$  could be easily tabulated.
- With addition of  $GdCl_3$ , the diffusion coefficients were declined by 12~35 % than the values from measurements with pure  $UCl_3$ . The apparent standard potentials and thermodynamic data remained around the same values with  $GdCl_3$  being added into the salt. The  $i_0$  values show the similar trends with the data sets measured with pure  $UCl_3$  salts.

The specific properties with co-existence of  $GdCl_3$  are summarized in Table 6.4.

**Table 6.4** Summary of the uranium properties with  $GdCl_3$  additions

No	Sample	D $\times 10^5$ (cm <sup>2</sup> s <sup>-1</sup> )	$E_{U^{3+}/U}^{0*}$ (V vs. Cl <sub>2</sub> /Cl)	$\Delta G_{UCl_3}^{0*}$ (kJ mol <sup>-1</sup> )	$\gamma_{U^{3+}}$ $\times 10^3$	$i_0$ $\times 10^3$ (A cm <sup>-2</sup> )
5	U0.5_Gd0.5	0.847	-2.46 $\pm 6.0 \times 10^{-3}$	-712.8 $\pm 17.4$	5.64 $\pm 1.53 \times 10^{-1}$	9.39 $\pm 0.284$
6	U1.0_Gd0.25	1.13	-2.46 $\pm 4.2 \times 10^{-4}$	-713.2 $\pm 1.2$	5.26 $\pm 9.8 \times 10^{-2}$	17.7 $\pm 0.679$
7	U1.0_Gd0.5	1.30	-2.47 $\pm 4.5 \times 10^{-5}$	-713.8 $\pm 1.3$	4.80 $\pm 9.7 \times 10^{-3}$	23.9 $\pm 0.548$
8	U1.0_Gd1.0	1.11	-2.46 $\pm 4.0 \times 10^{-4}$	-712.6 $\pm 11.6$	5.80 $\pm 1.1 \times 10^{-1}$	21.7 $\pm 0.93$
9	U2.0_Gd1.0	1.03	-2.46 $\pm 2.7 \times 10^{-4}$	-712.1 $\pm 7.6$	6.30 $\pm 7.5 \times 10^{-2}$	34.5 $\pm 0.537$
10	U2.0_Gd2.0	1.00	-2.46 $\pm 1.2 \times 10^{-4}$	-711.4 $\pm 3.5$	6.98 $\pm 3.8 \times 10^{-2}$	37.9 $\pm 0.213$

## 6.6 Future Works

Several suggestions of future work based on outcomes of the present study are as follows:

- Diffusion coefficients, the equilibrium potentials, and according thermodynamic properties need to be evaluated at concentrations higher than 5 wt% ( $\text{UCl}_3$  concentration in Mark IV ER system is between 5 wt% and 10 wt%).
- The phenomenon of decreasing of diffusion coefficients with increasing concentration needs to be elucidated with proper methodologies. Equations for irreversible soluble-insoluble system need to be derived for using the fast scan rates in CV experiments, which may be applicable at high concentrations.
- The above properties need to be further investigated in multi components salt systems including An, Ln, and alkaline earth materials (which are likely in the ER system) for understanding the physical and chemical associations among the elements.

## Reference

1. Nuclear Technology Review 2015, reported by the Director General, GC(59)/INF/2, July (2015).
2. Spent Fuel Reprocessing Options, IAEA-TECDOC-1587.
3. Nuclear Energy Data, NEA No. 7246, OECD 2015.
4. M. F. Simpson and Jack D. Law, Nuclear Fuel Reprocessing, INL/EXT-10-17753, February (2010).
5. T. Todd, Nuclear regulatory Commission Seminar, March 25 (2008).
6. S. Phongikaroon, EGMN 691 – Nuclear Fuel cycle, Lecture #1, Fall (2015).
7. M. Iizuka, “Diffusion Coefficients of Cerium and Gadolinium in Molten LiCl-KCl,” *Journal of The Electrochemical Society*, **145**, 84-88 (1998).
8. Y.I. Chang, “The Integral Fast Reactor,” *Nuclear Technology*, **88**, 129-138 (1989).
9. J.P. Ackerman, “Chemical Basis for Pyrochemical Reprocessing of Nuclear Fuel,” *Industrial and Engineering Chemistry Research*, **30**, 141-145 (1991).
10. C.E. Till and Y.I. Chang, Plentiful Energy - The Story of the Integral Fast Reactor, ISBN: 978-1466384606 (2011).
11. Z. Wang, D. Rappleye, M. F. Simpson, “Voltammetric Analysis of Mixtures of Molten Eutectic LiCl-KCl Containing LaCl<sub>3</sub> and ThCl<sub>4</sub> for Concentration and Diffusion Coefficient Measurement,” *Electrochimica Acta*, **191**, 29-43 (2016).
12. The Fukushima Daiichi Accident, Report by the Director General, GC(59)/14.
13. Pyrochemical Separations in Nuclear Applications, A Status Report, NEA No. 5427 (2004).

14. H.Lee, G. Park, J. Lee, K. Kang, J. Hur, J. Kim, S. Paek, I. Kim, and I. Cho, "Current Status of Pyroprocessing Development at KAERI," *Science and Technology of Nuclear Installations*, **2013**, Article ID 343492 (2013).
15. E. Choi, S. Jeong, "Electrochemical Processing of Spent Nuclear Fuels: An Overview of Oxide Reduction in Pyroprocessing Technology," *Progress in Natural Science Materials International* (2015).
16. S.D. Herrmann, S. X.Li, M.F. Simpson, "Electrolytic Reduction of Spent Light Water Reactor Fuel# Bench-Scale Experiment Results," *Journal of Nuclear Science and Technology*, **44**, 361–367 (2007).
17. K. Uozumi, M. Iizuka, T. Kato, T. Inoue, O. Shirai, T. Iwai, and Y. Arai, "Electrochemical Behaviors of Uranium and Plutonium at Simultaneous Recoveries into Liquid Cadmium Cathodes," *Journal of Nuclear Materials*, **325**, 34 - 43 (2004).
18. T. Koyama, M. Iizuka, Y. Shoji, R. Fujita, H. Tanaka, T. Konayashi, and M. Tokiwai, "An Experimental Study of Molten Salt Electrorefining of Uranium Using Solid Iron Cathode and Liquid Cadmium Cathode for Development of Pyrometallurgical Reprocessing," *Journal of Nuclear Science and Technology*, **34**, 384 (1997).
19. M. F. Simpson, "Developments of Spent Nuclear Fuel Pyroprocessing Technology at Idaho National Laboratory," DOI: 10.2172/1044209 (2012).
20. S.X. Li, T.A. Johnson, B.R. Westphal, K.M. Goff, and R.W. Benedict, "Electrorefining Experience for Pyrochemical Processing of Spent EBR-II Driver Fuel," *Proceedings of GLOBAL 2005*, Tsukuba, Japan, October 9-13 (2005).
21. S.X. Li and M.F. Simpson, "Anodic Process of Electrorefining Spent Driver Fuel in Molten LiCl-KCl-UCl<sub>3</sub>/Cd System," *Minerals and Metallurgical Processing*, **22**, 192-198 (2005).



22. R.O. Hoover, "Uranium and Zirconium Electrochemical Studies in LiCl-KCl Eutectic for Fundamental Applications in Used Nuclear Fuel Reprocessing," Ph.D. Thesis, University of Idaho, Idaho Falls, ID (2014).
23. O. Shirai, M. Iizuka, T. Iwai, Y. Arai, "Electrode Reaction of the  $\text{Np}^{3+}/\text{Np}$  Couple in LiCl-KCl Eutectic Melts," *Journal of Applied Electrochemistry*, **31**, 1055-1060 (2001).
24. G. Cordoba, C. Caravaca, "An Electrochemical Study of Samarium Ions in the Molten Eutectic LiCl + KCl," *Journal of Electroanalytical Chemistry*, **572**, 145–151, (2004).
25. J.A. Plambeck, "Encyclopedia of Electrochemistry of the Elements," Fused salt systems. Vol. X., 1976.
26. S. Kim, D. Yoon, Y. You, S. Paek, J. Shim, S. Kwon, K. Kim, H. Chung, D. Ahn, H. Lee, "In-situ Observation of a Dendrite Growth in an Aqueous Condition and a Uranium Deposition into a Liquid Cadmium Cathode in an Electrowinning System," *Journal of Nuclear Materials*, **385**, 196–199 (2009).
27. D. Vaden, S. X. Li, B. R. Westphal, K. B. Davies, T. A. Johnson, D. M. Pace, "Engineering-Scale Liquid Cadmium Cathode Experiments," INL/CON-06-11544.
28. Robin Taylor, Reprocessing and Recycling of Spent Nuclear Fuel, ISBN-13: 978-1782422129.
29. Y. Castrillejo, M. R. Bermejo, P. D. Arocas, A. M. Martinez, and E. Barrado, "The Electrochemical Behaviour of the Pr(III)/Pr Redox System at Bi and Cd Liquid Electrodes in Molten Eutectic LiCl–KCl," *Journal of Electroanalytical Chemistry*, **579**, 343 (2005).
30. G. Kim, D. Yoon, S. Paek, S. Kim, T. Kim, D. Ahn, "A Study on the Electrochemical Deposition Behavior of Uranium Ion in LiCl-KCl Molten Salt on Solid and Liquid Electrode," *Journal of Electroanalytical Chemistry*, **682**, 128-135 (2012).

31. T. Murakamia, Y. Sakamura, N. Akiyama, S. Kitawakib, A. Nakayoshi, “Electrochemical Measurement of Diffusion Coefficient of Actinides and Rare Earths in Liquid Cd,” *Procedia Chemistry*, **7**, 798 - 803 (2012).
32. O. Shirai, K. Uozumi, T. Iwai, and Y. Arai, “Electrode Reaction of the  $U^{3+}/U$  Couple at Liquid Cd and Bi Electrodes in LiCl-KCl Eutectic Melts,” *Analytical Sciences*, **17**, i959-i962 (2001).
33. J. Zhang, “Electrochemistry of Actinides and Fission Products in Molten Salts—Data,” *Journal of Nuclear Materials*, **447**, 271-284 (2014).
34. G. Janz, *Molten Salt Handbooks*, New York and London: Academic Press (1967).
35. G. J. Janz, G. L. Gardner, U. Krebs, and R. P. T. Tomkins, *Molten Salts: Volume 4, Part 1, Fluorides and Mixtures Electrical Conductance, Density, Viscosity, and Surface Tension Data*, New York (1974).
36. G. J. Janz, R. P. T. Tomkins, C. B. Allen, J. R. Downey, Jr, G. L. Gardner, U. Krebs, and S. K. Singer, *Molten Salts: Volume 4, Part 2, Chlorides and Mixtures—Electrical Conductance, Density, Viscosity, and Surface Tension Data*, New York (1975).
37. P. Masset, D. Bottomley, R. Konings, R. Malmbeck, A. Rodrigues, J. Serp, and J. Glatz, “Electrochemistry of Uranium in Molten LiCl-KCl Eutectic,” *Journal of The Electrochemical Society*, **152**, A1109-A1115 (2005).
38. P. Masset, R. J.M. Konings, R. Malmbeck, J. Serp, J. Glatz, “Thermochemical Properties of Lanthanides ( $Ln = La, Nd$ ) and Actinides ( $An = U, Np, Pu, Am$ ) in the Molten LiCl-KCl Eutectic,” *Journal of Nuclear Materials*, **344**, 173-179 (2005).
39. S.A. Kuznetsov, H. Hayashi, K. Minato, and M. Gaune-Escard, “Electrochemical Transient Techniques for Determination of Uranium and Rare-Earth Metal Separation Coefficients in

- Molten Salts,” S. A. Kuznetsov, H. Hayashi, K. Minato, and M. Gaune-Escard, *Electrochimica Acta*, **51**, 2463-2470 (2006).
40. O. Shirai, H. Yamana, and Y. Arai, “Electrochemical Behavior of Actinides and Actinide Nitrides in LiCl–KCl Eutectic Melts,” *Journal of Alloys and Compounds*, **408–412**, 1267–1273 (2006).
41. J.J. Roy, L.F. Grantham, D.L. Grimmett, S.P. Fusselman, C.L. Krueger, T.S. Storvick, T. Inoue, Y. Sakamura, and N. Takahashi, “Thermodynamic Properties of U, Np, Pu, and Am in Molten LiCl–KCl Eutectic and Liquid Cadmium,” *Journal of the Electrochemical Society*, **143**, 2487-2492 (1996).
42. R. O. Hoover, M. R. Shaltry, S. Martin, K. Sridharan, S. Phongikaroon, “Electrochemical Studies and Analysis of 1–10 wt%  $\text{UCl}_3$  Concentrations in Molten LiCl–KCl Eutectic,” *Journal of Nuclear Materials*, **452**, 389–396 (2014).
43. L. Martinot, “Gmelin Handbuch der Anorganischen Chemie,” Springer-Verlag, New York (1984).
44. Y. Sakamura, T. Hijikataa, K. Kinoshitaa, T. Inouea, T.S. Storvickb, C.L. Kruegerb, J.J. Royc, D.L. Grimmett, S.P. Fusselman, R.L. Gay, “Measurement of Standard Potentials of Actinides (U,Np,Pu,Am) in LiCl–KCl Eutectic Salt and Separation of Actinides from Rare Earths by Electrorefining,” *Journal of Alloys and Compounds*, **271–273**, 592-596 (1998).
45. B.P. Reddy, S. Vandarkuzhali, T. Subramanian, P. Venkatesh, “Electrochemical Studies on the Redox Mechanism of Uranium Chloride in Molten LiCl–KCl Eutectic,” *Electrochimica Acta*, **49**, 2471-2478 (2004).

46. M. M. Tylka, J. L. Willit, J. Prakash, and M. A. Williamson, "Application of Voltammetry for Quantitative Analysis of Actinides in Molten Salts," *Journal of The Electrochemical Society*, **162**, H852-H859 (2015).
47. W. Zhou, J. Zhang, "Chemical Diffusion Coefficient Calculation of  $U^{3+}$  in LiCl-KCl Molten Salt," *Progress in Nuclear Energy*, **91**, 170-174 (2016).
48. I. Choi, B. E. Serrano, S. X. Li, S. Hermann, S. Phongikaroon, "Determination of Exchange Current Density of  $U^{3+}/U$  Couple in LiCl-KCl Eutectic Mixture," *Proceedings of GLOBAL 2009*, Paris, France, Sept. 6-11 (2009).
49. S. Ghosh, S. Vandarkuzhali, N. Gogoi, P. Venkatesh, G. Seenivasan, "Anodic Dissolution of U, Zr and U-Zr alloy and Convolution Voltammetry of  $Zr^{4+}/Zr^{2+}$  Couple in Molten LiCl-KCl Eutectic," *Electrochimica Acta*, **56**, 8204-8218 (2011).
50. M. A. Rose, M. A. Williamson, and J. Willit, "Determining the Exchange Current Density and Tafel Constant for Uranium in LiCl/KCl Eutectic," *ECS Electrochemistry Letters*, **4**, C5-C7 (2015).
51. K. H. Lim, S. Park, and J. Yun, "Study on Exchange Current Density and Transfer Coefficient of Uranium in LiCl-KCl Molten Salt," *Journal of The Electrochemical Society*, **162**, E334-E337 (2015).
52. Christopher M. A. Brett and Ana Maria Oliveira Brett, *Electrochemistry Principles, Methods, and Applications*, Oxford University Press Inc., New York.
53. Barin, *Thermochemical Data of Pure Substances*, Third Edition, Wiley-VCH Verlag GmbH, 1995.

54. W. Zhou and J. Zhang, "Direct Calculation of Concentration-Dependent Activity Coefficient of  $\text{UCl}_3$  in Molten  $\text{LiCl-KCl}$ ," *Journal of The Electrochemical Society*, **162**, E199-E204 (2015).
55. A. J. Bard, L. R. Faulkner, *Electrochemical Methods, Fundamentals and Applications*, New York: Wiley (2001).
56. P. Delahay, *New Instrumental Methods in Electrochemistry: Theory, Instrumentation and Application to Analytical and Physical Chemistry*, Interscience, New York (1954).
57. T. Berzins and P. Delahay, "Oscillographic Polarographic Waves for the Reversible Deposition of Metals on Solid Electrodes," *Journal of American Chemical Society*, **75**, 555-559 (1953).
58. H. D. ErtuğruL and Z. O. Uygun, "State of the Art in Biosensors - General Aspects," book edited by Toonika Rinken, ISBN 978-953-51-1004-0.
59. A. Lisa, *Electrochemical Impedance Spectroscopy and Its Applications*, New York: Springer (2014).
60. L. Yang and R.G. Hudson, "Some Investigations of the  $\text{Ag/AgCl}$  in  $\text{LiCl-KCl}$  Eutectic Reference Electrode," *Journal of the Electrochemical Society*, **106**, 986-990 (1959).
61. K. C. Marsden and B. Pesic, "Evaluation of the Electrochemical Behaviors of  $\text{CeCl}_3$  in Molten  $\text{LiCl-KCl}$  Eutectic Utilizing Metallic Ce as an Anode," *Journal of Electrochemical Society*, **159**, F111-F120 (2011).
62. R. D. Shannon, "Revised Effective Ionic Radii and Systematic Studies of Interatomic Distances in Halides and Chalcogenides," *Acta Crystallographica*, **A32**, 751- 767 (1976).

63. D. K. Sahoo, A. K. Satpati, and Krishnamurthy, "Electrochemical Properties of Ce(III) in an Equimolar Mixture of LiCl–KCl and NaCl–KCl Molten Salts," *The Royal Society of Chemistry*, **5**, 33163-33170 (2015).
64. S. Kim, Seungwoo Paek, Tack-Jin Kim, Dae-Yeob Park, Do-Hee Ahn, "Electrode Reactions of  $\text{Ce}^{3+}/\text{Ce}$  Couple in LiCl–KCl Solutions Containing  $\text{CeCl}_3$  at Solid W and Liquid Cd Electrodes," *Electrochimica Acta*, **850**, 332-335 (2012).
65. Y. Castrillejo, M. Bermejo, R. Pardo, and A. Martinez, "Use of Electrochemical Techniques for the Study of Solubilization Processes of Cerium–Oxide Compounds and Recovery of the Metal from Molten Chlorides," *Journal of Electroanalytical Chemistry*, **552**, 124-140 (2002).
66. S.A. Kuznetsov, H. Hayashi, K. Minato, and M. Gaune-Escard, "Electrochemical Behavior and Some Thermodynamic Properties of  $\text{UCl}_4$  and  $\text{UCl}_3$  Dissolved in a LiCl–KCl Eutectic Melt," *Journal of the Electrochemical Society*, **152**, C203-C212 (2005).
67. O. Shirai, M. Iizuka, T. Iwai, Y. Suzuki, Y. Arai, "Electrode reaction of plutonium at liquid cadmium in LiCl–KCl eutectic melts," *Journal of Electroanalytical Chemistry*, **490**, 31-36 (2000).
68. Y. Castrillejo, R. Bermejo, A. M. Martinez, E. Barrado, P. Diaz Arocas, "Application of Electrochemical Techniques in Pyrochemical Processes – Electrochemical Behavior of Rare Earths at W, Cd, Bi, and Al Electrodes," *Journal of Nuclear Materials*, **360**, 32-42 (2007).
69. Y. Castrillejo, P. Hernandez, R. Fernandez, E. Barrado, "Electrochemical Behavior of Terbium in the Eutectic LiCl–KCl in Cd Liquid Electrodes. – Evaluation of the Thermochemical Properties of the  $\text{TbCd}_x$  Intermetallic Compounds," *Electrochimica Acta*, **147**, 743-751 (2014).

70. H. Shibata, H. Hayashi, M. Akabori, Y. Arai, M. Kurata, "Evaluation of Gibbs Free Energies of Formation of Ce–Cd Intermetallic Compounds Using Electrochemical Techniques," *Journal of Physics and Chemistry of Solids*, **75**, 972-976 (2014).
71. R. N. Lyon, Liquid-Metals Handbook, Oak Ridge National Laboratory (1952).
72. J. M. P. Q. Delgado and M. Vazquez da Silva, Analytical Solutions of Mass Transfer Around a Prolate or an Oblate Spheroid Immersed in a Packed Bed, Multiphase System and its Applications, ISBN: 978-953-307-215-9, InTech (2011).
73. M. A. Lewis and T. R. Johnson, "A Study of the Thermodynamic and Reducing Properties of Lithium in Cadmium at 773 K," *Journal of The Electrochemical Society*, **137**, 1414-1418 (1990).
74. F. Lantelme, T. Cartailier, Y. Berghoute, "Physicochemical Properties of Lanthanide and Yttrium Solutions in Fused Salts and Alloy Formation with Nickel," *Journal of The Electrochemical Society*, **148**, C604-C613 (2001).
75. K. A. Gschneidner Jr. and F. W. Calderwood, "The Cd-Ce (Cadmium-Cerium) System," *Bulletin of Alloy Phase Diagrams*, **9**, 21 (1988).
76. M. Kurata and Y. Sakamura, "Thermodynamic Assessment of Systems of Actinide or Rare earth with Cd," *Journal of Phase Equilibria*, **22**, 232-240 (2001).
77. K. Serrano, P. Taxil, "Electrochemical Reduction of Trivalent Uranium ions in Molten Chlorides," *Journal of Applied Electrochemistry*, **29**, 497 (1999).
78. D. Yoon and S. Phongikaroon, "Electrochemical Properties and Analysis of  $\text{CeCl}_3$  in LiCl-KCl Eutectic Salt," *Journal of The Electrochemical Society*, **162**, E237-E243 (2015).

79. D. Yoon, S. Phongikaroon, and J. Zhang, "Electrochemical and Thermodynamic Properties of  $\text{CeCl}_3$  on Liquid Cadmium Cathode (LCC) in LiCl-KCl Eutectic Salt," *Journal of The Electrochemical Society*, **163**, E97-E103 (2016).
80. D. Yoon and S. Phongikaroon, "Measurement and Analysis of Exchange Current Density for  $\text{U}/\text{U}^{3+}$  Reaction in LiCl-KCl Eutectic Salt via Various Electrochemical Techniques," **Submitted** in *Electrochimica Acta* (2016).



## Appendix A. Data from Literatures

**Table A.1** Summary of literatures performed to understand U properties in application of pyroprocessing technology

Reference	Concentration & Temperature	Elements	Properties	Measurement methods used
Masset [37]	C: $9.87 \times 10^{-5}$ mol cm <sup>-3</sup> T: 673 K – 823 K	U	D, E <sup>0*</sup> , $\Delta G^*$ , $\gamma$	CV, CP
Masset [38]	C: $9.87 \times 10^{-5}$ mol cm <sup>-3</sup> T: 673 K – 823 K	U, Pu, Np, Am, La, Nd	D, E <sup>0*</sup>	CV, CP
Kuznetsov [39]	C: $6.26 \times 10^{-5}$ mol cm <sup>-3</sup> T: 723 K – 823K	U, Np, Pu, Am	D, E <sup>0*</sup> , $\gamma$ , $k_0$	CV, LSV, CP, CA, EIS
Shirai [40]	C: $8.8 \times 10^{-4}$ mol frac. T: 773 K	U, Np, Pu	E <sup>0*</sup>	CV
Roy [41]	T: 673 - 723 K	U, Np, Pu, Am	E <sup>0*</sup> , $\gamma$ , $\Delta G^*$	OCP
Hoover [42]	C: 1 – 10 wt% T: 773 K	U	E <sup>0*</sup> , D, $\gamma$ , $\Delta G^*$	CV, CP, ASV
Martinot [43]		U	E <sup>0*</sup>	
Sakamura [44]	C: 0.0016 mol frac. T: 723 K	U, Np, Pu, Am	E <sup>0*</sup>	OCP
Reddy [45]	C: 0.474 mol % T: 755 K	U	E <sup>0*</sup> , D	CV, CP, EIS
Tylka [46]	C: 0.5 – 4.3 wt% T: 773 K	U, Pu	D	CV
Gha-Young [30]	C: 1.0 wt% T: 773 K	U (LCC)	D, impedance	CV, EIS
Shirai [32]	C: 0.5 – 1.0 wt% T: 723 K - 823 K	U (LCC)	E <sup>0*</sup> , $\Delta G^*$	CV
Murakami [31]	C: 1.6 wt% T: 723 K - 773 K	U, Pu, La, Pr, Nd, Gd, Y, Sc (LCC)	D, $\Delta G^*$	CV, CP
Choi [48]	C: 3.3 wt% T: 773 K	U	$i_0$	LP
Rose [50]	C: 5.0 wt% T: 723 K - 923 K	U	$i_0$	Tafel
Ghosh [49]	C: 4.0 wt% T: 773 K	U, Zr	D, $i_0$	CV, Tafel
Lim [51]	C: 1.0 wt% T: 738 K - 773 K	U	$i_0$	Tafel, LP

**Table A.2** Summary of diffusion coefficients for  $U^{3+}$  in LiCl-KCl from literatures

Reference	Diffusion coefficient of $U^{3+}$ , $D \times 10^5$ ( $cm^2 s^{-1}$ )			
	698 K	723 K	773 K	823 K
Masset [37]	1.71 (CP)		3.8 (CP) 2.5 (CV) 3.1 (Conv.)	4.92 (CP) 2.84 (CV) 3.99 (Conv.)
Masset et al		2.7 (CV)		
Kuznetsov [39]		1.02 (CV)	1.45 (CV)	1.97 (CV)
Hoover [42]			1.04 (CP)	
Reddy [45]		0.552 (CV) 0.68 (CP)	0.98 (CV) 1.03 (CP)	1.36 (CP)
Tylka [46]			1.52 (CV)	
Martinot [43]		0.68 (CV)		

**Table A.3** Summary of apparent standard potentials of  $U/U^{3+}$  from literatures

Reference	Apparent standard potential, $E^{0*}$ (V vs $Cl_2/Cl^-$ )			
	698 K	723 K	773 K	823 K
Masset [37]	-2.588 (CP) -2.561 (CV) -2.58 (Conv.)		-2.516 (CP) -2.491 (CV) -2.518 (Conv.)	-2.481 (CP) -2.437 (CV) -2.469 (Conv.)
Masset [38]	-2.60 (CV)		-2.484 (CV)	-2.462 (CV)
Kuznetsov [39]		-2.541 (CV)	-2.514 (CV)	-2.487 (CV)
Shirai et al. [40]		-2.484 (CV)	-2.453 (CV)	-2.422 (CV)
Roy [41]	-2.515 (OCP)	-2.498 (OCP)		
Hoover [42]			-2.568 (CP)	
Martinot [43]		-2.52 (OCP)	-2.489 (OCP)	-2.459 (OCP)
Sakamura [44]		-1.283 (OCP)		

**Table A.4** Thermodynamic properties of  $\text{UCl}_3$  in  $\text{LiCl-KCl}$  reported by literature

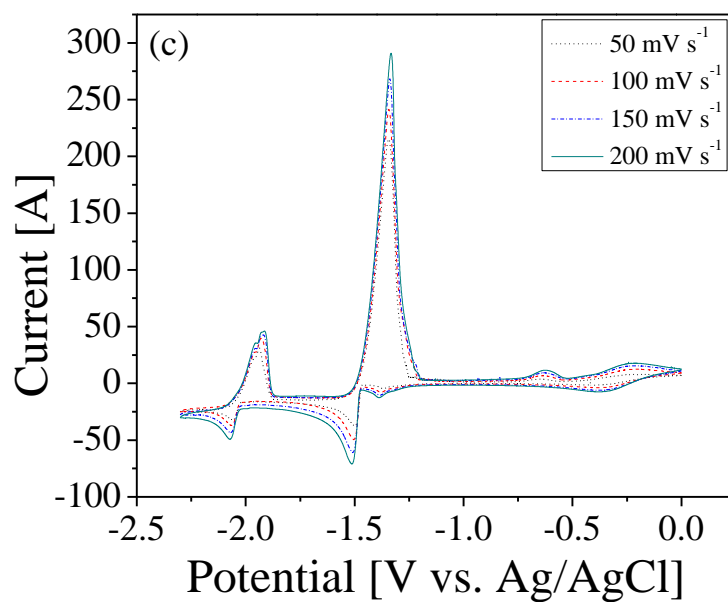
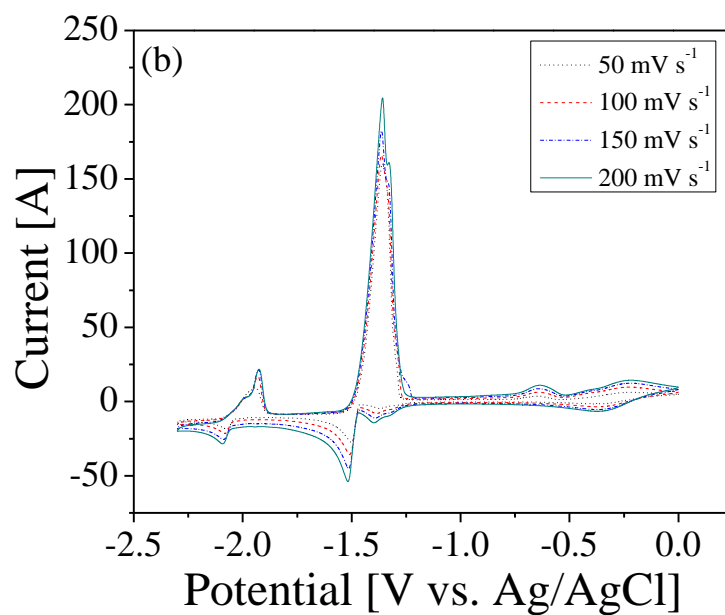
Literature	T (K)	Concentration	$\Delta G$ [kJ mol <sup>-3</sup> ]	$\gamma \times 10^3$	Methods
Masset [38]	673	$9.87 \times 10^{-5}$ (mol cm <sup>-3</sup> )	-745.1	0.29	CV, CP
	703		-741.8	0.35	
	773		-726.2	1.39	
	823		-712.9	4.47	
Kuznetsov [39]	723	$6.26 \times 10^{-5}$ (mol cm <sup>-3</sup> )		0.41	CV, LSV, CP, CA, EIS
	773			0.57	
	823			0.81	
Roy [41]	673		-731.7	2.0	OCP
	694		-726.4	3.2	
	723		-723.1	3.1	
Shirai [40]	773	$8.8 \times 10^{-4}$ (mol fraction)	-710.1		CV
Wentao [54]	723	$4.98 \times 10^{-3}$		8.42	Computational modeling
		$9.90 \times 10^{-3}$		11.5	
		$1.48 \times 10^{-2}$		15.4	
		$1.96 \times 10^{-2}$		20.2	
		$2.44 \times 10^{-2}$		26.8	
		$2.91 \times 10^{-2}$ (mole fraction)		34.5	

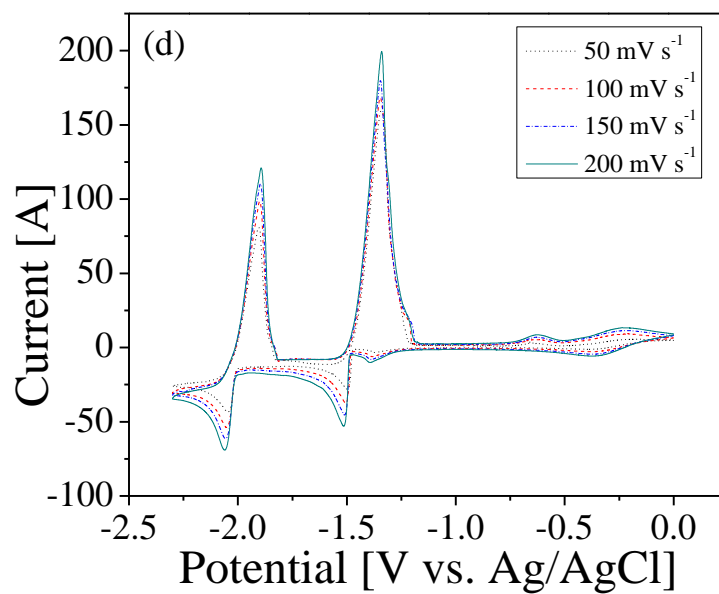
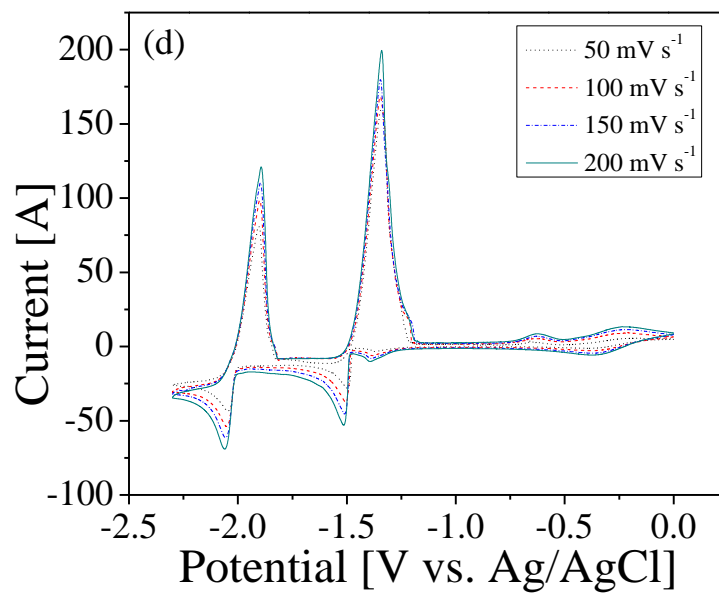
**Table A.5** Exchange current density of  $\text{U/U}^{3+}$  in  $\text{LiCl-KCl}$  from literature studies

Reference	Concentration	Exchange current density, $i_0$ (A cm <sup>-2</sup> )			
		723 K	773 K	798 K	923 K
Choi [48]	3.3 wt%		0.0584 (W) 0.0398 (C) 0.0204 (SS) 0.0202 (Zr)		
Rose [50]	5 wt%	0.0695			0.22
Ghosh [49]	4 wt%			0.008	
Lim [51]	1 wt%		0.01295	0.01833	0.02146

\*W: tungsten, C: carbon based, SS: stainless steel, and Zr: zirconium.

## Appendix B. Data from U-Gd mixtures





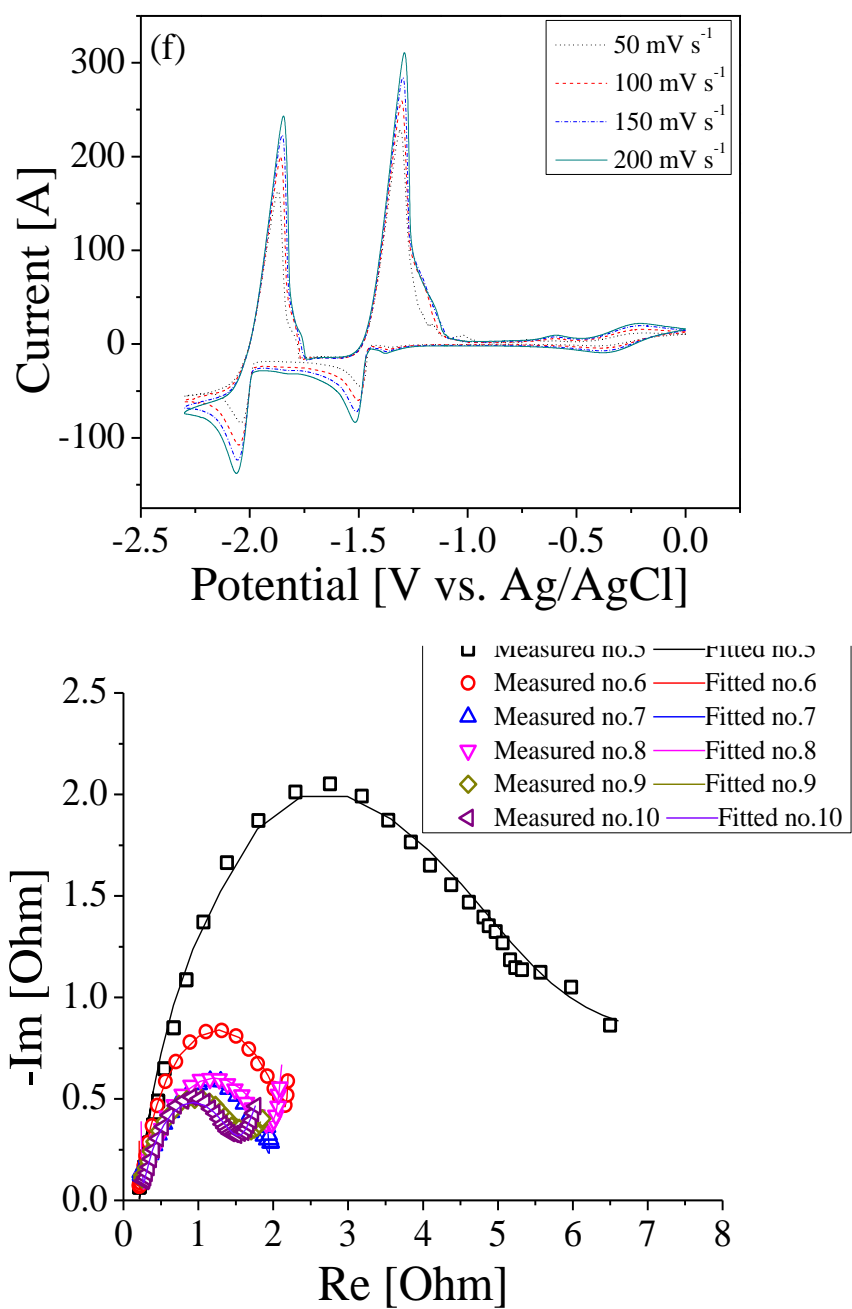


**Figure B.1** Cyclic voltammogram in (a) sample no. 5, (b) sample no. 6, (c) sample no. 7, (d) sample no. 8, (e) sample no. 9, (f) sample no. 10 at temperature of 773 K. The scan rate was ranging from 50 mV s<sup>-1</sup> to 200 mV s<sup>-1</sup>.

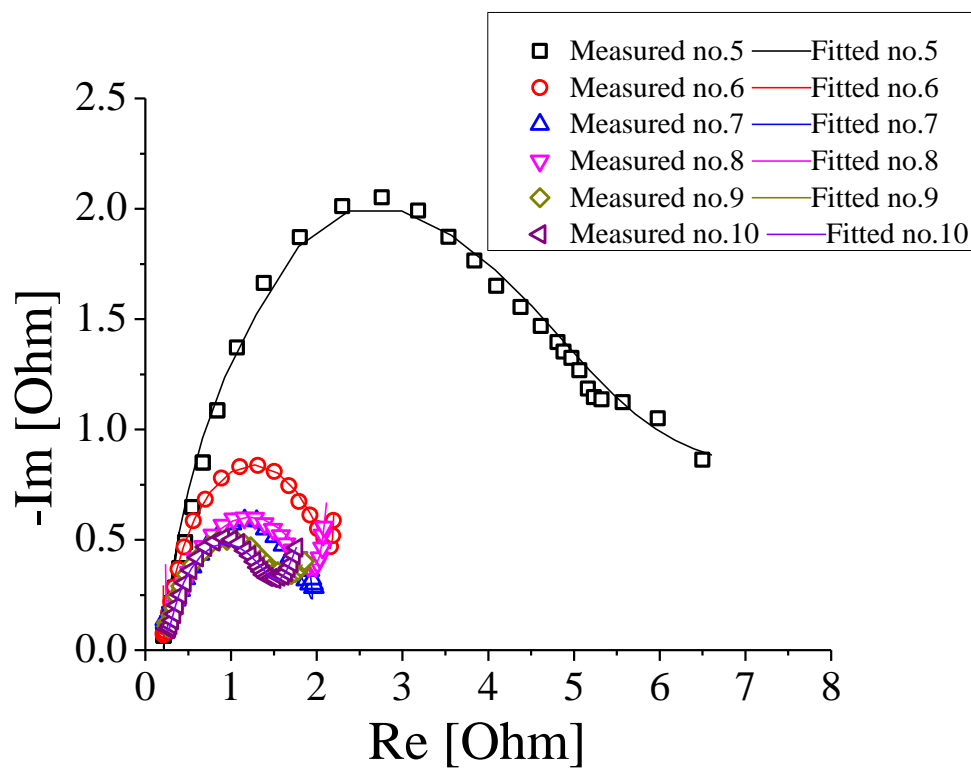


**Figure B.2** The measured and fitted impedance spectra in the mixture salts (sample no. 5 – 10) at 773 K.

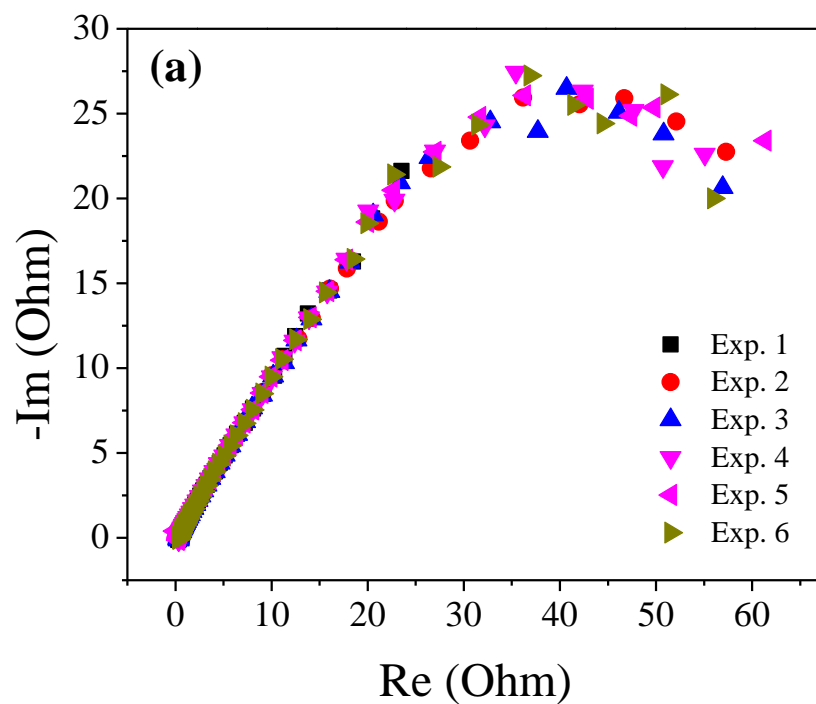
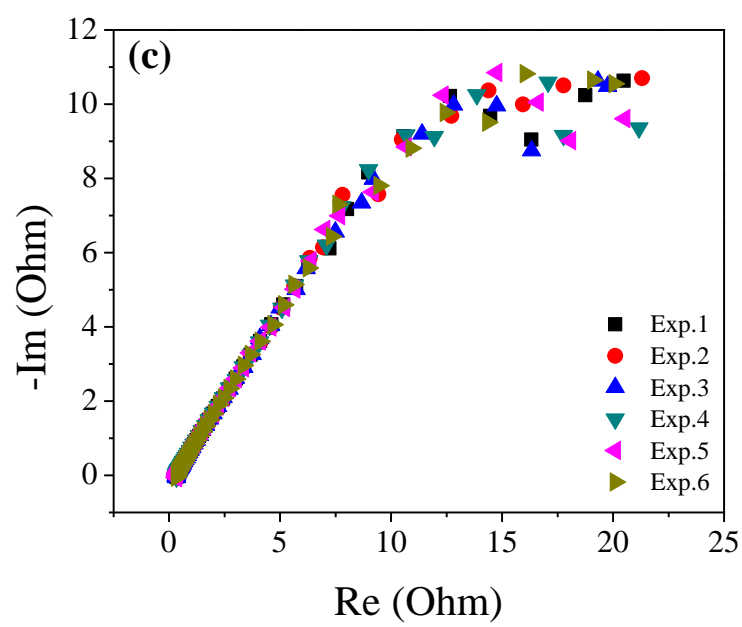
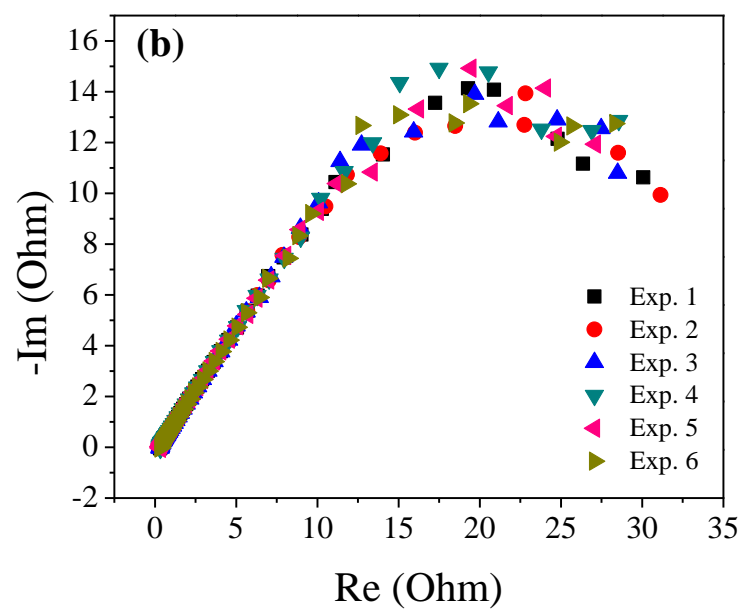


**Figure B.3** Equilibrium potentials of  $U^{3+}/U$  in  $LiCl-KCl-UCl_3-GdCl_3$  samples (no. 5 – 10), measured by OCP method. U metal was pre-deposited on the tungsten rod by applying potential at -1.6 V (vs. Ag/AgCl) for 30 seconds.



## **Appendix C. Exchange Current Density of $\text{Sm}^{3+}/\text{Sm}^{2+}$ Reaction in LiCl-KCl Molten Salt**

For the further observations of  $i_0$  kinetics in soluble-soluble system, samarium chloride ( $\text{SmCl}_3$ ) was examined as a surrogate material for actinides. EIS technique was conducted to determine the  $i_0$  of  $\text{Sm}^{3+}/\text{Sm}^{2+}$  in LiCl-KCl- $\text{SmCl}_3$  salt. Based on the calculated equilibrium potentials, Nyquist plots of EIS were obtained with concentrations from 1 wt% to 3 wt% at different temperature ranging from 673 K to 823 K. Two series of Voigt models composed with resistances and constant phase elements were applied as an equivalent circuit. By fitting the EIS spectra to the equivalent circuit, the charge transfer resistance along with other impedance parameters could be determined. From the measured charge transfer resistance, the  $i_0$  of  $\text{Sm}^{3+}/\text{Sm}^{2+}$  were calculated, ranging from  $1.04 \times 10^{-6} \text{ A cm}^{-2}$  to  $2.97 \times 10^{-6} \text{ A/cm}^{-2}$ . The temperature effect on  $i_0$  was evaluated by using Arrhenius temperature dependence and activation energy for  $\text{Sm}^{3+}/\text{Sm}^{2+}$  reaction was calculated to be  $-16.5 \text{ kJ mol}^{-1}$ . The experiments were prepared and conducted by Dr. Kerry Allahar under the support of Idaho National Laboratory-Laboratory Directed Research and Development (INL-LDRD).



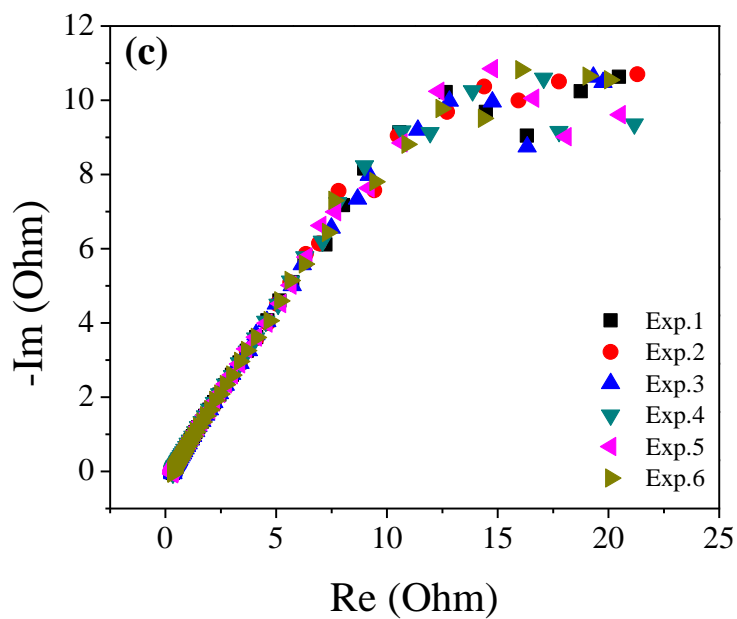


**Figure C.1** Nyquist plots of  $\text{Sm}^{3+}/\text{Sm}^{2+}$  at 773 K at concentrations of (a) 1 wt%  $\text{SmCl}_3$  (b) 2 wt%  $\text{SmCl}_3$  (c) 3 wt%  $\text{SmCl}_3$ . The electrode area was  $0.911 \text{ cm}^2$ .

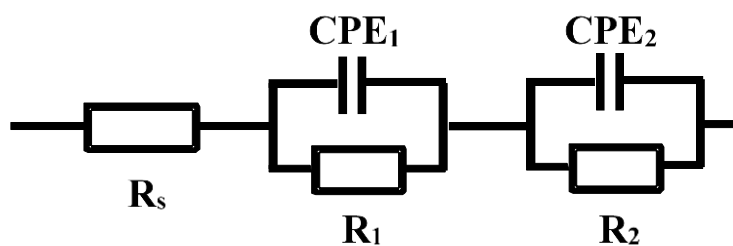


**Figure C.2** The equivalent circuit for the interface between the electrode and bulk salt, which is composed with resistances and CPEs.

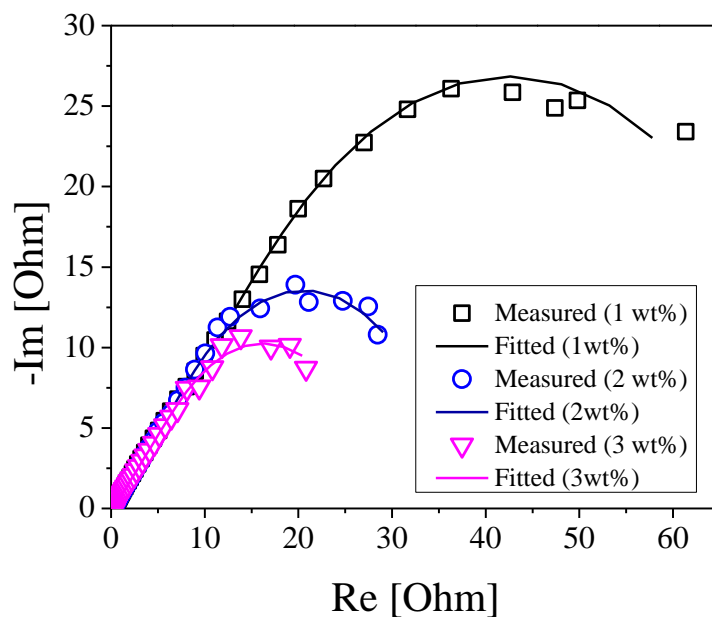


**Figure C.3** Examples of the measured and fitted Nyquist plots at 773 K.  $\chi^2 < 0.07$ .

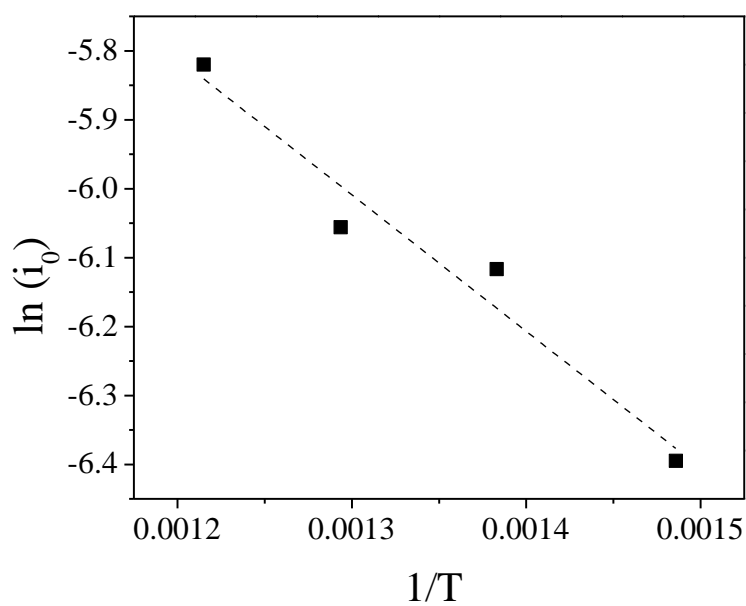


**Figure C.4** Plot of  $\ln(i_0)$  against  $1/T$  to show the Arrhenius temperature dependence.

**Table C.1** Impedance parameters measured from the curve fitting analysis

SmCl <sub>3</sub>	T	R <sub>s</sub>	CPE <sub>1</sub>	$\phi_1$	R <sub>1</sub>	CPE <sub>2</sub>	$\phi_2$	R <sub>2</sub>
(wt%)	(K)	(Ohm)	(F s $\phi^{-1}$ )		(Ohm)	(F s $\phi^{-1}$ )		(Ohm)
1	773	0.273	0.048	0.558	22.96	0.157	0.95	47.64
2	773	0.272	0.108	0.524	19.91	0.430	1	18.84
3	673	0.325	0.130	0.527	17.12	0.618	1	21.12
	723	0.303	0.145	0.512	16.09	0.65	1	14.93
	773	0.293	0.158	0.511	18.30	0.801	1	12.96
	823	0.276	0.168	0.547	22.02	0.52	0.94	9.50

**Table C.2** The calculated  $i_0$  and  $k^0$  at different concentrations and temperatures

SmCl <sub>3</sub>	T	No. exp	$i_0 \times 10^3$
(wt%)	(K)		(A cm <sup>-2</sup> )
1	773	8	$1.04 \pm 0.038$
2	773	7	$1.89 \pm 0.11$
3	673	9	$1.67 \pm 0.096$
	723	8	$2.21 \pm 0.043$
	773	8	$2.34 \pm 0.105$
	823	7	$2.97 \pm 1.18$